UNIVERSITÉ PARIS-SUD XI

École Doctorale : Particules, Noyaux, Cosmos

THÈSE DE DOCTORAT
présentée par

Nour Makke

Institut de Recherche sur les lois Fondamentales de l'Univers
CEA Saclay

Pour obtenir

Le GRADE de DOCTEUR EN SCIENCES
DE L'UNIVERSITÉ PARIS-SUD XI

Sujet:

Measurement of the polarization of strange quarks in the nucleon and determination of quark fragmentation functions into hadrons

soutenue le vendredi 28 octobre 2011 devant le jury composé de:

Franco Bradamante	(président)
Daniel de Florian	(rapporteur)
Jorg Pretz	(rapporteur)
Etienne Augé	(examinateur)
Fabienne Kunne	(directrice de thèse)

À mes parents, mes soeurs
à Ali et à Stefano.

Remerciements

Mes premiers mots s'adressent à ma directrice de thèse, Fabienne Kunne. Je la remercie pour la confiance qu'elle m'a montrée dès le début de ma thèse, pour la disponibilité et le support qu'elle m'avait accordés tout au long des trois années de doctorat. Je la remercie également pour ses conseils, ses questions, ses remarques et son soutien ainsi que pour m'avoir donné l'occasion d'encadrer le travail de la jeune étudiante L. Shilton. Finalement j'apprécie le respect qu'elle a montré face à mon activité d'enseignement qui a pris sans doute du temps de ma thèse.

Je remercie également tous les membres du jury de ma thèse. Merci à Franco Bradamante pour avoir accepté d'être un membre du jury et de le présider. Je remercie également Etienne Augé qui a attentivement examiné ma thèse et accepté de faire partie du jury. Un chaleureux remerciement à Daniel de Florian pour l'intérêt qu'il a montré à ma thèse en acceptant d'être rapporteur et pour le temps qu'il a accordé et qu'il accorde encore à nos discussions qui m'ont été d'une grande utilité. Jörg Pretz m'a fait le grand plaisir d'être rapporteur de ma thèse. Finalement je les remercie tous pour le temps qu'ils ont consacré à la la lecture de ma thèse.

Mes sincères remerciements s'adressent à Michel Garcon, chef du service de physique nucléaire, et à Françoise Augé, son adjointe. Je les remercie de m'avoir bien accueilli dans le service, d'avoir tenu à suivre mon travail ainsi que pour le soutien, la confiance et le support qu'ils m'ont montrés.

Je ne peux certainement pas oublier tout le groupe COMPASS du SPhN. Je remercie chaleureusement Damien qui a supervisé mon travail sur les détecteurs avec beaucoup de disponibilité, de confiance et de bonne humeur. Merci aussi pour m'avoir aidé dans tous mes soucis quotidiens, avoir Damien dans son équipe est une chance. Je tiens aussi à remercier Yann. J'ai toujours apprécié ses divers talents, ses compétences, ses multiples idées, ses questions de perspectives, sa patience et sa motivation. Je remercie Claude Marchand pour ses conseils, son soutien et ses remarques. J'apprécie énormément sa rigueur et son intuition scientifiques. Merci à Stephane, Étienne, Andrea. Je tiens aussi à remercier chaleureusement Nicole pour la disponibilité et la confiance qu'elle m'a témoignées ainsi que pour le soutien et l'intérêt avec lesquels elle a suivi mon travail. Je voudrais finalement remercier les jeunes chercheurs Astrid Morreale, Liugi Capozza et Maxence Vandenbroucke pour tous les moments qu'on a passés ensemble. Je n'oublie pas Florent qui m'a dévoilé les secrets de COMPASS pendant mes premiers pas en thèse. En plus du groupe COMPASS du SPhN, j'adresse mes remerciements à tous mes collègues de le collaboration. J'adresse finalement un merci tous mes collègues du SPhN, en particulier Herve Moutarde, Frank Gunsing.

Je tiens à remercier très chaleureusement Stefano Panebianco pour avoir été à mon côté à tout moment de mon doctorat. Stefano, je t'adresse un merci du fond du coeur pour ta franchise, ton honnêteté, ta compréhension, tes précieux conseils et pour l'appréciation que tu as montré pour mon travail de recherche. Merci pour le temps que tu as consacré pour nos discussions scientifiques et générales.

Un grand merci s'adresse à Achille Stocchi, le directeur du laboratoire de l'accélérateur linéaire. Je ne trouve pas de mots à la hauteur de ce que j'ai à te dire. Ton estime, ta confiance et ton soutien m'ont fait honneur. Je t'adresse un très chaleureux merci pour ton suivi constant depuis mon arrivée en France. Ta confiance m'a été et m'est toujours importante et j'espère ne jamais la décevoir.

Mes derniers mots et mes plus chers remerciements s'adressent à mes parents et mes soeurs. Mes expressions ne seront certainement pas à la hauteur du soutien et de la confiance que vous m'avez toujours témoignés en particulier au cours de ces trois années de doctorat. Á la fin je remercie ma copine Samira Hassani dont le soutien était essentiel et motivant. Je te remercie Samira pour l'affection que tu m'as témoignée et que je n'oublierai jamais.

Contents

Chapter 1

Introduction

The structure of matter can be explored starting from the structure of the most abundant element in the universe, the proton. The internal structure of the proton determines its fundamental properties, which in turn influence the properties of the nuclei. Understanding how the proton is built in terms of its quarks and gluons constituents is one of the most important and challenging questions in hadronic physics. One of the best tools to probe the nucleon structure is the electromagnetic interaction because of the well known underlying theory, Quantum Electrodynamics (QED), in addition to the validity of its perturbative approach since $\alpha_{QED} \sim 1/137$. The nucleon internal structure can thus be studied by scattering electrons (or muons) off nucleons, in a similar way that atoms can be studied through scattering of X-rays, neutrons and electrons. The most useful scattering processes are: Elastic Scattering where the nucleon remains unchanged, and Deep Inelastic Scattering where one of the proton building blocks, quarks, antiquarks and gluons, interacts with the virtual photon and the proton gets smashed into many hadrons due to the quark fragmentation process. While elastic scattering gives access to the charge density distribution inside the nucleon, DIS allows one to map out the quark and gluon distributions in momentum space as well as to study the spin structure of the nucleon, which is another fundamental and challenging question in hadronic physics.

Deep inelastic scattering has been first realized at the Stanford Linear Accelerator Center (SLAC) in the 1960s, resulting in the first experimental evidence that the proton has a substructure of point-like particles called partons. These point-like objects were then identified to the quarks earlier introduced by Gell-Mann to explain the spectrum of hadrons observed in different scattering experiments. The Gell-Mann's quark model presented quarks as fermions, with electric charges of fractions of 1/3 and 2/3 of the electron charge. In this picture, quarks must obey the Pauli exclusion principle. However the latter seemed to be violated with the discovery of the Δ^{++}, a particle formed by three quarks of the same flavor, with all spins aligned (spin 3/2). The conservation of the Pauli principle leads then to the introduction of a new quantum number, the color charge, in the context of a new theory of strong interaction, Quantum ChromoDynamics (QCD). In this theory, the strong interaction between colored objects is mediated by bosons called gluons, which carry themselves color charge in contrast to the QED mediators. This leads to the self-coupling of the gluons and consequently to a coupling constant α_{QCD} dependent on the scale at which the interaction is observed. This scale dependence of α_{QCD} gives rise to two QCD fundamental properties: asymptotic freedom and confinement. At short distances (large energies), the interaction between colored objects decreases and α_{QCD} tends to zero. This is known as asymptotic freedom. In other words quarks and gluons behave like quasi-free particles and the scattering between quarks can be calculated using a perturbative approach. At large distances however, the interaction between colored objects increases and α_s tends to infinity, giving rise to the confinement of quarks and gluons inside colorless particles. The interaction can not be described using a perturbative approach in this case because the perturbative expansion diverges. It must be parametrized by phenomenological models. In DIS, the separation between short distance sub-process (quark-photon interaction) and large distance process (quark fragmentation into final state hadrons) is ensured by the factorization theorem. The latter gives access to two phenomenological parametrization: parton distribution functions which describe

the nucleon initial state and quark fragmentation functions which parametrize the fragmentation of quarks into final state hadrons. This marks the great power of DIS.

In its naïve picture, the proton consists of three "valence" quarks. In the QCD picture, the effects of the gluons and the sea of virtual quark-antiquark pairs are added to the three valence quarks. Since strange quark-antiquark pairs are only part of the sea, the strangeness content of the proton is of crucial importance and addresses fundamental questions whether the strange quark s and antiquark $\bar{s}$ distributions are the same, whether the strangeness contribution to the spin is positive or negative... All these questions motivated the present work which deals with basics of hadronization of quarks (named fragmentation).

The strangeness content of the proton can be studied using the weak interaction via parity-violating electron scattering or using the electromagnetic interaction via deep inelastic scattering of leptons off nuclear targets at moderate energies. The current knowledge of the strange quark distribution (s) is provided by parametrization, where in most cases, s is assumed to be related to the non-strange sea quark distributions $\bar{u}$ and $\bar{d}$. A recent measurement of the sum of strange quark and antiquark distributions ($s + \bar{s}$) has been performed by the Hermes collaboration in a limited kinematic domain. The result was found to be lower than predictions, by a factor larger than 2, in the covered kinematic range. This observation highlights the need for further measurements of s.
The contribution of the spin of strange quarks to the nucleon spin remains an issue. This quantity, Δs, is accessible within some assumptions via inclusive DIS, where only the scattered lepton is detected in the final state, and also via semi-inclusive DIS where, in addition to the scattered lepton, a hadron carrying strange quarks is detected in coincidence. While all inclusive measurements result in negative value of Δs, semi-inclusive measurements result in a values compatible with zero. The results depend crucially on the choice of quark fragmentation functions (FFs) into hadrons, in particular, the fragmentation function of strange quarks into kaons, still poorly known. This marks the need of a direct extraction of FFs from experimental data. All these observations highlight the poor knowledge of the strangeness content of the proton and indicate the need of further measurements in both the polarized and the unpolarized sectors.

The present work is dedicated to the study of the strangeness content of the proton and consists in two measurements: the contribution of the spin of strange quarks to the nucleon spin and the extraction of quark fragmentation functions into hadrons. The measurements are performed using experimental data collected by the COMPASS experiment at CERN by scattering a muon beam, provided by the CERN Super Proton Synchrotron (SPS), on both proton (NH_3) and deuterium (^{6}LiD) polarized targets. COMPASS has a 50 m long spectrometer equipped with different tracking detectors and provides the particle identification facilities, in particular the kaon identification.
The determination of the strange quark contribution to the nucleon spin Δs is performed using spin asymmetries of cross sections of kaon production in semi-inclusive DIS. The extraction of the quark fragmentation functions into pions and kaons is performed using hadron multiplicities, defined as the average number of hadrons produced per DIS event. For this purpose, pion and kaon multiplicities are measured in bins of different kinematic variables.

Finally, a part of the present work is devoted to the study of the performances of Micro-pattern Gaseous detectors, the pixelized Micromegas. They are developed in the context of a project aiming to replace the present micromegas detectors. To fulfill the new requirements needed for the COMPASS II program, the new detectors must stand a hadron beam flux more than five times higher than presently. In addition, they must be active in the central part, and must be equipped with readout electronics lighter than presently used electronics. Two prototypes fulfilling the new requirements were tested in nominal COMPASS conditions.

Chapter 2

Nucleon Spin Structure

Hard scattering processes are the best tools to probe the nucleon internal structure. One of these processes is the Deep Inelastic Scattering (DIS) which consists in probing the internal structure of a nucleon (composite object) using a leptonic beam. The leptonic beam interacts with one nucleon in the target by exchanging a virtual photon (electromagnetic interaction) or a Z boson (weak interaction). At sufficiently high momentum transfer the interaction occurs between lepton and almost free partons, quarks and anti-quarks, which fragment (or hadronize) into final state hadrons. figure 2.1 shows the Feynman diagram of the deep inelastic scattering process. Three kinds of reaction can be defined depending on the selected final state: inclusive, semi-inclusive and exclusive. In inclusive reactions $[l + N \rightarrow l' + X]$, only the scattered lepton is detected in the final state. In semi-inclusive reactions $[l + N \rightarrow l' + h + X]$, one or more of the final state hadrons are detected in coincidence with the scattered lepton. Finally, in exclusive reactions $[l + N \rightarrow l' + h]$,x all final state hadrons are detected.

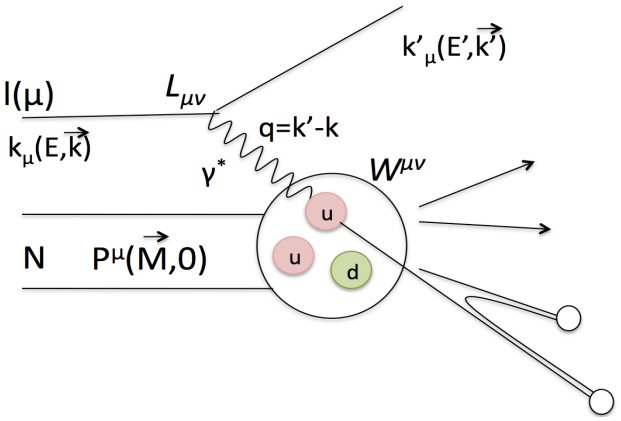

Figure 2.1: Shematic view of a deep inelastic scattering event of a lepton l with a four-momentum k_μ and energy E scattering off a nucleon N with a four-momentum P and mass M through the exchange of a virtual photon (γ^*).

2.1 Deep Inelastic Scattering

A deep inelastic scattering event is described by its kinematic which can be calculated using the four-momenta of the incident lepton $[k = (E, \overrightarrow{k})]$ and the scattered lepton $[k' = (E', \overrightarrow{k'})]$ as well as the four-momentum of the target nucleon $[P = (M, \overrightarrow{P})]$. These vectors allow to define three Lorentz invariant variables [2] which characterize the deep inelastic scattering event:

$$Q^2 = -q^2 = -(k - k') \simeq^{lab} 4EE' \sin^2\left(\frac{\theta}{2}\right) \tag{2.1}$$

$$W^2 = (P+q)^2 \simeq^{lab} M^2 + 2M\nu - Q^2 \tag{2.2}$$

$$s = (P+k)^2 \simeq^{lab} M^2 + 2ME \tag{2.3}$$

The equations 2.1, 2.2 and 2.3 in the laboratory frame hold for a fixed target ($\vec{P} = \vec{0}$). The lepton mass has been neglected since only the ultra relativistic limit is considered in the following. Q^2 is the squared four momentum of the virtual photon (γ^*). It represents the resolution of the electromagnetic probe and defines the scale at which the nucleon structure is being investigated in the reaction. W^2 denotes the squared invariant mass of the outgoing hadronic system and s denotes the center of mass of the interaction. The elastic lepton-nucleon scattering is defined by $W^2 = M^2$ so that the proton remains unchanged and $Q^2 = 2M\nu$. The so called Bjorken scaling variable (x_B) is defined as:

$$x_B \equiv x = \frac{Q^2}{2P.q} = \frac{Q^2}{2M\nu} \tag{2.4}$$

In elastic scattering $x = 1$ while in inelastic scattering x measures the inelasticity of the event and consequently $0 < x_B < 1$. This variable is interpreted in the parton model (section 2.2.2) as the fraction of the proton momentum carried by the quark that absorbs the virtual photon. From the theoretical point of view, the deep inelastic scattering domain is defined by $Q^2 > 1$ GeV^2 and $W^2 > 4$ GeV^2. The first requirement ensures a sufficiently high resolution to probe the internal structure of the nucleon and the second one avoids the resonance regions [2]: At moderate Q^2, one might excite the proton into a Δ-state and thus produce a π-meson [$ep \to e\Delta^+ \to ep\pi^0$]. For these events, $W^2 = M_\Delta^2$.

The relevant kinematic variables that characterize deep inelastic scattering event and final state hadrons are defined in table 2.1.

$Q^2 = -q^2 = 4EE'\sin^2(\theta/2)$	Negative squared four-momentum transfer
$x = Q^2/2P\cdot q = Q^2/2M\nu$	Bjorken scaling variable (fraction of the nucleon's momentum carried by the struck quark)
$\nu = P\cdot q/M = E - E'$	Lepton energy transferred to the virtual photon γ^*
$y = P\cdot q/P\cdot k = \nu/E$	Fraction of the lepton energy transferred to the virtual photon γ^*
$W^2 = (P+q)^2 = M^2 + 2M\nu - Q^2$	Invariant mass of the outgoing hadronic system
$p \equiv (E_h, \overrightarrow{p})$	Four-momentum of a final state hadron h
$z = P\cdot p/P\cdot q = E_h/\nu$	Energy fraction of the virtual photon carried by a final state hadron h
θ_h	Hadron polar angle with respect to the virtual photon direction
$p_T = p\sin(\theta_h)$	Hadron momentum component transverse to the photon momentum in the center-of-mass frame
$p_\parallel = \vec{p}\cdot(\vec{q}/\|\vec{q}\|)$	Hadron momentum component parallel to the photon momentum in the center-of-mass frame
$x_F = p_\parallel/\|\vec{q}\|$	Feynman variable

Table 2.1: Definition of the kinematic variables used in deep inelastic scattering. The top part includes variables that characterize a DIS event. The bottom part includes semi-inclusive variables that characterize final state hadrons.

2.2 Cross section and structure functions F_1 and F_2

The inclusive deep inelastic scattering differential cross section [3] can be factorized as the contraction of the leptonic tensor $L_{\mu\nu}$ and the hadronic tensor $W^{\mu\nu}$, which describe respectively the emission and the absorption of the virtual photon by the incident lepton and the target nucleon.

$$\frac{d^2\sigma}{dE'd\Omega} = \frac{\alpha^2}{2MQ^4} \cdot \frac{E'}{E} \cdot L_{\mu\nu}W^{\mu\nu} \tag{2.5}$$

where the cross section is already summed over the final lepton spin since the latter cannot be measured in practice. $\alpha = e^2/4\pi \approx 1/137$ is the electromagnetic coupling constant, also known as the fine structure constant. Since leptons are point-like particles, the expression of the leptonic tensor is known and is calculated in Quantum electrodynamics. The hadronic tensor, however, is unknown and parametrize our total ignorance of the nucleon structure.

2.2.1 Unpolarized Cross Section

In the unpolarized case the leptonic tensor, which is calculated in Quantum Electrodynamics (QED), is given by [3]:

$$L_{\mu\nu} = 2 \cdot \left[k_\mu k'_\nu + k'_\mu k_\nu - g_{\mu\nu}(k \cdot k' - m^2)\right] \tag{2.6}$$

Here m denotes the lepton mass and $g_{\mu\nu}$ denotes the metric tensor, i.e. a diagonal matrix with $g_{00} = 1$ and $g_{11} = g_{22} = g_{33} = -1$. Since the hadronic tensor encodes our ignorance of the structure of the target nucleon and cannot be calculated exactly, it can be written in general form as a linear combination[1] of the metric tensor $g_{\mu\nu}$ and the independent momenta P_μ and q_μ. The contents of $W^{\mu\nu}$, however, are constrained by symmetry requirements as Lorentz invariance and parity conservation. These requirements reduces $W^{\mu\nu}$ to the expression [3]:

$$W^{\mu\nu} = -W_1 g^{\mu\nu} + W_2 \frac{P^\mu P^\nu}{M^2} + W_3 \frac{q^\mu q^\nu}{M^2} + W_4 \frac{P^\mu q^\nu + P^\nu q^\mu}{M^2} \tag{2.7}$$

where W_i are functions of the Lorentz variables ν and Q^2. The further requirement of the electromagnetic current conservation ($q_\mu W^{\mu\nu} = 0$) reduces $W^{\mu\nu}$ to only two terms:

$$\frac{1}{2M}W^{\mu\nu} = \left(-g^{\mu\nu} - \frac{q^\mu q^\nu}{Q^2}\right).W_1(\nu, Q^2) + \frac{1}{M^2}\left(p^\mu + \frac{P.q}{Q^2}q^\mu\right)\left(p^\nu - \frac{Pq}{Q^2}q^\nu\right).W_2(\nu, Q^2) \tag{2.8}$$

The functions $W_1(\nu, Q^2)$ and $W_2(\nu, Q^2)$ are called structure functions and parametrize the internal structure of the target nucleon. By combining equations (2.5), (2.6) and (2.8), the cross section can be derived and one obtains the following expression:

$$\frac{d^2\sigma}{dE'd\Omega} = \left(\frac{d\sigma}{d\Omega}\right)_{Mott} . \left\{W_2(\nu, Q^2) + 2W_1(\nu, Q^2)\tan^2\left(\frac{\theta}{2}\right)\right\} \tag{2.9}$$

where

$$\left(\frac{d\sigma}{d\Omega}\right)_{Mott} = \frac{4\alpha^2 E'^2}{Q^4}\cos^2\left(\frac{\theta}{2}\right) \tag{2.10}$$

denotes the Mott cross section which describes the scattering of leptons off spin-less and point-like particles. The structure functions $W_1(\nu, Q^2)$ and $W_2(\nu, Q^2)$ thus parametrize the deviation of the nucleon cross section from the point-like particle behavior. They can be written as:

$$W_1(\nu, Q^2) = \frac{Q^2}{4M^2}\delta\left(\nu - \frac{Q^2}{2M}\right) \tag{2.11}$$

$$W_2(\nu, Q^2) = \delta\left(\nu - \frac{Q^2}{2M}\right) \tag{2.12}$$

In the so called Bjorken limit, defined by $Q^2 \to \infty$ for a fixed ratio $(Q^2/P.q)$, the structure functions can be expressed in terms of the Bjorken variable x only:

$$MW_1(\nu, Q^2) = F_1(x, Q^2) \to F_1(x) \tag{2.13}$$

[1] The antisymmetric contributions to the hadronic tensor $W^{\mu\nu}$ are omitted because they vanish after insertion in Eq.2.5 due to the symmetric expression of the leptonic tensor.

$$\nu W_2(\nu, Q2) = F_2(x, Q^2) \to F_2(x) \tag{2.14}$$

where $F_1(x, Q^2)$ and $F_2(x, Q^2)$ are the dimensionless structure functions in terms of which the cross section is usually expressed. The independence of F_1 and F_2 structure functions upon the resolution at given x indicates that, at sufficiently high energies, the virtual photon is indeed interacting with point-like free particles inside the nucleon, i.e. the constituents of the nucleon. This behavior, known as the Bjorken scaling, has been predicted by Bjorken and subsequently measured at SLAC in the 60's. Comparing Eq (2.9) with the cross section for scattering off spin-1/2 point-like particles gives

$$2xF_1(x) = F_2(x) \tag{2.15}$$

This equation is called the *Callan-Gross* relation. It was obtained assuming that the constituents of the nucleon have spin 1/2; thus the interaction in the nucleon occurs on spin-1/2 point-like particles. The experimental verification of the *Callan-Gross* relation proves that the constituents of the nucleon are indeed spin-1/2 objects.
The unpolarized cross section can be written as a function of x_B and Q^2 in terms of the dimensionless structure functions :

$$\frac{d^2\sigma}{dxdQ^2} = \frac{4\pi\alpha^2}{xQ^4}\left[xy^2F_1(x, Q^2) + (1 - y - \frac{\gamma^2y^2}{4})F_2(x, Q^2)\right] \tag{2.16}$$

where the lepton mass terms are neglected and $\gamma^2 = \frac{Q^2}{\nu^2} = \frac{2Mx}{\nu} << 1$. The measurement of the cross section permits the access to the structure functions F_1 and F_2 (figure 2.4).

2.2.2 Interpretation within the Parton Model

The Parton Model provides a simple and naïf view of the internal structure of the nucleon. In this model, the nucleon is considered to be composed of point-like particles called partons which do not interact with each other. It is formulated in the so called *infinite momentum frame* where the nucleon is moving with high momentum along the z axis such that partons masses and momenta transverse to z can be neglected. It can be viewed as a beam of parallel moving partons. The model relies on the feature that the interaction between the individual partons is weak at short distances (high energies). As a consequence, if the interaction with the lepton occurs on sufficiently short time scales, the mutual influence among the partons inside the nucleon are frozen and the partons can be treated as free. If ξ is the fraction of the nucleon longitudinal momentum carried by a given parton, after absorption of the virtual photon, the four-momentum of the parton is given by :

$$(\xi P + q)^2 = 0 + q^2 + 2\xi P.q = 0$$
$$\Rightarrow \xi = -q^2/2P.q = x$$

The Bjorken variable thus represents, in the infinite momentum frame, the fraction of the nucleon longitudinal momentum carried by the parton which absorbs the virtual photon. In this naïve picture, the virtual photon can only interact with a parton (a quark) since gluons are neglected in addition to the feature that gluons do not carry an electromagnetic charge. This picture allows to introduce the parton distribution functions (PDFs) q_i which describe the density probability to find a quark of flavor i carrying a fraction x of the nucleon longitudinal momentum. The lepton-nucleon cross section can thus be written as an incoherent sum over the lepton-quark cross section :

$$\left(\frac{d^2\sigma}{dxdQ^2}\right)_{lN\to lX} = \sum_i \int_0^1 d\xi q_i(\xi)\left(\frac{d^2\sigma}{dxdQ^2}\right)_{lq_i\to lq_i} \tag{2.17}$$

Here the sum runs over all quark flavors $q \in [u, d, s, c, b, t]$[2] and their anti-quarks. Neglecting quark masses, the lepton-quark cross section can be written as

[2]The contribution of heavy quarks is expected to be negligible.

$$\left(\frac{d^2\sigma}{dxdQ^2}\right)_{lq_i\to lq_i} = \frac{2\pi\alpha^2 e_i^2}{Q^4}\left(y^2-2y+2\right)\delta(\xi-x)$$

Here, e_i denotes the fractional charge of the quark of flavor i in terms of the electron charge. Combining this expression with Eq (2.17) and integrating over ξ yields the lepton-nucleon cross section

$$\left(\frac{d^2\sigma}{dxdQ^2}\right)_{lN\to lX} = \frac{2\pi\alpha^2}{Q^4}\left(y^2-2y+2\right)\sum_i e_i^2 q_i(x) \tag{2.18}$$

The comparison of Eq (2.17) with Eq (2.18) leads to

$$xy^2F_1(x,Q^2)+(1-y)F_2(x,Q^2) = (y^2-2y+2)\sum_i e_i^2 q_i(x)$$

$$2xF_1(x,Q^2) = F_2(x,Q^2) = \sum_i e_i^2 x q_i(x) \tag{2.19}$$

The total fraction of the nucleon longitudinal momentum carried by quarks of all flavors is given by the sum $\sum_i \int_0^1 xq_i(x)$ which should be 1 in the naïve parton model picture. However, using experimental measurements of the structure functions F_1 and F_2, it turns out to be of the order of 0.5. This observation implies the existence of additional constituents in the nucleon, which are electrically neutral. They have been then identified to the strong interaction messengers, the gluons. Their role is discussed in an improved version of this model.

2.2.3 QCD improved parton model

In order to take into account the new constituents of the nucleon, the parton model has been developed within the context of Quantum Chromodynamics (QCD), which is a gauge theory of the strong interaction [2]. While QED is based on the abelian group U(1) and the photons do not carry electric charge, QCD is based on the non abelian group SU(3) and consequently gluons themselves carry color charge. This fundamental property implies two consequences. The first consequence corresponds to the gluon self-coupling, i.e. gluons can couple directly to one another giving rise to three-gluon vertices and four-gluon vertices. The second consequence represents the scale dependent coupling constant of the strong interaction (α_S) which decreases (increases) at high energy scales (low energy scales). This phenomenon is known as asymptotic freedom, meaning that quarks and gluons behave like free particles at high energies. At low energy scales (large distances), α_S increases giving rise to the property of confinement, i.e. only colorless objects can be observed in the hadronic final states (colored objects as quarks and gluons appear only as hadron constituents).
This behavior of α_S implies two regimes: perturbative and non perturbative. Processes which involve low energy scale are called soft and cannot be calculated within a perturbative approach while processes which involve high energy scale are called hard processes and can be computed perturbatively. For example, color interactions between quarks and gluons at sufficiently high energies[3] can be computed using the perturbative techniques of QCD. The large energy scale hadronic structure, however, cannot be computed in perturbative QCD. To define the limit between the perturbative regime and the non perturbative one, a factorization scale Λ is introduced. Depending on the renormalization scheme and the considered reaction, Λ has a value of $200-300$ MeV. For deep inelastic scattering for example, the scale of the interaction is defined by Q^2. For sufficiently large Q^2 (e.g. > 1 GeV^2), the cross section can be factorized in terms of the cross section of a hard sub-process (involving quarks and gluons and computed in perturbative QCD) and a soft part parametrizing the hadronic structure in terms of PDFs. The parton model is then equivalent to the leading order of perturbative QCD in which PDFs are independent of Q^2. When the resolution of the probe Q^2 increases, the picture can be seen as follows [2]. As Q^2 increases, the resolution of the photon allows to probe the point-like valence quarks within the proton. If quarks are non-interacting, no further structure can be resolved as Q^2 increases further. However, QCD predicts that with increasing Q^2, each quark is surrounded by a cloud of

[3] like proton-proton collisions at the center of mass of 7 TeV

quarks and gluons. The nucleon appears to be composed of a larger number of resolved quarks and gluons, all sharing the total nucleon longitudinal momentum. As a consequence, the number of partons that carry a high fraction x of the total nucleon momentum decreases while the number of partons that carry a low fraction of the nucleon momentum increases.

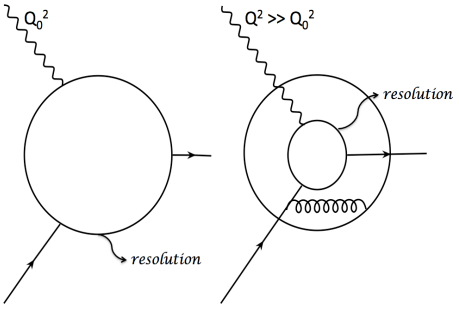

Figure 2.2: The quark structure [2] of the proton probed at different scales Q^2. At Q_0^2, the virtual photon probes only point-like valence quarks. As far as Q^2 increases, the resolution of the virtual photon allows to separate the probed quark from the cloud of quarks and gluons which surround it.

This behavior is described by the Dokshiter-Gribov-Lipatov-Altarelli-Parisi (DGLAP) Q^2 evolution equations [Eqs. 2.20 and 2.21]. Using the $SU(3)$ flavor symmetry one can distinguish different combinations of the parton distribution functions : the flavor singlet (S) combination [4] $\Sigma = u + d + s$, and the non-singlet (NS) combination $u - d$ or $u + d - 2s$. The Q^2 evolution of the non-singlet combination is given by:

$$\frac{d}{d\ln Q^2} q^{NS}(x, Q^2) = \frac{\alpha_s(Q^2)}{2\pi} P_{qq}^{NS} \otimes q^{NS}, \tag{2.20}$$

The Q^2 evolution of the gluon distribution couples to that of the singlet distribution as follows:

$$\frac{d}{d\ln Q^2} \begin{pmatrix} \Sigma(x, Q^2) \\ g(x, Q^2) \end{pmatrix} = \frac{\alpha_s(Q^2)}{2\pi} \begin{pmatrix} P_{qq}^S & 2n_f P_{qg} \\ P_{gq} & P_{gg} \end{pmatrix} \otimes \begin{pmatrix} \Sigma(x, Q^2) \\ g(x, Q^2) \end{pmatrix} \tag{2.21}$$

where n_f is the number of flavors. Equations 2.20 and 2.21 reflect the feature that, at given Q^2, a quark of flavor q, carrying the fraction x of the nucleon longitudinal momentum, can be radiated from a quark or a gluon that carried a higher fraction x' of the nucleon momentum. $P_{ab}(x/x')$ are called splitting functions. They define the probability that a parton b radiates a parton a. Once $\Sigma(x, Q^2)$ and $g(x, Q^2)$ are known at some Q^2 scale, the DGLAP equations allow to compute them at other scales as far as perturbation theory holds.

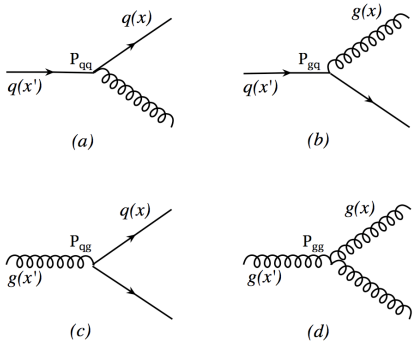

Figure 2.3: Splitting functions [2] $P_{ab}(\xi, Q^2)$ where b denotes the initial parton and a denotes the final parton with the fractional energy $\xi = x/x'$.

[4] In the singlet combination all coefficients are identical, while in the non-singlet combination the sum of the coefficients is zero.

2.2.4 The F_2 structure function

The measurement of the structure function F_2 is of special interest because it is the main source of information about parton distribution functions. These functions can be determined by performing the so called QCD global analysis of the existing F_2 measurements and using the DGLAP equations.

The structure function F_2 has been measured in fixed target experiments with the center of mass energy of $\sim 10 - 30$ GeV as well as in ep collisions with larger center of mass energy of 300 GeV, providing a very wide kinematic range in x and Q^2. Figure 2.4 shows the Q^2 dependence of F_2 measured by different experiments in a wide x range. F_2 is found to be independent of Q^2 for intermediate x as expected from the parton model. However for smaller and larger x, the Bjorken scaling is broken due to the large contribution of the gluons in these regions. One can evaluate this contribution using a NLO QCD global analysis of F_2 data, as shown in Figure 2.5.

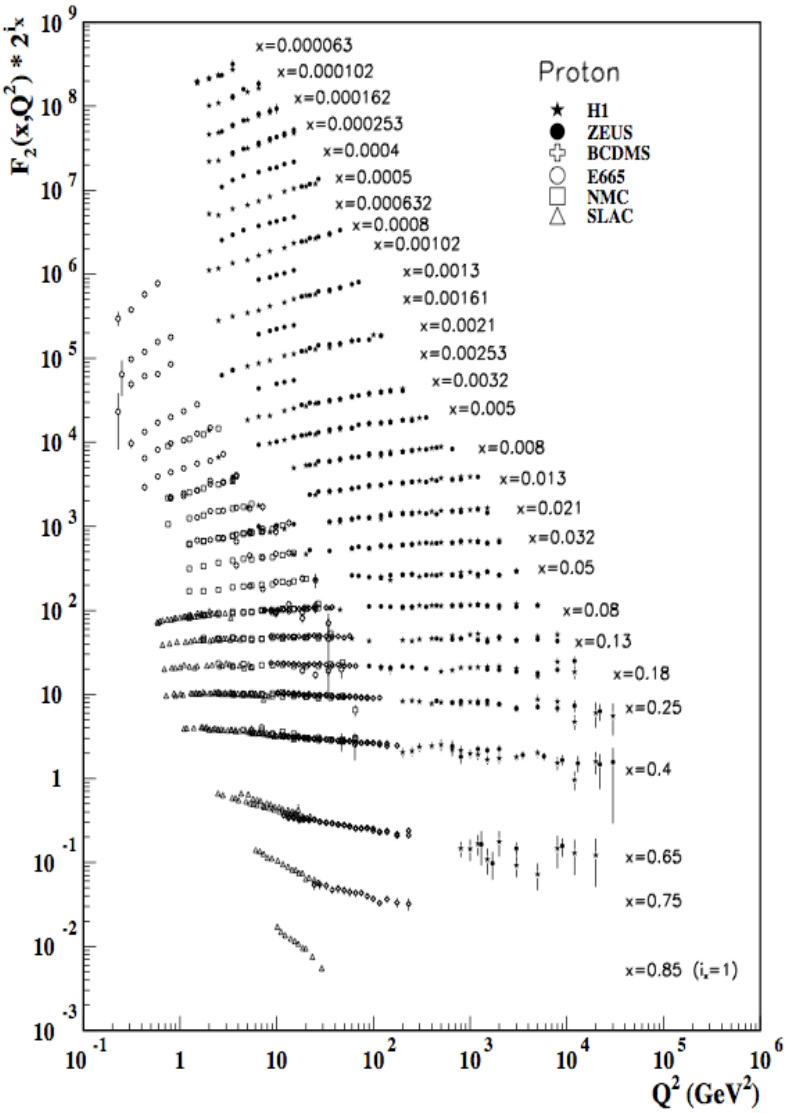

Figure 2.4: The proton structure function F_2^p as a function of Q^2 for different x bins starting from $x = 0.000063$ up to $x = 0.65$. The results shown correspond to data from ep collider experiments (ZEUS, H1) as well as data from fixed target experiments using muons (BCDMS, E665, NMC). Statistical and systematic errors are added in quadrature. The ZEUS binning in x is used in the plot; all other data are re-binned to the x values of the ZEUS data. The plot has been taken from [4].

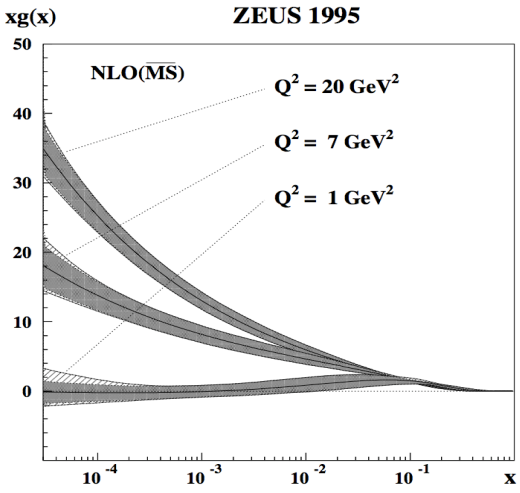

Figure 2.5: The gluon distribution [5] evaluated at NLO in the $\overline{MS}$ scheme from the scaling violations of the structure function $F_2(x, Q^2)$ through the DGLAP evolution equations.

2.2.5 Parton Distribution Functions

The parton distribution functions reflect the non-perturbative long-distance dynamics of the proton constituents. In the two last decades, a large variety of highly precise measurements has been performed in addition to large theoretical effort. Since short distance (high energies) processes and large distances (low energies) processes can be separated due to the factorization theorem, the PDFs are process independent, i.e. they are universal quantities which enter the computation of many processes (DIS, proton-proton collisions, Drell-Yann process, ...).

The unpolarized PDFs are determined by a *QCD global analysis* which consists in fitting simultaneously different sets of data covering different kinematic domains and provided by different experiments. To perform a global QCD analysis, two inputs are required. The first input corresponds to experimental data collected by experiments which investigate the nucleon internal structure. In the current global analyzes, all included data are provided by studying the following processes: e, μ, ν deep inelastic scattering, lepton pair production (Drell-Yann), high p_T inclusive jets, dimuon production in neutrino scattering, HERA charm (c) and bottom (b) production, HERA charged currents. On the theoretical side, the expressions of hard scattering processes are needed in addition to their Q^2 evolution, which are calculated using DGLAP equations. The second input to the QCD global analysis corresponds to the functional form used to describe the parton distributions at given starting momentum scale Q_0^2. Eq. 2.22 represents a functional form assumed for the PDFs, where i denotes the flavor of the quark and A_i, α_i, β_i and γ_i are free parameters to be fitted.

$$f_i(x, Q_0^2) = A_i x^{\alpha_i}(1-x)^{\beta_i}(1+\gamma_i x) \tag{2.22}$$

The starting momentum scale is usually chosen in a range where the parton distribution are dominated by valence quarks. In a first step, the PDFs are computed for $Q^2 > Q_0^2$ using the DGLAP evolution equations. The cross sections of the different hard scattering processes are computed using the techniques of perturbative QCD (up to NLO or NNLO). In a second step the cross sections are calculated at the corresponding experimental Q^2, a χ^2 is then computed in order to measure the agreement between the predictions and the measurements. In a last step, the χ^2 is minimized to find the best fit.

All existing QCD global analyses of the PDFs agree relatively well with one another within the estimated uncertainties. An example of these distributions is shown in Fig 2.6; it is given by a recent analysis [11] done by A.D. Martin, W.J. Stirling, R.S. Thorne and G. Watt (MSTW). In summary, the current knowledge of the PDFs is very precise except for the strange quark distribution which remains an issue in the unpolarized sector.

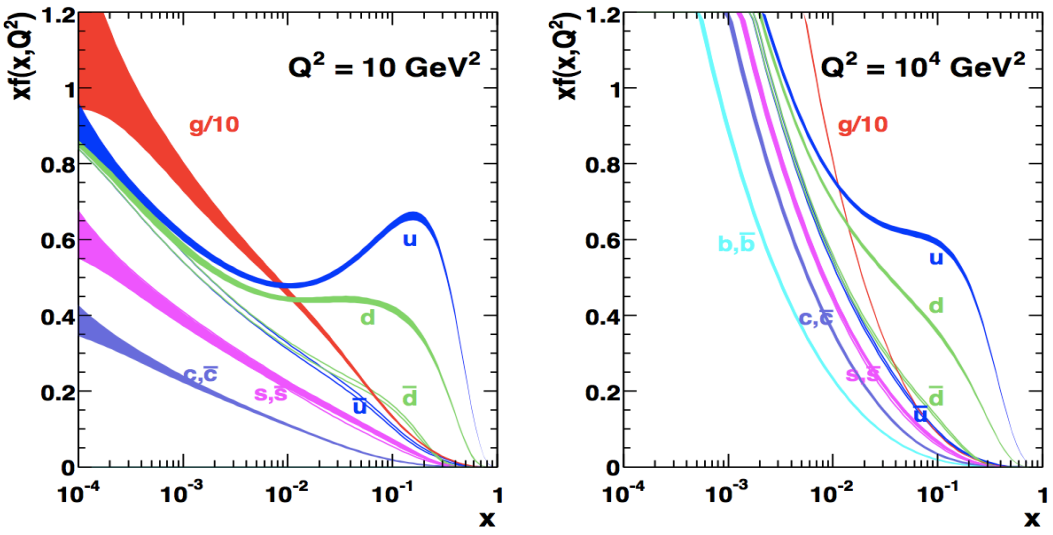

Figure 2.6: Unpolarized parton distribution functions given by the MSTW [11] (A.D. Martin, W.J. Stirling, R.S. Thorne and G. Watt) parametrization evaluated at $Q^2 = 10$ and $Q^2 = 10^4$. The valence quarks dominate for $x \to 1$ and gluons dominate for $x \to 0$, especially at large Q^2.

2.3 Spin dependent cross section and structure functions g_1 and g_2

2.3.1 Spin dependent structure functions g_1 and g_2

In order to study the spin structure of the nucleon, the lepton and the nuclear target must be both polarized. In this case the leptonic ($L_{\mu\nu}$) and the hadronic ($W^{\mu\nu}$) tensors must contain spin dependent terms and can be decomposed into a symmetric (S) part and an antisymmetric (A) part under μ, ν interchange. The leptonic tensor can be written as follows:

$$L_{\mu\nu}(k, s; k') = 2\left[L^{(S)}_{\mu\nu}(k; k') + iL^{(A)}_{\mu\nu}(k, s; k')\right] \tag{2.23}$$

where

$$L^{(S)}_{\mu\nu}(k, k') = k_\mu k'_\nu + k'_\mu k_\nu - g_{\mu\nu}(k.k' - m^2)$$
$$L^{(A)}_{\mu\nu}(k, s; k') = m\epsilon_{\mu\nu\alpha\beta}s^\alpha q^\beta$$

Here s^α denotes the four-vector spin of the lepton with $s^2 = -1$ and $s.k = 0$; $\epsilon_{\mu\nu\alpha\beta}$ denotes the Levi-Civita tensor which is totally antisymmetric with $\epsilon_{1234} = 1$. The antisymmetric part of $L_{\mu\nu}$ is proportional to the lepton spin. Similar to Eq. 2.23, the hadronic tensor is given by:

$$W^{\mu\nu}(q; P, S) = W^{\mu\nu(S)}(q; P) + iW^{\mu\nu(A)}(q; P, S) \tag{2.24}$$

where the symmetric part corresponds to the one given in unpolarized case (Eq.(2.8)). Similarly to the unpolarized case, by taking into account all symmetry requirements the antisymmetric term is reduced and expressed in terms of the spin dependent structure functions $G_1(\nu, Q^2)$ and $G_2(\nu, Q^2)$. It is given by the following expression:

$$\frac{1}{2M}W^{\mu\nu(A)}(q; P, S) = \epsilon^{\mu\nu\alpha\beta}q_\alpha\left[MS_\beta G_1(\nu, Q^2) + [(P.q)S_\beta - (S.q)P_\beta]\frac{G_2(\nu, Q^2)}{M}\right]$$

Here also, the antisymmetric term is proportional to the spin. In this polarized case, the cross section is obtained by contracting the leptonic and hadronic tensors and is usually expressed in terms of the dimensionless spin dependent structure functions g_1 and g_2 defined in the Bjorken limit by:

$$\frac{(P \cdot q)^2}{\nu}G_1(\nu, Q^2) = g_1(x, Q^2) \to g_1(x) \tag{2.25}$$

$$\nu(P\cdot q)G_2(\nu,Q^2) = g_2(x,Q^2) \to g_2(x) \tag{2.26}$$

The spin structure functions g_1 and g_2 can be both accessed from the difference of polarized DIS cross sections in different spin configurations. While the lepton beam is always longitudinally polarized, the nuclear target can be polarized longitudinally or transversely to the beam direction. In the first case when the nucleon is longitudinally polarized, the difference of cross sections for parallel and anti-parallel lepton and nucleon spins is:

$$\frac{d^2\sigma^{\rightarrow\Rightarrow}}{dxdy} - \frac{d^2\sigma^{\rightarrow\Leftarrow}}{dxdy} = \frac{16\pi\alpha^2}{Q^2}\left[(1-\frac{y}{2})g_1(x,Q^2) - \frac{2M^2xy}{Q^2}g_2(x,Q^2)\right] \tag{2.27}$$

In the case of transversely polarized target, the difference is given by:

$$\frac{d^2\sigma^{\rightarrow\Uparrow}}{dxdy} - \frac{d^2\sigma^{\rightarrow\Downarrow}}{dxdy} = -\frac{16\alpha^2}{Q^2}\left(\frac{2Mx}{Q}\right)\sqrt{1-y}\left[\frac{y}{2}g_1(x,Q^2) + g_2(x,Q^2)\right] \tag{2.28}$$

In the **parton model**, the g_1 structure functions has a form similar to the unpolarized structure function F_1 and it is given by :

$$g_1(x) = \frac{1}{2}\sum_q e_q^2\left[\Delta q(x) + \Delta\bar{q}(x)\right] \tag{2.29}$$

where $\Delta q(x) = q^+(x) - q^-(x)$, q^+ ($q^-(x)$) corresponds to the density of quarks of flavor q carrying a fraction x of the nucleon momentum, with a spin parallel (anti-parallel) to the nucleon spin. Therefore, g_1 and its first moment $\Gamma_1 = \int_0^1 g_1(x)dx$ encode information about the contributions of the spins of quarks to the nucleon spin. Γ_1 is related to the total contribution of the spin of the quarks to the nucleon spin and is written as :

$$\Gamma_1 = \int_0^1 dx g_1(x) = \frac{1}{2}\sum_q e_q^2\Delta q = \frac{1}{2}\sum_q e_q^2\int_0^1\left[\Delta q(x) + \Delta\bar{q}(x)\right]$$

The quantities $\Delta q = \int_0^1\left[\Delta q(x) + \Delta\bar{q}(x)\right]dx$ define the difference between the density of quarks of flavor q with spin parallel and that of quarks with spin anti-parallel to the nucleon spin, for all momentum fractions x. At LO, the first moment g_1 can be written as :

$$\Gamma_1 = \frac{1}{2}\sum_q e_q^2\Delta q = \frac{1}{2}\left[\frac{4}{9}\Delta u + \frac{1}{9}\Delta d + \frac{1}{9}\Delta s\right] \tag{2.30}$$

Contrary to F_2, the spin dependent structure function g_2 does not have any interpretation in the parton model where $g_2 = 0$.

2.3.2 Spin Asymmetries

The virtual-photon absorption cross section is related, via the optical theorem, to the imaginary part of the forward Compton amplitudes $\mathcal{A}_{\Lambda\lambda,\Lambda'\lambda'}$, where Λ and λ denote the helicities of the photon and the nucleon respectively. By imposing helicity conservation as well as parity and time reversal invariance, only four independent amplitudes exist. They are related, via their corresponding absorption cross sections, to the structure functions as follows:

$$\sigma^T_{\frac{3}{2}} = \frac{4\pi^2\alpha}{K}\mathcal{A}_{1\frac{1}{2}1\frac{1}{2}} = \frac{4\pi^2\alpha}{MK}(F_1 + g_1 - \gamma^2 g_2)$$

$$\sigma^T_{\frac{1}{2}} = \frac{4\pi^2\alpha}{K}\mathcal{A}_{1-\frac{1}{2}1-\frac{1}{2}} = \frac{4\pi^2\alpha}{MK}(F_1 - g_1 + \gamma^2 g_2)$$

$$\sigma^{TL} = \frac{4\pi^2\alpha}{K}\mathcal{A}_{1-\frac{1}{2}0\frac{1}{2}} = \frac{4\pi^2\alpha}{MK}\gamma(g_1 + g_2)$$

$$\sigma^L = \frac{4\pi^2\alpha}{K}\mathcal{A}_{0\frac{1}{2}0\frac{1}{2}} = \frac{4\pi^2\alpha}{MK}((1+\gamma^2)\frac{F_2}{2x} - F_1)$$

Here, $K = \nu + q^2/2M$[5] and $\sigma^T_{3/2}$ and $\sigma^T_{1/2}$ denote the transverse virtual photon absorption

[5] according to the Hand convention

cross sections when the sum of the spin projections ($m_{\gamma^*+m_N}$) is 3/2 and 1/2, respectively. The spin average $\sigma^T = \frac{1}{2}(\sigma^T_{3/2} + \sigma^T_{1/2}) = (4\pi^2\alpha)F_1$ is spin independent and it involves unpolarized structure functions only. Similarly, the longitudinal virtual photon absorption cross section σ^L is spin independent. The ratio $R = \sigma^L/\sigma^T = (1+\gamma^2)(F_2/2xF_1) - 1$ relates the two structure functions F_1 and F_2 and is used in the extraction of F_2. Finally, the interference term between the transverse and the longitudinal cross sections, given by σ^{TL}, is spin independent. The virtual-photon spin asymmetries are thus defined as:

$$A_1 = \frac{\sigma^T_{1/2} - \sigma^T_{3/2}}{\sigma^T_{1/2} + \sigma^T_{3/2}} = \frac{g_1 - \gamma^2 g_2}{F_1}, \qquad A_2 = \frac{\sigma^{TL}}{\sigma^T} = \frac{\gamma[g_1 + g_2]}{F_1} \tag{2.31}$$

The spin asymmetries (A_1, A_2) are the best tool to learn about the quark helicity distributions (Δq) since they are related to the spin dependent structure functions g_1 and g_2 which in turn are related to Δq. These virtual-photon asymmetries (Eq. 2.31) cannot be measured. However they are related to the experimentally measured longitudinal and transverse spin asymmetries defined as :

$$A_\parallel = \frac{\sigma^{\rightarrow\Leftarrow} - \sigma^{\rightarrow\Rightarrow}}{\sigma^{\rightarrow\Leftarrow} + \sigma^{\rightarrow\Rightarrow}}, \qquad A_\perp = \frac{\sigma^{\rightarrow\Downarrow} - \sigma^{\rightarrow\Uparrow}}{\sigma^{\rightarrow\Downarrow} + \sigma^{\rightarrow\Uparrow}} \tag{2.32}$$

where, $\sigma^{\rightarrow\Rightarrow}$ ($\sigma^{\rightarrow\Leftarrow}$) denotes the cross section in the case where longitudinally polarized lepton and nucleon have their spins parallel (anti parallel); $\sigma^{\rightarrow\Downarrow}$ ($\sigma^{\rightarrow\Uparrow}$) denotes the cross section for longitudinally polarized lepton and transversely polarized nucleon. The lepton spin asymmetries (Eq. 2.32) are related to the virtual-photon asymmetries through $A_\parallel = D(A_1 + \eta A_2)$ and $A_\perp = d(A_2 - \zeta A_1)$ where η and ζ are kinematic factors, D is the virtual photon depolarization factor which denotes the fraction of the lepton polarization transferred to the virtual photon. In practice, $\eta \ll 1$ and $\zeta \ll 1$; thus the expressions relating A_1 and A_2 to the experimentally measured asymmetries reduce to $A_\parallel = DA_1$ and $A_\perp = dA_2$.

Within the quark parton model, the photon-nucleon polarized cross section can be understood intuitively in the so called *Breit frame*, where the struck quark has its momentum $p' = -p$ after the absorption of the virtual photon. In the case of a transverse virtual photon with a spin projection $m_\gamma = +1$ (Figure 2.7(a)), only quarks which have the spin projection $m_q = -1/2$ can absorb it and will have $m_q = 1/2$ after the interaction. Quarks with spin projection $m_q = 1/2$ (figure 2.7(b)), however, cannot absorb the virtual photon in such case because the total spin projection would be 3/2 and the final quark cannot have $m_q = 3/2$, as described in figure 2.8.

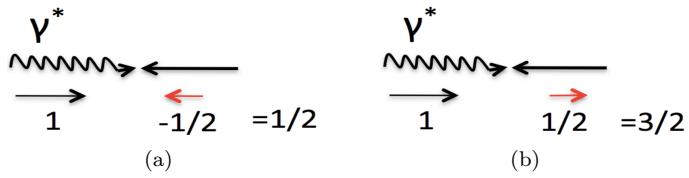

(a) (b)

Figure 2.7: Spin projections of the transverse virtual photon and the quarks in the *Breit* frame.

As a consequence, when a transverse virtual photon characterized by $m_\gamma = 1$ interacts with a nucleon with a spin projection $m_N = -1/2$ (figure 2.8(a)), the interaction occurs only on quarks with spin parallel to the nucleon spin, i.e. on quarks which have $m_q = -1/2$. The photon-nucleon cross section $\sigma_{1/2}$ is then proportional to the density of quarks with spin parallel to the nucleon spin ($\sigma_{1/2} \propto q^+(x)$). Similarly, the cross section of the interaction between a transverse virtual photon with $m_\gamma = 1$ and a nucleon with $m_N = 1/2$ (figure 2.8(b)) is proportional to the density of quarks with spin anti-parallel to the nucleon spin ($\sigma_{3/2} \propto q^-(x)$).

In summary, $(\sigma_{1/2} + \sigma_{3/2})$ counts the total number of quarks with all spins and $(\sigma_{1/2} - \sigma_{3/2})$ counts the difference between the number of quarks with spin parallel to the nucleon spin and the number of quarks with spin anti-parallel to the nucleon spin.

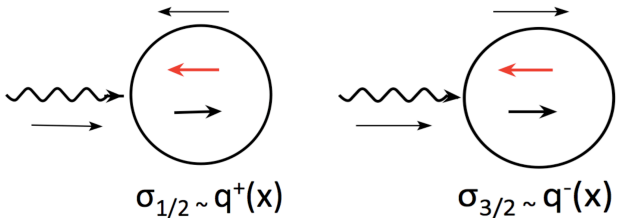

(a) (b)

Figure 2.8: Spin projections of the transverse virtual photon and the quarks in the *Breit* frame.

2.3.3 QCD improved parton model

At Leading-Order (LO) in QCD, the spin structure function g_1 depends only on polarized quark distributions. At Next-to-Leading-Order (NLO), however, g_1 depends also on the contribution of the spins of gluons to the nucleon spin (ΔG) (due to the QCD radiative effects) and has the following form:

$$g_1(x,Q^2) = \frac{1}{2}\sum_i e_i^2 C_q(x,\alpha_s) \otimes \Delta q_i(x,Q^2) + \frac{1}{N_f} C_g(x,\alpha_s) \otimes \Delta G(x,Q^2)^6 \tag{2.33}$$

Here, N_f denotes the number of active quark flavors in the nucleon (= 3 neglecting the heavy flavors in this regime) and the sum runs over the active quarks. C_q and C_g are the Wilson coefficients which can be computed in perturbative QCD. At LO, $C_q^0 = \delta(1-x)$ and $C_g^0 = 0$ and Eq. (2.9) reduces to the g_1 expression in the naïve parton model. Similarly to the unpolarized case, the Q^2 evolution of g_1 is given by the DGLAP evolution equations:

$$\begin{aligned} \frac{d}{d\ln Q^2}\Delta q_{NS}(x,Q^2) &= \frac{\alpha_S(Q^2)}{2\pi} P_{qq}^{NS} \otimes \Delta q_{NS} \\ \frac{d}{d\ln Q^2}\begin{pmatrix} \Delta\Sigma \\ \Delta G \end{pmatrix} &= \frac{\alpha_S(Q^2)}{2\pi}\begin{pmatrix} Pqq & P_{qg} \\ P_{gq} & P_{gg} \end{pmatrix} \otimes \begin{pmatrix} \Delta\Sigma \\ \Delta G \end{pmatrix} \end{aligned} \tag{2.34}$$

where the non-singlet quark distribution $\Delta q_{NS}(x,Q^2)$ is defined as

$$\Delta q_{NS}(x,Q^2) = (\Delta u + \Delta\bar{u}) - \frac{1}{2}(\Delta d + \Delta\bar{d}) - \frac{1}{2}(\Delta s + \Delta\bar{s}) \tag{2.35}$$

The splitting functions [42] and the Wilson coefficients [41] have been computed up to NLO. A very important aspect of the Q^2 dependence of g_1 is the sensitivity to the gluon spin distribution (Δg). By deriving $\partial g_1/\partial \ln Q^2$ and using the DGLAP equations, $\Delta\Sigma$, Δq_{NS} and Δg can be extracted. All existing measurements of the spin structure function g_1 are performed only in fixed target experiments, providing a limited range of Q^2. As a consequence, a precise determination of g_1 is not possible. In addition to the limited Q^2 range, the g_1 expression does not allow to separate the quark and anti-quark distributions; this is only possible by including the semi-inclusive spin asymmetries where final state hadrons are detected. Figure 2.9 shows the existing measurements for g_1 for both proton and deuteron targets.

2.3.4 First moment of g_1 and sum rules

The main interest in measuring the spin structure function $g_1(x,Q^2)$ is in its first moment which can be compared to several predicted sum rules, in particular, the *Bjorken* [6] and *Ellis-Jaffe* [7] sum rules. These sum rules are derived using the formalism of the operator product expansion (OPE) which relates a moment of a structure function of the nucleon to its matrix element. At leading order (LO), the first moment of the spin structure function g_1 for the proton is given by [8]:

[6] the convolution $\otimes$ is defined as $C(x,Q^2) \otimes q(x,Q^2) = \int_x^1 \frac{dy}{y} C\left(\frac{x}{y},\alpha_S\right) q(x,Q^2)$

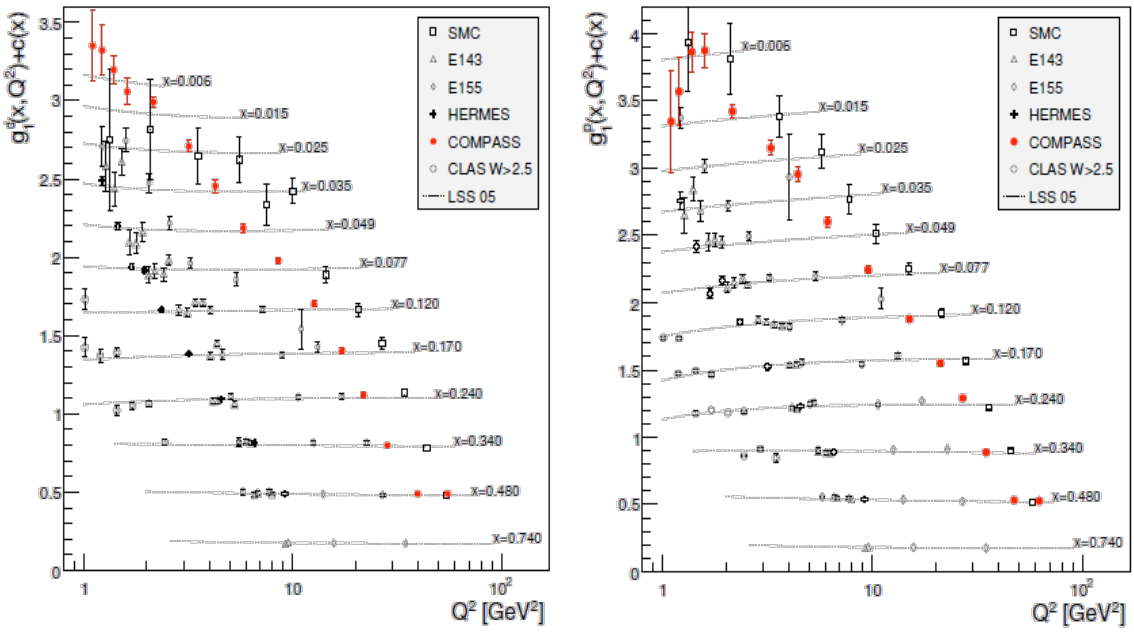

Figure 2.9: The spin-dependent structure function $xg_1(x)$ of the proton, deuteron and neutron measured in deep inelastic scattering experiments of polarized electrons/positrons ($E143$, $E155$, CLAS, HERMES) and muons (SMC, COMPASS). The LSS parametrization of parton distribution functions is also shown.

$$\Gamma_1^p = \int_0^1 g_1^p(x)dx = \frac{1}{2}\left[\frac{4}{9}a_u + \frac{1}{9}a_d + \frac{1}{9}a_s\right] \tag{2.36}$$

where $a_q s^\mu = \langle N|\bar{q}\gamma_\mu\gamma_5 q|N\rangle$ is the axial matrix element of the nucleon for flavor q. In the parton model, a_q is interpreted as the total contribution of the spin of quarks with flavor q to the nucleon spin.

$$a_q = \int_0^1 [\Delta q(x) + \Delta\bar{q}(x)]dx = \Delta q$$

and consequently

$$\Gamma_1^p = \int_0^1 g_1^p(x)dx = \frac{1}{2}\left[\frac{4}{9}(\Delta u + \Delta\bar{u}) + \frac{1}{9}(\Delta d + \Delta\bar{d}) + \frac{1}{9}(\Delta s + \Delta\bar{s})\right] \tag{2.37}$$

Eq. 2.37 corresponds to the expression obtained within the parton model (2.30) picture. Assuming $SU(3)$ flavor symmetry, the matrix elements a_q can be combined in three configurations : one singlet combination $a_0 = a_u + a_d + a_s$ and 2 non-singlet combinations $a_3 = a_u - a_d$ (triplet) and $a_8 = a_u + a_d - 2a_s$ (octet).

$$\begin{aligned} a_0 &= (\Delta u + \Delta\bar{u}) + (\Delta d + \Delta\bar{d}) + (\Delta s + \Delta\bar{s}) \\ a_3 &= \quad\quad (\Delta u + \Delta\bar{u}) - (\Delta d + \Delta\bar{d}) \\ a_8 &= (\Delta u + \Delta\bar{u}) + (\Delta d + \Delta\bar{d}) - 2(\Delta s + \Delta\bar{s}) \end{aligned}$$

The first moment Γ_1^p can thus be written as a function of these three combinations

$$\Gamma_1^p = \int_0^1 g_1^p(x)dx = \frac{1}{9}a_0 + \frac{1}{12}a_3 + \frac{1}{36}a_8 \tag{2.38}$$

At higher order, Γ_1^p is written as:

$$\Gamma_1^p = \frac{1}{9}C_S a_0 + C_{NS}\left[\frac{1}{12}a_3 + \frac{1}{36}a_8\right] \tag{2.39}$$

where C_S and C_{NS} are the singlet and non-singlet Wilson coefficients. At LO, $C_S = C_{NS} = 1$ and at NLO $C_S = C_{NS} = 1 - \alpha_S(Q^2)/\pi$. The moment of the spin structure function of the neutron Γ_1^n can be deduced from (2.38) using the isospin symmetry ($SU(2)$ flavor symmetry) between up and down flavors.

Bjorken Sum rule : Using the isospin invariance, one can relate the matrix element $a_u - a_d = \langle p|\bar{u}\gamma_\mu\gamma^5 u - \bar{d}\gamma_\mu\gamma^5 d|p\rangle$ to the neutron weak decay constant $\langle p|\bar{u}\gamma_\mu\gamma^5 d|p\rangle = g_A/g_V$ which is measured experimentally and found to be equal to 1.2573 ± 0.0028. This gives rise to a QCD prediction, known as the *Bjorken sum rule* [6] :

$$\Gamma_1^p - \Gamma_1^n = \frac{1}{6}(a_u - a_d)C_{NS} = \frac{1}{6}\frac{g_A}{g_V}C_{NS} \tag{2.40}$$

In order to compare the experimental results with this prediction, the integral of the measured $g_1(x, Q^2)$ in the full x range has to be calculated at fixed Q^2. However, the current experiments cannot cover the full x range and an extrapolation of g_1 over the uncovered regions of x is consequently needed. For the large x region, the behavior of $g_1(x)$ is expected to be similar to that of the unpolarized distributions, i.e. $g_1(x)$ is expected to approach zero as $x \to 1$. The problem appears at small x since there is no clear x dependence of g_1 and this dependence cannot be predicted. Currently, the NLO calculations use the Regge parametrization to describe the x dependence of g_1 and thus predict the low x behavior of g_1 at the Q^2 of the considered experiment. The *Bjorken sum rule* has been tested by several experiments starting from the EMC experiment at CERN, and found to be conserved.

Ellis-Jaffe sum rule:The $SU(3)$ flavor symmetry permits to express the ratio g_A/g_V for hyperon beta decays in terms of the octet term such that $a_8 = 3F - D$. With the additional assumption that the role of the strange quarks in the nucleon is negligible ($a_s = 0$), a second prediction can be made for Γ_1^p and Γ_1^n :

$$\Gamma_1^{p(n)} = \frac{1}{9}C_S(3F - D) + C_{NS}\left[+(-)\frac{1}{12}g_A/g_V + \frac{1}{36}(3F - D)\right] \tag{2.41}$$

This is called the *Ellis-Jaffe sum rule* [7]. In contrast to the *Bjorken sum rule*, the *Ellis-Jaffe* sum rule was found to be strongly violated. The LO analysis related this violation to the assumption made on a_s which must have a non-zero value.

2.4 Determination of quark helicity distributions from spin asymmetries

While inclusive polarized DIS provides information about the spin structure only for the sum over all quark and antiquarks, semi-inclusive polarized DIS permits to access the individual quark flavor contribution to the nucleon spin and allows to separate contributions of quarks and antiquarks. Within the QCD improved parton model, the cross section for the hadron production in lepton-nucleon hard scattering can be decomposed into an x-dependent term and a z-dependent term due to the LO assumption of factorization. The cross section for hadron lepto-production is then given by:

$$\frac{1}{\sigma^{DIS}}\frac{d\sigma^h}{dxdzdQ^2} = \frac{\sum_q e_q^2 q(x, Q^2) D_q^h(z, Q^2)}{\sum_q e_q^2 q(x, Q^2)} \tag{2.42}$$

where σ^{DIS} denotes the inclusive deep inelastic scattering cross section; $D_q^h(z, Q^2)$ denotes the quark fragmentation function into hadron which defines the mean number of hadrons of type h with fractional energy z produced by the fragmentation (or hadronization) of a quark of flavor q. The fragmentation functions encode information about the fragmentation of quarks into final state hadrons. The quark fragmentation process is not yet completely understood. Several phenomenological models were developed to understand it. In parallel, several QCD global analyzes have been performed to extract the fragmentation functions.

An interesting variable for the quark fragmentation is the Feynman variable $x_F = 2p_\parallel/W$, where $p_\parallel$ is the hadron momentum projection along the virtual photon momentum in the photon-nucleon center of mass frame and W is the invariant mass of the hadronic system (see table 2.1). The quark which absorbs the virtual photon has $p_\parallel > 0$ while the other quarks continue with their $p_\parallel < 0$. As a consequence, hadrons with $p_\parallel > 0$ are produced in the so called "current fragmentation region[7]", while hadrons with $p_\parallel < 0$ are produced in the so called "target fragmentation region".
The longitudinal double spin asymmetry (2.31) for the lepto-production of hadron is given, in the case of a proton target, by Eq. 2.43 and Eq. 2.44 for inclusive and semi-inclusive cases.

Inclusive DIS

$$A_1(x,Q^2) \simeq \frac{g_1}{F_1}(x,Q^2) = \frac{\sum_q e_q^2 \left[\Delta q(x,Q^2) + \Delta\bar{q}(x,Q^2)\right]}{\sum_q e_q^2 \left[q(x,Q^2 + \bar{q}(x,Q^2)\right]} \tag{2.43}$$

Semi-Inclusive DIS (for final state hadron of type h)

$$A_1^h(x,Q^2) = \frac{\sum_q e_q^2 \left[\Delta q(x,Q^2) D_q^h(z,Q^2) + \Delta\bar{q}(x,Q^2) D_q^h(z,Q^2)\right]}{\sum_q e_q^2 \left[q(x,Q^2) D_q^h(z,Q^2) + \bar{q}(x,Q^2) D_q^h(z,Q^2)\right]} \tag{2.44}$$

Since Δq in the A_1^h expression are weighted by the fragmentation functions, the contributions of individual quark (antiquark) flavors can be extracted. As a consequence, the measurement of A_1 and A_1^h ($h = \pi, K$) for both proton and deuteron targets gives rise to a linear system of equations allowing to extract the unknowns $\Delta q(x,Q^2)$ for all involved flavors (up, down and strange).

2.4.1 LO determination of quark helicity distributions from inclusive and semi-inclusive spin asymmetries

In this section, explicit formula for the extraction of polarized parton distribution functions at LO are derived. For a proton and a deuterium targets, the inclusive (Eq. 2.45) and the semi-inclusive (Eq. 2.46) asymmetries are written in terms of the parton distribution function $q \equiv q(x,Q^2)$, the fragmentation functions $D_q^h \equiv D_q^h(Q^2) = \int_{z_{min}}^{z_{max}} D_q^h(z,Q^2)$ and the quark helicity distributions $\Delta q \equiv \Delta q(x,Q^2)$.

Inclusive DIS[8]

$$A_{1,p} = \frac{4(\Delta u + \Delta\bar{u}) + (\Delta d + \Delta\bar{d}) + (\Delta s + \Delta\bar{s})}{4(u+\bar{u}) + (d+\bar{d}) + (s+\bar{s})}$$

$$A_{1,d} = \frac{5(\Delta u + \Delta d) + 5(\Delta\bar{u} + \Delta\bar{d}) + 2(\Delta s + \Delta\bar{s})}{5(u+d) + 5(\bar{u}+\bar{d}) + 2(s+\bar{s})} \tag{2.45}$$

Semi-Inclusive DIS

$$A_{1,d}^h = \frac{(4D_u^h + D_d^h)(\Delta u + \Delta d) + (4D_{\bar{u}}^h + D_{\bar{d}}^h)(\Delta\bar{u} + \Delta\bar{d}) + 2(D_s^h \Delta s + D_{\bar{s}}^h \Delta\bar{s})}{(4D_u^h + D_d^h)(u+d) + (4D_{\bar{u}}^h + D_{\bar{d}}^h)(\bar{u}+\bar{d}) + (D_s^h s + D_{\bar{s}}^h \bar{s})}$$

$$A_{1,p}^h = \frac{4(D_u^h \Delta u + D_{\bar{u}}^h \Delta\bar{u}) + (D_d^h \Delta d + D_{\bar{d}}^h \Delta\bar{d}) + (D_s^h \Delta s + D_{\bar{s}}^h \Delta\bar{s})}{4(uD_u^h + \bar{u}D_{\bar{u}}^h) + (dD_d^h + \bar{d}D_{\bar{d}}^h) + (sD_s^h + \bar{s}D_{\bar{s}}^h)} \tag{2.46}$$

These equations can be summarized in a matrix form:

$$\vec{A} = \mathcal{B}\vec{\Delta q} \tag{2.47}$$

where $\quad \vec{A} = \left(A_{1,d}, A_{1,p}, A_{1,d}^{\pi^\pm}, A_{1,d}^{K^\pm}, A_{1,p}^{\pi^\pm}, A_{1,p}^{K^\pm}\right) \qquad \Delta\vec{q} = \left(\Delta u, \Delta\bar{u}, \Delta d, \Delta\bar{d}, \Delta s, \Delta\bar{s}\right)$

[7] Hadrons resulting from the fragmentation of the struck quark are said to be produced in the current fragmentation region while hadrons resulting from the fragmentation of the target remnant are said to be produced in the target fragmentation region

[8] The indices p and d denote the type of the target.

$\vec{A}$ denotes the vector of asymmetries, $\Delta\vec{q}$ denotes the vector of unknowns and $\mathcal{B}$ denotes a matrix whose elements depend on parton distribution functions (PDFs) and on quark fragmentation functions into hadrons (FFs). To extract the polarized quark distributions $\Delta q(x)$, Eq(6.7) can be solved using the least-square estimation. For this goal, the χ^2 is minimized in each x bin:

$$\chi^2 = (\vec{A} - \mathcal{B}\Delta\vec{q})^T (\mathrm{Cov}_A)^{-1} (\vec{A} - \mathcal{B}\Delta\vec{q}) \tag{2.48}$$

$\mathrm{Cov_A}$ denotes the covariance matrix of the experimentally measured asymmetries. The extraction of the quark helicity distributions requires the knowledge of the unpolarized quark distribution functions as well as the fragmentation functions. Using a parametrization for unpolarized PDFs and one parametrization for fragmentation functions, the matrix $\mathcal{B}$ can thus be calculated and the system of equations (6.7) can be solved. The experimental extraction of Δq has been performed using data collected by the COMPASS experiment and will be presented in chapter 6.

2.4.2 NLO determination of quark and gluon helicity distributions from global QCD analysis

The access to the quark helicity distributions can be provided by several high energy processes where at least one produced hadron is detected in the final state. Each process provides different type of information about the polarized quark and gluon helicity distributions in different kinematic regions. The universality of the PDFs and the scale evolution permit to tie all these processes together by performing a global analysis. The idea behind it is to extract the PDFs by optimizing the agreement between the measured spin asymmetries from DIS, SIDIS and pp scattering through variation of the shapes of quark helicity distributions.
Currently, several LO/NLO analysis of DIS data performed by different groups exist; they use different assumptions and different functional forms but agree among themselves. Two recent NLO analysis of combined DIS and SIDIS data have been performed. The first one was done by D. de Florian, R. Sassot, M. Stratmann and W. Vogelsang (DSSV [37]) and the second one by E. Leader, A. Sidorov and D. Stamenov (LSS [14]). As an example, the DSSV parametrization [37] assumes the following functional form for the quark helicity distributions:

$$x\Delta q_i(x, Q_0^2) = N_i x^{\alpha_i} (1-x)^{\beta_i} (1 + \gamma_i \sqrt{x} + \eta_i x) \tag{2.49}$$

where N_i, α_i, β_i, γ_i and η_i are free parameters and i denotes a quark of some flavor or a gluon. The same procedure described in section 2.2.5 is used for the quark heilicity distributions .

A comparison between different existing parametrization for different quark helicity distributions is shown in Fig 2.10. The polarized quark distributions given by different parametrizations (BB [15], DSSV [37], LSS05 [16], AAC08 [17]) agree for the shape and the sign of the valence quark helicity distributions as well as for $\bar{d}$. However, they disagree for $\bar{u}$ and s. For the strange quark helicity distribution, all QCD analyzes containing inclusive DIS data give negative distribution for Δs while the QCD analyzes of combined inclusive and semi-inclusive DIS data (as DSSV and LSS10) give a sign changing distribution for Δs. This discrepancy is essentially due to the poorly known strange quark fragmentation functions into kaons and to the lack of kaon's data. The dependence of Δs on the quark fragmentation functions has been quantified by COMPASS [10] (see chapter 6). It has been confirmed later by the LSS parametrization [18].

2.5 Summary

The internal structure of the nucleon has been widely investigated for the two last decades. The nucleon momentum structure is nowadays precisely known except for the strange quarks for which the distribution is poorly known and still under investigation. The situation is similar for the nucleon spin structure which is still partially known. All existing measurements of the contribution of quark spins to the nucleon spin result in a value of $\sim 30\%$ and no further measurements are needed in this sector. However the strange quark contribution to the nucleon spin remains an issue.

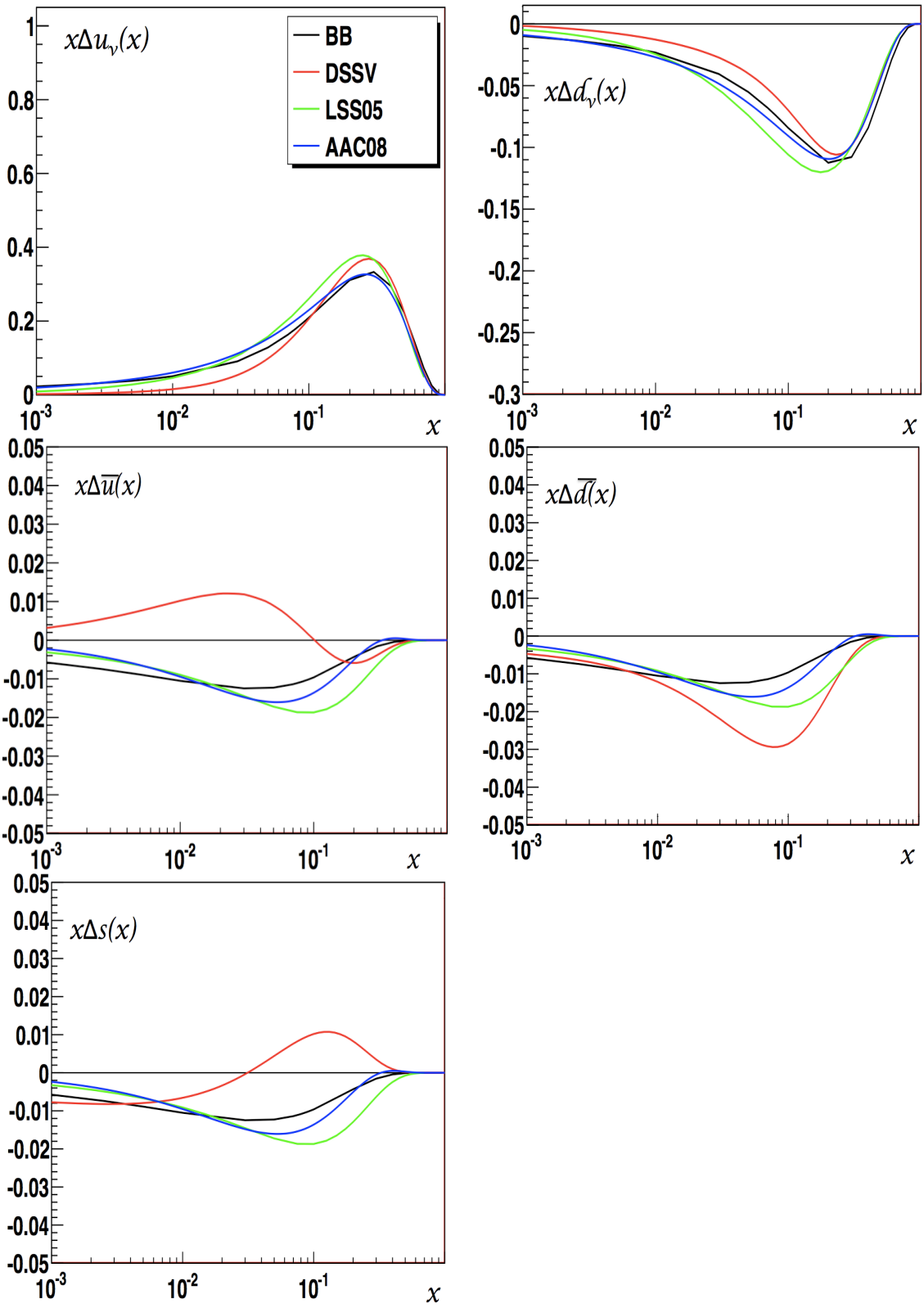

Figure 2.10: Comparison between different NLO QCD analysis of polarized parton distribution functions for valence and sea quarks at $Q^2 = 3$ GeV^2. BB (J. Bluemlein and M. Boettcher [15]), LSS05 (E. Leader, Sidorov and D. Stamenov [16]) and AAC08 (Asymmetry Analysis Collaboration [17]) use inclusive DIS data while DSSV (D. de Florian, R. Sassot, M. Stratmann and W. Vogelsang [37]) use both inclusive and semi-inclusive DIS data.

This thesis is dedicated to the study of the strangeness content of the nucleon. For this purpose, two measurements have been performed using data collected by the COMPASS experiment. The first measurement corresponds to the LO extraction of quark helicity distributions Δq, using data taken by scattering polarized muons off polarized protons and deuterons. The second measurement corresponds to the determination of hadron multiplicities and the extraction of quark fragmentation functions into hadrons, in particular, the fragmentation function of strange quark into kaons. All measurements are presented in the following chapters.

Chapter 3

Quark Fragmentation Process

The fragmentation process, also called hadronization process, is a fundamental mechanism in Quantum Chromodynamics and describes the transition of quarks, defined as elementary particles and colored objects in a QCD picture, into final state hadrons. Since this large distances process can not be calculated in perturbative, the only way to understand it consists on studying the properties of the detected final state particles.

Much effort has been done in order to understand the fragmentation process, resulting in a number of phenomenological models which try to simulate it. A brief overview of these models is given in section 3.1. The fragmentation process is also described by the *quark fragmentation functions into hadrons*. These functions enter the computation of cross sections of many reactions. Their precise knowledge is crucial for the interpretation of physical results. Their definition and properties are described in section 3.2, and their measurement is explained in section 3.3.

3.1 Quark Fragmentation Models

Different models have been developed to explain the fragmentation process. They are based on experimental data and theoretical approaches. Such models form an essential ingredient for Monte Carlo simulations and propose an illustration of how quarks of different flavors confine together to make a hadron. Three main schools of thought exist : Independent fragmentation, Lund fragmentation and Cluster fragmentation. These models are briefly discussed in the following.

3.1.1 The Independent Fragmentation Model

The first attempt to describe the fragmentation process was proposed out in the seventies (1978) by Field and Feynman [26], to explain the limited transverse momenta observed in hadron jets in e+e- annihilation. This model is based on the simple assumption that each parton fragments independently from the rest. Consider a quark q produced with a specific momentum and energy. At a certain point, this quark will confine with an anti-quark $\bar{q'}$ originating from vacuum fluctuations to produce the first rank primary[1] meson ($q\bar{q'}$) carrying a fraction z of the energy of the original quark, while the remaining quark $q^{'}$ will carry (1-z) of the original energy (figure 3.1). This energy sharing is described by a probabilistic function $f(z)$ which is assumed to be independent from the remaining energy at each step. In other words, $f(z)dz$ gives the probability that a primary meson leaves a fraction of its momentum between z and $z + dz$ to the remaining cascade. This process is iterated up to a certain threshold (energy cutoff) and the last quark with an energy below this threshold is discarded.

The independent fragmentation model is based on the probability to find a first rank primary meson with energy $\in [z, z + dz]$ in a jet of hadrons, given by:

[1]The produced mesons are said to be primary mesons when they originate directly from the fragmentation of the original quark. If they decay, the corresponding products are called secondary mesons and so on.

$$F(z)dz = f(1-z)\mathrm{dz} + \int_{\mathrm{z}}^{1} \mathrm{f}(\eta)\mathrm{d}\eta\mathrm{F}(\mathrm{z}/\eta)\mathrm{dz}/\eta \tag{3.1}$$

where $f(1-z)$dz denotes the probability that the corresponding meson is of first rank. If this meson is not of first rank, $f(\eta)d\eta$ parametrizes the probability that an energy fraction η is left to the remaining cascade and $F(z/\eta)dz/\eta$ represents the probability to find a first rank meson in the remaining cascade. The Field-Feynman parametrization of $f(z)$ is the ansatz which provides a simple solution to Eq. 3.1:

$$f(z) = 1 - a + 3a(1-z)^2 \tag{3.2}$$

with a default value of a = 0.77 [26]. In this model, the "rank" of a specific hadron is the ordering in production time in the center-of-mass system, starting from the hadron that contains the struck quark. Although this model does not predict an ordering according to the momenta of produced hadrons, the first rank hadron has the highest momentum and higher rank hadrons possess lower momentum. The vector meson production with respect to pseudoscalar meson production is 1 : 1, and the flavor production ratios are $u\bar{u} : d\bar{d} : s\bar{s} : 1 : 1 : 0.5$. The transverse momentum of the produced hadron is assumed to have a Gaussian shape with $<P_{\perp}> = 0.35$ $(\mathrm{GeV/c})^2$. Finally, the produced hadrons are not correlated with each others.

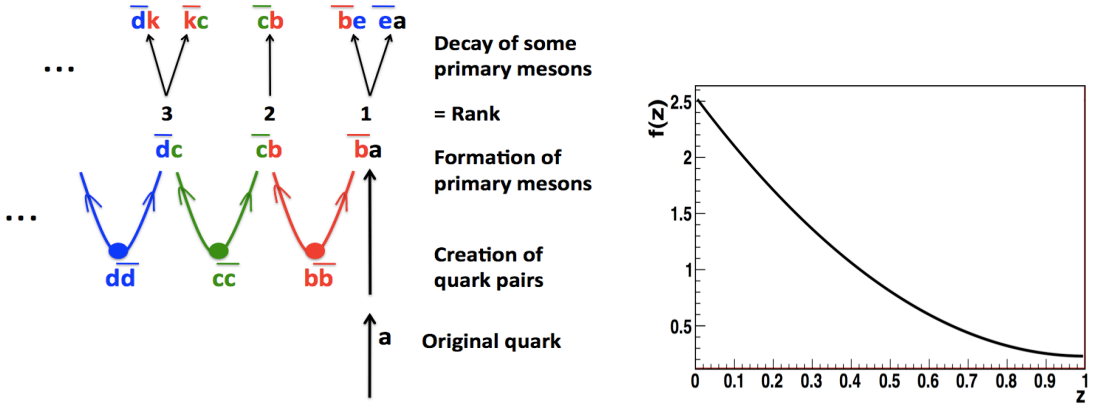

(a) (b)

Figure 3.1: (a)Hierarchy of the final mesons produced from the fragmentation of a quark of type **a** into hadrons within the independent fragmentation model. Starting from the quark **a**, new pairs $\mathbf{b\bar{b}}$, $\mathbf{c\bar{c}}$, etc., are created from vacuum fluctuations allowing to produce "primary" mesons. The primary meson $\bar{b}a$ that contains the original quark have the rank one and the meson $\bar{c}b$ have the rank two,... Finally some of the primary meson decay into secondary mesons. The illustration is taken from [26]. (b) The Field-Feynman fragmentation function (Eq. 3.2) as a function of z.

Many properties of hadronic jets are well described by independent fragmentation. However, this model suffer from many shortcomings. For example, the neglect of the quark of highest rank in a jet causes small violations of energy, momentum and flavor quantum number conservation. Also, the particle multiplicities depend on the reference frame. All these weaknesses led to the development of other models used in the Monte Carlo simulations.

3.1.2 The Lund String Fragmentation Model

The first version of the string fragmentation model was developed in 1974 by X. Artru and G. Mennesier [22]. The Lund string model [24] appeared later in 1977. The Lund string fragmentation model is based on QCD prediction of confinement which causes the potential energy of the color field stretched between a pair of quarks to increase with distance. The underlying principle of the Lund model is illustrated in Figure 3.2.

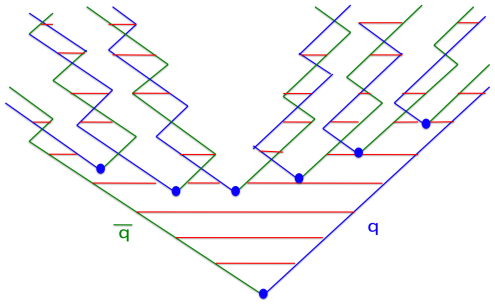

Figure 3.2: Illustration of the motion of quarks and antiquarks in a $q\bar{q}$ system in the Lund string model for the fragmentation process. Starting from the original $q\bar{q}$ pair, new pairs can be produced along the string causing a breakup of the string into separate bound states. Each bound state contains a fraction of the total, initial, energy. The color of the lines correspond to the color charge of quarks and antiquarks and blue points represent breakup vertices. The fragmentation starts in the middle and spreads outwards. This illustration is taken from [25].

Consider a quark and an anti-quark moving apart in opposite directions. Due to the gluon self-coupling, the color field lines between the quark and the anti-quark compresses into a tube-like region (string), in opposite to the electromagnetic field case where all lines spread out over all space. From the available field energy, new $q\bar{q}$ pairs can be created, the original string breaks into two smaller strings moving in opposite directions, one with fractional energy z, the other with energy $(1-z)$. For each string, the same process continues until a quark-anti-quark string is close to the mass shell of a hadron. The decision of the final state hadron type is made according to a random choice based on three parameters:

- The flavor production ratios $u\bar{u} : d\bar{d} : s\bar{s} = 1 : 1 : 0.3$. These flavor suppression are predicted in terms of quark masses. The suppression of $s\bar{s}$ production is left as a free parameter in the model, the default value being 0.3.

- The ratio between quark and diquark production. This parameter controls the ratio between mesons and baryons through three parameters: the relative probability to select a diquark rather than a quark, the suppression factor associated with a diquark containing a strange quark and the suppression of spin 1 diquark relative to spin 0 ones.

- The ratio between vector and pseudoscalar meson production 1 : 1.

In contrast to the independent fragmentation model, the Lund string model conserves energy, momentum and all internal quantum numbers in the fragmentation process. It consists in an iterative approach, each iteration is based mainly on three steps :

Flavor selection : In the first step, the flavor of the newly created $q\bar{q}$ pair is chosen. Massless quark-anti quark without transverse momentum are then produced at one point and pulled apart by the color field (Figure 3.3). If masses and transverse momenta of the $q\bar{q}$ pair are taken into account, the quark and anti-quark of the pair shall be produced at a certain distance so that the field energy between them can be transformed into the sum of the two transverse masses $m_\perp = \sqrt{m^2 + p_\perp^2}$. In quantum mechanics, quark and anti-quark are produced at one point and then tunneled out to the allowed region, with a certain probability:

$$P \sim \exp\left(-\frac{\pi m_{\perp q}^2}{\kappa}\right) = \exp\left(-\frac{\pi p_{\perp q}^2}{\kappa}\right) \exp\left(-\frac{\pi m_q^2}{\kappa}\right) \tag{3.3}$$

The gaussian $p_\perp$ spectrum is common for all primary hadrons, i.e is flavor independent due to the factorization of the transverse momentum and the mass terms. However, since a hard scattering is associated with gluon radiation, further $p_\perp$ contributions from unresolved radiation as well as the decays of the resonances modify differently the spectra of mesons and baryons. Experimental results show that the assumed gaussian shape is a good approximation.
The tunneling probability gives rise to the suppression of the heavy quarks production ($u\bar{u} : d\bar{d} : s\bar{s} : c\bar{c} \approx 1 : 1 : 0.3 : 10^{-11}$).

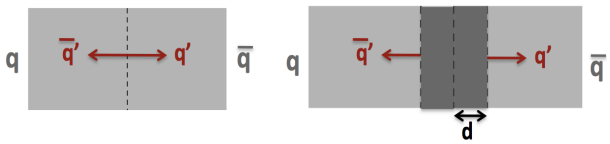

Figure 3.3: String breaking modeled by tunneling [25].

Mesons & **Baryons selection** : In a second step, quarks combine to produce a hadron with a specific spin state (singlet or triplet) and angular momentum. If the spins of quarks and anti-quarks are randomly distributed, a vector meson to pseudoscalar meson ratio of 3:1 is expected. However, the production of vector mesons is suppressed due to the spin-spin interaction of the meson's constituents which leads to a commonly ratio of 1:1.
In addition to mesons, baryons can also be produced. Several approaches exist for the simulation of the baryon formation mechanism. This formalism is described in the following example. In a first approach (Figure 3.4(a)), the baryons can be produced in a stepwise manner, e.g. along the color field between a red-(anti-red) pair, a new blue-(anti-blue) pair is created, the non-vanishing field in the center is of type green-(anti-green). Finally a new quark-(anti-quark) pair can be created and breaks the original string to yield a baryon and anti-baryon.
A second approach (Figure 3.4(b)) is based on the creation of a diquark and anti-diquark $qq - \bar{q}\bar{q}$ pair instead of a $q - \bar{q}$ pair, the produced baryon and anti-baryon are strongly correlated.
It exists a third approach (Figure 3.4(c)) called "pop corn" where no diquarks are produced but several $\bar{q}q$ pairs are created which leads to the formation of baryons as well as mesons in-between.

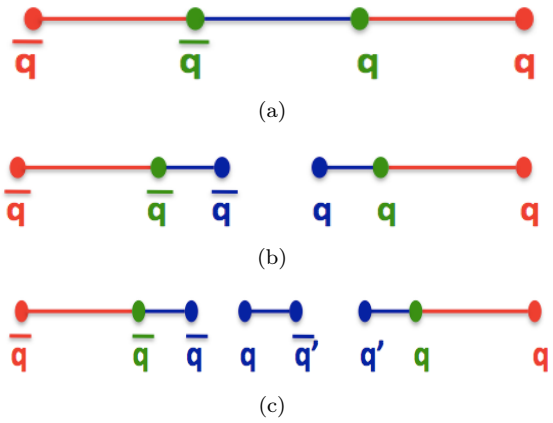

Figure 3.4: First (a), second (b) and third (c) approach for baryon production.

Further, one may imagine that the baryon production is related to the production of heavy quarks, or that it happens at the end of the color field.

String Fragmentation : Once the type of the hadron is selected as well as its spin and transverse momentum components, the longitudinal momentum of the hadron have to be determined. The energy fraction to be assigned to the new hadron is given by the *Lund symmetric fragmentation function*:

$$f(z) \sim \frac{(1-z)^a}{z} \exp\left(-\frac{bm_\perp^2}{z}\right) \tag{3.4}$$

where $m_\perp$ is the transverse mass squared $m_\perp^2 = m^2 + p_\perp^2$, a and b are free parameters which must be determined from data. These parameters are essential to regulate the energy distribution across the final states. Figure 3.5 shows the properties of the function for different values of a and b.
In the following, a short explanation is given for some features of this model.

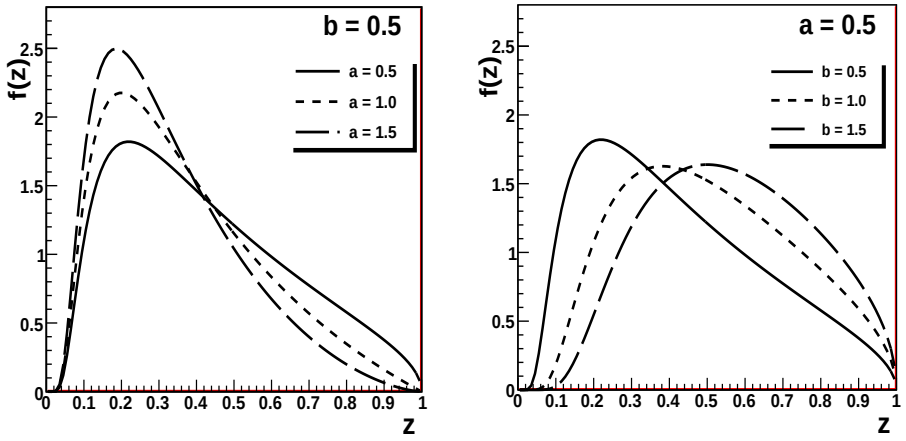

Figure 3.5: The symmetric Lund fragmentation function for different values of a and b.

3.1.2.1 The space-time description

The model provides a solution to the controversy between the iterative cascade hadronization model and the Landau-Pomeranchuk phenomena described below.

In the context of QED Bremsstrahlung, Landau and Pomeranchuk consider the concept of 'formation time'. The problem is to determine at what time one can distinguish between a state containing a single charged particle and a state containing the particle accompanied by a photon.

They point out that in a Lorentz frame where a particle is moving along the z-axis and the photon is moving transversely, it is necessary to wait at least a time corresponding to a wavelength which is inversely proportional to the transverse momentum of the photon, $\tau_0 = k_t^{-1}$. In a frame where the particle has an energy E, that time will change due to the time-dilation factor, $\tau = \tau_0 \cdot \frac{E}{k_t} = \frac{E}{k_t^2}$. In any covariant and causal setting, this formalism should provide a 'time ordering process'. In other words, the 'slowest' particles are emitted first while the high energy particles take a time proportional to their energies. In the hadronization cascade model, the first rank particle containing the struck quark takes a fraction z of its energy and leaves the rest to the remaining cascade. Therefore, the first rank particles are generally faster than the rest which is in contradiction with the Landau-Pomeranchuck prescription. However, in the Lund model, the rank-ordering corresponds to an ordering along the light cone of the string breakup points (as shown in Fig 3.6). As a consequence, the slowest particles are produced first which is in accordance with the Landau-Pomeranchuk description.

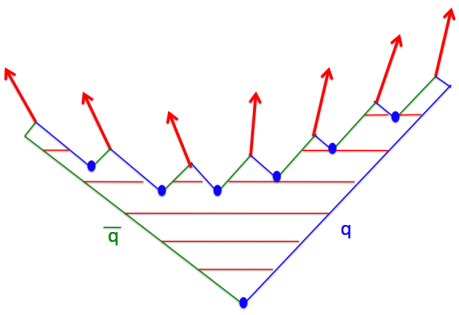

Figure 3.6: Breaking of one dimension string [25] in the LUND String Model. The slow particles are produced first in the middle and the fragmentation spreads outwards.

3.1.2.2 The unique breakup probability

In the Lund model, the probability to find a set of mesons with momenta (p_j) and masses m_j, $j = 1, ..., n$, is proportional to

$$\Pi_{j=1}^{n} N\delta(p_j^2 - m_j^2)\delta(\sum p_j - P_{tot})exp(-bA) \tag{3.5}$$

where A is the area spanned before the decay of the string. Two factors are of relative importance. The phase space increases with the multiplicity but the exponential term suppresses large areas. The result of this competition is that the vertices tend to have the same proper time τ, i.e. there is a unique decay distribution for the string breakups. As a consequence, the produced vertexes are causally disconnected such that the breakup can proceed in arbitrary order and the left-right symmetry is respected ($\mathcal{P}(1,2) = \mathcal{P}(1) \times \mathcal{P}(1 \to 2) = \mathcal{P}(2) \times \mathcal{P}(2 \to 1)$). This in turn means that the string breakups depend on the reference frame, thus there is no universal first and last vertices.

3.1.2.3 The Lund gluon model

The basic concept of the Lund model is that the final state particles emerge from the color field between the partons and not from any single parton by itself as in the independent fragmentation model. In the massless relativistic string, one can have 'internal' excitations which behave as massless particles. Such an excitation will drag the string along and create two segments of the string as shown in figure 3.7. Each one will decay locally as it was discussed earlier. The difference with respect to the case where gluons are not considered is that some of the particles will be pushed outwards by the motion of the string segment. No particle stems from a single q, $\bar{q}$ or g but all pick up some of the energy momentum of at least two of the original partons. In consequence, there will be particles produced between q and g and between g and $\bar{q}$, but no particles will be produced directly between q and $\bar{q}$. This is known as the "string effect".

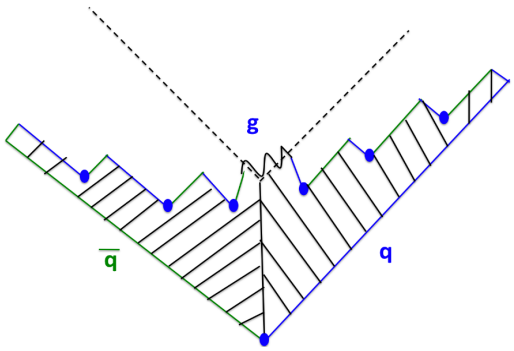

Figure 3.7: Breaking of a 1-D string in the Lund Model with an emission of a single extra gluon.

The Lund model takes into account the correlation between the produced hadrons. It is the most widely used model to simulate the properties of the fragmentation process in conjunction with the Monte Carlo generators as LEPTO [43], PYTHIA [44],... In the Monte Carlo simulation done in this thesis, the Lund model was used with the LEPTO generator.

3.1.3 The Cluster fragmentation Model

The cluster fragmentation model is based on the cluster formation through preconfinement and provides a unified description of longitudinal and transverse fragmentation properties, which is absent in both independent and string fragmentation models. In the Cluster model, the fragmentation process can be divided into three steps. In a first step, the initial partons, far off mass-shell, are evolved into partons nearer to mass-shell via the parton showers . The energy sharing in the vertices $q \to qg$, $g \to gq$ and $g \to gg$ is given by the Altarelli-Parisi splitting functions P_{ab}. In a second step, partons in the same region of phase space are grouped together into clusters which have a wide energy spectrum with a tail towards high masses. The clusters

with high masses are broken up into smaller ones. Finally, the clusters decay isotropically into hadrons. The cluster fragmentation of a pair of quarks is shown in Fig 3.8.
The HERWIG [45] Monte Carlo program is based upon a cluster fragmentation model developed by Weber and Maschesini which is the most prominent one against various existing models. In general, the cluster models contain few adjustable parameters like the QCD scale parameter and energy cut-offs.

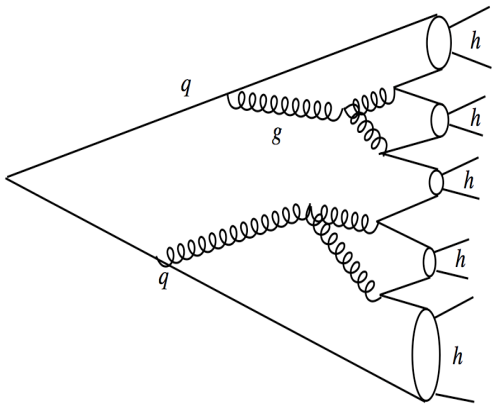

Figure 3.8: Hadron formation in the Cluster fragmentation model picture.

In conclusion, each model has its advantages and disadvantages. The Lund model has a large number of parameters which makes it more difficult to handle in the Monte Carlo program. However, it gives a better description for the baryon production as compared to the cluster fragmentation model.

3.2 Definition of Quark Fragmentation Functions into Hadrons

We discussed in the last section different models aiming to illustrate the transition between the quarks and the final state hadrons. Each model is characterized by an intrinsic fragmentation function $f(z)$ which describes the fragmentation process at the 'microscopic' level. These functions do not contain any information about the quark flavor initiating the fragmentation process or the type of the final state hadrons. They differ from the fragmentation functions $D_q^h(z)$ introduced in chapter 2 which give the formation probability of a hadron of type h from a quark of type q. The properties of these functions are discussed in this section.

3.2.1 Forward and backward hemispheres

In the deep inelastic scattering process, in the center of mass system of the virtual photon and the target nucleon, the struck quark and the remnant diquark, moving away from each other in opposite directions, stretch between them a color field. New $q\bar{q}$ pairs are then created along the color field and hadrons are formed. Hadrons which have been produced in space-time neighbourhood of the struck quark are said to be correlated, in flavor, to the struck quark. This leads to the formation of hadrons in two hemispheres (forward and backward hemispheres) defined with respect to the direction of the virtual photon in the center of mass of the photon-nucleon system.
The forward hemisphere, also called current fragmentation region, comprises hadrons which are correlated to the struck quark and are characterized by positive x_F, the fraction of the energy of the nucleon-photon system held by the hadron in the virtual photon direction (see table 2.1). The hadron selection must be restricted to the current fragmentation region to study the fragmentation process of interest. The target fragmentation region comprises the hadrons which are produced by the spectator quarks. They are characterized by negative values of x_F.
An appropriate variable, equivalent to x_F, is currently used to select hadrons in the current fragmentation region. It corresponds to z, the energy fraction of the virtual photon carried by the hadron, and it is used in this work.

3.2.2 Properties of Quark Fragmentation Functions

The QCD symmetries lead to a certain number of properties of the quark fragmentation functions. These symmetries are generally used in the extraction of fragmentation functions from experimental data and will be discussed in the following.

3.2.2.1 Factorization and Universality

In hard scattering interactions, all processes with an observed hadron in the final state can be described using a perturbative hard scattering cross section and non perturbative and universal functions: the quark fragmentation functions which describe the formation of hadrons. These functions depend only on the initial parton and the final state hadron without any dependence on the process from which they originate. The universality of the fragmentation functions predicted by the factorization theorem has been experimentally tested by comparing data on hadron production in e^+e^- collisions with similar data from deep inelastic scattering. Both data sets were found to be in agreement. Another test has been performed using NLO quark fragmentation functions extracted from data in e^+e^- annihilation. The resulting functions describe reasonably experimental data from $p\bar{p}$ and ep collisions.
A factorization breaking later investigated was the dependence of fragmentation functions upon the Bjorken variable x. A slight x dependence of the hadron multiplicities in deep inelastic muon-scattering has been seen at the EMC experiment at CERN.

3.2.2.2 Scaling and Evolution

The Quark Parton Model predicts the scaling of the fragmentation functions, i.e. fragmentation functions do not depend on Q^2 . However, a hard scattering is associated with gluon radiation which leads to some dependence of fragmentation functions on Q^2. This Q^2 dependence is calculated using the GLAP evolution equations (Eq. 3.6). The various fragmentation functions are assumed to evolve in Q^2 in a similar way.

$$\frac{d}{d\ln Q^2} D_q^h(z,Q^2) = \frac{\alpha_S(Q^2)}{2\pi} \sum_{q'} \int_z^1 \frac{d\xi}{\xi} P_{qq'}(\frac{z}{\xi}, Q^2) D_{q'}^h(\xi, Q^2) \tag{3.6}$$

The $P_{qq'}$ parametrizes the splitting of a parton q with momentum fraction z into two partons q and q', with momentum fractions z/ξ and ξ respectively. In other terms, they account for the possibility that the fragmentation of the parton q may happen via the radiation of a parton q' which fragments into a hadron h. This equation can be solved using the Mellin transformation technique which transforms convolutions into products. The products can then be evolved analytically by applying an evolution operator, the evolved products are then re-transformed numerically by applying the inverse Mellin transformation which yields the evolved fragmentation functions. The resulting fragmentation functions depend on Q^2.

3.2.2.3 Momentum and charge conservation

The fragmentation functions, defined as probability densities, are constrained by conservation laws. The momentum conservation implies that the momentum of a parton q is equal to the total momentum of all hadrons that originate from its fragmentation; this corresponds to the momentum sum rule (Eq 3.7). In parallel to the momentum conservation, the charge conservation implies the charge sum rule (Eq 3.8).

$$\sum_h \int_0^1 dz\ z D_q^h(z,Q^2) = 1 \tag{3.7}$$

$$\sum_h \int_0^1 dz\ e_h D_q^h(z,Q^2) = e_q \tag{3.8}$$

where e_h (e_q) is the electric charge of a hadron of type h (parton of type q) and the summation is over all hadron species h. One should note that the momentum sum rule is not used to impose a precise constraint on fragmentation functions. For example in global fits of fragmentation

functions, Eq 3.7 do not impose any constraint in the case of a specific hadron since the sum is over all hadron species (in Eq 3.7). The momentum sum rule therefore gives an upper limit for the fragmentation functions values and must be checked in their phenomenological extraction. Finally the probability conservation imposes an additional sum rule on the fragmentation function:

$$\sum_q \int_{z_{min}}^{1} \left[D_q^h(z) + D_{\bar{q}}^h(z)\right] dz = \eta_h \tag{3.9}$$

where z_{min} is the minimal energy required to produce a hadron, and η_h is the average multiplicity of hadrons of type h.

3.2.2.4 Isospin and Charge Conjugation Invariance

The definition of quark fragmentation function into hadron is valid for any type of quark and hadron. These fragmentation functions are subject, in the QCD improved parton model, to some QCD symmetries like charge conjugation and isospin invariance. This leads to some relations between different fragmentation functions. For example the charge conjugation symmetry relates the quark and anti-quark fragmentation functions as follows:

$$D_q^{h^+} = D_{\bar{q}}^{h^-} \tag{3.10}$$

and the isospin invariance implies, for pions,

$$D_u^{\pi^+} = D_d^{\pi^-} \tag{3.11}$$

Pion Fragmentation Functions: Starting with twelve fragmentation functions (six for each charge) and taking into account the above symmetries, the number of light quark fragmentation functions into pions is reduced to five: two "favored"[2] (Eq 3.12), two "unfavored"[3] (Eq 3.13) and one strange quark (Eq 3.14) fragmentation functions.

$$D_{fav,1}^{\pi} = D_u^{\pi^+} = D_{\bar{u}}^{\pi^-}, \quad D_{fav,2}^{\pi} = D_{\bar{d}}^{\pi^+} = D_d^{\pi^-} \tag{3.12}$$

$$D_{unf,1}^{\pi} = D_u^{\pi^-} = D_{\bar{u}}^{\pi^+}, \quad D_{unf,2}^{\pi} = D_{\bar{d}}^{\pi^+} = D_{\bar{d}}^{\pi^-} \tag{3.13}$$

$$D_s^{\pi} = D_s^{\pi^+} = D_s^{\pi^-} = D_{\bar{s}}^{\pi^+} = D_{\bar{s}}^{\pi^-} \tag{3.14}$$

In addition to the light quark fragmentation functions, the fragmentation functions of heavy quarks and gluons into pions should be considered. However they will not be discussed in this work since the mass thresholds for heavy quarks are higher than the covered kinematic domain and their production is expected to be small.

Kaon Fragmentation Functions: In the case of kaons, only the charge conjugation invariance is involved and reduces the number of fragmentation functions into six, if we neglect the heavy quarks and gluons fragmentation functions.

$$D_{fav,1} = D_{\bar{s}}^{K^+} = D_s^{K^-} \tag{3.15}$$

$$D_{fav,2} = D_u^{K^+} = D_{\bar{u}}^{K^-} \tag{3.16}$$

$$D_{\bar{u}}^{K^+} = D_u^{K^-}, \quad D_d^{K^+} = D_{\bar{d}}^{K^-}, \quad D_{\bar{d}}^{K^+} = D_d^{K^-}, \quad D_s^{K^+} = D_{\bar{s}}^{K^-} \tag{3.17}$$

In the case of pions and kaons, further assumptions can be made on fragmentation functions in order to extract them from experimental data. These assumptions are in general ad-hoc and their choice is usually made according to the data sets used in the fit. This will be discussed in details in chapter 9.

[2] A fragmentation function D_q^h is called favored when q is a valence quark in the corresponding hadron h.
[3] A fragmentation function D_q^h is called unfavored when q is a sea quark in the corresponding hadron h.

3.3 Measurements and Parametrizations

All hard scattering processes, e^+e^- annihilation, $pp(\bar{p})$ collision and deep inelastic scattering, are good tools to study the fragmentation process and to extract fragmentation functions. The interesting feature of the annihilation process is the relative simplicity and cleanliness compared to other processes. In e^+e^- annihilation, the interaction occurs between point-like particles for which the interaction can be calculated from perturbative QED. For $pp(\bar{p})$ collision and deep inelastic scattering, however, the parton distribution functions which describe the unknown nucleon structure, play an important role in the interaction and are involved in the cross sections. They are therefore an essential ingredient in the hard scattering cross section and their precise knowledge is important.

3.3.1 EMC, JLab and COMPASS Measurements

A direct access to the quark fragmentation functions is provided in the semi-inclusive deep inelastic scattering process, via the hadron multiplicities defined as the average number of hadrons produced per DIS interaction (see chapter 7). The hadron multiplicities are expressed, in the QCD improved parton model, in terms of parton distribution functions and in terms of quark fragmentation functions as given in Eq. 3.18.

$$\frac{1}{\sigma^{DIS}(x,Q^2)}\frac{d\sigma^h(x,Q^2,z)}{dxdQ^2dz} = \frac{\sum_q e_q^2 q(x,Q^2) D_q^h(z,Q^2)}{\sum_q e_q^2 q(x,Q^2)} \tag{3.18}$$

where σ^{DIS} denotes the cross section for DIS interaction and σ^h denotes the cross section for hadron production in DIS. The first measurement of fragmentation functions in deep inelastic scattering has been performed by the EMC [30] collaboration at CERN. EMC was a fixed target experiment which used a 280 GeV muon beam to scatter off nuclear targets (proton and deuterium). The EMC apparatus was designed to cover a large geometrical acceptance and equipped with detectors allowing particle identification. The latter is crucial for fragmentation function analysis since it allows flavor separation. Favored and unfavored fragmentation functions into pions have been extracted from muon-deuterium deep inelastic scattering. By neglecting the sea quark contribution, the isoscalar target permits a LO extraction of pions fragmentation functions without any assumption about the parton distributions. However, the influence of the sea quarks increases at low x limiting the validity of the approach.

In a late EMC publication [31], a LO extraction of fragmentation functions has been performed without neglecting the sea quark contribution. The data analysis covered the kinematic domain defined by a four momentum transfer squared $Q^2 > 4$ GeV^2, an invariant mass squared W^2 in the range [16, 200] GeV^2, a energy transfer ν in the range [20, 260] GeV and $x > 0.12$. The final statistics include ~ 8000 DIS events for each target type (proton and deuterium). The strange fragmentation function into pion D_s^π was assumed to be equal to the unfavored fragmentation function while for kaons and protons, ah-hoc assumptions have been made ($\frac{1}{2}(D_s^{K^+} + D_{\bar{s}}^{K^+}) = D_u^{K^+}$, $\frac{1}{2}(D_s^p + D_{\bar{s}}^p) = D_{\bar{u}}^p$). The parton distribution functions were assumed to be known and were taken from a parametrization. The method presented in this publication allowed to extract the up quark and anti-quark fragmentation functions into charged pions, kaons and protons, for both proton and deuterium targets. The fragmentation functions obtained independently from both targets were found to be in agreement within statistical errors as expected. These data, measured in bins of z, are often referred to as the"EMC parametrization of fragmentation functions", with a value of $D_{\bar{s}}^{K^+}$ taken equal to $D_u^{\pi^+}$ using the SU(3) flavor symmetry.

The experimental extraction of quark fragmentation functions has been performed recently by two experiments: COMPASS (this thesis) and E00-108 [57] in Hall C at Jefferson Lab (JLab). The E00-108 experiment extracted only the ratio of unfavored to favored pion fragmentation functions. The analyzed data were taken in 2003 by scattering a 5.479 GeV electron beam on proton and deuterium targets. The deep inelastic scattering region was limited to $2 < Q^2 < 4$ (GeV/c)^2, $W^2 > 4$ (GeV/c)^2 and the Bjorken variable was restricted to $0.2 < x < 0.6$. The final state hadrons are selected with a fractional energy z ($= E_h/E_\gamma$) in the range [0.2, 1] and with small transverse momenta with respect to the virtual photon direction $P_t^2 < 0.2$ (GeV/c)^2.

Finally the E00-108 experiment can not identify kaons and consequently do not provide kaon fragmentation functions.

The COMPASS collaboration performed the extraction of fragmentation functions (this thesis) using data collected by scattering a 160 GeV/c muon beam scattering off a deuteron target (^{6}LiD). The kinematic region was restricted to: $Q^2 > 1$ (GeV/c)^2, $0.1 < y < 0.9$, $4 \cdot 10^{-2} < x < 0.7$, $W > 7$ (GeV/c) and $0.2 < z < 0.85$. COMPASS has the advantage of covering a wide kinematic domain in addition to providing high statistics with respect to EMC and JLab. The results for charged pion and kaon fragmentation functions versus z and (Q^2,z) are presented and discussed in chapter 9. They are shown in comparison with EMC and JLab results.

3.3.2 Parametrization for Fragmentation Functions

Besides the experimental extraction of fragmentation functions, another approach can be used for their extraction. It consists in fitting experimental data collected by studying processes where fragmentation functions are involved. The fit makes use of a LO or a NLO ansätze for the cross section of the considered processes and for the fragmentation functions. In the existing fragmentation functions analyzes the bulk of data used rely on electron-positron annihilation into charged hadrons (LEP). These data have the advantage of being very precise due to the high statistics measurements, however, they do not allow to disentangle quark from anti-quark fragmentation functions. In addition, the gluon fragmentation is not constrained. Complementary information on the quark fragmentation process are provided by proton-proton collision and deep inelastic lepton-nucleon scattering processes. The inclusion of these processes yields a much more complete picture of the quark fragmentation process since it increases statistics and weigh differently the contributions of partons of different flavors. As a consequence, the individual quark and anti-quark fragmentation functions of different flavors can be extracted.

Currently, different parametrization (QCD global analysis) for quark fragmentation functions exist. They differ by the used data sets and by the assumptions they make in the analysis. A summary of the existing parametrization is given in table 3.1 and followed by an overview for some of the listed parametrization.

Parametrization (& corresponding authors)	year	Data sets
KKP (B. A. Kniehl, G. Kramer and B. Potter) [32]	2000	e^+e^-
KRE (S. Kretzer) [33]	2001	e^+e^-
DSS (D. de Florian, R. Sassot and M. Stratmann) [34]	2007	e^+e^-, pp, SIDIS
HKNS (M. Hirai, S. Kumano, T. H. Nagai and K. Sudoh) [35]	2007	e^+e^-
AKK (S. Albino, B. A. Kniehl and G. Kramer) [36]	2008	e^+e^-, pp

Table 3.1: Existing parametrizations for quark fragmentation functions. The first column shows the name of the parametrization and the corresponding authors. The second column is the year of publication and the last one shows the data sets used.

3.3.2.1 Kretzer parametrization

A global fit of quark fragmentation functions for $\pi^{\pm}$ and $K^{\pm}$ was performed by S. Kretzer in [33]. This fit includes high statistics e^+e^- annihilation data collected by SLD [27] at SLAC, ALEPH [28] at LEP and by TPC [29]. The fragmentation functions were constrained to respect the conservation laws (momentum and charge sum rules) as well as the charge conjugation and the isospin invariance symmetries. In addition to the symmetries, the unfavored fragmentation functions are assumed to be equal for both pions ($D_{\bar{u}}^{\pi^+} = D_{d}^{\pi^+} = D_{\bar{s}}^{\pi^+} = D_{s}^{\pi^+}$) and kaons ($D_{\bar{u}}^{K^+} = D_{s}^{K^+} = D_{d}^{K^+} = D_{\bar{d}}^{K^+}$). Further assumptions are made depending on each case (π or K). The analysis was performed at Next-to-Leading order in the $\bar{MS}$ factorization scheme and using the functional form for $D_i^h(z, \mu_0^2)$ given by:

$$D_i^h(z, \mu_0^2) = N_i^h z^{\alpha_i^h} (1 - z)^{\beta_i^h} \tag{3.19}$$

In the case of pions, the two favored fragmentation functions are assumed to be equal (Eq 3.20). In addition, favored and unfavored fragmentation functions are assumed to be related via a z-dependent term (3.21). As a consequence, only two FFs are fitted.

$$D_u^{\pi^+} = D_{\bar{d}}^{\pi^+} \tag{3.20}$$

$$D_s^{\pi^+} = D_{\bar{s}}^{\pi^+} = (1-z)D_u^{\pi^+} \tag{3.21}$$

In the case of kaons, the two favored fragmentation functions ($D_u^{K^+}$, $D_{\bar{s}}^{K^+}$) are considered to be related (Eq 3.22). Furthermore, the unfavored fragmentation function is related to the favored one (Eq 3.23). Finally, three fragmentation functions are fitted.

$$D_u^{K^+} = (1-z)D_{\bar{s}}^{K^+} \tag{3.22}$$

$$D_d^{K^+} = D_{\bar{d}}^{K^+} = D_s^{K^+} = (1-z)^2 D_{\bar{s}}^{K^+} \tag{3.23}$$

The charm and bottom quark fragmentation functions as well as the gluon fragmentation functions are fitted. They are parametrized using the same function form (Eq 3.19). Furthermore, charm and bottom fragmentation functions are assumed to be equal for positive and negative hadrons.

3.3.2.2 DSS parametrization

In Ref. [34] D. de Florian, M. Stratmann and R. Sassot (DSS) performed a global fit of fragmentation functions for $\pi^{\pm}$, $K^{\pm}$ and $p/\bar{p}$. The data sets used in this fit include e^+e^- reaction data from LEP, pp collisions data from the BRAHMS, PHENIX and STAR experiments at RHIC and semi-inclusive deep inelastic scattering data from the HERMES experiment at HERA. The measurements performed by the HERMES collaboration are charge separated and thus provide the needed constraints on the valence quark fragmentation functions. The gluon fragmentation function is well constrained with respect to the Kretzer case due to the use of pp collision data. Similarly to the Kretzer case, the conservation laws as well as the charge conjugation are taken into account. However, the isospin invariance is not respected. Individual fragmentation functions for quark and antiquarks of all flavors as well as gluon fragmentation functions have the same functional form given by:

$$D_i^H(z,\mu_0) = \frac{N_i z^{\alpha_i}(1-z)^{\beta_i}\left[1+\gamma_i(1-z)^{\delta_i}\right]}{B[2+\alpha_i,\beta_i+1]+\gamma_i B[2+\alpha_i,\beta_i+\delta_i+1]} \tag{3.24}$$

where $B[a,b]$ is the Euler Beta-function and N_i represents the contribution of D_i^H in the momentum sum rule. Due to the limited number of free parameters that can be fitted from experimental data, favored and unfavored fragmentation functions are assumed to be proportional. In the case of pions, the two favored (unfavored) fragmentation functions are related with the proportionality factor $\mathcal{N}$ ($\mathcal{N}'$) (Eq 3.25). As a consequence, two favored ($D_u^{\pi^+}$, $D_{\bar{d}}^{\pi^+}$) and two unfavored ($D_{\bar{u}}^{\pi^+}$, $D_s^{\pi^+}$) fragmentation functions are fitted.

$$D_u^{\pi^+} = \mathcal{N} D_{\bar{d}}^{\pi^+}, \quad D_s^{\pi^+} = \mathcal{N}' D_{\bar{u}}^{\pi^+} \tag{3.25}$$

In the case of kaons, since data are scarce and do not permit to discriminate different flavors, all unfavored fragmentation functions are assumed to be equal (Eq 3.27). No assumption however has been made for the favored fragmentation functions. This leads to two favored ($D_u^{K^+}$, $D_{\bar{s}}^{K^+}$) and one unfavored ($D_{\bar{u}}^{K^+}$) fragmentation functions to be fitted.

$$D_u^{K^+}, D_{\bar{s}}^{K^+} \tag{3.26}$$

$$D_{\bar{u}}^{K^+} = D_d^{K^+} = D_{\bar{d}}^{K^+} = D_s^{K^+} \tag{3.27}$$

3.3.2.3 AKK parametrization

The AKK parametrization [36] refers to the global fit of fragmentation functions for $\pi^{\pm}$, $K^{\pm}$, $p/\bar{p}$, K^0_S and $\Lambda/\bar{\Lambda}$. This fit includes pp reaction data from the BRAHMS, PHENIX and STAR collaborations at RHIC, $p\bar{p}$ reaction data from the CDF collaboration at the Tevatron and e^+e^- reaction data from LEP. The fragmentation functions are parametrized with the functional form:

$$D_i^h(z,Q^2) = N_i z^{\alpha_i}(1-z)^{\beta_i}(1+\gamma_i(1-z)^{\delta_i}) \tag{3.28}$$

The fragmentation functions are constrained by the conservation laws and symmetries. Further assumptions have been made in each case (π or K) separately. For pions, all favoured fragmentation functions are assumed to be equal (Eq 3.29). The same assumption is made for the unfavored non-strange (left hand side of Eq 3.30) and for the unfavored strange fragmentation functions (right hand side of Eq 3.30). This leads to three unknown fragmentation functions.

$$D_u^{\pi^+} = D_{\bar{d}}^{\pi^+} \tag{3.29}$$

$$D_d^{\pi^+} = D_{\bar{u}}^{\pi^+}, \quad D_s^{\pi^+} = D_{\bar{s}}^{\pi^+} \tag{3.30}$$

In the case of kaons, in addition to the charge conjugation symmetry, it is assumed that unfavored non-strange fragmentation functions are equal giving rise to five unknown fragmentation functions (Eq 3.32).

$$D_d^{K^+} = D_{\bar{d}}^{K^+} \tag{3.31}$$

$$D_u^{K^+}, D_{\bar{s}}^{K^+}, D_s^{K^+}, D_{\bar{u}}^{K^+}, D_d^{K^+} \tag{3.32}$$

3.3.2.4 HKNS parametrization

The HKNS parametrization provides fragmentation functions for $\pi^{\pm}$, $K^{\pm}$ and $p/\bar{p}$ by fitting e^+e^- annihilation data with identified final state hadrons. The data with unidentified hadrons are excluded to avoid any contamination to the π, K and p samples. All favored fragmentation functions are assumed to be equal. Similarly all unfavored fragmentation functions are supposed to be equal. As a consequence, in both pion and kaon cases, only two fragmentation functions are fitted.

3.3.2.5 Comparison

A comparison between different LO parametrization at $Q^2 = 3.5$ GeV/c^2 is shown in figure 3.9 for pions and in figure 3.10 for kaons. In the case of pions, a relatively good agreement is found among the different parametrization. For D_u^{π}, KRE, DSS and KKP parametrization agree among themselves within 20% while the HKNS parametrization differ by 40-50% at small z (< 0.45) and by 80% at higher z. The same observation can be drawn in the case of d, $\bar{u}$ and $\bar{d}$ fragmentation functions. For the strange quark s, however, the parametrizations differ by a factor of two at small z (up to 0.45) and even more at higher z ($0.45 < z < 1$). For the the charm fragmentation functions, similar distributions are obtained by the different parametrizations and agree within 40%-60% in the full z range. This result is not surprising since the same assumptions are made in the charm sector in nearly all parametrizations. Note that the charm fragmentation function is not given by the KKP parametrization.
In the case of kaons, the parametrization disagree for nearly all quark fragmentation functions except for the charm case. This disagreement can be due the different assumptions used in different parametrization and/or to the lack of experimental data in the kaon sector. Currently the reason for the disagreement is not known, however, the most widely used parametrization is the DSS because it is the only one that includes all existing data and covers the largest number of reactions (pp collisions, e^+e^- annihilation, SIDIS reactions).

3.4 Summary

Several models simulating fragmentation process have been developed and used in different Monte Carlo simulations. The Lund model is the most widely used because it gives a rather complete picture for the quark fragmentation into hadrons. In addition it gives a better description of experimental data. It is used in the presented work.

The fragmentation functions distributions, which enter the computation of cross section for hadron production, can be extracted from experimental data by assuming some functional form with a certain number of free parameters. Several parametrization exist and differ by large factors, in particular for kaons fragmentation functions. This observation highlights the need of further experimental and theoretical studies. This work represents an experimental contribution to the knowledge of the fragmentation (hadronization) process.

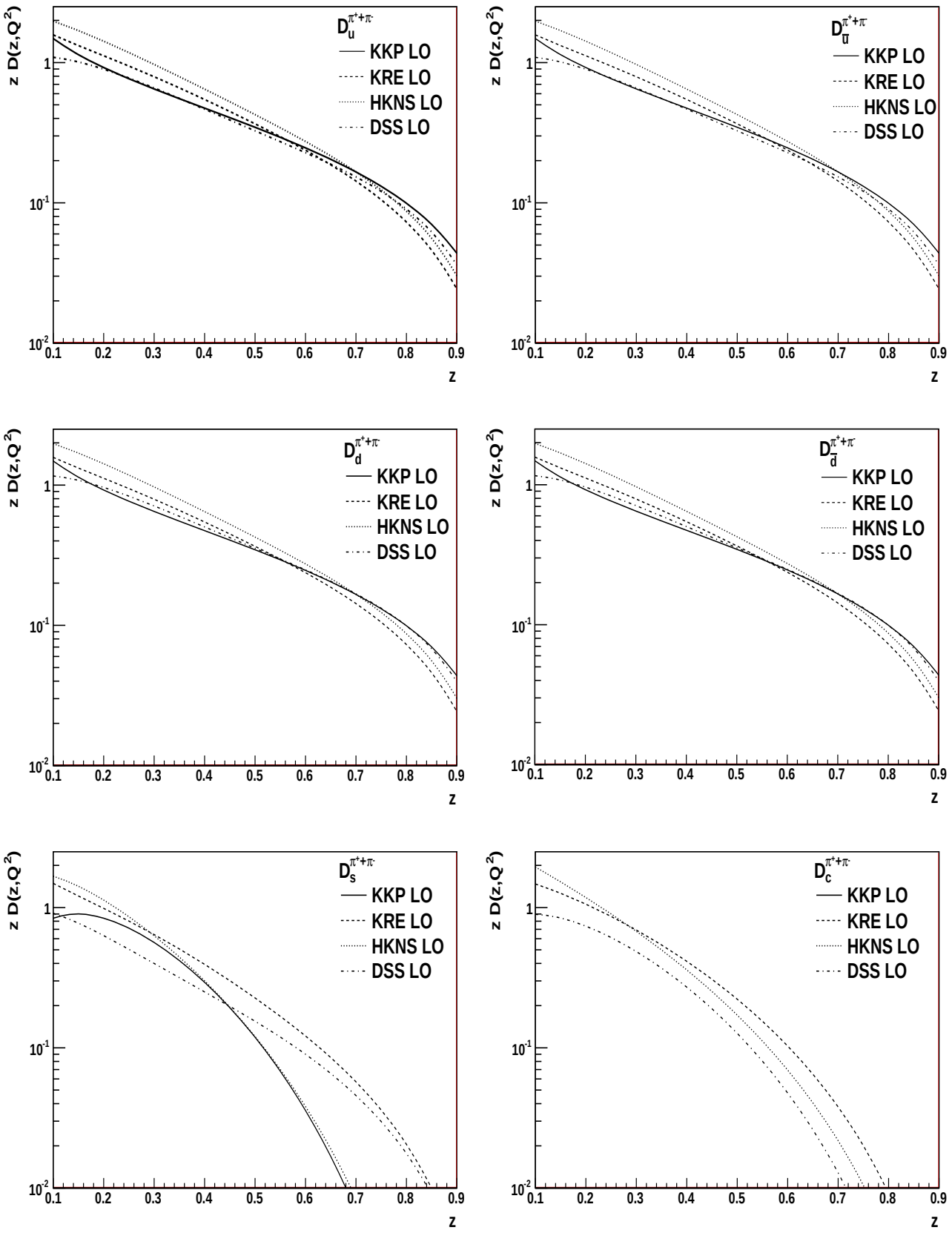

Figure 3.9: Comparison of different LO parametrization for $D_u^{\pi^+ + \pi^-}$, $D_{\bar{u}}^{\pi^+ + \pi^-}$, $D_d^{\pi^+ + \pi^-}$, $D_{\bar{d}}^{\pi^+ + \pi^-}$, $D_s^{\pi^+ + \pi^-}$ and $D_c^{\pi^+ + \pi^-}$; the fragmentation functions values are evaluated at $Q^2 = 3.5$ $(\mathrm{GeV/c})^2$ using the FORTRAN code of each parametrization, in [55].

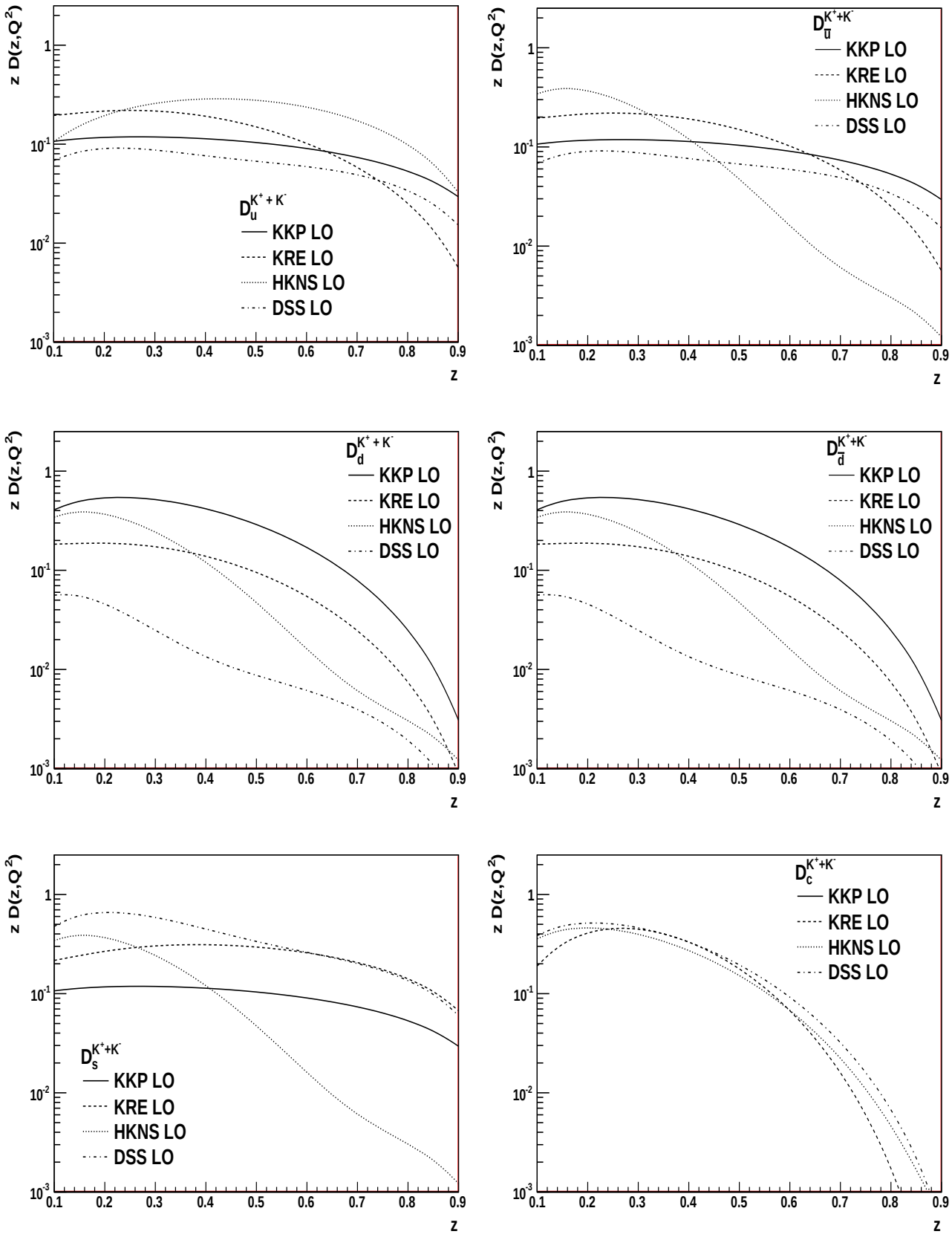

Figure 3.10: Comparison of different NLO parametrization for $D_u^{K^+ + K^-}$, $D_{\bar{u}}^{K^+ + K^-}$, $D_d^{K^+ + K^-}$, $D_{\bar{d}}^{K^+ + K^-}$, $D_s^{K^+ + K^-}$ and $D_c^{K^+ + K^-}$; the fragmentation functions values are evaluated at $Q^2 = 3.5$ $(\mathrm{GeV/c})^2$ using the FORTRAN code of each parametrization, in [55].

Chapter 4

The COMPASS experiment

COMPASS (*COmmon Muon and Proton Aparatus for Structure and Spectroscopy*) is a fixed target experiment based at CERN and dedicated to the study of the nucleon spin structure and the hadron spectroscopy. Several programs of measurements have been realized using muon and hadron beams on various target types. The main goal of the COMPASS muon program was the determination of the quark and the gluon polarizations inside the nucleon by measuring spin asymmetries in processes sensitive to quark and gluon distributions. To accomplish these measurements, the muon beam and the nucleon target must be both longitudinally polarized. In parallel, by summing over the two polarizations, further measurements can be performed as absolute cross sections, hadron production, quark fragmentation functions into hadrons,...The main goals of the COMPASS muon program are about to be achieved and a new proposal for the COMPASS II was accepted by the CERN SPSC [66]. The new physics program splits into several topics which include the study of Generalized Parton Distributions (GPD) from Deeply Virtual Compton Scattering (DVCS), the test of the chiral perturbation theory via Primakoff reactions, the Drell-Yan (DY) and further measurements in hadron and light mesons spectroscopy. The spectroscopy program aims to search for exotic states and to measure the pion polarizability. This program requires a hadron beam which was used from 2008 and 2009 after a beam test in 2004.
The work presented in this thesis comprises results of two studies. The first one consists in determining the quark helicity distributions from double spin asymmetries (chapter 6). The second part, which is the most important part of this work, consists in measuring hadron multiplicities (chapter 7) and quark fragmentation functions from unpolarized data. A detailed description of the beam, the target and the apparatus is given in this chapter.

4.1 Polarized Beam

The COMPASS experiment is installed in the M2 beam line of the CERN SPS (*Super Proton Synchrotron*) which can provide various high intensity beams. Initially, a primary proton beam is accelerated in the SPS up to the energy of 450 GeV/c with an intensity of 10^{13} protons during 4.8s long spills, within a 16.8s long SPS cycle.
After the acceleration, the primary beam impinges on a beryllium target generating secondary pions and kaons. The momentum selected pions and kaons are transported through a 600 m long decay channel equipped by a hadron absorber . Along this channel, about 5% of pions decay into muons and neutrinos. When operating with a muon beam, the remaining hadrons are stopped at the end of the channel in the hadron absorber. A set of hodoscopes, forming the *Beam Momentum Station* (BMS, figure 4.1) and located upstream of the experimental hall, perform the measurement of the beam momentum with a precision of 0.5%. The muon momentum is chosen to be around $90 - 94\%$ of the central hadron momentum in order to provide the best compromise between the muon flux and the polarization.
After the BMS the muon beam is focused on the COMPASS polarized target located in the experimental hall. The nominal intensity of the beam is in average $2 \cdot 10^8$ muons per 4.8s SPS spill. The beam is naturally polarized due to the parity violation of the $\pi \to \mu\nu$ decay channel.

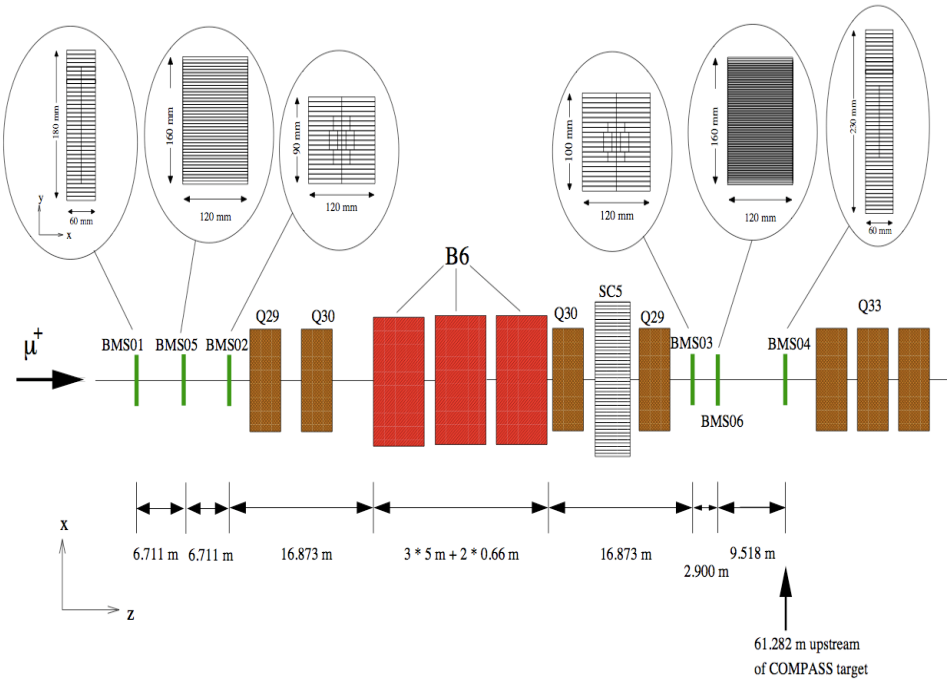

Figure 4.1: Schematic view of the Beam Momentum Station [53] (BMS) consisting of six stations BMS01-06 of hodoscopes of scintillators.

In the pion rest frame, the polarization of the muon is 100%. In the laboratory frame, the muon polarization is a function of pion (E_π) and the muon (E_μ) energy and is given by the formula:

$$P_{\mu^\pm} = \pm \frac{m_\pi^2 + \left(1 - 2\frac{E_\pi}{E_\mu}\right) m_\mu^2}{m_\pi^2 - m_\mu^2} \tag{4.1}$$

where the polarization sign refers to positive and negative muons. In average, the polarization is of the order of $(80 \pm 4\%)$, as calculated by the Monte Carlo simulation.

4.2 Solid Polarized Target

The COMPASS solid polarized target [53] was initially designed with two cylindrical cells - each cell being 60 cm long with a diameter of 3 cm - separated by 10 cm. To obtain an isoscalar target, the two cells are filled with a deuterated lithium (^6LiD) which is considered as a ^4He nucleus (spin 0) and a deuteron (spin 1); the fraction of polarisable material is approximately 50%. For a proton target, NH_3 is used and the fraction of polarized material is $\sim 18\%$. The target is placed in the magnetic field produced by a superconducting system which consists of a solenoid with a longitudinal field of 2.5 T and a dipole magnet providing a perpendicular field of 0.5 T. The dipole field is used to reverse the target polarization as well as to hold the spin direction transverse to the beam when needed (tranversity measurements).
The standard method used to polarize matter is based on the Zeeman effect. In a low temperature (below 1 K) and a strong magnetic field, electrons spins are nearly 100% polarized while nuclear spin polarization is negligible due to the small magnetic moment of the nucleons. The Dynamic Nuclear Polarization (DNP) is used to reach a high level of nuclear polarization by tranfering the high electron polarization to the nucleons. The polarized material is maintained in a high magnetic field and at low temperature ($50 - 70$ mK) such that a high electron polarization is achieved. The target is then exposed to the microwave radiation of energy required to flip simultaneously the electron and the proton spins. Since the energy of the radiation depends on the total spin state of the $e-p$ system, the frequency of the microwave is selected according to the required orientation of the nucleon spin with respect to the magnetic field. Within milliseconds, the electron relax to a lower energy state in contrast to the proton which has a very low probability

to change its spin due to its small magnetic moment. Once the nuclear polarization has achieved a reasonable level ($\sim$ 50% for ^{6}LiD, $\sim$ 90% for NH_3), the microwaves are switched off and the temperature is reduced to 50 mK. The nuclear polarization can be maintained in this mode, the *frozen spin* mode, for several days in the solenoid field. The target cells are polarized in opposite directions to minimize the systematic error in the spin asymmetry measurement.

4.3 Spectrometer

The COMPASS spectrometer [53] allows to reconstruct the tracks of all particles involved in a scattering event, i.e. the incident muon, the scattered muon and all final state hadrons. Since the kinematic of a deep inelastic event is entirely reconstructed from the kinematics of the incident muon and the scattered one, their tracks must be precisely reconstructed. In addition, a precise kinematic reconstruction and an efficient particle identification are needed to study hadronic final states. This is ensured by the two stages in the spectrometer (figure 4.2).

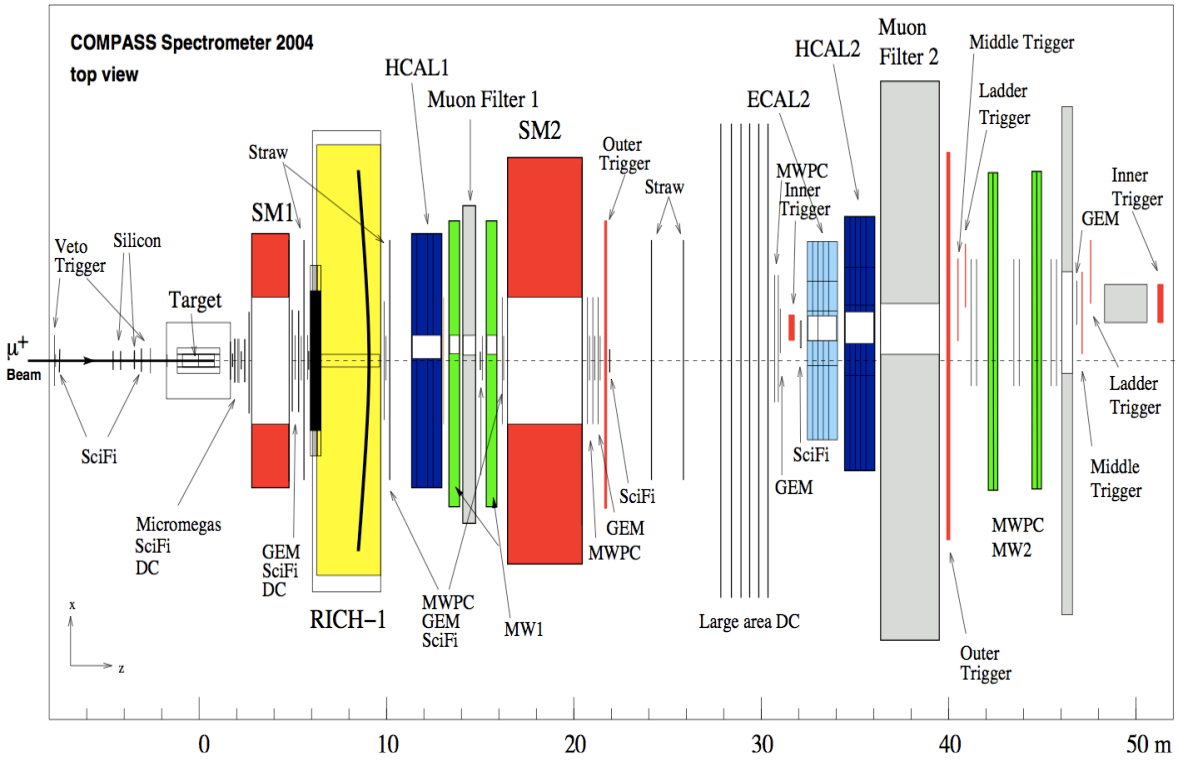

Figure 4.2: Sketch of the COMPASS spectrometer.

4.3.1 Track reconstruction

The spectrometer [53] consists of two main parts downstream of the target. Each one is built around a dipole magnet with vertical magnetic field, preceded and followed by sets of tracking detectors dedicated to the track reconstruction. The first part, i.e. the Large Angle Spectrometer (LAS), is used to detect the low momentum particles (0.5 GeV/c $<$ p $<$ 5 GeV/c) emitted at large angles with respect to the beam axis. It is equipped with a 110cm long magnet, the SM1 magnet, covering an angular acceptance of $\pm$180 mrad. The second part, i.e. the Small Angle Spectrometer (SAS), is dedicated for the detection of high momentum particles (p $>$ 5 GeV/c) emitted at small angles. It includes the 4m long SM2 magnet which covers a 30 mrad angular acceptance and a total field integral of 4.4 Tm. The two stages structure ensures a precise track reconstruction for a large momentum range and large angular acceptance.

The incident particle flux varies by several orders of magnitude in the different regions covered by the overall spectrometer acceptance. In the region close to the beam, the detectors must have a high particle rate capability with a spatial resolution better than 100 μm. In the regions far from the beam, the spatial resolution requirement can be relaxed while large areas have to be covered. In order to fulfill all requirements related to rate capability, spatial resolution, time resolution as well as the size of the areas to be covered, different tracking detectors with different techniques are used. The tracking detectors can be are assembled in three groups.

- The **VSAT** (Very Small Area Trackers) covers the most central area of 5×5 cm^2 around the beam . The detectors must stand a high beam flux (which reaches up to 50 MHz/cm^2). In addition they must have excellent spatial and time resolutions. To match these requirements six scintillating fiber (SciFi) stations, whose sizes vary between 4×4 cm^2 and 12×12 cm^2, are distributed along the beam axis. Each station consists of at least two projections: horizontal and vertical. Three stations comprise an additional projection inclined by 45°.The detection efficiency was measured and found to be between 96% and 99% for the various stations. The lower value is obtained in the high intensity region due to large occupancy in the readout. The time resolution is found to be better than 500 ps and the spatial resolution lies between 130 μm and 200 μm.

- The **SAT** (Small Area Trackers) is defined for distances larger than 2.5 cm from the beam where the particle flux can reach up to $3 \cdot 10^5$ Hz/cm^2. This region comprises detectors characterized by high spatial resolution and low material budget, with an inactive zone in the beam area. Two types of micro-pattern gaseous detectors (MPGD) have been chosen: the Micromegas and the triple GEMs.

  The Micromegas (**MiCRO MEsh GAseous Structure**) detectors were developed by the CEA Saclay in collaboration with CERN and operated for the first time in the COMPASS experiment. The concept of the micromegas detector is explained in chapter 5. Three Micromegas stations were installed between the target and the SM1 magnet. Each station comprises four planes (V, U, X and Y) and cover an active area of 40×40 cm^2. The 12 detectors operate with a detection efficiency of a 98% and with a spatial resolution of100 μm.

  The triple "GEM detectors" (**G**as **E**lectron **M**ultiplier) is a gaseous detector consisting of three amplification stages stacked on top of each other. They are built using three GEM foils and a 50 μm thin foil of polyimide and an electrical insulator, covered with thin layers of copper on both sides. The GEM holes, with an outer diameter of 70 μm and an equidistant pitch of 140 μm, are etched into the copper and the foil, with a diameter of 70 μm. By applying a high potential difference between both sides of the foil, a high electric field (of 50 kV/cm) is induced inside the holes (cf. figure 4.3). The GEMs operate with a mixture of 70/30 Ar and CO_2 and cover an active area of 31×31 cm^2. The signals on the strips are read out using the APV25 front-end chip. Their use is explained in chapter 5. 11 GEM stations are installed in the COMPASS spectrometer. They are assembled in doublets of two detectors placed back to back and rotated by 45° with respect to one another; each doublet measures four coordinates. At nominal muon beam conditions, the GEM detectors operate with a detection efficiency of $\sim 97\%$, a spatial resolution of ~ 70 μm and a time resolution of 12 ns. Both Micromegas and GEM detectors have central dead zones with 5 cm of diameter.

- The **LAT** (Large Area Trackers) system is dedicated to the detection of large angle particles. Detectors with good spatial resolution and large areas are required. The LAT comprises drift chambers, straw drift tubes and multi-wire proportional chamber.

  In the initial COMPASS setup up to 2004, three drift chambers (DC) were installed in the COMPASS setup; two DCs were installed upstream of the SM1 dipole magnet and one other was installed downstream of SM1. Each DC has an active area of 180×127 cm ^{2} and consists of eight layers which correspond to four projections: vertical (Y), horizontal (X) and inclined by 20° (U) and by $-20°$ (V) with respect to the vertical direction. In nominal

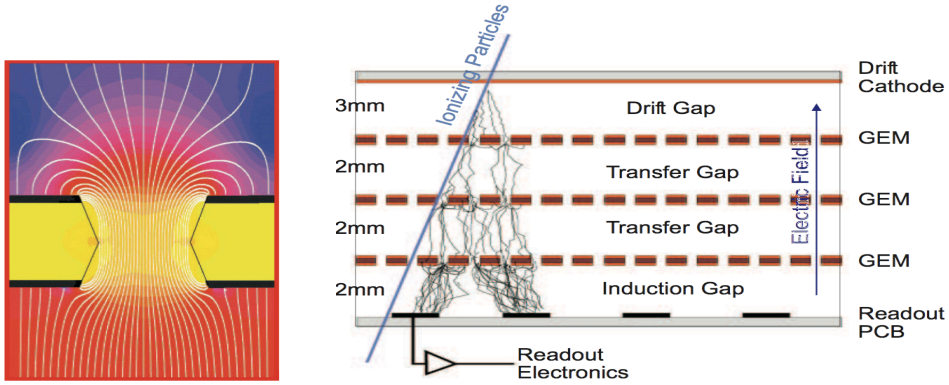

(a) Simulation of the electric field inside a GEM hole

(b) Cut through a typical GEM detector with penetrating charged particle and propagating avalanche

Figure 4.3: Shematic view of a COMPASS GEM detector

beam conditions, the DCs operate with an efficiency of $\sim 95\%$ and a spatial resolution of 270 μm. This value is due to the large halo which surrounds the high intensity beam and to the large fringe field of the SM1 magnet.

Three stations of straw drift tubes are located after the SM1 magnet. Each station consists of three detectors: one vertical, one horizontal and one rotated by 10° with respect to the vertical one. Each straw detector has an active area of 323×280 cm^2 with a central dead zone of 20×20 cm^2. The straw tubes operate at a high voltage of 1950 V, corresponding to a gain of $6 \cdot 10^4$.

In the region downstream of the RICH up to the end of the setup, the particles are detected by 14 multiwire proportional chambers (MWPC). Each chamber consists of two cathodes separated by 16 mm and a wire plane characterized by a pitch of 2 mm. Three types of MWPC are used in COMPASS. The first type consists of three layers of anode wire, one horizontal and two inclined by $\pm 10.14°$ with respect to the vertical axis. An active area of 178×120 cm ^{2} is covered by this type. The second type is similar to the first one with an additional vertical wire layer. The last type covers a smaller active area of 178×80 cm^2. The MWPCs operate with a detection efficiency of $\sim 99\%$ and a spatial resolution of about 600 μm. The three types have a central inactive area with a diameter that depends on the location of the chamber along the beam axis.

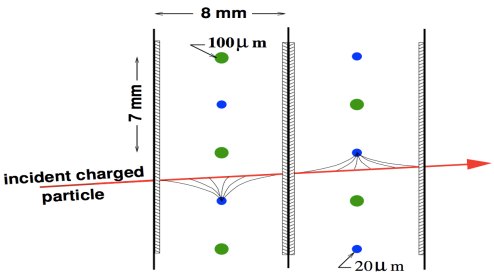

Figure 4.4: Geometry of the COMPASS drift chambers.

The main characteristics of the tracking detectors (efficiency, spatial resolution and time resolution) used in the COMPASS setup are summarized in table 4.1.

4.3.2 Particle Identification

The COMPASS spectrometer is equipped with hadron calorimeters, RICH and muon filters. Two hadron calorimeters measure the energy deposited by hadrons in order to discriminate between hadrons and muons. The RICH (**R**ing **I**maging **CH**erenkov) separate between pions, kaons and protons. Finally, two muon filters, one in each stage, are used to identify muons.

detector	# of planes	efficiency	spatial resolution [μm]	time resolution [ns]
SciFi	8	99	130-210	0.4
Silicon	2	-	8-11	2.5
Micromegas	12	97	90	9
GEM	22	97	70	12
DC	3	95	190	-
Straw	6	99	190	-
MWPC	14	99	1600	-

Table 4.1: Performances of the tracking detectors of the COMPASS experiment [53].

4.3.2.1 Hadron Calorimeter

Each stage of the spectrometer is equipped with a hadron calorimeter (HCAL) used to measure the energy of the hadrons produced in the target. The hadron calorimeters also used in the trigger system for semi-inclusive DIS events. Both calorimeters have a modular structure with iron and scintillator plates. The first calorimeter (HCAL1), located in the LAS, has an active area of 4.2×3 m^2 with a central hole of 1.2×0.6 m^2, used for the passage of the beam. The second calorimeter (HCAL2) has an active area of 4.4×2.0 m^2 with a central hole of 40×40 cm2.

4.3.2.2 Muon Filter

Muon filters are made of a hadron absorber preceded and followed by two sets of tracking stations, used for the reconstruction of the muon trajectory. The first muon filter, located in the LAS, consists of a 60 cm thick iron absorber located between two stations of MDTs (Mini Drift Tubes). It has an active area of 5×4 m^2 and a hole in the center of 1.5×0.8 m^2. The second muon filter, located in the SAS, consists of a 2.4 m thick concrete absorber preceded and followed by two layers of drift tubes for the muon trajectory reconstruction.

4.3.2.3 The RICH detector

The use of the RICH detector is crucial for the analysis presented in this thesis, especially for the kaon identification. The COMPASS RICH detector performs the hadron identification in the momentum range from 2.5 GeV/c to 43 GeV/c. To match the overall spectrometer acceptance requirement ($\pm$250 mrad $\times \pm$ 180 mrad), a large photon detector surface, of 5.6 m^2, was used. The photon detectors are placed far from the beam axis and outside the spectrometer acceptance in order to minimize the amount of material in the covered region, resulting in a large transverse dimensions (6.6×5.3 m^2). An opaque tube, with a radius of 5 cm and filled with helium, is placed in the RICH central part crossed by the beam. Its role consists of absorbing the Cherenkov photons emitted by the beam muons and the halo muons, which form a large background in the reconstruction of the rings. A shematic view of the COMPASS RICH detector is shown in figure 4.5.

RICH Gas System

The RICH gas vessel is filled with C_4F_{10} radiator gas. The latter is characterized by a refractive index of $n \sim 1.0015$ in the UV domain, which allows to separate between pion and kaon up to 50 GeV. The radiator gas is also characterized by its low chromaticity ($dn/dE \sim 5 \cdot 10^{-5}$ eV^{-1} at 7 eV) and its transparency in the very UV, making it an optimal choice for particle identification above 10 GeV. The water vapor and oxygen contamination of the C_4F_{10} radiator gas affect the light transmission in the UV domain due to their large UV light absorption cross section. This problem is remedied by continuously circulating the gas in a closed loop circuit in order to remove oxygen and water vapor traces as well as to keep an optimum transparency in the UV domain. The cherenkov thresholds for different particles are given in table 4.2.

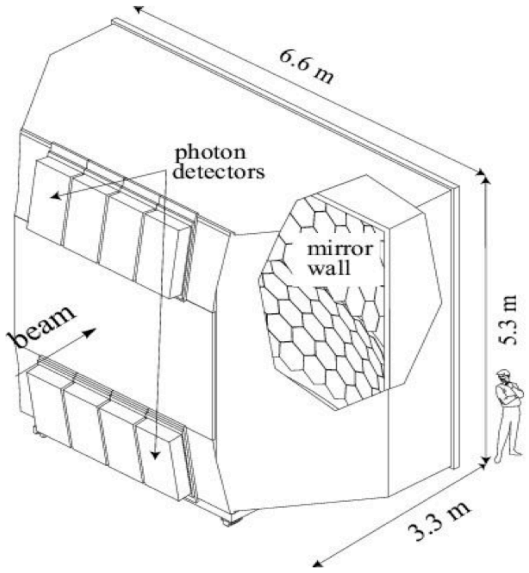

Figure 4.5: Shematic view of the COMPASS RICH detector [53].

Particule	threshold [GeV/c]
e	0.0
μ	1.9
π	2.5
K	8.9
p	16.9

Table 4.2: Cherenkov thresholds for different particle types when using C_4F_{10}.

RICH optical system

The optical system consists of two spherical focal surfaces with a radius of 6.6 m. Each focal surface consists of 58 spherical mirror units with different forms (hexagons and pentagons) and different sizes. The two focal surfaces cover a large area of 21 m^2 and are placed outside the spectrometer acceptance to minimize the material in the detection region. The rings produced by incident particles are subject to a geometrical aberration due two limitations. Firstly, the *spherical* focal surface is approximated by a *plane* surface of the photon detectors. Secondly $\sim 4\%$ of reflecting surface is lost due to the clearance between adjacent mirrors. This aberration has to be taken into account in the ring reconstruction. The mirror substrate is a glass of 7 mm of thickness covered by 80 nm reflective layer of aluminium and 30 nm protective layer of MgF_2. The reflectance of the optical system was measured in the wavelength range [165,200 nm] and found to be in the range 83-87%.

Photon detectors and readout system

The photon detection is ensured by eight multiwire proportional chambers (MWPC). Each chamber consists of two segmented photocathode surfaces and an anode wire plane with 20 μm diameter wires and 4 mm wire pitch. The photocathode is covered by a 500 nm thick CsI layer to ensure the conversion of the Cherenkov photons into electrons. The MWPCs are filled with methane (CH_4) due to its transparency to photons in the full energy range. They are separated from the gas vessel via 5 mm thick quartz windows. The anode wire plane is placed at 2 mm from the photocathode. The eight photon detectors have a total of 82944 which are read by front-end boards called BORA with 432 input channels each. They are coupled to the GASSIPLEX amplifier chips of 16 input channels each, and a readout time smaller than 500 ns.

The RICH operated with this system until 2004. For the 2006 data taking, an important upgrade of the RICH detector has been implemented in order to improve the RICH performances. Two main limitations have been improved in the upgrade project. The first limitation was the high electronic occupancy which degrades the signal-to-background ratio, in particular in the central region. The second limitation corresponds to the large dead time of the GASSIPLEX chip. These limitations were remedied using new technologies for the photon detection and the readout systems.

- In the very central region of the RICH, the MCPC chambers were replaced by a new photon detection system based on **M**ulti-**A**node **P**hoto **M**ultiplier **T**ubes (MAPMT). These new devices have the advantage of increasing the number of detected Cherenkov photons which, in turn, enlarges the momentum range of identified particles. The time resolution of the new devices, of a few ns, allows to suppress the high background due to uncorrelated events with the trigger. The new devices allows to detect visible photons in addition to the UV ones. The number of photons per ring, detected with the new system, is larger than the old one by a factor of four. The separation pion-kaon is possible up to 50 GeV/c with the new system compared to 43 GeV/C for the old one.

- In the peripherally region (75% of the active area of the RICH), the MWPC chambers continue to ensure the photon detection. The readout system, however, was replaced with a new one based on the APV25 chip. The use of this new electronics allowed to reduce the readout dead time. The time gate of the RICH was also reduced to 400 ns compared to 3.5 μs for the old readout system. This resulted in a signal-to-background ratio, in the central region where the halo is most important, a factor of 5-6 larger.

4.4 Triggering system

The large amount of data recorded by the COMPASS spectrometer requires a dedicated electronic systems to select events for which an interaction in the target has occurred within a high particle fluxes (up to 2.10^8 muons per spill). For the muon program, the COMPASS setup covers a wide kinematic domain starting from $Q^2 \approx 0$ up to the maximum allowed by the kinematics of the order of 60 $[\mathrm{GeV/c}]^2$.

For relatively high Q^2, the events are triggered using the information of the scattered muon only. The latter has an energy loss and a non-zero scattering angle after the interaction. The scattered muons are detected using at least two scintillator hodoscopes in order to determine the muon scattering angle. The resulting hodoscope's signals are then discriminated and fed into a *coincidence matrix* which distinguishes between scattered muon tracks (positive coincidence) and beam halo tracks (negative coincidence). In order to suppress events due to halo muons, a veto system is added to the trigger system. The veto detectors are installed before the target such that only muons which are away from the beam axis can produce a signal. Therefore, a signature of a scattered muon is a positive coincidence in the matrix without any signal from the veto counters.

At low Q^2 the muon scattering angle is close to zero and the muon trajectory is very close to the beam axis. In this quasi-real photon regime, several background processes contribute such as elastic muon scattering off target electrons, radiative scattering off target nuclei as well as halo muon scattering contributions. To suppress these background processes, an energy deposit in the hadronic calorimeter in coincidence with the trigger is required (figure 4.6).

In order to select muons coming from events of different energies, four different sets of hodoscopes are needed: the inner (H4I, H5I), the ladder (H4L, H5L), the middle (H4M, H5M) and the outer (H3O, H4O) hodoscopes. The inner hodoscopes are the smallest ones and cover essentially the low Q^2 domain while the outer hodoscopes are the biggest ones and cover the region of high Q^2. Other trigger types exist as the veto trigger, the beam trigger and the random trigger. The data taken with these modes of triggers are used to perform the detector calibration, the efficiency study and the alignment.

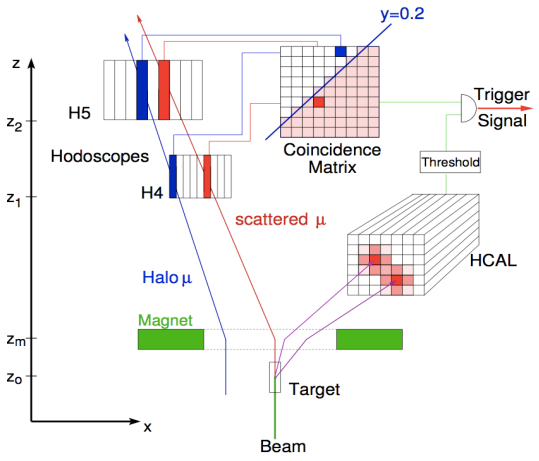

Figure 4.6: Concept of the COMPASS trigger for a quasi-real photo-production with high energy loss [53]. The scattered muon leads to a positive coincidence in the coincidence matrix while the halo muon gives rise to a negative coincidence.

The measurement of hadron multiplicities, presented in this thesis, requires the selection of inclusive deep inelastic scattering events ($Q^2 > 1$). Triggers using only the muon scattering information are consequently used in the DIS event selection. They correspond to the outer trigger and the inclusive middle trigger. They cover the high Q^2 region ($Q^2 > 1$) and the y range from 0.1 to 0.9.

4.5 Data Acquisition System

The **D**ata **AQ**uisition (DAQ) system aims to record, for each triggered event, all data registered by the detectors. All detectors are equipped with preamplifiers and discriminators. Upon the arrival of a trigger signal (via the *Trigger Control System*), the data are transferred to readout driver modules: CATCH and GeSiCA. These modules combine data from front-end cards to readout-buffer PCs (ROB) via S-LINK. Event builders then merge the information of all sub-systems for each trigger with an online filter. Events passing the filter are recorded into raw data files, divided into 1-gbyte-sized chunks and recorded on tape remotely at the CERN central data recording facility in the computer center. The architecture of the data acquisition system is shown in figure 4.7.

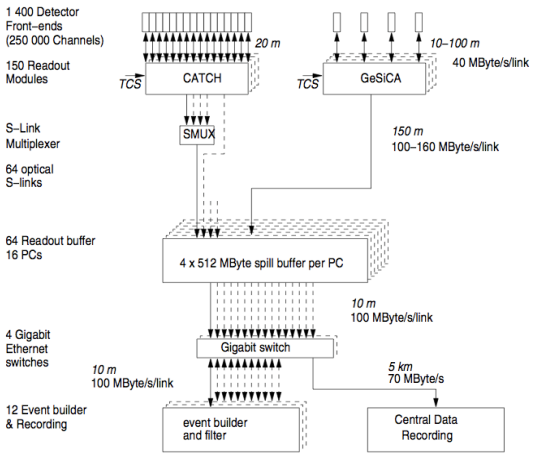

Figure 4.7: Architecture of the COMPASS DAQ

4.6 Event reconstruction

The raw data, recorded by the DAQ, are later processed by a reconstruction program named CORAL (for **CO**mpass **R***econstruction*__A__lgorithm **L***ibrary*) [40], resulting in DST (for **D**ata **S**ummary **T**apes) files.

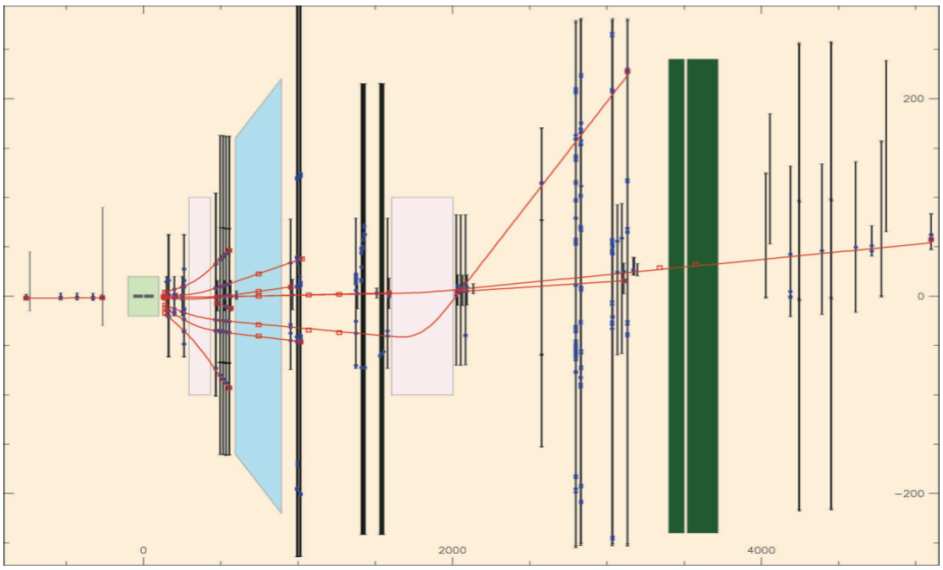

Figure 4.8: A typical reconstructed DIS event in the COMPASS spectrometer, consisting of: clusters (dark blue), charged particles (red), detector planes (black) and target (light green).

The CORAL program consists of reconstructing the primary vertex of the interaction, the trajectories of the incident muon, the scattered muon and final state hadrons. For the track reconstruction, specific algorithms are used to decode the data registered by the detectors read out channels and to translate them into hits in the corresponding detector plane. When the information is provided by adjacent channels, data are usually combined into *clusters of hits* using specific clustering algorithm. Then the data of several detectors are combined by fitting the particle trajectories to the clusters. The spectrometer is divided into different zones where straight tracks are reconstructed. For one track, different pieces reconstructed in different zones are then bridged to form one continuous track. A global fit is then performed to determine the tracks parameters. Figure 4.8 shows an event reconstructed by the event display in CORAL, where single clusters as well as reconstructed tracks can be identified in the spectrometer.

Chapter 5

Micromegas Detectors

The Micromegas (**Micro ME**sh **GA**seous **S**tructure) is a gaseous detector which has been developed by the CEA Saclay in collaboration with the CERN to operate in the in a high rate environments (flux up to 500 kHz/cm^2) with a spatial resolution better than 100 μm and with a good time resolution. They have been used for the first time in the COMPASS experiment, and play an essential role in the data reconstruction. The description of the Micromegas is given in this chapter and comprises two parts: the first one introduces an historical view on the gaseous detectors starting from the basic proportional counters up to the Micromegas microstructure detectors. The second part describes the study of the performance of a new generation of Micromegas which were developed to fulfill the new COMPASS requirements.

5.1 Historical View on Gaseous Ionization Detectors

The first ionization detectors (ionization chamber, proportional counter and Geiger Müller counter) [63] were developed in the late 1935's. Although their simple concept of operation, they were not used by nuclear and particle physics experiments and their use was limited to the radiation monitoring. However, their basic principles of operation were adopted in the development of new ionization detectors for high-energy physics experiments, with more sophisticated electronics and data acquisition.

5.1.1 Gaseous Ionization Detectors

The basic concept of a gaseous ionization detector [63] consist on collecting charges from the gas ionization produced by the passage of a charged particle. Three basic types of gaseous ionization detectors were firstly developed: the ionization chamber, the proportional counter and the Geiger Müller counter. They operate at different voltages but all of them have the same design which consists of a thin metal wire stretched along the axis of a conducting cylinder. This latter is filled with a suitable gas (figure 5.1), usually a noble gas is chosen. A difference of potential is then created between the cylinder and the wire to which a positive voltage, relative to the cylinder, is applied. A radial electric field is established in the system; it is maximum at the surface of the wire anode and decreases as r^{-1} around the cylindrical cathode (right part of figure 5.1).
When a charged particle penetrates in the gas volume, a number of primary ionization occur and consequently a number of electron-ion pairs is produced. The mean number of pairs created is proportional to the energy deposited in the chamber. In the absence of electric field, positive ions can be neutralized by recombination with electrons in the gas volume and no signal can be detected in this case. However, when an electric field is applied, the electrons drift towards the anode while the positive ions drift towards the cathode. When the electric field increases, a larger number of pairs is then collected before they can recombine. At some value of the electric field E_0, all pairs will be collected and the produced signal does not change with the electric field strengh. In this regime, the counter operates in the ***ionization chamber*** mode. Two types of ionization chambers exist: the pulse counting ionization chamber where the pulses are detected when charged particles traverse the chamber, and the integrating chamber in which the pulses are added and the integral of the total ionization produced in a certain period of time

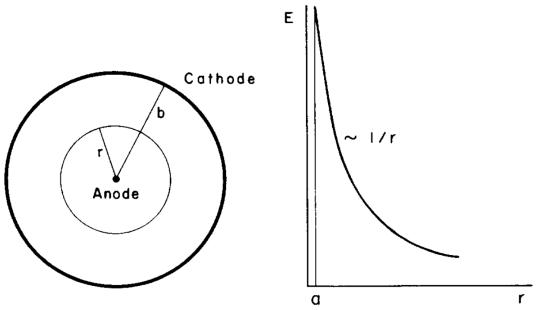

Figure 5.1: The cylindrical coaxial geometry of the counter (left) and the shape of the electric field around the anode (right) as a function of r; r measures the distance from the center of the anode. (Illustration from [62])

is measured. An integrating ionization chamber are used as monitoring instruments to measure large fluxes of radiation, as in COMPASS.

Increasing again the electric field above E_0 allows the primary electrons to increase their energies between two collisions with the gas molecules. When their energies become larger than the ionization potential, they produce secondary ionization in the gas volume and consequently secondary electron-ion pairs are created. Secondary electrons are then accelerated by the electric field, increase their energies and produce further ionization in the gas volume and so on. This progressive multiplication of charges is called "avalanche". It occurs entirely very close to the wire where the electric is very strong, and allows to generate M electrons from the primary one. The detected charge is proportional to the original deposited charge through the multiplication factor M. This latter can reach 10^6 allowing to detect the signal. The counter is said to operate in a ***proportional counter*** mode.

For even higher values of the electric field, the energy transferred by the electric field to the electrons is sufficient to produce ionization as well as inelastic process like photon emission from the desexcitation of the gas molecules. The photons then travel to parts of the chamber and cause further ionization. A chain reaction of several avalanches diffuse along the entire anode. The avalanches propagate in the counter such that the anode wire is fully surrounded by electrons and ions. The output current saturates and a discharge occurs in the gas. The counter enters a saturated mode which is defined as the ***Geiger-Müller counter*** operation mode.

5.1.2 Multiwire Proportional Chamber

Although the proportional counters are widely used in several domains (nuclear industry, medical radiotherapy, ...), their use in nuclear physics experiments is limited due to their limited localization accuracy. Using the same concept of a proportional counter, a new gaseous detector was invented by G. Charpak et al. in 1967-68, called MultiWire Proportional Chamber (MWPC). It's basic design consists of a plane of parallel, equally spaced thin anode wires, centered between two cathode planes. The gap between the anode wires and the cathode plan is normally three to four times larger than the anode wire spacing. This latter is the most important geometrical parameter in multiwire proportional chambers because it determines the localization accuracy and consequently the resolution. Figure 5.2 shows the typical structure of a multiwire proportional chamber (left) and the field equipotentials and field lines of the electric field developed between the two electrodes (right). Except for the region very close to the wires, the field lines are almost parallel. The signal measured by one wire anode provides information along only one coordinate. To measure the trajectory of an incident particle, a set of aligned chambers is needed.
These chambers can operate in high particle fluxes and have a spatial resolution of typically one-half of the wire spacing whose typical value lies between 1 and 5 mm. Therefore for a MWPC with 2 mm wire spacing, the spatial resolution is 1 mm. It can be decreased by using a finer spacing; however a 1 mm wire spacing is already hard to operate due to the electrostatic forces that make the anode wires in unstable equilibrium conditions [62]. The MWPCs are widely used

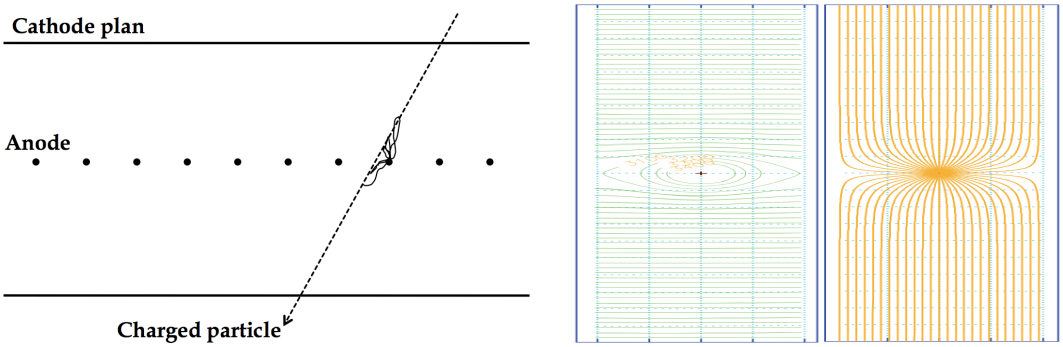

Figure 5.2: Left: Structure of a multiwire proportional chamber. Right: Electric field equipotentials and field lines (Illustration from [61]).

in high energy physics experiments; the COMPASS spectrometer comprises 34 planes. They have however one limitation. In most of the gas volume, the charges liberated by ionization events drift along the electric field lines: electrons to the anodes and ions to the cathodes. When the avalanches takes place, the positive ions created are accumulated and provoke local modifications of the electric field between the two electrodes. This reduces the gain in the corresponding area of the detector and affect the total efficiency of the detector. Two solutions can be tested to overcome this limitation. The first possibility is to reduce the inter-wire pitch; however this parameter cannot be reduced below 1 mm due to mechanical and electrostatic limitations[1] (see [62]). The second possibility is to reduce the time of ion evacuation by reducing the gap between the anodes and the cathodes. For this goal a new technique has been developed; it consists of replacing the anode wires by strips printed on an insulating surface. By applying a difference of potential, a high electric field is developed between the thin cathode and the anode strips allowing for electron multiplication. A new detector **M**icroStrip **G**as **C**hamber (MSGC) has been constructed using this technique. Due to the small pitch, the spatial resolution can reach 35 μm. In addition, the fast collection of charges allows to stand high counting rates (flux up to 10^6 particles/mm^2/s). Its gain however cannot exceed 10^4 limiting the avalanche multiplication; this is due to breakdown on the insulating surface of the detector.

These limitations encountered in different structures and configuration pushed the studies towards the creation of a new detector based on the same concepts with a different structure, the Micromegas detector.

5.1.3 Micromegas Detector

The MICROMEGAS is a gaseous detector developed by G. Charpak, Y. Giomataris, P. Rebourgeard and J.P. Robert [60] in 1995. Its main feature (figure 5.3) is the presence of a micromesh electrode separating the gaseous volume into two spaces:

- The conversion space used to drift the ionization electrons resulting from the energy deposition of an incident charged particle. It is limited between the drift electrode and the cathode micromesh and has a thickness of few mm (cf. figure 5.3). A low electric field (of ~ 1 KV/cm) must be applied in this space.
- The amplification space used to multiplicate the ionization electrons under the action of a high electric field (50-100 kV/cm). It is limited between the cathode micromesh and the anode and has a thickness of about 100 μm. The thickness of this amplification space is chosen to be small in order to achieve a good spatial resolution and time resolution.

When a charged particle traverses the conversion space, its electromagnetic interaction with the gas molecules creates a discrete number of primary ionization collisions which liberate electron-ion

[1] The anode wires in a multi wire proportional chamber are not in stable equilibrium condition. It has been shown in practice that above a certain value of the operational voltage, the wires are unstable and and are alternatively displaced.

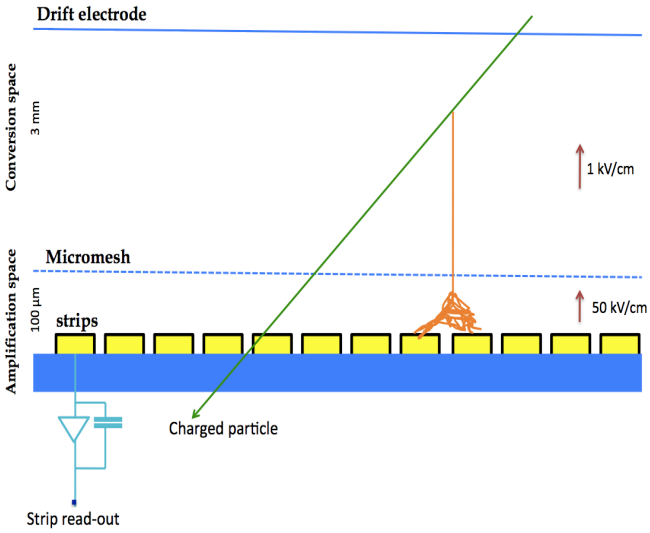

Figure 5.3: Basic concept of the Micromegas detector.

pairs in the gas. The electrons drift towards the micromesh electrode and reach the amplification space where the high electric field (of 50 kV/cm) produces an avalanche. The structure of the electric filed lines is presented in figure 5.4. The field lines followed by the electrons are compressed into a small diameter in the middle of the openings of the micromesh. This configuration ensure that electrons are transferred to the amplification space and then collected by the anode microstrips while the positive ions are mostly collected by the micromesh electrode. A fraction of the positive ions escapes to the conversion space. This fraction depends the ratio ϵ between the electric field in the amplification space to that in the conversion space. For low values of ϵ, the majority of the electric lines leaving the first electrode reach the micromesh and the electron transmission in this case is very poor. At large ϵ values, however, most of the field lines pass through the micromesh holes and reach directly the second anode electrode. The electron transmission is fully reached and this case define the optimal operation of the device. The electric lines followed by the positive ions are stretched from the anode to the micromesh to ensure a very quick evacuation of the ion clouds. The ions drift a maximum distance of 100 μm and the width of the produced signal is 100 ns, mush shorter than in standard multi-wires chambers (about few μs).

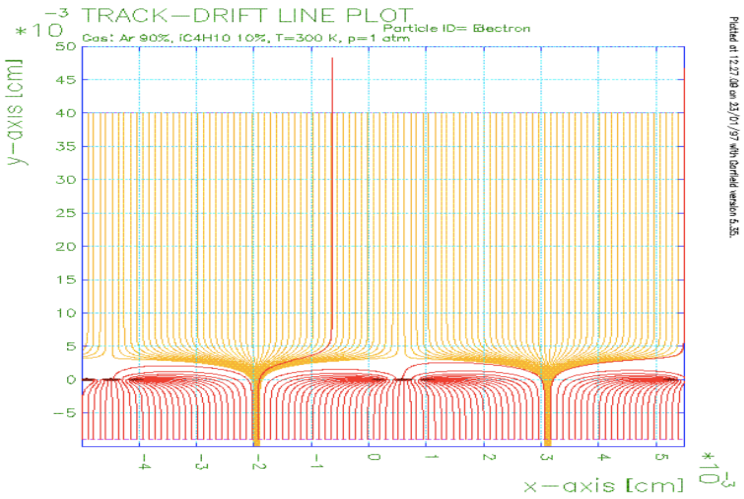

Figure 5.4: Electric field lines in the Micromegas [61].

5.2 Properties of a Gaseous Ionization Detector

Currently the ionization detectors are extensively used in high energy physics experiments. The concepts of ionization process as well as the movement of electrons and ions in gases are of special interest. Their understanding is extremely important as they affect many operating characteristics of the detector. In the following sections, these basic concepts as well as some properties of an ionization detector are reviewed.

5.2.1 Ionization and Excitation

When a charged particle penetrates in a gas volume, two kind of interactions with the medium can occur [63]: the excitation and the ionization of the gas molecules. The excitation correspond to a resonant reaction which requires the transfer of a specified amount of energy and where no free electrons or ions are created. The ionization, however, requires unspecified but relatively high energy transfer. In this reaction, a number of electron-ion pairs is generated. Primary electrons can have an energy larger than the ionization potential of the medium and consequently produces secondary electron-ion pairs and so on. Two characteristic quantities can be defined: the number of primary ionization per unit length (N_p) and the number of total ionization per unit length (N_t). The number of primary ionization follows Poisson-like statistics and is linearly dependent on the average atomic number of the gas Z. Each primary ionization produces 2-4 secondary ionization. The primary and the total ionization numbers have been measured for most gases; the experimental values of N_p and N_t for minimum ionizing particles per unit length are given in table 5.1 for some gases.

gas	Z	N_p (cm^{-1})	N_t (cm^{-1})
Ne	10	12	43
CH_4	16	22	53
Ar	18	23	94
C_2H_6	30	41	111
CF_4	48	51	100

Table 5.1: Number of primary ionization and number of total ionization for minimum ionizing particles per unit length traversing a gas volume at 20 °C and 10^5 Pa (from [64]).

Finally, one must note that the mean energy required for electron-ion pair creation shows only a weak dependence on the particle and the gas types.

5.2.2 Transport of Electrons and Ions in Gases

Many characteristics of an ionization detector are related to the motion of the electrons and ions in gases [63]. A good understanding of this motion is very important to optimize the functioning of the detector. Two important phenomena in the motion of charges in gases are highlighted: diffusion and drift.

5.2.2.1 Diffusion

In the absence of an electric field, the electrons and the ions created from ionization diffuse from their point of creation uniformly. During their passage through the gas, they loose their energy due to multiple collisions with the gas molecules. They reach a thermal equilibrium with the gas and therefore recombine. The distribution of charges after diffusion is a Gaussian shaped distribution with a root mean square:

$$\sigma = \sqrt{2Dt} \tag{5.1}$$

where D is the diffusion coefficient (Eq.5.3) and depends on the gas type.

5.2.2.2 Drift

Under the action of an electric field, the electrons and the positive ions are accelerated along the field lines towards the anode and the cathode respectively. The multiple collisions with the gas molecules limits the average velocity of the charge along the field direction, also called drift velocity. Together with the value of the electric field E, the drift velocity u define the so called mobility of a charge moving in a given gas by

$$\mu = u/E \tag{5.2}$$

For ions, the value of the mobility depends upon the ion nature and the gas type. Since their drift velocity is proportional to the electric field E. As a consequence, their mobility μ is independent of E. It depends however on the collisions cross section which is constant if the energy of the ions does not change with the electric field value. Since the energy transferred to the ions by the electric field is negligible compared to their thermal energy, their mobility is constant. It was measured and found to be about 1 cm^2 V^{-1} sec^{-1}. For electrons the mobility is not constant. Due to their small mass, electrons can increase their energy between collisions with the gas molecules under the action of an electric field. In addition it has been found that for some gases, the collision cross section varies very strongly with the electric field. As a consequence, the shape of the energy distribution changes and the average energy can exceed the thermal energy by several orders of magnitude at high fields. This result in an E dependent diffusion coefficient defined by

$$\frac{D}{\mu} = \frac{kT}{e} \tag{5.3}$$

where e denotes the electric charge. For some gases, called "fictitious gases", the energy of electrons does not increase with electric field and electrons remain very close to the thermal limit. In these cases, the electron velocity is independent of the electric field. The diffusion of charges in a time t over a length x follow a Gaussian distribution with a standard deviation given by

$$\sigma = \sqrt{\frac{2Dx}{\mu E}} = \sqrt{\frac{2kTx}{eE}} \tag{5.4}$$

A small diffusion coefficient is consequently needed for a best accuracy. For 1 cm drift under the influence of an electric field of 1 kV/cm, $\sigma \sim 100\mu$m for "fictitious gases" while σ can reach 1 mm for other gases (more details can be found in [62]).

5.2.3 Avalanche

The charge multiplication in ionization detectors is conditioned by the amount of energy gained by the primary electrons from the accelerating electric field. A sufficient energy allows to produce secondary electrons which can produce tertiary ionization and so on. The total number of electrons created from the primary one allows to define the so called *multiplication factor*. The number of electrons that can be created from n primary electrons traveling in a uniform electric field in a path dx is

$$dn = n\alpha dx \tag{5.5}$$

where α[2] represents the probability of ionization per unit lenght. It is defined as the inverse of the mean free path of the electron and called *first Townsend cofficient*. By integrating Eq. 5.5, one obtains the total number of electrons created in a path x. This leads to the definition of a fundamental property of a gas detector which is the multiplication factor M, also called gain.

$$n = n_0 e^{\alpha x} \quad \Rightarrow \quad M = \frac{n}{n_0} = e^{\alpha x} \tag{5.6}$$

To calculate the multiplication factor, the dependence of α on the electric field must be known. Various theoretical models have been developed to describe this dependence. A simple model for

[2] In the case of nonuniform electric field, α is a function of x.

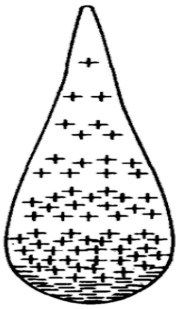

Figure 5.5: Avalanche Formation. Since electrons are faster than ions due to their higher masses, the avalanche has a drop-like shape where the ions are left behind the electron front.

α is given in Eq.5.7, where P is the gas pression and A and B are constants which characterize the gas.

$$\frac{\alpha}{P} = Ae^{-BP/E} \tag{5.7}$$

In summary, some of the basic processes used in a gaseous ionization detector were reviewed. The ionization mechanism, on which the ionization detector is based, was firstly presented. It consists of creating electron-ion pairs in a gas volume. The mobility of the created charged particles in the gas volume was then discussed and the two most important phenomena were reviewed: the diffusion and the drift. Finally the gain of a detector, which is a very interesting characteristic, was defined.

5.3 Micromegas of COMPASS

The COMPASS spectrometer comprises 12 Micromegas detectors installed next to the target and contribute to the detection of small angles particles. They are grouped in three stations of four detectors each, allowing to measure four coordinates: X (0°), Y (90°), V (-45°) and U (45°). They are characterized by an amplification space of 100 μm and an ionization space of 5 mm. This latter has been changed to 5 mm in 2006 in order to reduce the gain when running with hadron beams. Each detector has an active area of 40×40 cm^2 with an inactive zone of 5 cm of diameter in the beam area. Figure 5.6 shows one station with four plans.

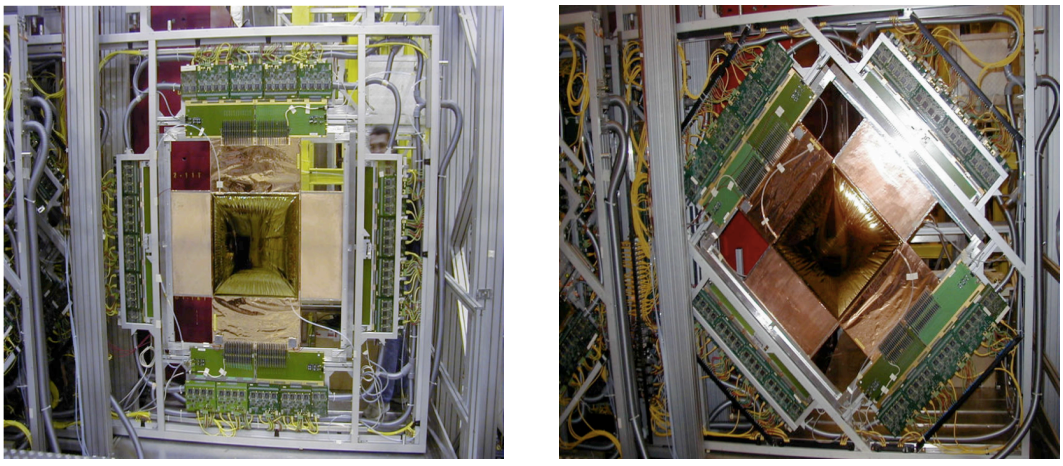

(a) XY Doublet (b) UV Doublet

Figure 5.6: Micromegas detectors in the COMPASS spectrometer

5.3.1 Construction

The anode copper strips, with a thickness of 7 μm and a width of 250 μm are printed on a 100 μm thick epoxy foil. They are extended beyond the active area by 30 cm to shift the electronic

cards beyond the Micromegas acceptance in order to reduce the material budget. The strips have a pitch of 360 μm in the central region, where the electronic occupancy is too large, and of 420 μm in the peripheral region. The foil is glued on a supporting panel consisting of a 5 mm thick fiber honeycomb, which in turn is glued on a 100 μm thick carbon epoxy foil. This step is required to improve the rigidity of the anode foil. Further details can be found in [65].

To define the amplification space, cylindrical spacers, made of photoresist with a thickness of 100 μm and a width of 150 μm, are fixed to the anode strips. The strips located in the center of the detector stand the highest intensity muon beam and consequently are subject to large electronic occupancy. To overcome this limitation, a thin coverlay photoresist disk with a diameter of 5 cm was introduced in the amplification space. The conversion space is limited between the drift electrode and the micromesh. Each of them is an electroformed nickel grid[3] and both are glued on a glass fiber support with a thickness of 4 μm which defines the conversion gap. The voltage applied on the amplification gap lies in the range [400,420 V] giving rise to a gain in the range [3000,6000]. Finally the mass of the device is less than 500 g.

5.3.2 Choice of gas mixture

The most critical issue in an ionization detector is the choice of a filling gas. It is dominated by several factors as low voltage, high gain and high rate capability. Since a pure gas cannot fulfill all these requirements, a gas mixture is instead used. Usually noble gases are chosen because they require the lowest electric field intensities for avalanche formation, in particular the argon due to its higher ionization capability and its lower cost. However noble gases provoke continuous discharge for gains larger than 10^3. This is due to the high energy photon emission by excited atoms formed in the avalanche. The photons cause further ionization and further avalanches. The solution to this problem consists of adding polyatomic gas, such as methane. Its molecules play the role of quenchers, i.e. they absorb the radiated photons and dissipate their energy through dissociation or elastic collisions without producing further ionization. Only a small amount of polyatomic gas is sufficient to increase the detector gain by a factor of 10^3.

Previous studies [65] have been performed to determine the optimum gas mixture for a best functioning device. The suitable mixture consists of 80% of Neon, 10% of ethane (C_2H_6) and 10% of fluorocarbone (CF_4). Three choices of quenchers were tested and the ethane was finally chosen because it tends to reduce the time needed for ion evacuation. These studies have shown that the inclusion of CF_4 into the gas mixture tends to increase the drift velocity u of electrons resulting in an improvement of the spatial resolution by 30% and the time resolution by a factor of 2.

5.3.3 Read-out Electronics

The signal, formed on the anode wires, is first amplified, then discriminated and finally digitized. The read-out electronics consists of SFE16 amplifiers/discriminators [65] (16 channels per card) associated to F1 Time-to-Digit Converter [63] (TDC) board (64 channels per board).

5.3.4 Micromegas performances

The twelve Micromegas detectors are characterized by a relatively good detection efficiency; which is better than 98% at low beam intensities ($\sim 10^6$ particle/spill) and decreases to 96% for higher beam intensities ($\sim 10^8$ particle/spill) due to the large electronics occupancy. Their spatial resolution lie in the range [90, 100 μm] in nominal high flux. The properties of the present micromegas, recently evaluated in [68], are summarized in table 5.2.

5.3.5 Performances in hadron beam conditions

During the built up of the new prototypes, the Micromegas detectors were used to test their functioning [69], especially the gain stability as well as the discharge rate, with the high flux

[3]The nickel was replaced by copper In 2006

Station	Plan	Angle	z position [cm]	ϵ	$\sigma_s[\mu m]$	σ_t[ns]
MM01	MM01V1	-45°	141.5	0.953	97	13.8
	MM01U1	45°	142.5	0.950	107	13.7
	MM01X1	0°	150.4	0.959	91	13.2
	MM01Y1	90°	151.3	0.0957	97	14.8
MM02	MM02V1	-45°	191.0	0.954	91	12.1
	MM02U1	45°	192.0	0.917	122	12.7
	MM02X1	0°	200.8	0.945	109	17.1
	MM02Y1	90°	201.8	0.923	89	16.9
MM03	MM03V1	-45°	240.2	0.935	138	14.2
	MM03U1	45°	241.3	0.962	144	15.3
	MM03X1	0°	249.8	0.960	201	16.8
	MM03Y1	90°	250.8	0.950	96	14.1

Table 5.2: Efficiency (ϵ), spatial resolution (σs) and time resolution (σ_t) of the twelve planes of the Micromegas detectors. For each plane, the name is given in the second column, the angle in the third column and the position along the beam axis in the the fourth column. MM denotes the word Micromegas.

hadron beam in 2008. For this purpose, two detectors were shifted by 60 mm such that the beam cross their active area. In order to maintain a reasonable discharge rate, the gas mixture of the detectors was tuned to a combination of 85% of Neon, 10% of C_2H_6 and 5% of CF_4. In addition the voltage applied on the mesh was reduced to 390 V instead of 400 V in the case of muon beam. With a hadron beam of $4 \cdot 10^6$ particles/s on a 40 cm liquid hydrogen target the maximum counting rate reaches 130 KHz/channel compared to 230 KHz/channel with muon beam of 10^7 particles/s. In addition, the discharge rate was found to be 0.2-0.3 discharges/s while no discharge was seen with the muon beam. The detection efficiency was measured for the channels which were crossed by the beam and found to be less than 90%. The loss of $\sim 6\%$ is entirely due to the electronics occupancy since the gain remains unchanged at the highest hadron beam flux.

5.4 New Pixelized Micromegas

To perform the measurements proposed in the COMPASS II proposal, very high hadron beam intensities are required. Since the present Micromegas detectors cannot stand these high hadron beam intensities, some effort has been done to overcome their limitations. A new generation of these instruments has been developed to fulfill the new COMPASS requirements which can be summarized by the following items:

- New detectors must stand very high hadron beam intensities.
- New detectors must have lower discharge rate (factor of 10-100) than the present detectors.
- The central region of the new detectors must be active and equipped with pixelized readout.
- The read-out electronics must be lighter than the present ones although the increased number of channels in the new generation of detectors.
- New detectors must be more robust than the previous ones.

In 2009 data taking, two prototypes were built and placed across the COMPASS beam line to study their operating performances in the COMPASS experimental conditions. The main characteristics of the new detectors are given in the following sections.

5.4.1 Pixelized Read-out in the central region

The acceptance of the new detectors must cover the central region (beam area) where the beam flux is very high, of the order of 200 KHz/mm^2. The trivial choice would be a read-out with strips. Under a beam flux of 500 KHz/cm^2, the hit rates of a read-out strip is of the order of 150 KHz/channel resulting in a detection efficiency of 96% in the active zone of the present detectors. In the central region, one expect a hit rates of the order of 500 KHz/channel leading to a deterioration in the detection efficiency due to the largest electronic occupancy.

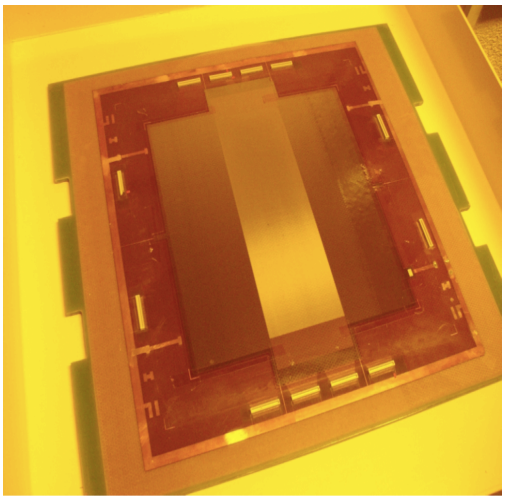

(a) Photograph of the fully equipped Pixel Micromegas detector prototype

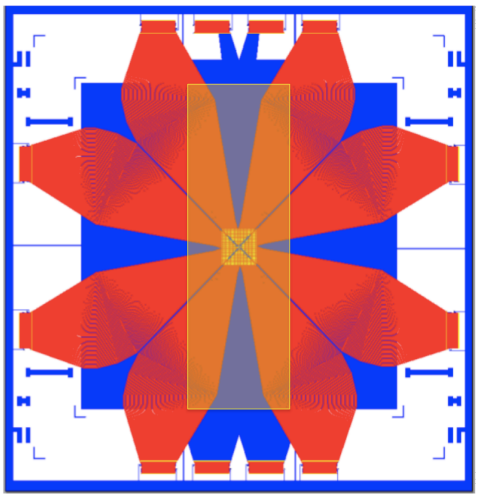

(b) Shematic view of the read-out prototype. The active area is the 10×30 cm^2 in the middle and the pixels in the very center

Figure 5.7: Pixelized Micromegas detectors tested in 2009

A suitable solution is to use a pixelized read-out, each pixel has an area of 1 mm^2. This has the advantage of reducing the hit rates to 200 KHz/cm^2 instead of 500. In summary, the read-out of the tested prototypes (figure 5.7) consists of two parts. A pixel part in the center with a size of 3.2×3.2 cm^2, and a strip part of an overall 10×30 cm^2. The pixel plane comprises 32×32 pixels and the strips plane comprises strips with two sizes: 30 cm long strips which cover the complete active area and 50 cm long strips which had to end at the pixels. This design was taken by the CEA Saclay from an original one developed by the Technische Universität München (TUM) group.

5.4.2 Read-out electronics

A total number of 1536 channels (1024 for pixels and 512 for pixels) have to be read out for one detector. In this case, the number of electronic cards required increases by a factor of 1.5 with respect to the present detectors. The use of the current electronic cards is discarded due to two main reasons. Firstly the geometrical space needed for one card is quite important. Secondly, the power consumption per detector is relatively high, of the order of 500 W and requires a high cooling power.
These two limitations push the choice towards the APV25 chips [67]which were developed for the CMS[4] silicon trackers. The chip has 128 channels, each one containing a preamplifier and a shaper of $\sim$ 150 ns peaking time, followed by a memory to which the analog values are sampled at 40 MHz. An important feature of the APV is its pipeline which saves up to 160 25 ns-spaced analog samples for each channel. The chip can operate in three modes: peak mode, in which the output sample corresponds to the peak amplitude following a trigger, deconvolution mode where the output corresponds to the peak amplitude of the APSP[5] deconvolution filter and multi-mode where three samples are read out following a trigger. The samples will be multiplexed into one

[4]Compact Muon Solenoid, one of the Large Hadron Collider (LHC) experiments
[5]Analog Pulse Shape Processor, http://www.hephy.at/user/friedl/html/node34.html

analog output stream per APV chip and sent to a digitization card. To calculate the time at which he particle crossed the detector with respect to the trigger, the shape of the signal must be known. To reconstruct the signal shape, the three samples must sit on the rising edge of the signal. Figure 5.8 shows the signal sampled by the APV where the optimal positions of the three samples (amp_0, amp_1, amp_2) are illustrated too.

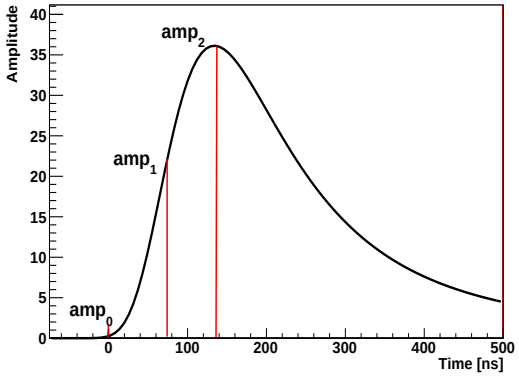

Figure 5.8: Processed samples for a typically shaped signal

In total, one detector read-out need 16 APV25 chips, each one placed on an APV card. The 16 APV cards are then connected to one ADC[6] board which can process 2048 channels.

5.4.3 Pixelized Micromegas Prototypes

The first test of pixelized Micromegas was performed in 2009 using two prototypes. Both consist of 32×32 mm^2 of 1 mm^2 pixels in the central area surrounded by strips in the rest of the active area. The first prototype was built using a copper mesh and mounted with the usual technology and the second one was built using the new bulk technology (section 5.4.3.2). While the first prototype was used to test the concept of pixelizing the Micromegas detector, the second prototype was used to estimate the impact of the new technology on the detector performances, especially its gain, spatial resolution and its discharge rate. A detailed description of each prototype is given in the following.

5.4.3.1 Copper mesh prototype

This prototype was included into the COMPASS setup during the 2009 data taking with hadron beams. It is characterized by a 5 μm thick copper mesh with an amplification gap of 100 μm. With a hadron beam of $4 \cdot 10^6$ particles/s and a potential of 390 V on the amplification space, the discharge rate was estimated to be $0.2 - 0.3$ discharges/s. This result was expected from previous tests that have been made on the twelve present detectors with the same hadron beam.

5.4.3.2 Bulk prototype

The choice of a new technology was essentially made to improve the robustness of the detectors. In addition it allows to avoid several issues that are encountered with the present Micromegas, like the gluing defaults, the impurities below the mesh as well as the tightening of the copper mesh. The new technology consists of a woven stainless steel mesh laminated to the board between two photosensitive coverlays. To draw pillars on the coverlays, an UV insulation with appropriate masks is applied.

[6]Analog Digital Converter

5.5 Performances of Micromegas prototypes

The performances of a given detector can be summarized in three operating characteristics: detection efficiency, spatial resolution and time resolution. The measurement of these properties has been performed for two prototype detectors (copper mesh and bulk prototypes). Both detectors were placed in the COMPASS spectrometer during 2009 physics data taking. The definitions for detection efficiency, spatial resolution and time resolution, as well as the obtained results, are given in the following .

5.5.1 Data Selection

To study the performance of a given detector, one needs a sample of tracks whose position and time of passage are known. Their precise knowledge is very important not only for a precise determination of the efficiency and the spatial resolution, which can be the most affected by bad tracks, but also in different analysis where the hadronic final state is involved. The examined prototype was not included in the CORAL reconstruction procedure to avoid any bias to the performance study. The data used in this study were taken by scattering a 160 GeV/c muon beam off a proton target (NH_3) in order to study the DVCS[7] process.

The selected tracks are subject to different kinds of cuts. At first, only tracks which have their momentum > 0.5 GeV/c are selected. A χ^2 cut is also applied to select tracks reconstructed with a reliable precision. The last coordinate[8] of the particle track is required to lie after the SM1 magnet to ensure that the selected track fall inside the acceptance spectrometer. In addition, the track is required to extend both upstream and downstream the examined detector. Finally, the track must be correlated to the trigger time to avoid any contamination of the sample by pileup tracks. The effect of the applied cuts on the statistics is shown in table 5.3. The track distributions as a function of some variables (χ^2/Ndf, last Z coordinate, momentum and time) are shown in figure 5.9.

Cuts	Strips	pixels
No cuts	11543946	11543946
track has momentum	4986419	4986419
$\|P\| < 0.5$ GeV/c	4986322	4977405
χ^2/Ndf	4293283	4286295
Z_{Last}	2173725	2173576
$\|t\| < 2$ ns	776481	776415
Ndf > 8	765268	678470
Z_{min}	691222	611764

Table 5.3: Effect of the selection criteria on the statistics. The numbers of tracks correspond to one run of data taking at high beam intensities ($\sim 2 \cdot 10^8$ particles/spill).

5.5.2 Detection Efficiency

The detection efficiency ϵ is the most important characteristic of a tracking detector. It is defined as the fraction of the total number of tracks which are detected by the device. To measure it, the starting point consists on determining the so called apparent efficiency ϵ_{app} defined as the ratio of the number of detected tracks to the total number of tracks that crossed the detector:

$$\epsilon_{app} = \frac{N}{N_{tot}} = \frac{\text{\# of detected tracks}}{\text{\# of incident tracks}} \tag{5.8}$$

[7]DVCS (for Deeply Virtual Compton Scattering is a physical process used to study the generalized parton distribution functions (GPD)

[8]The last coordinate of a track corresponds to the Z coordinate of the last hitted detector.

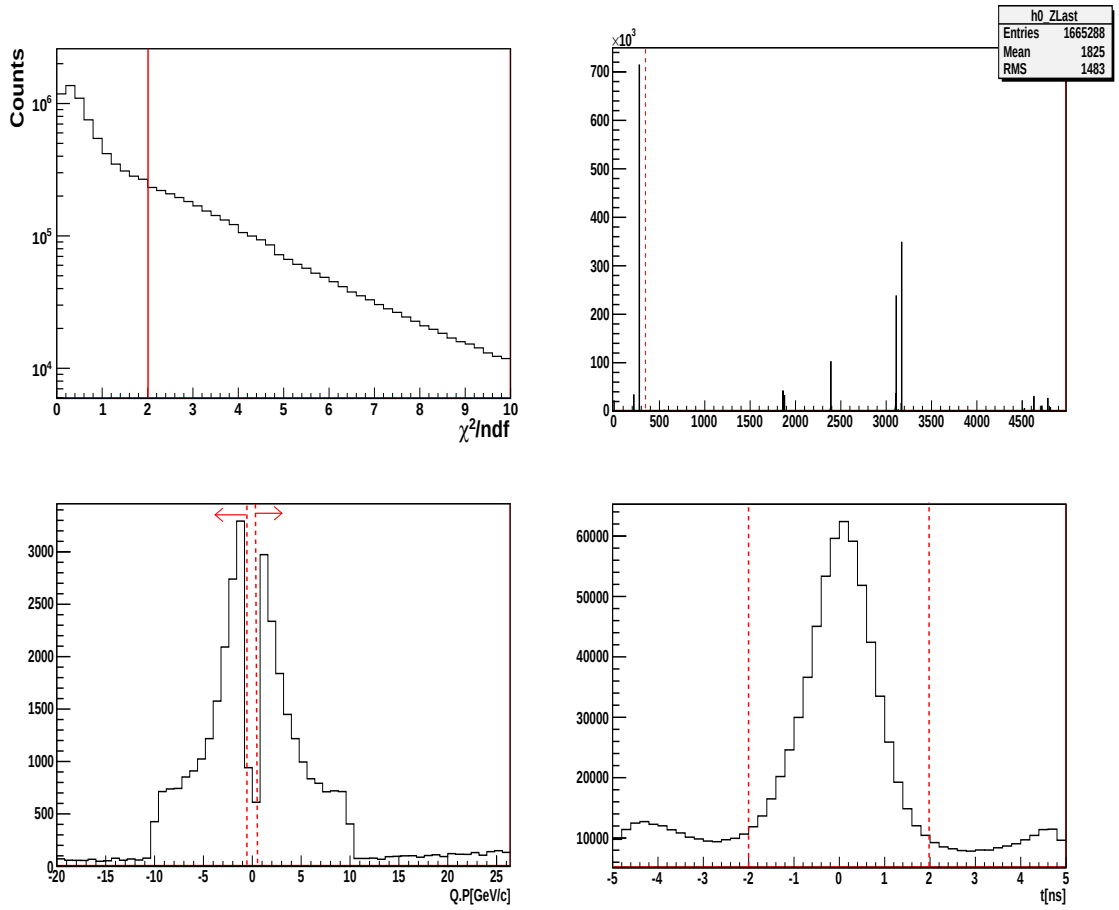

Figure 5.9: Properties for the sample of tracks used in the performances analysis. Red lines correspond to the selection limits. Distributions for the χ^2 distribution (top left), the coordinate of the last measured hit (top right), the momentum of the hadron (bottom left) and time of track with respect to the trigger (bottom right).

A track is marked as detected if a cluster[9] can be found inside a circle with a certain road width around it, which is generally a multiple of the spatial resolution. For a certain value of the road width, one cluster may be associated to more than one track, like in the reconstruction procedure. By increasing the road width around the track, the number of combinations of uncorrelated track and clusters increases leading to an overestimate in the apparent efficiency. As a consequence, the latter depends on the road width. The real detection efficiency ϵ, however, does not depend on the road width and is affected by the background. The latter may be created from noise in the electronics or may be caused by other particles that crossed the detector shortly before the triggered event. The probability to find at least one cluster within the road width around the track that is uncorrelated to the track is called background probability p_b and contributes to the apparent efficiency as follows:

$$\epsilon_{app} = \epsilon + p_b(1-\epsilon) \quad \Leftrightarrow \quad \epsilon = \frac{\epsilon_{app} - p_b}{1 - p_b} \tag{5.9}$$

The determination of the background is the most critical point in the detection efficiency determination. It is done on a track by track basis. For each track, two sets of hit clusters with all needed information (position, time, amplitude, ...) have been created. The first one contains all "good" clusters, i.e. clusters that are created by the tracks of the examined event. The second set is used to simulate the background and contains clusters which are uncorrelated to the tracks

[9]For a given detector plane, the signals handled by individual readout channels are translated into hits using specific algorithms. The information coming from adjacent channels is often combined to *clusters*. The clusters thus can be interpreted as space points.

of the examined event. It is created from the clusters of another event which is independent of the examined one. Once the background probability is evaluated, the real efficiency is calculated according to Eq. 5.9. This method is used to calculate the detection efficiency for both strip and pixel areas. To determine the detection efficiency, two parameters have to be optimized: the road width and the high voltage. In the following the results for the copper prototype will be presented. Results for the bulk prototype are grouped in another section.

5.5.2.1 Road Width selection

The detection efficiency has been computed for different road widths in order to select the optimal value. The resulting efficiencies are shown as a function of the road width in figure 5.10(a) (5.10(b)) for the strip (pixel) area. They have been calculating using data taken with a high intensity muon beam ($\sim 2 \cdot 10^8$ μ/spill).
For the strip area, the efficiency plateau is reached at a road width of 0.5 mm. The detection efficiency for the 15 cm long strips reaches a maximum value of 98% while the efficiency of the 30 cm long strips reaches only 94%. This difference is due to the large occupancy for the 30 cm strips, which is 30% larger than that of the 15 cm long strips. For the pixel area, the efficiency reaches its maximum of 98% at a road width of 0.8 mm. These optimal values of the road width will be used in the following.

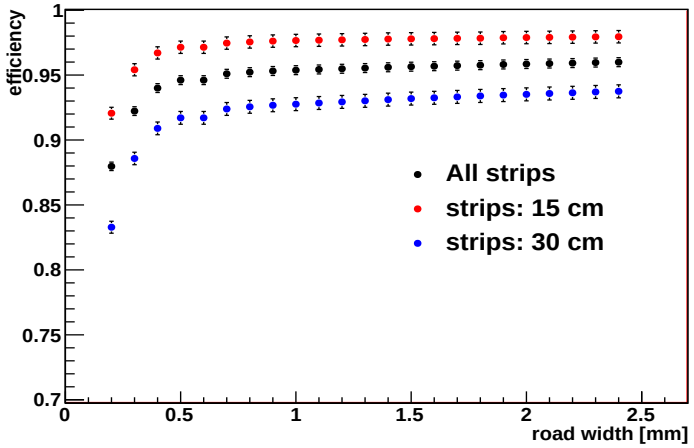

(a) All strips (black), 15 cm strips (red) and 30 cm strips (blue)

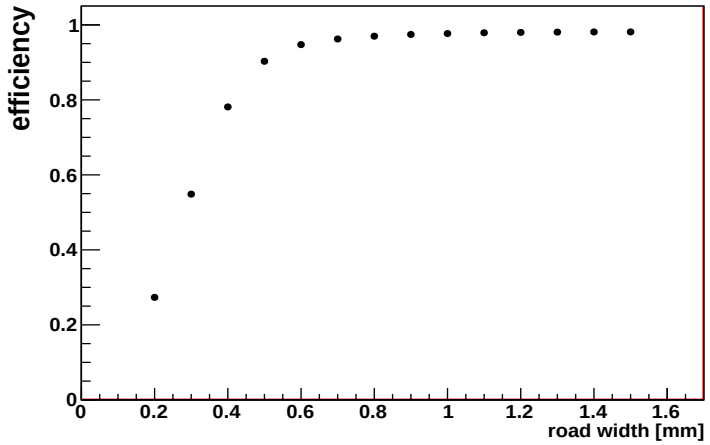

(b) Pixels

Figure 5.10: Road width dependence of the efficiency for the strip and the pixel areas for the voltage settings 410 V in high intensity muon beam.

5.5.2.2 High Voltage Scan

The efficiency has been computed for different high voltages on the mesh, varying from 360 V to 420 V in steps of 10 V, in order to determine the optimal high voltage at which the detector is fully efficient. The high voltage applied on the drift electrode is fixed at 840 V. The dependence of the efficiency on the high voltage is shown for both strip (figure 5.11(a)) and pixel figure (5.11(b)) areas.

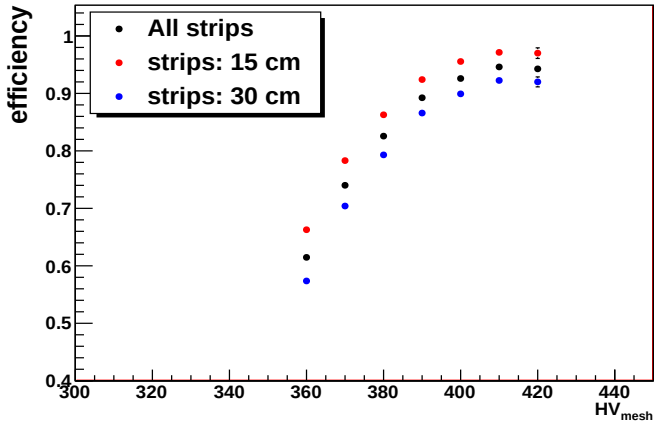

(a) All strips (black), 15 cm strips (red) and 30 cm strips (blue)

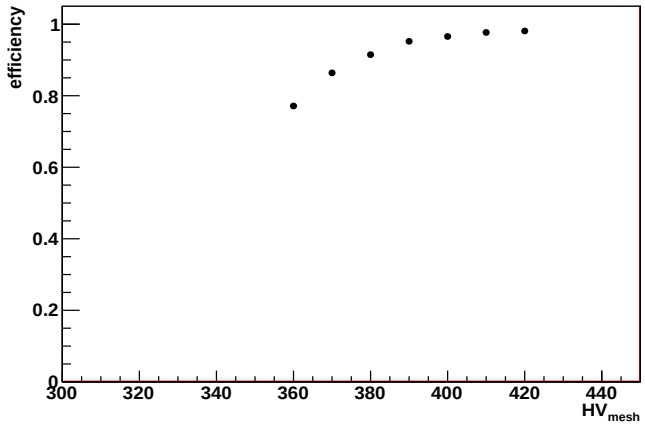

(b) Pixels

Figure 5.11: High voltage dependence of the efficiency in high intensity muon beam.

For the strips (15 cm and 30 cm) the detection efficiency reaches a maximum value of 96% in high beam intensity at the high voltage 410 V. This result is compatible with the detection efficiency of the present micromegas (section 5.3) under the same conditions. The low obtained value of 96% is mainly due to the 30 cm strips contribution. The electronic occupancy for these strips is larger by $\sim$ 30% than for the 15 cm strips due to their larger size. As a consequence their detection efficiency reaches only 94% at the nominal voltage while it reaches 98% for the 15 cm strips. The dependence of the detection efficiency on the voltage settings is shown in figure 5.11(a) for each type of strips. For the pixel area, the efficiency plateau is reached at the same high voltage with a value of 98% (cf. figure 5.11(b)). The apparent efficiencies (ϵ_a), the backgroud probabilities or occupancies (p_b) and the real efficiencies (ϵ) are given in table **??** for the strip and the pixel areas.

Using the optimal values of the road width and the high voltage (410 V), the two dimensional detection efficiency is estimated and shown in figure 5.12 for the strip and for the pixel areas; the corresponding background probability is shown as well. They are estimated in high intensity

muon beam. Under these conditions the background probability is found to be important in both cases (strip and pixel) and its correction is needed in the efficiency estimation. Several observations and remarks can be made for figure 5.12:

- The background probability estimated in the strip area is larger than that estimated in the pixel area, leading to lower efficiency for the strips.
- For strip area, the detection efficiency estimated in the 15 cm long strip area is larger than the one estimated in the 30 cm strip area. In parallel, the background probability is lower for the 15 cm strip are than for the 30 cm strip area.
- For pixels, one expect to have a square detection surface instead of the hourglass detection surface. This form is due to the limited number of pixel readout.
- Several strips and pixels with low efficiency can be seen due to high electronic noise. Such regions as well as the peripheral area will be discarded in the average efficiency calculation.

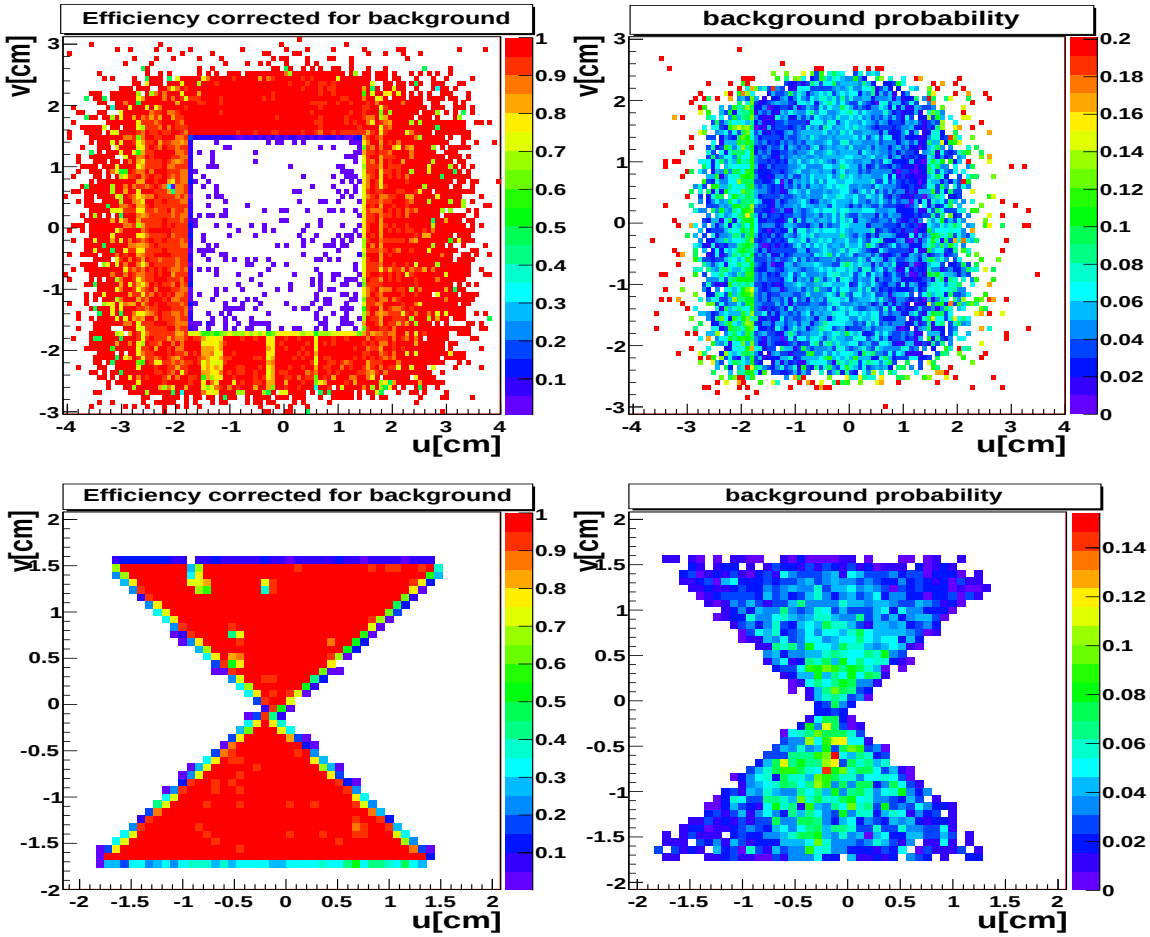

Figure 5.12: 2-dimension detection efficiency ϵ (left) and background probability p_b (right) for the strips (top) and for the pixels (bottom) evaluated at 410 V in high intensity muon beam.

The two dimensional efficiency for two extreme values of the high voltage (370 and 410 V) is shown in figure 5.13 for the strip and for the pixel area. As previously shown in figure 5.11(a), the device is fully efficient at the nominal voltage 410 V.

5.5.3 Spatial Resolution

A second important characteristic of a detector is its spatial resolution. It is defined as the uncertainty on the position measurement of a particle that crosses the detector plane. It can be

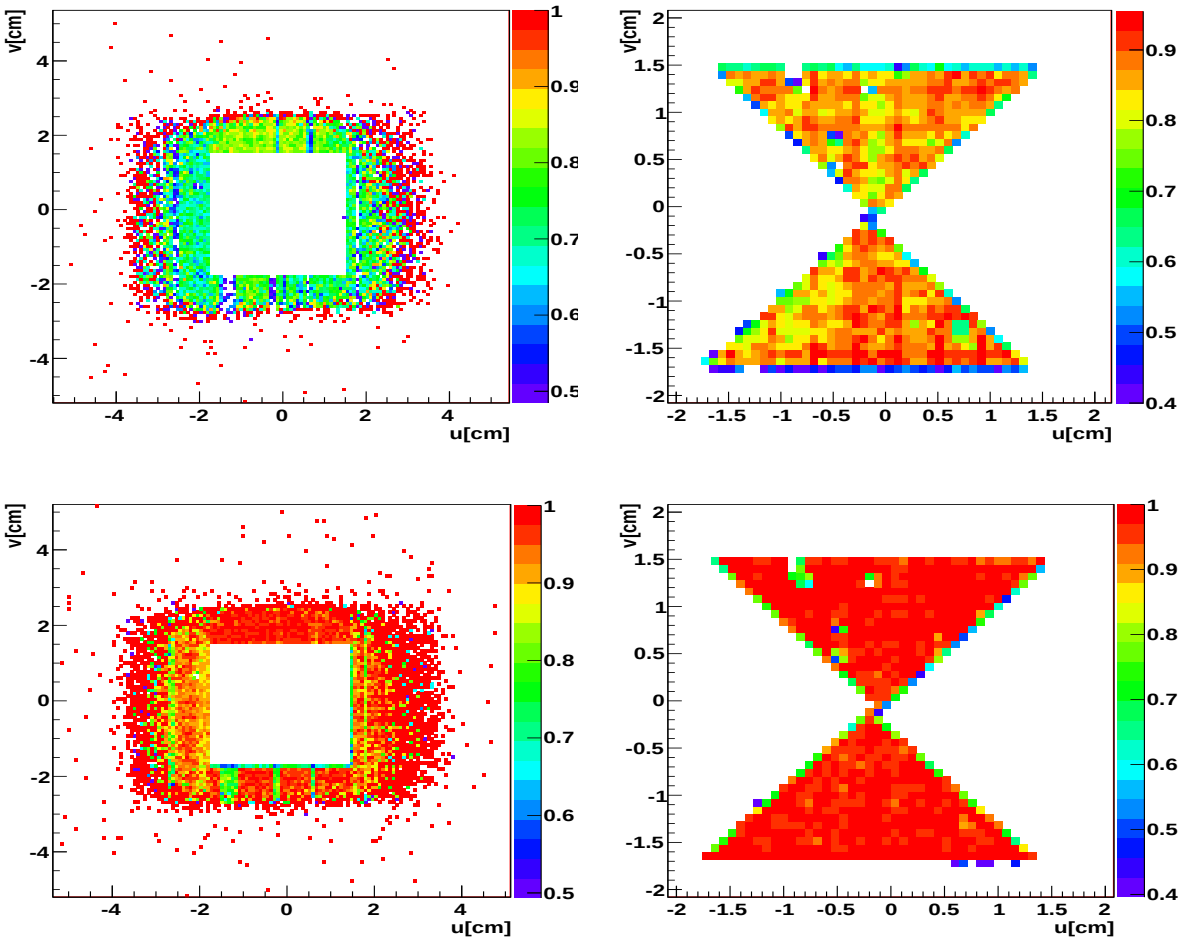

Figure 5.13: 2-dimension detection efficiency in strip (left part) and pixel (right part) areas versus u and v measured coordinates at 370 V (upper row) and at 410 (lower row).

calculated using the so called "residual" distribution. For this purpose, each track in the examined sample must be extrapolated to the detector position and then rotated into the coordinate system of the corresponding plane. The “residual”, defined as the difference between the known position of a reference track u_{Track} and the spatial position of a cluster u_{Cluster} recorded by the detector and associated to this track, is then calculated.

$$\Delta u = u_{\text{Track}} - u_{\text{Cluster}} \tag{5.10}$$

In the case of strips, only one coordinate (u) is measured and consequently one residual distribution is obtained. In the case of pixels, two coordinates (u & v) are measured for one cluster leading to three residual distributions: one dimensional distribution for each projection and one distribution for the radial coordinate ($r = \sqrt{u^2 + v^2}$). The residuals are calculated for all possible combinations of tracks and clusters resulting in a Gaussian shaped distribution with a flat background, which reflects the contribution of uncorrelated track-cluster pairs to the distribution. In the ideal case, the width of the residual distribution $\sigma_{residual}$ represents the spatial resolution along this coordinate. However $\sigma_{residual}$ is subject to two main effects. At first, a bad alignment of the detector, like a shift along the beam axis or a rotation around it, may affect the width of the residual distribution. This wrong position effect can be accounted for by performing a rotation of the detector plane in the corresponding direction. The second effect corresponds to the track reconstruction error σ_{Tracking} associated to the finite spatial precision of detectors used in the reconstruction procedure. This quantity has to be deconvolve from $\sigma_{residual}$ in order to estimate the spatial resolution (σ) of the detector, according to Eq. 5.11

$$\sigma = \sqrt{\sigma^2_{residual} - \sigma^2_{Tracking}} \tag{5.11}$$

The residual distribution cannot be fitted with a single Gaussian[10] because in this case a small χ^2-probability is obtained. A combination of two Gaussian ($g_1(u)$ & $g_2(u)$) with a flat background is used instead:

$$\Delta u = C_1 \exp\left(-\frac{(u-\bar{u_1})^2}{2\sigma_1^2}\right) + C_2 \exp\left(-\frac{(u-\bar{u_2})^2}{2\sigma_2^2}\right) + C_{BG} \tag{5.12}$$

The width of the residual distribution is calculated from the standard deviations of both Gaussian weighted with their integrals.

$$\sigma_{residual} = \frac{C_1\sigma_1 \cdot \sigma_1 + C_2\sigma_2 \cdot \sigma_2}{C_1\sigma_1 + C_2\sigma_2} \tag{5.13}$$

5.5.3.1 Results for Pixelized MM (copper mesh prototype)

The residual distribution along the measured coordinate (Δu) is shown for the strips at the nominal voltage 410 V in figure 5.14(a). The corresponding fitted function (Eq. 5.12) is displayed in blue and the two Gaussian contributions are displayed in red (g_1) and in green (g_2). The obtained $\sigma_{residual}$ is then corrected for the tracking contribution ($\sigma_{tracking} \sim 48$ μm) according to Eq. 5.11. The final spatial resolution is of 93 μm. This result is better than the expected value of 114 μm (strip pitch/$\sqrt{12}$). In figure 5.14(b) is shown the residual distribution (Δu) as a function of u. A very small dependence of the residual on the position is seen hinting towards a problem with the alignment for this detector plane.

For pixels, the residual distribution corrected for the background contribution is shown for both u (figure 5.15(a)) and v (figure 5.15(b)) projections, at the nominal voltage. In this case, the obtained distributions are not Gaussian shaped and $\sigma_{residual}$ is taken as the root mean square of the distribution. Corrected for the tracking contribution $\sigma_{tracking}$, the spatial resolution σ is found to be 282 μm for both u and v projections.

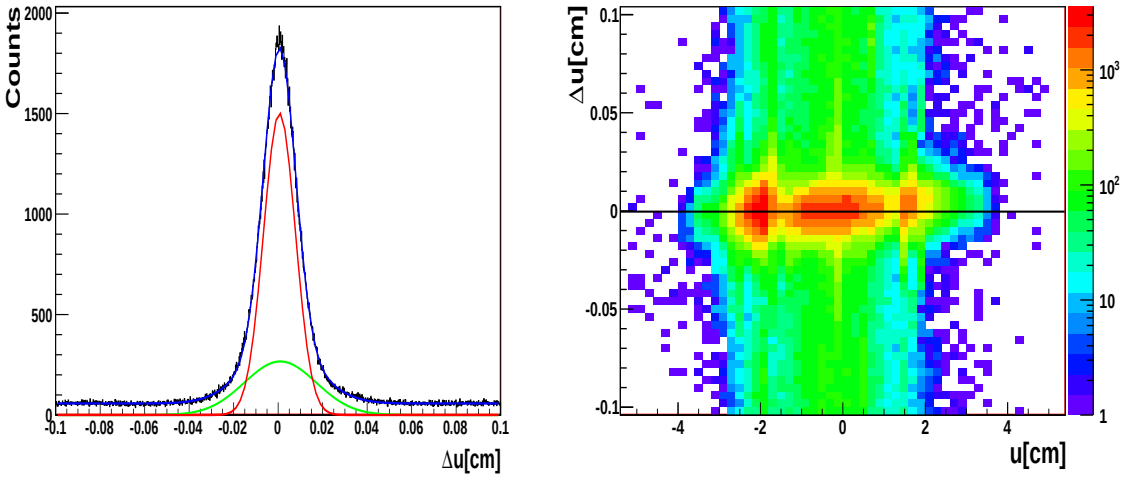

(a) Residual distribution

(b) $\Delta u(u)$

Figure 5.14: (a) Residual distributions for the strips for the voltage settings 410 V. (b) The residual distribution as a function of the measured coordinate.

[10] In principle, every cluster size have a slightly different residual than other sizes. As a consequence, one has to use one Gaussian for every cluster size.

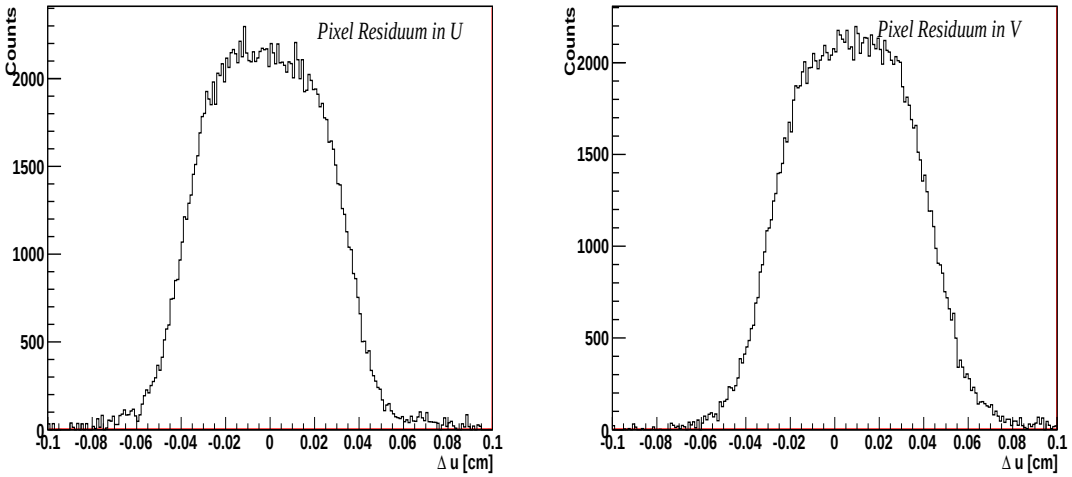

(a) Residual distribution in u

(b) Residual distribution in v

Figure 5.15: Residual distributions for the pixel plane for the detector settings 410 V for both projections: u (a) and v (b). The root mean square of these distributions correspond to the spatial resolution.

5.5.3.2 Dependence on the voltage settings

The dependence of the spatial resolution on the high voltage is presented in table 5.4 for both strips and pixels. Its was found to be similar for the strips and the pixels. At low voltages, the cluster might contain only one hit in one strip or one pixel. By Increasing the voltage, the gain of the detector increases resulting in bigger charge clouds and consequently more responding channels, which improves the position measurement. This explanation can be illustrated in the cluster size distribution, shown in figure 5.16 for strips for two high voltages 360 V and 420 V. Increasing the detector voltage by 60 V shifts the mean value from 1.4 to 2 for strips and from 1.3 to 1.8 for pixels. The mean values for the cluster size are given for each voltage in table 5.4.

HV_{mesh} [V]	$\sigma[\mu m]$ for strips	$\sigma[\mu m]$ for pixels		<Cluster size>	
		u	v	strips	pixels
360	114	266	283	1.45	1.34
370	230	290	287	1.50	1.40
380	118	289	289	1.60	1.45
390	139	279	279	1.70	1.50
400	99	285	285	1.80	1.60
410	93	282	282	1.91	1.65
420	93	300	300	2.02	1.81

Table 5.4: Dependence of the spatial resolution (σ) and the cluster size upon the high voltage for both strips and pixels (for the two projections u and v).

5.5.4 Time Resolution

As detailed in section 5.4.2, the signal of the pixelized micromegas is processed in an APV25 chip. The latter contains a shaper with a signal rise time of about 150 ns and a fall time of about 250 ns. Following a trigger, the shaped signal is sampled with a frequency of 38.88 MHz ad three samples (amp_0, amp_1, amp_2) are readout and processed. The latency, defined as the difference between the time the particle crosses the detector with respect to the trigger, must be adjusted such that these three samples are situated on the rising edge of the signal (see figure 5.8). The difference between the trigger time and the rising edge of the TCS clock is called the TCS phase.

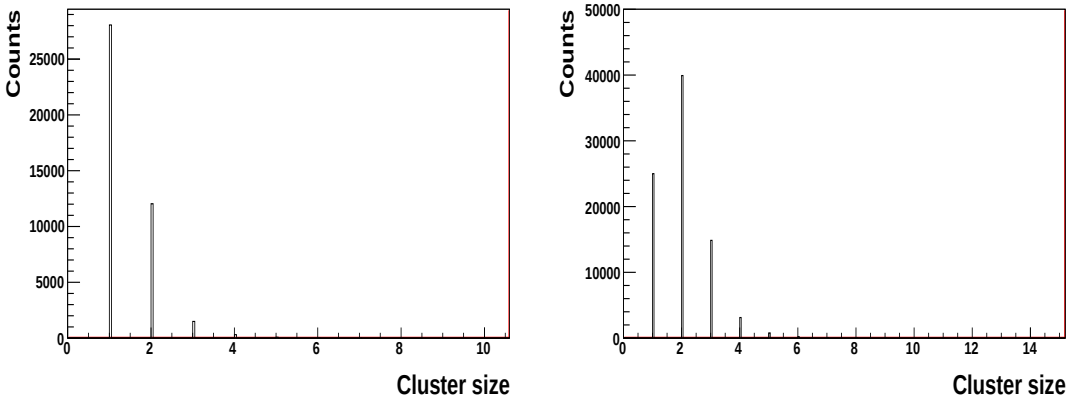

Figure 5.16: Cluster Size (in number of wires) distributions for the strips for the two voltage settings 370 V (left) and 420 V (right) with a mean value of 1.5 and 2. respectively.

Since the trigger time and the generation of a signal in the detector must be the same, the time can be reconstructed using the three samples and the TCS phase. The ratio $\text{amp}_1/\text{amp}_2$ versus the according TCS phase is shown in figure 5.17 for the pixels. The correlation between the ratio and the TCS phase is corrected for in the time resolution estimation.

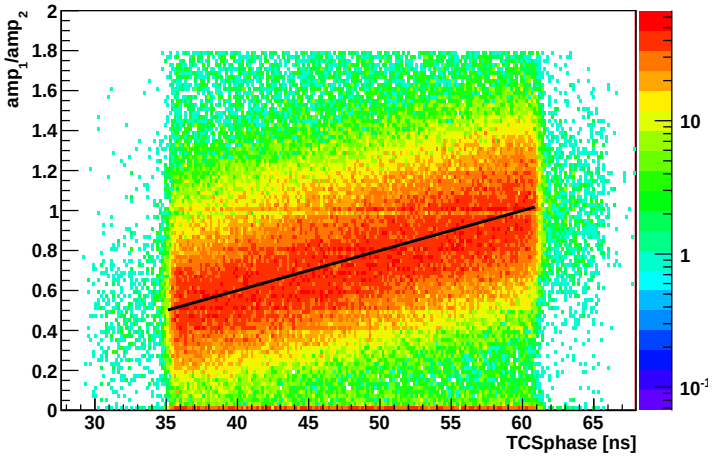

Figure 5.17: Ratio $\text{amp}_1/\text{amp}_2$ versus the TCS phase for the copper prototype. The correlation between the plotted parameters is taken into account in the time resolution estimation.

The time resolution is estimated from the time residual distribution. The latter is obtained from the difference between cluster time and track time. Since the track time is usually determined using detector with a very good time resolution, the width of the time residual distribution defines the time resolution. For the strips, the time resolution is found to be 15 ns while for the pixel it is 12.5 ns. An example of the time residual distribution is shown in figure 5.18. In contrast to the spatial resolution, the time resolution does not depend on the high voltage.

5.5.5 Results for Bulk Pixelized Micromegas

The bulk micromegas was placed in the spectrometer during data taking in 2009. It was operating at the high voltage 400 V for the mesh and 840 V for the drift electrode. For this detector, data were taken with a low intensity muon beam ($\sim 10^6$ μ/spill). Similarly to the first prototype, the performances of the bulk prototype are studied and its main characteristics (detection efficiency, spatial resolution, time resolutions) are measured.

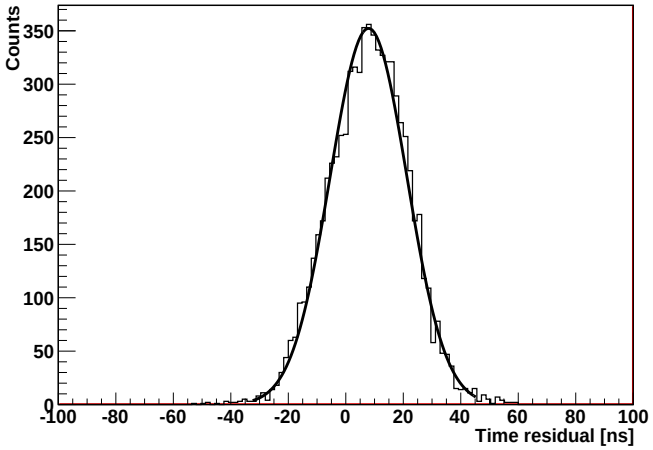

Figure 5.18: Time residual distribution.

As a first step, the dependence of the total efficiency on the road width is studied and presented in figure 5.19(a); the apparent efficiency and the background probability are presented too. While the apparent efficiency and the background probability increase with the road width, the total efficiency remains unchanged once the plateau is reached at ~ 1 mm. Using this road width value, the detection efficiency is calculated and found to be of 97% and 92% for strip and pixel areas respectively. The low detection efficiency for the pixel area can be caused by a bad alignment or a defect on the detector, as shown in figure 5.19(b).

The spatial resolution is measured and found to be 97μm for strips and $\sim$ 260 for pixels (260 μm in the u projection and 270 μm in the v projection). Finally, the time resolution for this detector is 15 ns for the strips and 13 ns for the pixels.

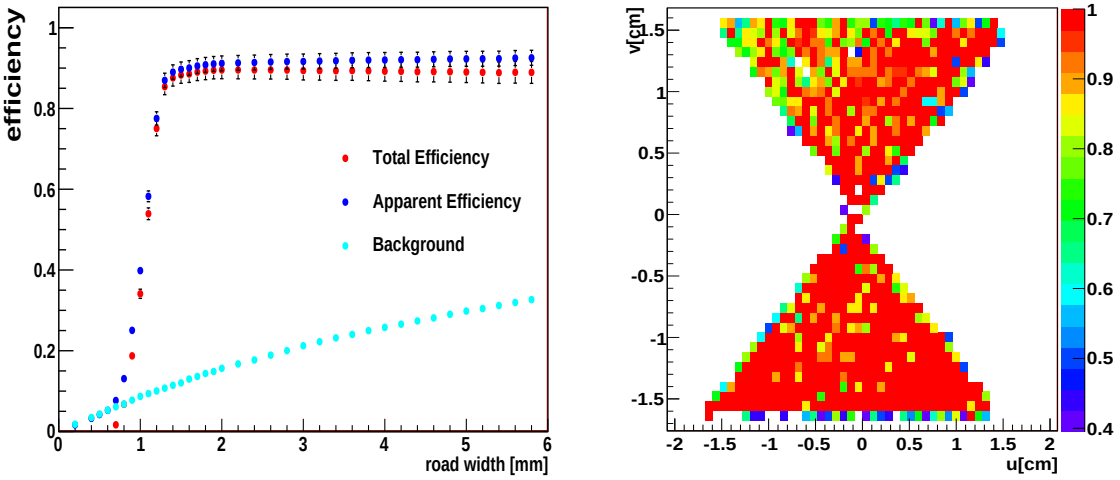

(a) Dependence of the efficiency on road width

(b) efficiency for pixel area

Figure 5.19: (a) Road width dependence of the efficiency for the strips for the voltage settings 410 V in low beam intensity for the bulk prototype. (b) 2-dimension efficiency for the pixel area of the bulk prototype.

5.6 Summary and Conclusions

The performances of two new micromegas prototypes were studied using COMPASS data collected during two weeks of 2009 data taking, by scattering a 160 GeV/c muon beam on a 40 cm long proton (NH_3) target.

The new prototypes were built and tested in the context of a new project which aims to upgrade the present micromegas detectors for the COMPASSII program [59]. Major upgrades have been implemented in the new prototypes compared to the present detectors. One important upgrade being the detection of the beam particles by occupying the central part of the new prototypes with pixelized read-out and using light and integrated electronics (APV25). In addition, in order to improve the robustness of the present detectors and to avoid all issues faced using a copper mesh, one of the two prototypes was built using the new bulk technology. The latter represents the main difference between the two prototypes (copper mesh for the first one and bulk technology for the second).

The first prototype (built with a copper mesh) operated at different high voltages starting from 360 V up to 420 V in high intensity muon beam ($\sim 2.7 \cdot 10^8$ μ^+/spill). The optimal high voltage was found to be 410 V at which the prototype operate with an efficiency of 96 % for the strip area and of 98 % for the pixel area. The efficiency of the strip area is similar to that of the present detectors when they operate in the same beam conditions. This value consists of the contributions of short (15 cm) and long (30 cm) strips. At the nominal voltage, the short strips operate with an efficiency of 98 % while the long strips operate with only 94 % due to their high electronic occupancy of 10%. Howevr, the pixels operate with a high efficiency. The spatial resolution is found to be of 93 μm for the strips and of 280 μm for the pixel in both u and v projections. These values are slighty better than expected which were deduced from the pitch that characterize both strips and pixels. Finally, the time resolution was also measured and a value of 13 ns (12.5 ns) is obtained for strips (pixels).

The performances of the second prototype were studied using data taken in low intensity muon beam ($\sim 10^6$ μ^+/spill). The device operated with a high voltage of 400 V on the mesh and of 840 V on the drift electrode. The strip area is characterized by an efficiency of $\sim$ 98 %, a spatial resolution of 97 μm and a time resolution of 15 ns. For the pixel area, the efficiency is found to be 92 %. This lower value may be caused by a bad alignment or a defect on the detector. The spatial resolution is of 260 μm for the two projections (corresponding to the two measured coordinates) and the time resolution is of 13 ns. The performances of this prototype are similar to those of the first prototype.

Finally, the central part of the new detectors is found to operate with a very good efficiency of $\sim$ 98% at a high intensity muon beam and with a spatial resolution of 280 μm. To improve the latter, a new prototype was buit in 2010 by replacing the square pixels in the central part with rectangular ones. The prototype was tested in real data taking conditions in order to study its performances.

Chapter 6

Extraction of Quark Helicity Distributions

The result of a leading order extraction of quark helicity distributions from COMPASS data is presented. As discussed in chapter 2, direct access to the separated valence and sea quarks as well as separated flavor contributions to the nucleon spin is possible via semi-inclusive deep inelastic scattering. These distributions have been measured by previous experiment at CERN and SLAC albeit with poor precision. The SMC (*Spin Muon Collaboration*) experiment at CERN made the extraction of the polarized valence and sea distributions using the semi-inclusive asymmetries of charged hadrons in both proton and deuterium targets [9] although particle identification was limited and thus a full flavor separation was not possible. At SLAC, the HERMES experiment had the advantage of collecting larger statistics and was equipped with a RICH detector providing a good particle identification; this allows to extract the individual flavor contributions. However, due to the low beam energy, the kinematic range covered by HERMES is reduced with respect to the SMC range.
The COMPASS experiment has the advantage of covering a wider x range with the possibility of particle identification allowing to perform a full flavor separation in a large x domain with good precision. The measurement of spin asymmetries from muon-proton DIS as well as the extraction of quark helicity distributions are presented in this chapter.

6.1 Spin Asymmetries

COMPASS has collected data from 2002 to 2006 by scattering a 160 GeV polarized muon beam off a polarized deuterium target ^{6}LiD, covering a large x range from 0.004 to 0.7. A previous analysis [21] of these data has been performed giving rise to the extraction of the separate valence and sea contributions. In 2007, COMPASS collected data with a polarized proton target NH_3 and the spin asymmetries have been extracted. This allows to perform a full flavor separation of quark contributions.
The deep inelastic scattering domain was defined by the kinematic cuts on the photon virtuality $Q^2 > 1$ (GeV/c)^2 as well as on the fraction of the lepton energy transferred to the virtual photon $0.1 < y < 0.9$. In addition, the energy of the beam was constrained to be in the range $140 < E_\mu < 180$ GeV. The selected events must have their reconstructed primary vertex inside one of the target cells and all particles originating from this primary vertex are selected as hadrons. The hadrons produced in the current fragmentation region are excluded by applying a cut on the fractional energy of the hadron $z > 0.2$. Similarly, the cut $z < 0.85$ exclude hadrons produced by diffractive processes. Finally, the momentum range of the selected hadrons is chosen between 10 and 50 GeV where both pions and kaons can be identified by the RICH detector.
The inclusive asymmetry $A_{1,p}$ and the semi inclusive asymmetries $A_{1,p}^{\pi^\pm}, A_{1,p}^{K^\pm}$ extracted from proton data are shown in Fig 6.1 at their (x,Q^2) values. The asymmetries for inclusive DIS and for pions extracted by the HERMES collaboration are also shown as well as the predictions given by the DSSV parametrization [37] for polarized PDFs. The extracted asymmetries are found to be in agreement with the prediction and with the HERMES ones.

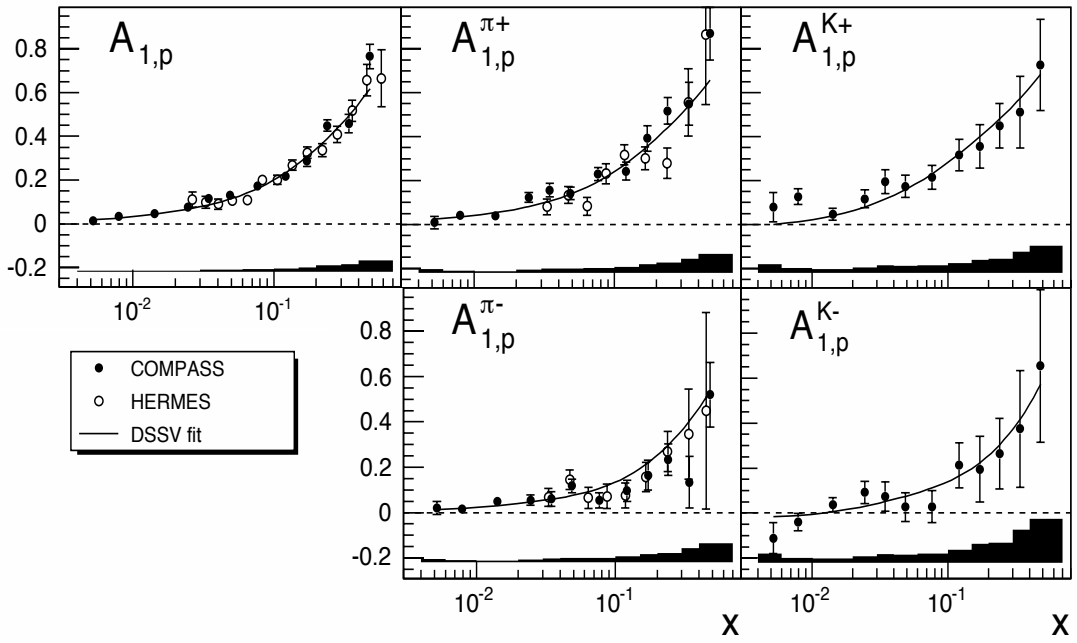

Figure 6.1: The inclusive asymmetry $A_{1,p}$ and the semi-inclusive asymmetries $A_{1,p}^{\pi^+}$, $A_{1,p}^{\pi^-}$, $A_{1,p}^{K^+}$, $A_{1,p}^{K^-}$ extracted from COMPASS data collected using a proton target. The errors correspond to the statistical ones and the systematic errors are presented by the bands. The curves are given by the DSSV [37] prediction and the open markers correspond to the result of the HERMES collaboration.

6.2 LO Extraction of Quark Helicity Distributions

6.2.1 Method of Extraction

Assuming the factorization of the cross-section for lepto-production of a hadron, the asymmetry can be expressed in the quark parton model at LO as the sum of the quark Δq and anti-quark $\Delta\bar{q}$ helicity helicity distributions weighted by the corresponding fragmentation functions D_q^h and $D_{\bar{q}}^h$. The semi-inclusive asymmetries are given by :

$$A_1^h(x,z,Q^2) = \frac{\sum_q e_q^2 \left(\Delta q(x,Q^2) D_q^h(z,Q^2) + \Delta\bar{q}(x,Q^2) D_{\bar{q}}^h(z,Q^2)\right)}{\sum_q e_q^2 \left(q(x,Q^2) D_q^h(z,Q^2) + \bar{q}(x,Q^2) D_{\bar{q}}^h(z,Q^2)\right)} \tag{6.1}$$

The asymmetries are measured at the average Q^2 values in each x bin starting from 1.3 GeV^2 at smallest x up to 60 GeV^2. Since no significant dependence upon Q^2 has been observed, the measured asymmetries at the Q^2 mean value are assumed to be equal to those at $Q^2 = 3$ GeV^2. To extract Δq, the unpolarized PDFs $q(x,Q^2)$ have been taken from the MRST parametrization [38]. They originate from the measured structure function F_2 in which the ratio $R = \sigma_L/\sigma_T$ is different from zero while this ratio is assumed to be zero at LO. To correct for this, the asymmetries are divided by $(1 + R(x,Q^2))$. On the other hand, the fragmentation functions $D_q^h(z,Q^2)$ are taken from the DSS parametrization [34]. Integrating over z and neglecting the Q^2 dependence of the asymmetries, (6.1) is reduced to :

$$A_1^h(x) = \frac{\sum_q e_q^2 \left(\Delta q(x) D_q^h + \Delta\bar{q}(x) D_{\bar{q}}^h\right)}{\sum_q e_q^2 \left(q(x) D_q^h + \bar{q}(x) D_{\bar{q}}^h\right)} \tag{6.2}$$

Here, D_q^h are integrated in the range [0.2, 0.85]. For each hadron type (π^+, π^-, K^+, K^-), the semi-inclusive asymmetry (Eq. 6.2) can be written in the case of a deuteron target (Eq. 6.3) as well as in the case of a proton target (Eq. 6.4). A total number of eight equation is obtained, all

expressed in terms of the six quark helicities (Δu, $\Delta\bar{u}$, Δd, $\Delta\bar{d}$, Δs, $\Delta\bar{s}$), the unpolarized PDFs and the fragmentation functions (D_q^h).

$$A_{1,p}^h = \frac{4(D_u^h\Delta u + D_{\bar{u}}^h\Delta\bar{u}) + (D_d^h\Delta d + D_{\bar{d}}^h\Delta\bar{d}) + (D_s^h\Delta s + D_{\bar{s}}^h\Delta\bar{s})}{4(uD_u^h + \bar{u}D_{\bar{u}}^h) + (dD_d^h + \bar{d}D_{\bar{d}}^h) + (sD_s^h + \bar{s}D_{\bar{s}}^h)} \tag{6.3}$$

$$A_{1,d}^h = \frac{(4D_u^h + D_d^h)(\Delta u + \Delta d) + (4D_{\bar{u}}^h + D_{\bar{d}}^h)(\Delta\bar{u} + \Delta\bar{d}) + 2(D_s^h\Delta s + D_{\bar{s}}^h\Delta\bar{s})}{(4D_u^h + D_d^h)(u + d) + (4D_{\bar{u}}^h + D_{\bar{d}}^h)(\bar{u} + \bar{d}) + (D_s^h s + D_{\bar{s}}^h\bar{s})} \tag{6.4}$$

In a similar way the inclusive asymmetry can be written in both proton (Eq. 6.5) and deuteron (Eq. 6.6) targets, giving rise to two equations expressed as a function of the six quark helicities.

$$A_{1,p} = \frac{4(\Delta u + \Delta\bar{u}) + (\Delta d + \Delta\bar{d}) + (\Delta s + \Delta\bar{s})}{4(u + \bar{u}) + (d + \bar{d}) + (s + \bar{s})} \tag{6.5}$$

$$A_{1,d} = \frac{5(\Delta u + \Delta d) + 5(\Delta\bar{u} + \Delta\bar{d}) + 2(\Delta s + \Delta\bar{s})}{5(u + d) + 5(\bar{u} + \bar{d}) + 2(s + \bar{s})} \tag{6.6}$$

Finally one obtains a total of ten equations of asymmetries which are experimentally measured. Assuming the knowledge of the unpolarized PDFs and the fragmentation functions, one can extract the six unknowns quark helicities. For this purpose, the system of equations given in 6.7 is solved.

$$\vec{A} = \mathcal{B}\vec{\Delta q} \tag{6.7}$$

$$\vec{A} = \left(A_{1,d}, A_{1,p}, A_{1,d}^{\pi^\pm}, A_{1,d}^{K^\pm}, A_{1,p}^{\pi^\pm}, A_{1,p}^{K^\pm}\right)$$

$$\vec{q} = \left(\Delta u, \Delta\bar{u}, \Delta d, \Delta\bar{d}, \Delta s, \Delta\bar{s}\right) \tag{6.8}$$

$\vec{A}$ is the vector of asymmetries, $\Delta\vec{q}$ is the vector of unknowns and $\mathcal{B}$ is a matrix whose coefficients depend on parton distribution functions (PDFs) and on quark fragmentation functions into hadrons. To extract the polarized quark distributions $\Delta q(x)$ as a function of x, the system of equations (Eq(6.7)) has be solved in each x bin by minimizing the χ^2 defined as :

$$\chi^2 = (\vec{A} - \mathcal{B}\vec{\Delta q})^T(\mathrm{Cov}_A)^{-1}(\vec{A} - \mathcal{B}\Delta\vec{q}) \tag{6.9}$$

Here, Cov_A is the covariance matrix of the experimentally measured asymmetries. The extraction of the quark helicity distributions requires the knowledge of the unpolarized quark distribution functions as well as the fragmentation functions. Using a parametrization for unpolarized PDFs and one parametrization for fragmentation functions, the matrix $\mathcal{B}$ can thus be calculated and the system of equations (6.7) can be solved. The extraction is performed independently in each x bin in the x range from 0.004 to 0.3. Above this limit, the up (Δu) and down (Δd) quark helicity distributions are fitted assuming that the sea contribution is zero.

6.2.2 Test of the assumption $\Delta s = \Delta\bar{s}$

In a first step, the extraction was performed with six unknowns including Δs and $\Delta\bar{s}$. The aim of this exercise is to check the assumption usually made on Δs to be equal to $\Delta\bar{s}$. The resulting distributions of $x\Delta s$ and $x\Delta\bar{s}$ as a function of x are shown in Fig 6.2; the difference $\Delta s - \Delta\bar{s}$ is also shown. Both distributions are compatible with zero as well as their difference.
The unpolarized strange and anti-strange quark distributions are assumed to be equal in the MRST parametrization. To check that this assumption do not affect the strange quark helicity distributions, the unpolarized strange quark distributions were scaled simultaneously by factors of 2 and 0.5. The extracted distributions $\Delta s(x)$ and $\Delta\bar{s}(x)$ are found to be independent of these variations. for any choice of fragmentation functions. In conclusion, the assumption $\Delta s = \Delta\bar{s}$ is valid in the covered x range. This conclusion remains valid regardless the fragmentation functions choice.

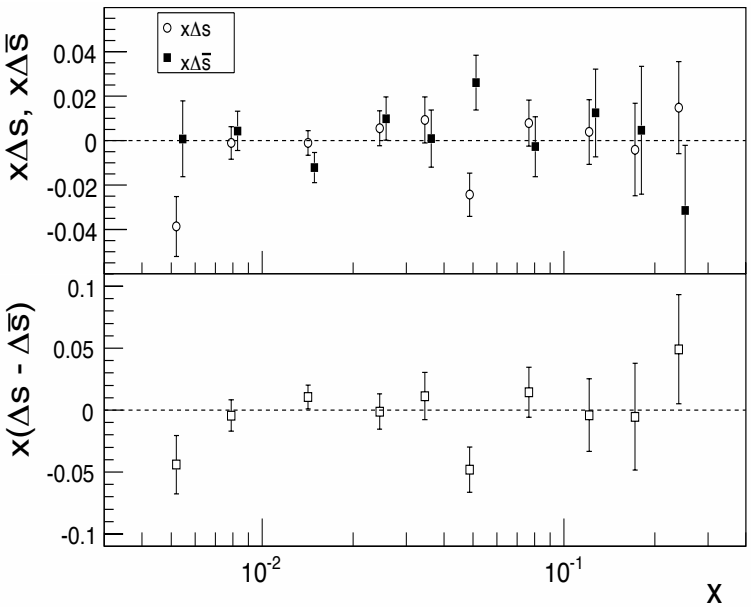

Figure 6.2: Results for the strange and anti-strange quark helicity distributions Δs and $\Delta\bar{s}$ and the corresponding values of the difference $\Delta s - \Delta\bar{s}$ as a function of the Bjorken variable x. Values are obtained from experimental asymmetries measured at $<Q^2> = 3$ and using the MRST parametrization for PDFs and the DSS parametrization for the fragmentation functions.

In the following, this assumption will be taken into account. In other terms, the extraction will be performed with only five unknowns (Δu, $\Delta\bar{u}$, Δd, $\Delta\bar{d}$, $\Delta s = \Delta\bar{s}$). This has the advantage of improving the statistical precision of the extracted distributions by at least a factor 1.5. The χ^2 of the fits performed varies from 1.8 to 8.5 with 5 degrees of freedom.

6.2.3 Results for Quark helicity Distributions

The extraction of the quark helicity distributions has been performed at LO with five unknowns (Δu, $\Delta\bar{u}$, Δd, $\Delta\bar{d}$, $\Delta s = \Delta\bar{s}$). The resulting distributions are presented in figure 6.3. They are in good agreement with the distributions predicted at Next to Leading Order (NLO) by the DSSV parametrization [37]. The comparison between the resulting distributions and the predicted ones is qualitatively good showing that a LO extraction of the quark helicity distributions is sufficient to estimate their shapes. The non strange sea quark distributions ($\Delta\bar{u}$, $\Delta\bar{d}$) are consistent with zero. The strange quark distribution is compatible with zero except the lowest x point which shows a deviation of about 2.5σ from zero.

6.2.4 First Moments of Δq

The first moment is thus $\Delta s = -0.01 \pm 0.01 \pm 0.01$ and shows a big discrepancy with the inclusive measurement obtained from the first moment of the spin structure function g_1. While the inclusive measurement relies on the octet axial charge a_8 introduced in section 2.3.4, the semi-inclusive measurement depend strongly on the choice of the fragmentation functions, in particular, the strange quark fragmentation functions.
The first moments of the quark helicity distributions have been evaluated in the covered x range at $Q^2 = 3$ GeV^2. The contributions from the uncovered x region to the first moments have been estimated by extrapolating the measured values or by using the DSSV parametrization. The resulting first moments of the valence quarks Δu_v and Δd_v estimated in both cases are close. For the sea quarks, the two methods give different results and it is more pronounced in the case of Δs. This is related to the fact that the DSSV parametrization includes a negative contribution to Δs for $x < 0.3$. The sum of the quark and antiquark helicity distributions in the full x range give $\Delta\Sigma = 0.32 \pm 0.03$ which is close to the estimated value from inclusive measurement $\Delta\Sigma = 0.33 \pm 0.03$ previously measured by COMPASS in [39].

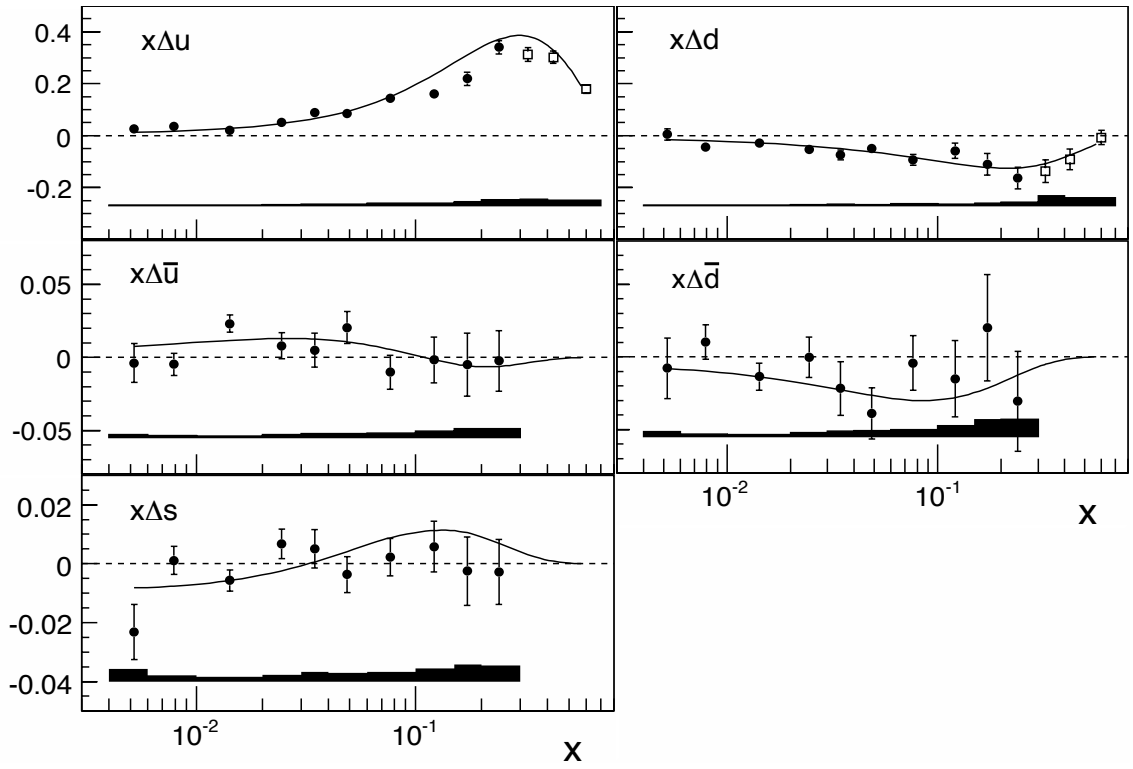

Figure 6.3: The quark helicity distributions $x\Delta u(x)$, $x\Delta\bar{u}(x)$, $x\Delta d(x)$, $x\Delta\bar{d}(x)$, $x\Delta s(x)$ extracted from the COMPASS spin asymmetries at $Q^2 = 3$ using the DSS parametrization for fragmentation functions and the MRST parametrization for unpolarized PDFs. For valence quarks, the values extracted above $x = 0.3$ are obtained assuming a zero contribution from the sea. The systematic errors are presented by the bands at the bottom of each plot. The curves correspond to the predicted distributions by the DSSV parametrization [37] at NLO.

6.2.5 Dependence on the Quark Fragmentation functions into Hadrons

In order to quantify the dependence of Δq upon quark fragmentation functions into hadrons, the first moments of the helicity distributions have been evaluated for different values of FFs. Instead of the individual fragmentation functions, one can express the asymmetries as a function of the ratios

$$R_{UF} = \frac{D_d^{K^+}}{D_u^{K^+}}, \qquad R_{SF} = \frac{D_s^{K^+}}{D_u^{K^+}} \tag{6.10}$$

Different sets of quark fragmentation functions give different values for these ratios. Using the DSS parametrization, $R_{UF} = 0.13$ and $R_{SF} = 6.6$ while with another set as the EMC one, R_{UF} becomes larger (0.35) while R_{SF} is smaller by a factor ~ 2. To estimate this dependence, the first moments have been evaluated by varying R_{SF} between 2 and 7and simultaneously R_{UF} between 0.45 to 0.1. The relation between R_{UF} and R_{SF} is constrained by the K^+ multiplicity which is imposed to be constant in the considered R_{SF} range. The resulting first moments are shown in Fig 6.4.

The down and anti-down helicity distributions do not depend on the ratio R_{SF} and remain constant when evolving R_{SF}. For the up and the anti-up helicity distributions, a standard deviation is observed when R_{SF} evolves from EMC value (3.2) to the DSS value (6.6). The most interesting dependence is seen for the strange distribution Δs which change by a factor 4 between the two choices of parametrization. Since the strange quark helicity depend critically upon the strange quark fragmentation functions, their experimental extraction is of special interest and would contribute to the understanding of the difference between the inclusive and semi-inclusive measurements.

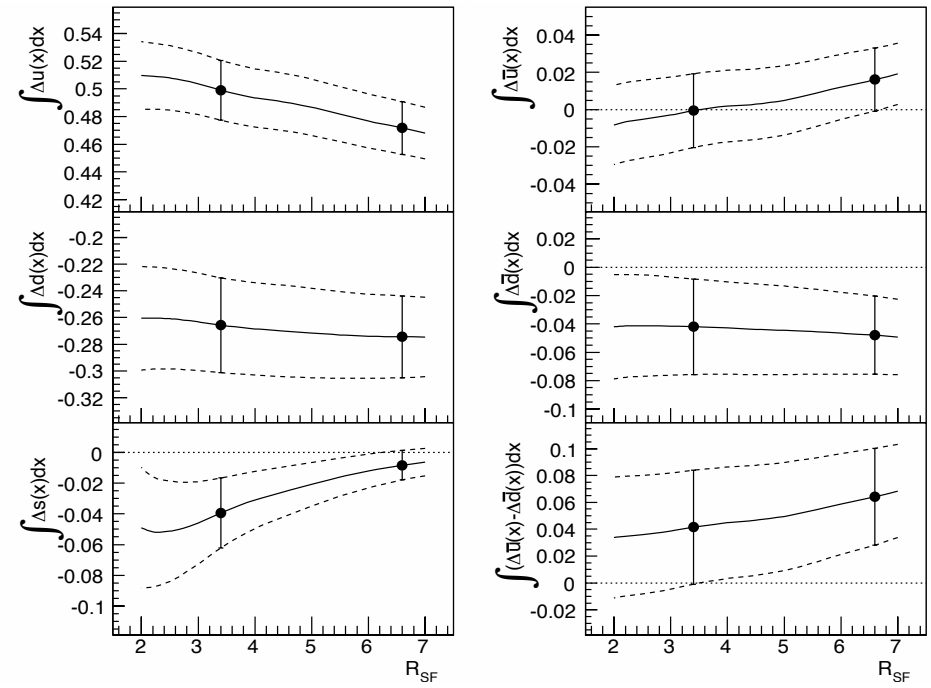

Figure 6.4: Dependence of quark polarization on fragmentation function values ($R_{SF} = D_{\bar{s}}^{K^+}/D_u^{K^+}$).

6.3 Summary and Conclusion

Since the quark fragmentation functions are universal objects that enter the computation of the cross sections of several processes (DIS, *pp* collisions, e^+e^- annihilation, Drell-Yann, ...), the best way to extract them is by performing a global QCD analysis. In the context of the DIS process, the contribution to a global fit will be the measurement of the so called "hadron multiplicities" which are related to the FFs in the QCD improved parton model picture.

Chapter 7

Hadron Multiplicities

The contribution of the spin of the strange quarks to the nucleon spin (Δs) remains an issue and a challenging question in polarized deep inelastic scattering process. While all inclusive measurements ($lN \to l'X$) converge to a negative value of Δs, all semi-inclusive measurements[1] ($lN \to l'hX$, $h \equiv \pi$,K,p), however, result in a slightly positive value. This discrepancy found between the two kind measurements could be due to several factors. An important one could be the assumption usually made in semi-inclusive measurements that strange quarks and antiquarks have the same polarizations, meaning that $\Delta s(x) = \Delta\bar{s}(x)$. However, the COMPASS collaboration rejected this possibility by examining in [19] this assumption which was found to be valid in the covered kinematic domain. Another crucial factor that can explain this discrepancy is the use of the quark fragmentation functions into hadrons which represent an essential ingredient in semi-inclusive measurements. Δs was found to be strongly dependent on the fragmentation function of strange quarks into kaons ($D_{\bar{s}}^{K^+}$) (cf chapter 6). Changing the latter by a factor two changes the moment of Δs by a factor four. Currently, the quark fragmentation functions into pions are known with a limited precision while the quark fragmentation functions into kaons are poorly known and need to be improved. In order to deepen our knowledge of the quark fragmentation process, high precision measurements have to be performed in high energy processes which involve final state hadron production. For this purpose, the hadron muoproduction was studied at COMPASS. COMPASS has the advantage of covering a wide kinematic domain and providing a huge statistics in addition to the particle identification facility which is ensured by the RICH detector. Finally COMPASS is the only running experiment which can perform measurements, with a high precision, in the small x region ($x \sim 10^{-3}$) where the contribution of the strange quark is the most pronounced.

Charge separated pion and kaon multiplicities were measured at COMPASS using 25 % of the 2004 data, collected by scattering a 160 GeV/c muon beam on a deuterium (^{6}LiD) target. The measurement was performed in bins of the kinematic variables x, Q^2 and z ($= E_h/(E_\mu - E_{\mu'})$), the latter being the relevant variable to study the fragmentation process. The analysis consists in three steps. In a first step, the "raw" pion and kaon multiplicities are extracted from experimental data as a function of the kinematic variables x, Q^2 and z (section 7.2). The second step consists in calculating the acceptance of the spectrometer (section 7.3.2) for each hadron type using a full MC chain. In the last step, the raw multiplicities are corrected for the evaluated acceptance as well as for radiative effects.

7.1 Hadron Multiplicity definition

The hadron multiplicity, experimentally defined as the averaged number of hadrons produced per deep inelastic scattering (DIS) event, is expressed in terms of the unpolarized parton distribution

[1] The inclusive measurement of Δs makes use of the first moment of the g_1 spin structure function ($\int_0^1 g_1(x)dx$). The latter is related to the contribution of spin of quarks of different flavors ($\int_0^1 dx g_1(x) = (\Delta u + \Delta\bar{u}) + (\Delta d + \Delta\bar{d}) + (\Delta s + \Delta\bar{s})$). Using the axial couplings from baryon β decays and SU(3) symmetry, one can deduce the contribution of the spin of strange quark to the nucleon spin. More details can be found in [3].

functions (PDFs) and the quark fragmentation functions into hadrons (FFs) in the QCD improved parton model. At LO, the differential hadron multiplicity is given by:

$$\frac{1}{\sigma^{DIS}(x,Q^2)}\frac{d\sigma^h(x,Q^2,z)}{dxdQ^2dz} = \frac{\sum_q e_q^2 q(x,Q^2) D_q^h(z,Q^2)}{\sum_q e_q^2 q(x,Q^2)} \tag{7.1}$$

where σ^{DIS} (σ^h) denotes inclusive (semi-inclusive) DIS cross section in the one-photon-exchange approximation and the sum ($\sum_q$) runs over light quarks (up, down and strange) and antiquarks. $q(x,Q^2)$ denotes the PDF of a quark of flavor q and $D_q^h(z,Q^2)$ denotes the fragmentation function which defines the mean number of hadrons of type h produced the fragmentation of a quark of flavor q and carrying an energy fraction $z \in [z, z+dz]$. The great power of the hadron multiplicity is the possibility to access to both PDFs and FFs due to the factorization theorem and to the tagging of the type of final state hadrons. At LO, the factorization of the hard-scattering subprocess and the soft hadronization process is expressed in the independence of the fragmentation functions on x, that is the fragmentation does not depend on the momentum fraction carried by the struck quark. The factorization thus allows to separate hard and soft processes by separating the x and z dependences in the hadron multiplicity definition. The separation between different quark flavors is possible due to the tagging of the type of final state hadron, the latter gives access to the flavor of the struck quark because the flavor of the struck quark and the type of the produced hadron are correlated. In order to extract the fragmentation functions, one can build a system of equations with n unknown fragmentation functions using Eq. 7.1. By assuming the knowledge of the parton distribution functions, the system can be solved.

7.2 Extraction of raw hadron multiplicities

The extraction of the raw hadron multiplicities (N^h/N^{DIS}) requires the extraction of the DIS events yields (N^{DIS}) and the yields of the produced hadrons (N^h) in bins of the kinematic variables x, Q^2 and z. To ensure the good quality of the analyzed data sample, several cuts are applied on the spill level to ensure an overall good performance of the spectrometer and the target. Additional cuts need to be applied on the event level in order to select the deep inelastic scattering domain, to avoid the resonance region and to ensure that all interactions occurred in the target material. Finally on the hadron level, some cuts are required to select only hadrons produced from the fragmentation of the quark which interacts with the beam and to reject hadrons which originate from other sources and contaminate the selected sample.

7.2.1 Spill selection

To ensure that physical measurement is not influenced by detector inefficiencies, a stability check [71] is performed in order to remove unstable experimental data. A selection based on the logbook [72] information is first achieved. It consists in removing all runs for which the beam or a magnet was not at its nominal setting. Runs affected by detector problems are not excluded from the reconstruction. For each run, a bad spill selection is performed and consists in removing individual spills where a detector problem is observed in the reconstructed data[2]. A spill is selected as bad if it deviates from the majority of other spills in at least one of three observables: "the number of reconstructed primary vertices per reconstructed event with secondary vertex", "the number of tracks in the primary vertex" and "the number of beam particles per reconstructed event". The bad spill list used in the present analysis is taken from [46].

7.2.2 Event Selection

Selected DIS events are required to have a reconstructed interaction point (primary vertex) to which a reconstructed track of the incoming muon and a reconstructed track of the scattered muon are associated. In some cases ($\sim 13\%$), where more than one primary vertex are reconstructed, the vertex with the maximum number of outgoing tracks is chosen. If two vertecies remain with the same number of outgoing tracks, the vertex with the smallest χ^2 is selected.

[2]The reconstructed data denote the experimental data which have been reconstructed (using the COMPASS reconstruction program) and contain interaction vertices, decay vertices, tracks for charged and neutral particles.

The primary vertex is required to be located within one of the two target cells. This requirement is ensured by several cuts:

- The Z position of the selected primary vertex is required to lie within one of the two target cells ($Z_V \in [-100\text{ cm}, -40\text{ cm}] \bigcup [-30\text{ cm}, 30\text{ cm}]$). Figure 7.1(a) shows the two cells as well as the gap between them. Note that the gap is filled with liquid helium, as a consequence, some events lie within the gap volume and are thus removed.

- The primary vertex is required to be within a radius of 1.4 cm from the target center in the plane perpendicular to the beam direction (the target cell has a radius of 1.5 ± 0.05 cm). The Y coordinate of the primary vertex is required to be smaller than 1 cm because the target cells are not fully filled at the top. These cuts delimit the target volume to a cylinder 1.4 cm and cut off 4 mm from the top. The transverse vertex distribution is shown in figure 7.1(b).

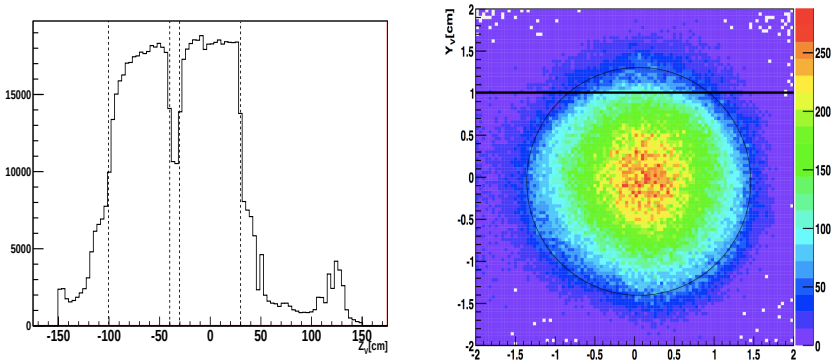

(a) (b)

Figure 7.1: (a) The longitudinal primary vertex distribution as a function of the Z_V position (the vertical lines delimit the two target cells [−100 cm, −40 cm] & [−30 cm, 30 cm]). (b) The primary vertex distribution in the plane perpendicular to the beam direction (the circle shows the target area with 1.4 cm of radius and the vertical line shows the Y_V cut).

The energy of the beam particle, which corresponds to the incoming reconstructed track associated to the primary vertex, is required to be in the range $[140, 180]$ GeV. The scattered muon is identified by requiring its reconstructed track to cross the second muon filter (MW2) and the hodoscopes of the selected trigger, to cross more than 30 radiation lengh and that the χ^2 of the track fit has to be better than 10. This is ensured by the COMPASS reconstruction program (CORAL). In addition, the scattered muon is required to cross both target cells such that both cells are exposed to the same beam flux. Although this requirement is not crucial for this analysis, it was applied to be consistent with the semi-inclusive analysis of single spin asymmetries. To select the kinematic domain, the following cuts are applied on the kinematic variables x, y, Q^2 and the invariant mass of the hadronic system W:

- The deep inelastic region is selected by the cut $Q^2 > 1$ [GeV/c]^2. This requirement selects the energy scale of deep inelastic scattering process.

- The fraction (y) of the lepton energy transferred to the virtual photon is restricted to be in the range $[0.1, 0.9]$. The cut $y > 0.1$ removes events with poorly reconstructed scattered muon and beam halo muons misidentified as scattered ones. The cut $y > 0.9$ removes events which are expected to have large radiative corrections (above 15%) and events with low μ' momentum. The low momentum μ' may come from pion decays and can be incorrectely identified as scattered muon.

- The covered x domain is restricted to $4.10^{-2} < x < 0.7$.

- A standard DIS cut on the invariant mass of the hadronic system $W \geq 3$ GeV is usually made in order to avoid the resonances region. However, due to the previous cut $y < 0.9$, the selected sample contains only DIS events with $W > 3$ GeV. In addition, the W range

[$\sim 3, \sim 5$] GeV is suppressed by the cut $y > 0.1$, as can be seen in figure 7.2(a). An explicit cut $W > 7$ GeV is applied in order to restrict the kinematic domain to a region where the acceptance estimated as a function of x and z is flat (especially for kaons, see section 9.15(c)). This rejects $\sim 25\%$ of DIS events in the region $0.1 < y < 0.18$, as can be seen in figure 7.2(b) where the number of DIS is drawn with and without the $W > 7$ GeV cut.

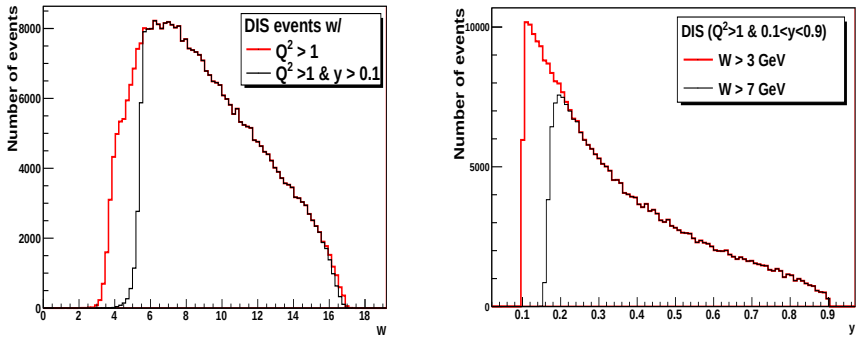

(a) (b)

Figure 7.2: (a) W distribution for DIS events before and after the cut $y > 0.1$. (b) y distribution for DIS events for two cuts: $W > 3$ GeV and $W > 7$ GeV.

Trigger selection: In order to select all deep inelastic scattering events, the events triggered by the inclusive middle (IMT) and the outer trigger (OT) systems - both purely inclusive - are selected. In order to prevent fake triggers the scattered muon track is required to have associated clusters from both stations of the hodoscopes that caused the trigger. The IMT covers the low Q^2 and low y region ($1 < Q^2 < 2.5$ & $y < 0.4$). The OT covers the high Q^2 and high y region ($Q^2 > 2.5$ & $y > 0.4$). $\sim 41\%$ of DIS events are triggered by the OT and $\sim 48\%$ of events are triggered by the IMT. The rest of events are accepted by both OT & IMT. The contribution from OT and IMT separately as well as from their sum is shown in figure 7.3.

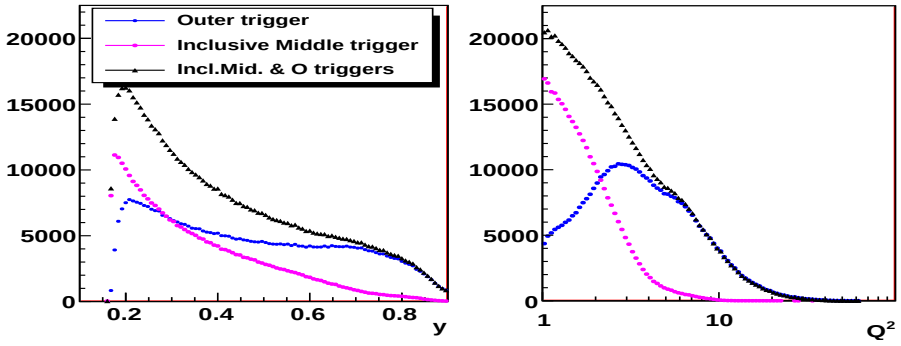

Figure 7.3: Composition of the inclusive trigger as a function of y and Q^2.

7.2.3 Hadron Selection

From the retained DIS events (cf. 7.2.2), all particles issued from the primary vertex are considered as hadron candidates except the scattered muon. Hadron candidates can also be: *i*) beam halo muons, *ii*) tracks created artificially by the reconstruction algorithm (ghost tracks), *iii*) electrons and positrons from photon conversion, *iv*) electrons from $e\mu$ scattering in the target, *v*) leptons and photons from hadrons decays. To ensure the good quality of the hadron sample, such tracks have to be rejected by applying the following cuts on hadron candidate tracks:

- The fractional energy $z = E_h/(E_\mu - E_{mu'})$ of the hadron candidate should satisfy the condition $z < 1$. This criteria rejects tracks for which the reconstruction quality is poor[3].
- The hadron track is required to have a hit in the detectors placed upstream ($z_{first} < 350$) and downstream ($z_{last} > 350$) of the $SM1$ magnet in order to avoid tracks reconstructed in the fringe field of SM1. Most of these tracks are poor quality tracks with a large probability to be ghost tracks.
- The hadron track is required to cross less than 30% of radiation length.
- The fractional energy z of the hadron candidate must be in the range [0.2, 0.85]. The cut $z > 0.2$ selects hadrons originating from the current fragmentation region ($\Leftrightarrow x_F > 0$). The requirement $z < 0.85$ ensures that exclusive production mechanisms do not contribute to the hadron sample.
- The allowed momentum range for hadrons is limited by the particle identification capabilities of the RICH detector. An upper cut of 50 GeV was applied because the separation between different hadron types cannot be achieved for $P > 50$ GeV. The lower momentum cuts for pion and kaon are 3 GeV and 10 GeV respectively and correspond to the identification thresholds (cf section 7.2.4).
- The angle between the hadron track extrapolated at the Z position of the RICH entrance ($Z = 615.6$ cm) and the beam direction is required to be in the range [10 mrad, 120 mrad]. The lower cut is to avoid the poorly efficient central part of the RICH. The upper cut is due to the limited range of particle identification in Monte Carlo simulation.

7.2.4 Particle identification

The type of final state hadron is an indispensable information because it is correlated to the flavor of the hadronized quark that interacts with the virtual photon. This information is ensured by the RICH detector (cf. section 4.3.2.3) which allows essentially to identify final state kaons since pions form $\sim 90\%$ of the sample of hadrons. Two main limitations of the RICH reduce the covered momentum range of identified particles. The first one corresponds to the momentum thresholds that condition the particle identifcation. With the refractive index $n \approx 1.0015$ of the used radiator gas (C_4F_{10}), the momentum threshold is 2.5 GeV/c for pions, 8.9 GeV/c for kaons and 17 GeV/c for protons. The second one is expressed in the high momentum region. The high momentum particles produce a Cherenkov light cones with similar Cherenkov emission angles ($\cos(\theta_c) \to 1/n$) such that particles cannot be identified. In the COMPASS case, the discrimination between pions and kaons cannot be achieved for $P > 50$ GeV/c. As a consequence, pions and kaons are identified in the momentum ranges $2.5 < P_\pi < 50$ GeV/c and $8.9 < P_K < 50$ GeV/c respectively. The dependence of the Cherenkov threshold on the momentum of the incident particle is shown in figure 7.4.
As stated in section 4.3.2.3, the RICH response is parametrized in terms of the likelihood functions which can be calculated for different mass hypotheses. The hadron type is then specified by comparing these likelihood functions. In the case of kaons, the corresponding likelihood is compared to the hypotheses: Background (L_K/L_{BG}), pion (L_K/L_π) and proton (L_K/L_p). For each hypothesis $X(BG, \pi, \mathrm{p})$, the factor of merit ($S/\sqrt{S+B}$) is calculated as a function of the likelihood ratio L_K/L_X. From the resulting distribution, a cut on the ratio is chosen such that the factor of merit is maximized. Similarly for pions, the corresponding likelihood is calculated and compared to the different hypotheses: background, kaon and proton. For the 2004 data, the following cuts were optimized [52]:

$$K^\pm \quad \text{identification}: \quad \mathrm{L}_\pi/\mathrm{L}_{\mathrm{BG}} > 1, \quad \mathrm{L}_\pi/\mathrm{L}_{\mathrm{K}} > 1, \quad \mathrm{L}_\pi/\mathrm{L}_{\mathrm{p}} > 1$$
$$\pi^\pm \quad \text{identification}: \quad \mathrm{L}_{\mathrm{K}}/\mathrm{L}_{\mathrm{BG}} > 1.24, \quad \mathrm{L}_{\mathrm{K}}/\mathrm{L}_\pi > 1.02, \quad \mathrm{L}_{\mathrm{K}}/\mathrm{L}_{\mathrm{p}} > 1$$

Figure 7.2.4 shows the likelihood ratios (L_K/L_{BG}, L_K/L_π). The vertical lines represent the cuts applied on the corresponding ratios.

[3] A particle track is reconstructed by fitting the clusters detected by several devices. A cluster, associated to track in one detector plane, corresponds to the combination of hits (interaction points) provided by adjacent readout channels of the detector.

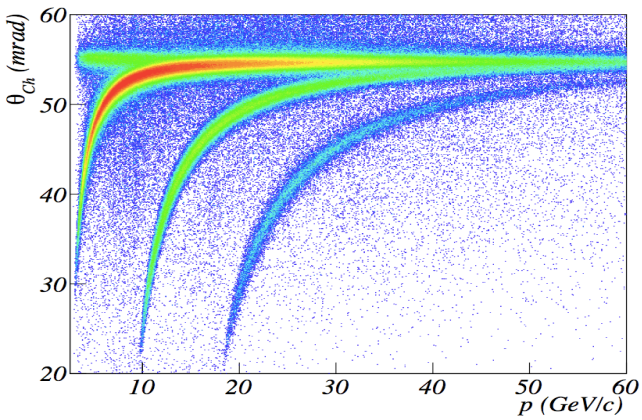

Figure 7.4: Momentum dependence of the Cherenkov angle for different hadron types (pion, kaon and proton).

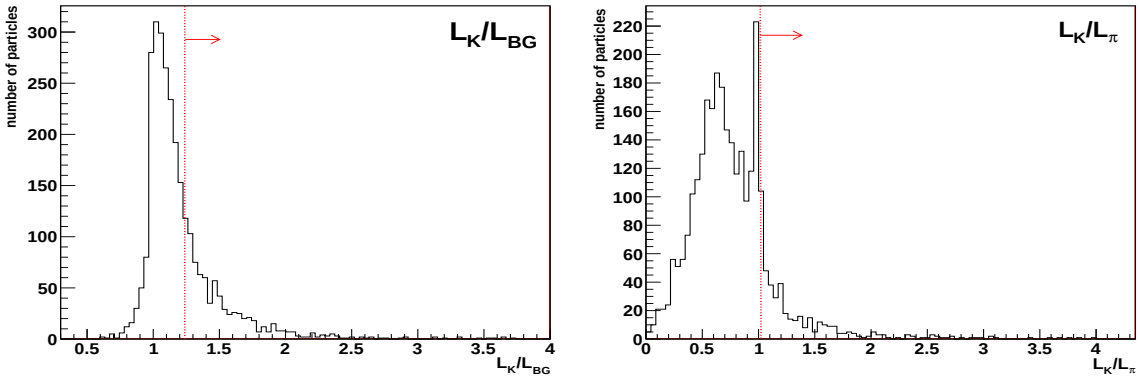

Figure 7.5: Likelihood ratios for kaon (L_K/L_{BG}, L_K/L_π). The vertical lines represent the cut applied in the analysis.

7.2.5 Final Statistics

Four weeks of the full 2004 data set were analyzed in this work. They consist of a total statistics of about 5.5×10^8 interaction events. After applying all cuts discussed in section 7.2.2, the final data sample contains almost 5.3×10^6 deep inelastic scattering (DIS) events. The statistical effect of the selection cuts on the initial data sample is presented in table 7.1 for DIS events.

The distributions of the selected DIS events are shown as a function of the kinematic variables x, y, Q^2 and W in figure 7.6, the correlation between x and Q^2 for the selected DIS events is shown in figure 7.7 (right) and finally the mean values of Q^2 are shown as a function of x plot in figure 7.7 (left).

Table 7.2 shows the effect of the quality cuts (section 7.2.3) applied for the selection of final state hadrons (for one week of data). The final number of DIS events as well as the number of charged pions and kaons are presented in table 7.3. They correspond to the raw numbers without any correction.
After all needed selections (sections 7.2.1-7.2.4), the number of DIS events (N^{DIS}) and the number of final state hadrons (N^h) can be determined in bins of x, Q^2 and z. The raw hadron multiplicities (M^h) are calculated in two-dimensional binning, (x, z) and (Q^2, z), as given in Eqs 7.2 and 7.3.

$$M^h(x,z) = \frac{N^h(x,z)}{N^{DIS}(x)} \tag{7.2}$$

Cuts for DIS event selection	#events	Fraction(%)	Reduction(%)
All Events	553719420	100	–
w/ BestPrimaryVertex.	523505179	94.54	5.46
w/ Reconstructed μ'	291156186	52.58	44.38
$140 < E_{beam} < 180$	288813825	52.16	0.79
PaAlgo::InTarget(1.4, 1.0)	156609848	28.28	45.77
PaAlgo::CrossCells(1.4, 1.0)	147919375	26.71	5.55
$Q^2 > 1$	19071630	3.44	87.11
$0.1 < y < 0.9$	12236073	2.21	35.84
Trigger selection	6993382	1.3	42.8
$W > 7GeV$	5306793	1	24.12
$4.10^{-3} < x < 0.7$	5297784	0.95	0.2

Table 7.1: Statistics of DIS events for all cuts. The first column shows the applied cuts; the second one shows the number of events remaining after each cut; the third one shows the fraction of remaining events and the last one shows the fraction of rejected events with respect to previous cut. The initial number of events denoted by "All events" corresponds to the events which originate from a list of good spills as defined in [46].

Cuts for hadron selection	# hadrons	Fraction(%)	Reduction(%)
All hadrons	12901887	100.0	0.00
not a μ'	9017509	69.89	30.11
$z < 1$	9011485	69.85	0.07
$z_{first} < 350$	8973744	69.55	0.42
$z_{last} > 350$	8714898	67.55	2.88
$XX0 < 30$	8687467	67.33	0.31

Table 7.2: Statistics of Hadrons after all quality cuts. The initial number "All hadrons" correspond to all hadron candidates associated to the primary interaction vertex of retained DIS events.

DIS events	h^+	h^-	$\pi^+(P > 3GeV/c)$	$\pi^-(P > 3GeV/c)$	$K^+(P > 10GeV/c)$	$K^-(P > 10GeV/c)$
5297784	1421201	1175989	1082139	959532	199299	135733

Table 7.3: Statistics of DIS and SIDIS events obtained from the "raw" data. The numbers correspond to the final statistics used in the analysis.

$$M^h(Q^2, z) = \frac{N^h(Q^2, z)}{N^{DIS}(Q^2)} \tag{7.3}$$

7.3 Correction for acceptance and radiative effects

The raw multiplicities are measured in the COMPASS acceptance, defined by geometrical limitations of the spectrometer as well as by detector inefficiencies. In order to compare the measurements with existing ones as well as with theoretical predictions, the measured raw multiplicities must be corrected for the limited COMPASS acceptance using a Monte Carlo simulation (section 7.3.3). In addition, they must be corrected for radiative effects (section 7.3.1) which introduce a systematic bias of the measured kinematics with respect to the true ones.

7.3.1 QED Radiative Effects

In the first order of QED, the muon interacts with the nucleon by the exchange of a virtual photon. The kinematics of the entire scattering process is reconstructed using the known energy of the

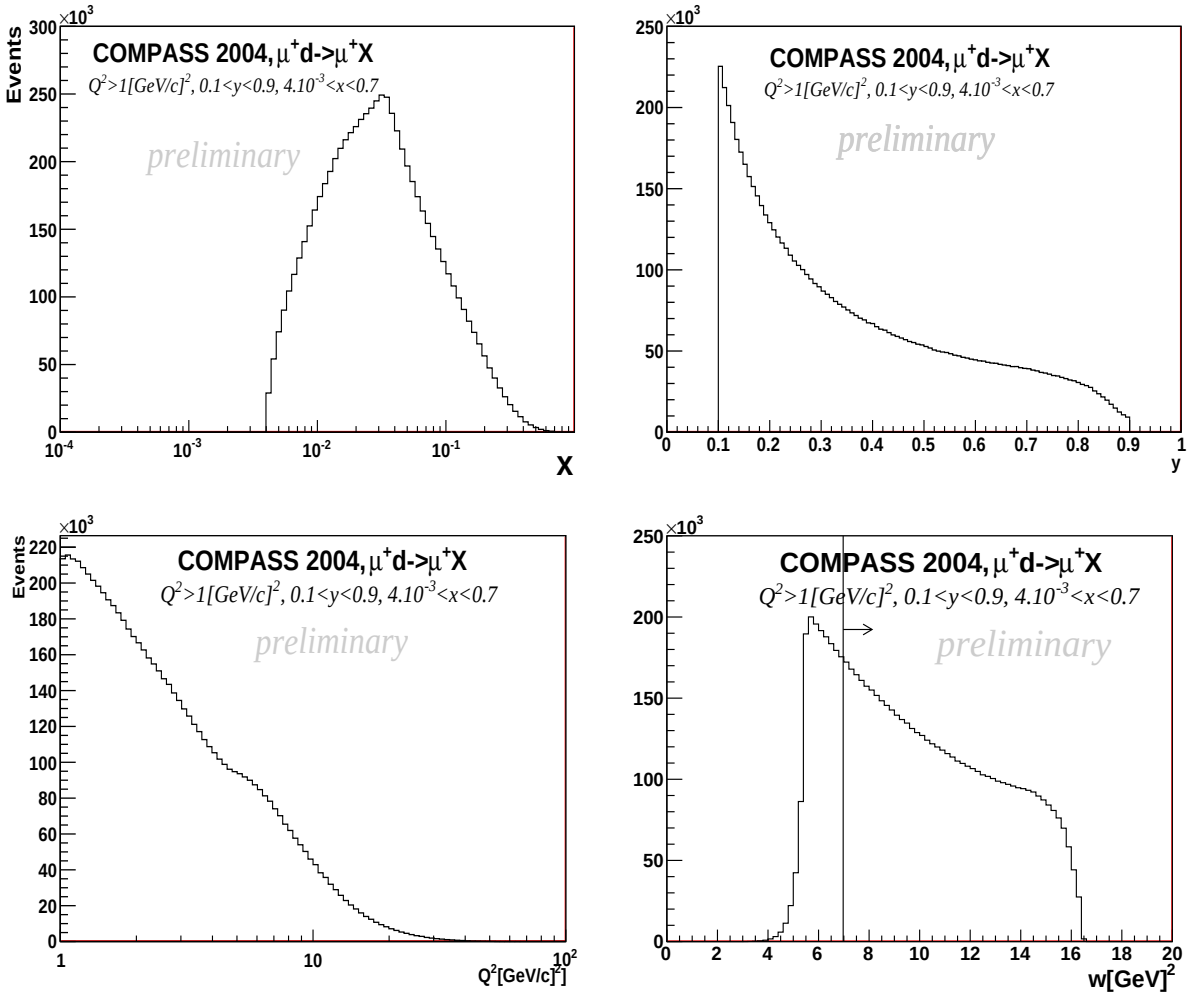

Figure 7.6: x, y, Q^2 and W distributions of the selected DIS events.

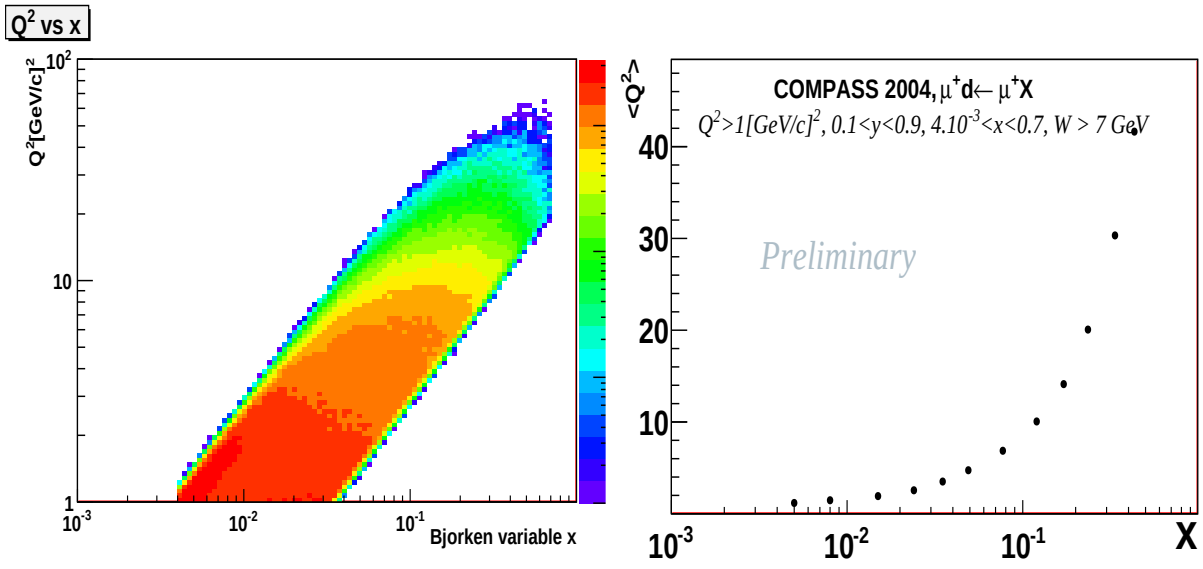

Figure 7.7: Left: Q^2 versus x for the selected DIS events. Right: Mean values Q^2 versus x.

incident muon and the properties of the scattered muon (namely the energy E' and the scattering angle) which are measured in the spectrometer. However, in addition to the first order process, there are infinite possibilities for higher order QED processes which introduce a systematic bias of the observed kinematics with respect to the true kinematics. Such contributions come essentially from initial and final state radiation, from vertex corrections and vacuum polarization, shown in figure 7.8. These effects were accounted for by using the radiative correction factor defined as:

$$\eta(x,y) = \frac{\sigma_{1\gamma}}{\sigma_{measured}} \tag{7.4}$$

Here, $\sigma_{1\gamma}$ denotes the cross section in the one photon exchange approximation and $\sigma_{measured}$ denotes the measured cross section which includes radiative effects. The radiative corrections are taken from precalculated tables given for different target types (for more details see [47]). The region $y > 0.8$ ($\Leftrightarrow 0.004 < x < 0.01$) is the most affected by radiative effects with a corrective factor of the order of $10 - 15\%$. For lower y values, the correction factor is negligible (less than 1%). The radiative correction factor is applied for experimental data.

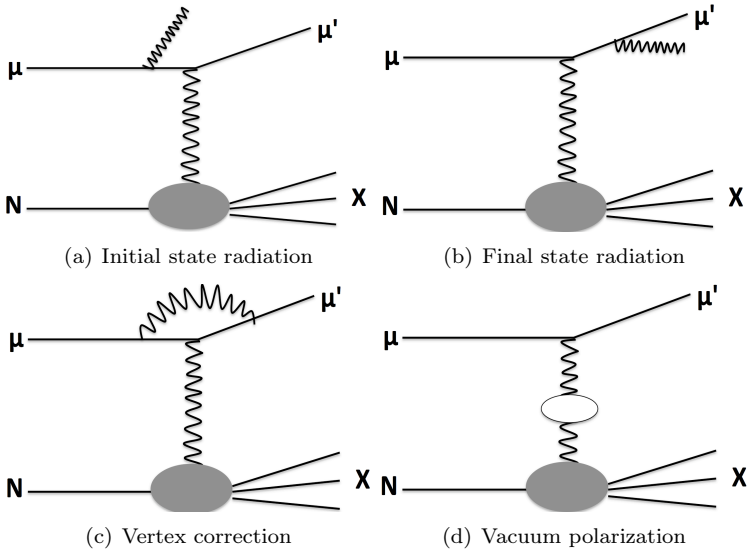

(a) Initial state radiation (b) Final state radiation

(c) Vertex correction (d) Vacuum polarization

Figure 7.8: Higher order QED contributions to the DIS process.

7.3.2 Acceptance Study

After the interaction occurs in the target, the final state hadrons leave the target volume. A fraction of the produced hadrons, which fall inside the solid angle covered by the COMPASS spectrometer and within the covered energy range, is detected. While traversing the detectors, the produced hadrons are subject to interactions with material which affect the energy and the direction of the hadron track. This causes deviations between the measured and the true properties of the track. All these effects have to be corrected for by calculating the spectrometer acceptance using a Monte Carlo (MC) simulation. The latter is based on models and parametrization used to simulate many aspects that affect experimental results but cannot be calculated analytically.

7.3.3 Monte Carlo Simulation

The Monte Carlo simulation is based on models and parametrization used to simulate the physical process of interest (deep inelastic scattering in this case) in an analytical way. Three steps are needed to build a complete Monte Carlo chain:

- Deep Inelastic Scattering events generation in the appropriate kinematic domain and simulation of the quark fragmentation into hadrons.
- Simulation of the COMPASS apparatus response.
- Reconstruction of DIS events and hadrons tracks.

7.3.3.1 DIS event generation

The first step in any Monte Carlo production is the generator program used to simulate the physical process of interest. In the presented analysis, the deep inelastic scattering is the process of interest and is simulated using LEPTO generator. This latter is based on the leading order electroweak cross section for the basic lepton-quark process and on the Lund model (as implemented in the JETSET [48] package) for the hadronization of the ensuing system into its final state hadrons. The generation of a DIS event consists of several steps:

- To generate the process of interest, the starting point is to choose the lepton and the nucleon momenta. For the lepton, the momentum is randomly chosen according to a simulated distribution of the beam energy. For the nucleon, the momentum of the nucleon is zero. In addition, the type of the nucleon (proton or neutron) is chosen randomly with the ratio 1/2:1/2.

- The two variables, in term of which the differential cross section is expressed, are randomly chosen in the corresponding phase space. Note that the choice of the two independent variables depend on the desired process to simulate. Other combinations of variables can be specified using the LST option.

- The flavor of the "struck" quark is chosen using the parton distribution functions (defined as the probability to find a quark or anti-quark of specific flavor carrying a fraction x of the nucleon momentum for the corresponding Q^2). The MSTW [11] LO parametrization is chosen for two reasons. Firstly, it is consistent with the LO approximation of the LEPTO generator. Secondly it is consistent with the F_2 structure function measurement by the NMC (since the NMC experiment covered the same kinematic domain as COMPASS).

- The interaction between the lepton and the quark is simulated according to the electroweak cross section. The final state contains the struck quark as well as the nucleon remnant, defined as the rest of quarks which did not participate in the interaction.

- All quarks in the final state hadronize into final state hadrons using the Lund model (see section 3.1.2). Two important sets of the JETSET parameters play an essential role in the hadronization process. The first set includes the parameters a (PARJ(41)) and b (PARJ(42)) which enter the Lund symmetric fragmentation function (Eq. 7.10). The second set includes the parameters PARJ(21), PARJ(23) and PARJ(24), used to simulate the transverse momentum of the hadron as a gaussian distribution with non−Gaussian tails [48]. The default values of these parameters were initially adjusted to describe the LEP (Large Electron and Positron Collider) data. Since COMPASS has a different kinematic regime, they have been optimized to better describe COMPASS data. The tuned values are given in section 7.3.3.4.

- the decay of unstable particles into stable particles is simulated according to the experimentally measured branching ratios.

Note that LEPTO includes the parton shower approach in order to take into account higher order QCD effects. In DIS, the struck quark can emit partons before and after the absorption of the virtual photon giving rise to initial and final parton shower respectively. In the incoming nucleon, the parton close to mass-shell initiates the parton shower where, in each branching, one parton becomes increasingly off-shell and the other is on-shell or has a time-like virtuality. The first parton interacts with the virtual photon and turns into a quark which is either on-shell or has a time-like virtuality. In the latter case, the parton shower starts and continues until all partons are on-shell.

7.3.3.2 MC Simulation of the spectrometer

The output of the generator cannot be used for a comparison with experimental data. Further effects, related to the apparatus, have to be taken into account. Depending on the kinematic regime, only a fraction of the final state particles propagate through the spectrometer. While

traversing the spectrometer, they may interact with detector (and target) material before their kinematic properties can be measured. In addition, the reconstructed track properties (momentum, angle, particle type, ...) are affected by inefficiencies, due to imperfections of detectors, like the limited detector resolution and efficiency, misidentifications or even complete particle loss. All these effects biase the track reconstruction and must be taken into account when simulating the apparatus.

The experimental setup is simulated by a program called COMGeant. It is based on the Geant toolkit and contains a description of the detector size and material, the interactions of particles (produced by LEPTO) with this material and the response of the detectors, the description of the magnetic fields and their impact on charged particles, etc. The COMGeant output contains the response of the detector components such as the signals from the individual wires of the tracking detectors. It is thus similar to the detector responses recorded from the experimental data and contains in addition the Monte Carlo information such as the true particle type and the originally generated particle kinematics. The RICH detector, responsible for particle identification, plays an essential role in this analysis. The response of the RICH is modeled by the so called "performance tables" [**?**]. These tables give both the efficiency and the purity for the identification of pion, kaon and proton as a function of two variables, the momentum p and and the angle at the RICH entrance θ_{RICH}. They are built, starting from a calibration based on real data. To determine the efficiency and purity for pion identification, π^+ and π^- originating from the decay of K^0 are used. Similarly kaons originating from the ϕ decay are used. Since the sample used for this RICH calibration does not contain particles emitted at angles above 120 mrad, a similar cut has been applied also on the real data sample. These tables are calculated without statistical or systematic errors.

7.3.3.3 MC Reconstruction of DIS events and hadron tracks

The COMGeant ouput can be fed into CORAL which is used to decode the detector responses of the experiment. CORAL has two interfaces: one for the real experiment and another one for Monte Carlo simulation data. In the latter case, the same experimental conditions are simulated using the efficiencies of the detectors as calculated from real data. The detector responses are used to reconstruct the vertices and tracks. The three parts of the full Monte Carlo chain (LEPTO + JETSET, COMGeant, CORAL) are summarized in figure 7.9 where the first part is splitted into two separated steps: LEPTO & LUND(JETSET).

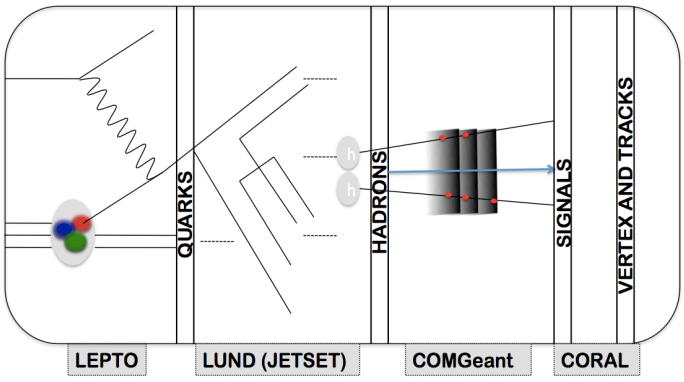

Figure 7.9: Shematic view of the full Monte Carlo chain divided into four steps. The first step, labeled "LEPTO", consists on generating DIS events by scattering muons off nucleon target using the LEPTO generator. After the interaction, the final state contains free quarks and gluons which confine later into hadrons via the fragmentation process. The quark fragmentation into hadrons is simulated in the second step using the LUND model. Later, the final state hadrons propagate inside a simulation of the spectrometer. This is performed in the third step using the COMGeant program and results in a set of hits in the detector planes. The last step consists on transferring the hits into vertecies and tracks. This last step is done using the COMPASS reconstruction program CORAL.

7.3.3.4 Tuning of JETSET fragmentation parameters

Two different tunings of the JETSET fragmentation parameters (table 7.4) were considered: the "default" one (default values in JETSET) and the "high P_T" one [49] (optimized for the COMPASS high p_T hadron production in deep inelastic scattering).

Tunings	PARJ(41)	PARJ(42)	PARJ(21)	PARJ(23)	PARJ(24)
Default Tuning	0.3	0.58	0.36	0.01	2
high P_TTuning	0.025	0.075	0.34	0.04	2.8

Table 7.4: Comparison of fragmentation parameters in "default" and "high P_T" tunings.

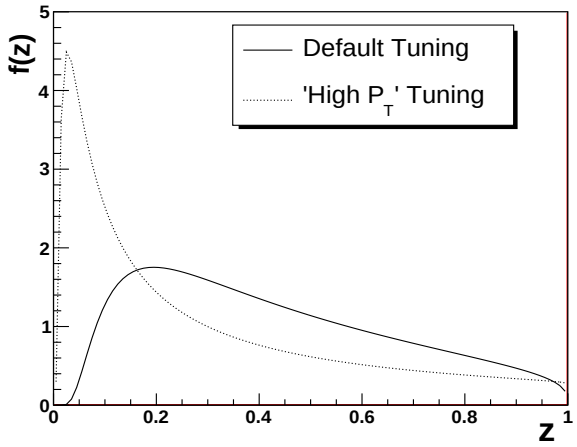

Figure 7.10: The symmetric Lund fragmentation function (Eq. 7.10) for the default tuning and the high P_T tuning.

Figure 7.10 shows the Lund fragmentation function (Eq. 7.10) as a function of z for both tunings. The high P_T tuning favors the fragmentation of quark into final state hadrons with a smaller fractional energy z.

7.3.3.5 Particle identification in the Monte Carlo

The response of the RICH detector in the Monte Carlo simulation is parametrized by the "performance tables". They provide the (mis)identification probability $P^{t\to i}$, i.e. the probability that a particle of true type t is identified as type i. The table element $P^{t\to i}$ is defined as the ratio of the number of particles of true type t which are identified as a type i normalized by the total number of particles of true type t. Since the RICH performance depends on the phase space of particles, the (mis)identification probabilities are calculated in bins of the momentum P of the hadron track and its polar angle (with respect to the beam axis) evaluated at the RICH entrance ($Z_{RICH} = 615.6$ cm). They are determined from experimentally reconstructed pions and kaons produced by K^0_S and ϕ-mesons decay ([**?**]). The definition of the matrix elements is given in the following:

$$P^{K\to\pi} = \frac{N^{K\to\pi}}{N_K} = \frac{N_\phi(K\pi)}{N_\phi(KH)} \qquad P^{\pi\to\pi} = \frac{N^{\pi\to\pi}}{N_K} = \frac{N_{K^0_S}(\pi\pi)}{N_{K^0_S}(\pi H)}$$

$$P^{K\to K} = \frac{N^{K\to K}}{N_K} = \frac{N_\phi(KK)}{N_\phi(KH)} \qquad P^{\pi\to K} = \frac{N^{\pi\to K}}{N_K} = \frac{N_{K^0_S}(\pi K)}{N_{K^0_S}(\pi H)} \tag{7.5}$$

The full 2004 statistics were used to determine the RICH performance tables in a fine binning in momentum and polar angle. Since a part of 2004 data was used for the hadron multiplicities

extraction, the performance tables were also determined for the reduced sample and found to be compatible with those determined from the full statistics (figure 7.11. The elements of the performance table ($P^{t\to i}$) are determined without statistical or systematic errors. Only the values of $P^{t\to i}$ are used in the particle identification.

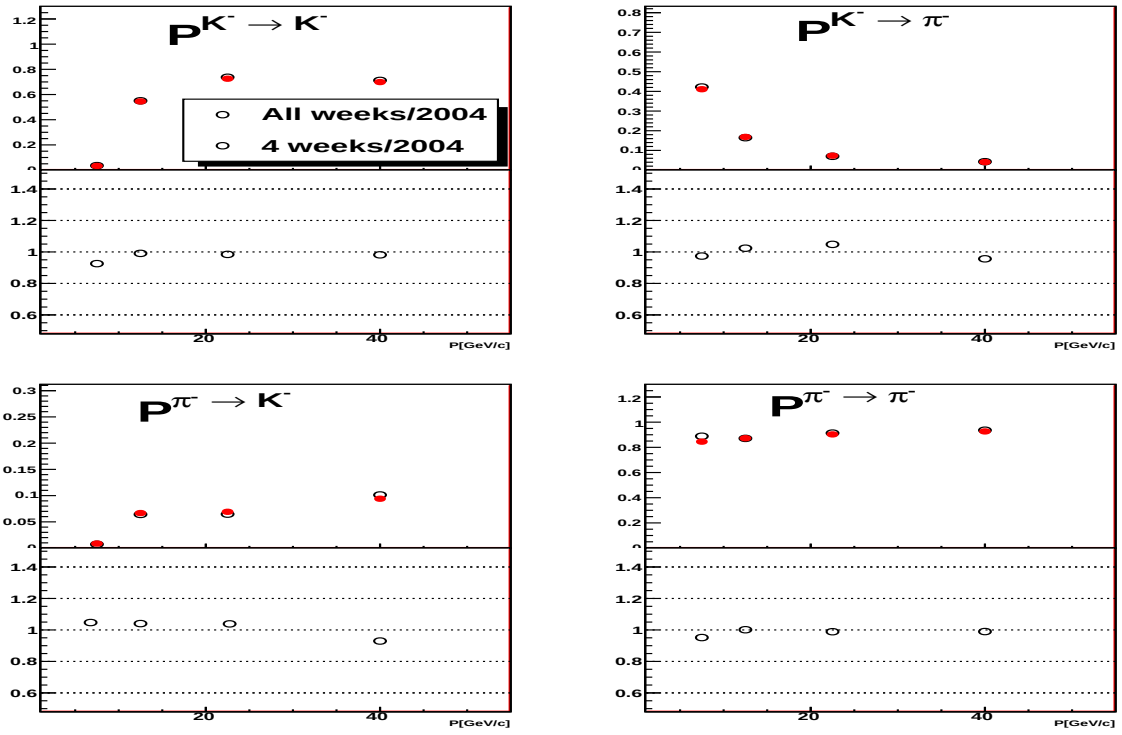

Figure 7.11: RICH performance table for negative hadrons: In the upper row are shown the (Mis)identification probabilities as a function of momentum extracted from all 2004 data (red markers) and from only 4 weeks (open markers). In the lower row is shown the ratio between the two distributions (4 weeks/All weeks).The elements of the performance table ($P^{t\to i}$) are determined without statistical or systematic errors.

7.3.3.6 Monte Carlo Production

Two Monte Carlo samples, each of $\sim 14 \cdot 10^7$ (with respect to $\sim 5 \cdot 10^6$ real data) DIS events, have been produced in the kinematic domain $Q^2 > 0.05$ [GeV/c]^2, $0.05 < y < 0.95$, $W > 0$ GeV/c and $10^{-4} < x < 0.99$. The kinematic range used in the DIS events generation was chosen larger than the one used in the analysis in order to take into account the smearing effects. The LO MSTW 2008 [11] parametrization was chosen for unpolarized parton distribution functions (PDFs) because of its validity domain ($10^{-6} < x < 1$, 1 [GeV/c]^2 $< Q^2 < 10^9$ [GeV/c]^2) which is suitable for the COMPASS phase space. It has been taken from the PDFs library LHAPDF (**L**es **H**ouches **A**ccord **PDF**s) [54]. The quark fragmentation process was simulated using the previously defined tunings for the JETSET fragmentation parameters (table 7.4). While the default tuning was used in the first MC sample, the high p_T tuning was used in the second. The longitudinal to transverse cross section ratio, R ($\equiv \sigma_L/\sigma_T$), which is neglected in the first sample, is taken into account in the second one using the longitudinal structure function F_L in LEPTO. The latter has an effect in the low-x region. In addition to F_L, the parton shower mechanism included in LEPTO was enabled in the second MC sample because it improves the descrption of the hadron transverse momentum [49]. The Monte Carlo sample produced using the default tuning was used in the systematic error studies.

7.3.3.7 Comparison of Data with Monte Carlo simulation

The comparison between experimental data and reconstructed MC data for inclusive DIS events ($\mu N \rightarrow \mu' X$) is shown in figure 7.12 for inclusive kinematic variables x, y ,Q^2 and W. Both Monte Carlo samples describe reasonably well the experimental data.

The comparison of the experimental data with reconstructed MC data for semi-inclusive DIS events ($\mu N \rightarrow \mu' h X$) is shown, as a function of the variables z, p_T and P, in figures 7.13-7.15 for the two tunings (table 7.4). The high p_T tuning (plot on the right) improves the data description, especially the P_T distribution (figure 7.13) as expected, since this set of fragmentation parameters had been optimized to well describe the p_T distribution. The high P_T tuning gives a better description of data also for p and for z which is the most relevant variable in the fragmentation process. Therefore, the high P_T tuning is used in the present analysis.

7.3.4 Acceptance Calculation

The acceptance correction is the crucial part of this analysis since it corresponds to the largest correction of the raw hadron multiplicities. The acceptance is calculated using a Monte Carlo simulation (section 7.3.3) of the physical process under study. For a physical quantity of interest M, the acceptance is defined as the ratio of reconstructed (M^{Rec}) to generated (M^{Gen}) M. The reconstructed MC is treated similarly to experimental data and the same selection cuts are applied in both cases (experimental data and reconstructed MC). Two methods of acceptance calculation, Method I (section 7.3.4.1) and Method II (section 7.3.4.2) are presented in the following. They differ in the manner of accounting for smearing (bin migration) effects.

7.3.4.1 Method I

This method [73] estimates acceptance and smearing effects using a "smearing matrix" defined, for DIS events[4], as:

$$S(i_r, i_g) = \frac{N^R(i_r, i_g)}{N^G(i_g)} \tag{7.6}$$

i_r (i_g) denotes the index of the kinematic bin where falls the reconstructed (generated) kinematic variable of interest v[5], $N^G(i_g)$ the number of generated events in a generated kinematic bin i_g, $N^R(i_r, i_g)$ the number of reconstructed events for which the reconstructed variable falls in bin i_r while the generated value falls in bin i_g. The indices run

$$i_r = 1, ..., N$$
$$i_g = 0, ..., N$$

N corresponds to the number of kinematic bins. The additional bin $i_g = 0$ contains events which would have been excluded from the sample by the original kinematics but migrate into the selected phase space due to the reconstruction procedure. The generated and the reconstructed inclusive and semi-inclusive DIS events can be related via the corresponding smearing matrices by:

$$N_h^R(i_r) = k \sum_{i_g=0}^{N} S_h(i_r, i_g).N_h^G(i_g) \tag{7.7}$$

$$N_{DIS}^R(i_r) = k \sum_{i_g=0}^{N} S_{DIS}(i_r, i_g).N_{DIS}^G(i_g) \tag{7.8}$$

where k denotes the experimental luminosity multiplied by a normalization constant. Since the semi-inclusive sample is a subset cancels in the ratio of the of the reconstructed hadron yields (Eq. 7.7) to the DIS events (SIDIS) yields (Eq. 7.8), which define the reconstructed multiplicities:

[4]The same definition is used for semi-inclusive DIS events

[5]The variable of interest is the variable as a function of which the acceptance is calculated. It can be any kinematic variable as x, Q^2, z, W,...

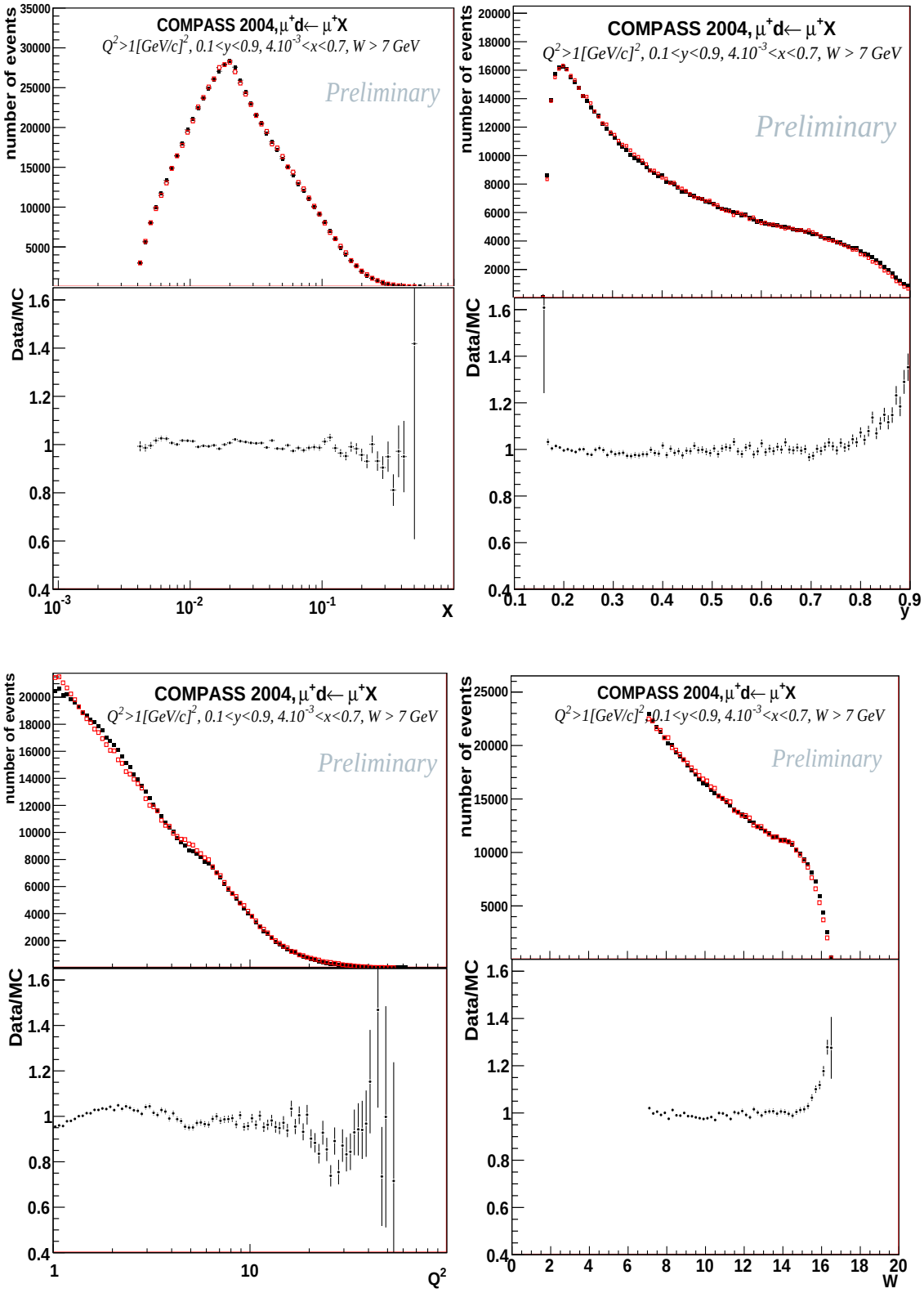

Figure 7.12: Comparison of raw data (black marker) corrected for radiative effects, and reconstructed MC data (red marker) for inclusive variables x, y, Q^2 & W. The upper row shows the kinematic distributions (normalized to their integrals) while the lower row shows the ratio Data/MC.

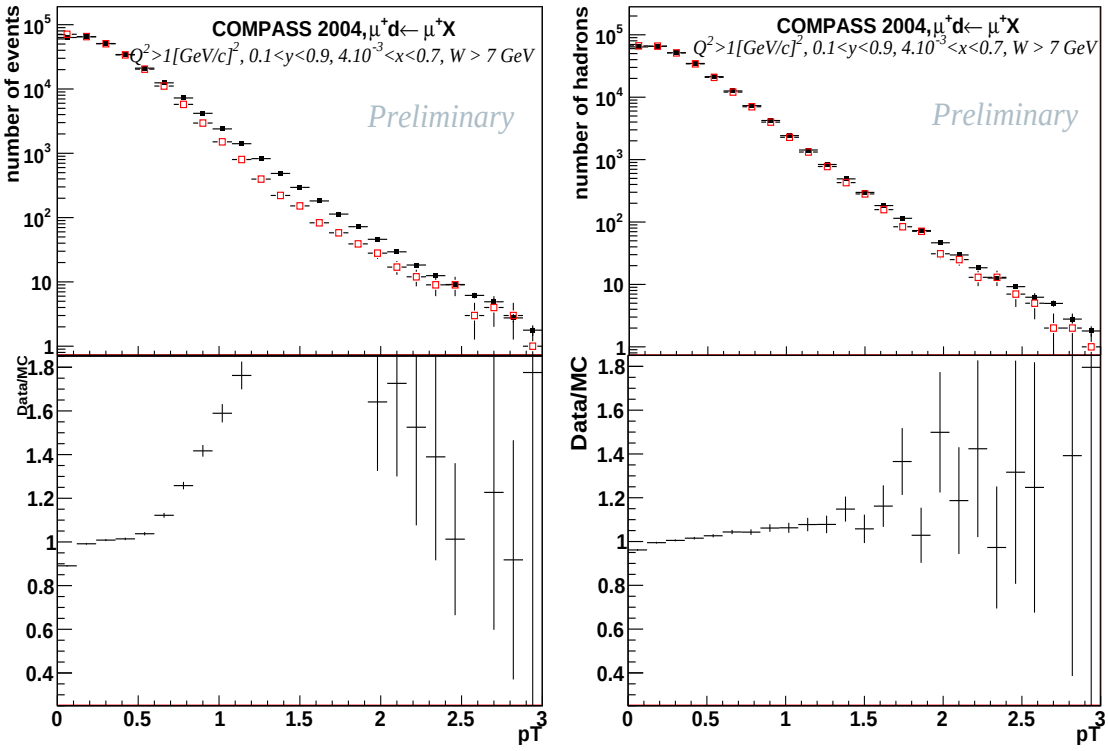

Figure 7.13: Upper row: Comparison of raw data (black) (corrected for radiative effects) and reconstructed MC data (red) for the transverse momentum P_T in the interval [0,3] for the default (left) and the high P_T (right) tuning. Lower row: Ratio Data/MC.

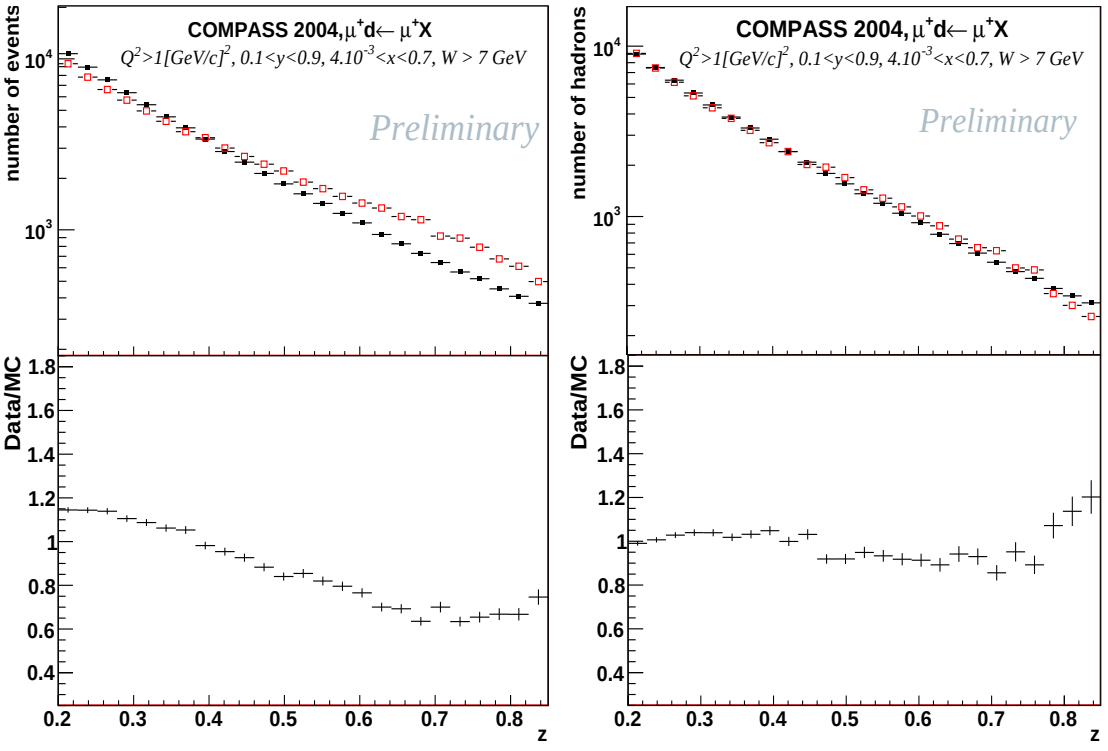

Figure 7.14: Upper row: Comparison of raw data (black, corrected for radiative effects) and reconstructed MC data (red) for the z variable in the range [0.2,0.85] for the default (left) and the high P_T (right) tuning. Lower row: Ratio Data/MC.

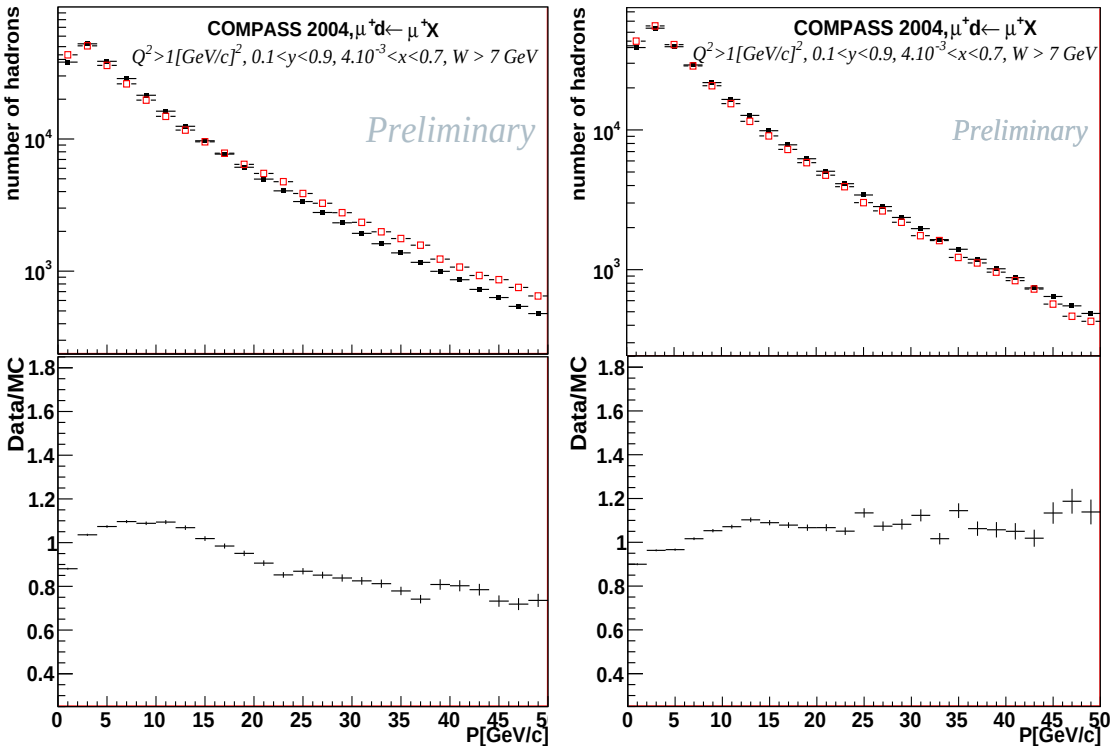

Figure 7.15: Upper row: Comparison of raw data (black) (corrected for radiative effects) and reconstructed MC data (red) for the momentum P in the range [0,50] for the default (left) and the high P_T (right) tuning. Lower row: Ratio Data/MC.

$$\frac{N_h^R(i_r)}{N_{DIS}^R(i_r)} = \frac{\sum_{i_g=1}^{N} S'_h(i_r,i_g)N_h^G(i_g) + S_h(i_r,0)N_h^G(0)}{\sum_{i_g=0}^{N} S_{DIS}(i_r,i_g).N_{DIS}^G(i_g)} \tag{7.9}$$

where $S'_h(i_r,i_g)$ results from S by separating the additional bin $i_g = 0$ from the other. By inverting the square matrix S'_h, one can derive the original number of hadrons (Eq.7.10) and consequently the original multiplicities (Eq.7.11).

$$N_h^G(i_g) = \sum_{i_r=1}^{N} [S'_h]^{-1}(i_g,i_r)\left[M_h^R.N_{DIS}^R(i_r) - N_h^R(i_r,0)\right] \tag{7.10}$$

$$M_h^G(i_g) = \frac{N_h^G}{N_{DIS}^G}(i_g) = \frac{1}{N_{DIS}^G(i_g)}.\sum_{r=1}^{N}[S'_h]^{-1}(i_g,i_r)\left[M_h^R.N_{DIS}^R(i_r) - N_h^R(i_r,0)\right] \tag{7.11}$$

Finally, one must note that this equation is valid if the Monte Carlo simulation reproduced correctly the unpolarized deep inelastic scattering cross section.

7.3.4.2 Method II

While Method I takes into account acceptance and smearing effects separately, Method II takes into account both acceptance and smearing effects in parallel in the correction of hadron multiplicities. Using Method II, the correction factor is defined in each kinematic bin i, covering the range $v_i \in [v_{i,1}, v_{i,2}]$, as the ratio of reconstructed over generated hadron multiplicity:

$$\epsilon_i = \frac{M_{MC}^R(i_r)}{M_{MC}^G(i_g)} \tag{7.12}$$

where i_r (i_g) denotes the index of the kinematic bin where falls the reconstructed (generated) variable. The raw hadron multiplicities (extracted from experimental data, Eqs 7.2 and 7.3) are then corrected for acceptance and smearing effects in each bin by dividing by the acceptance correction factor:

$$M^h_{cor}(i_r) = \frac{M^h_{data}(i_r)}{\epsilon_{i_r}} \tag{7.13}$$

To determine the best method of acceptance calculation, a test was performed for both methods. For this purpose, two Monte Carlo samples were used: one sample to estimate acceptance and smearing effects while the other to simulate experimental data, i.e. used to extract raw hadron multiplicities. The key point is that original (generated) multiplicities are known, in contrast to the real case. The raw multiplicities, simulated by one of the MC samples, are then corrected for acceptance and smearing effects, estimated from the other MC sample. If the correction method takes into account correctly all effects, the corrected and the generated multiplicities should be identical. Otherwise, the method is not valid.
This test was done by calculating the acceptance correction and the multiplicities as a function of (x,z). While method II gave identical values for the corrected and the generated multiplicities, method I gave corrected values different by $\sim 5\%$ from the generated multiplicities, almost in the last z bin. From this check, the method I was rejected and method II was used to calculate the acceptance correction.

7.4 Results for Acceptance

The acceptance correction factor are calculated according to method II for each hadron type ($h \equiv \pi^+$, π^-, K^+, K^-) in bins of the kinematic variables x, Q^2 and z. Figure 7.16(a) shows the acceptance for charge separated pions and kaons in bins of x and z as follows:

$$\text{4 z bins} : 0.2, 0.3, 0.45, 0.65, 0.85$$

$$\text{12 x bins} : 0.004, 0.006, 0.01, 0.02, 0.03, 0.04, 0.06, 0.1, 0.15, 0.2, 0.3, 0.4, 0.7 \tag{7.14}$$

For pions ($\pi^\pm$), the acceptance reaches a maximum value of $\sim 60\%$ in the x range $[0.01, 0.1]$ for $z \in [0.2, 0.65]$ while it decreases to values smaller than 10% at small x ($x > 0.01$) and high z ($z > 0.65$). The shape of the acceptance distributions is due to the cuts which were applied in the selection of events and hadrons and is well understood. For kaons, the acceptance is $\sim 50\%$ at small x and z and can reache $\sim 70\%$ for high x ($x > 0.1$) and z ($z > 0.45$), as shown in figure 7.16(a). Similarly to pions, the shape of the acceptance for kaons is well understood.
Figure 7.16(b) shows the acceptance calculated in bins of Q^2 and z (Eq. 7.15) for positive pions and kaons.

$$\text{12 z bins} : 0.2, 0.25, 0.3, 0.35, 0.4, 0.45, 0.5, 0.55, 0.6, 0.65, 0.7, 0.75, 0.85$$

$$\text{9 Q}^2 \text{ bins} : 1, 1.35, 1.83, 2.5, 3.5, 5, 7, 10, 15, 100 \tag{7.15}$$

For π^+, the acceptance vary from 60% at small Q^2 to $\sim 50\%$ at high Q^2. Similar acceptances are found for K^+ except at small z where the acceptance decreases to $\sim 40\%$. In the range $z \in [0.2, 0.4]$, the majority of generated kaons have their momentum below 10 GeV/c and they are rejected due to the kaon identification threshold. As a consequence, the acceptance is smaller in this z range. In almost all bins, the acceptance is determined with a statistical precision of $\sim 3\%$.

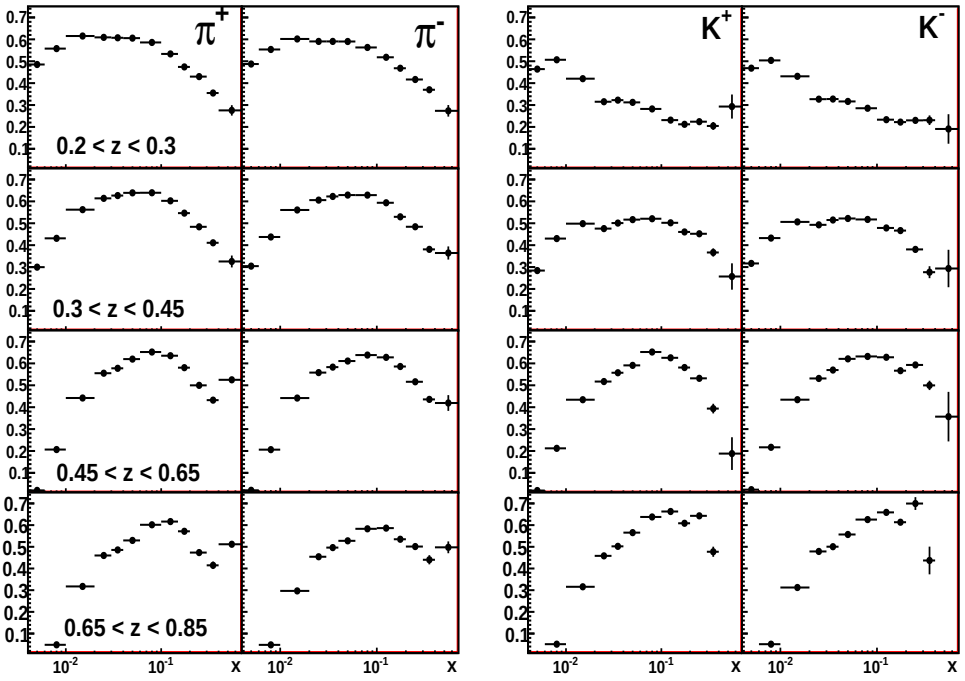

(a) Acceptance in bins of x and z

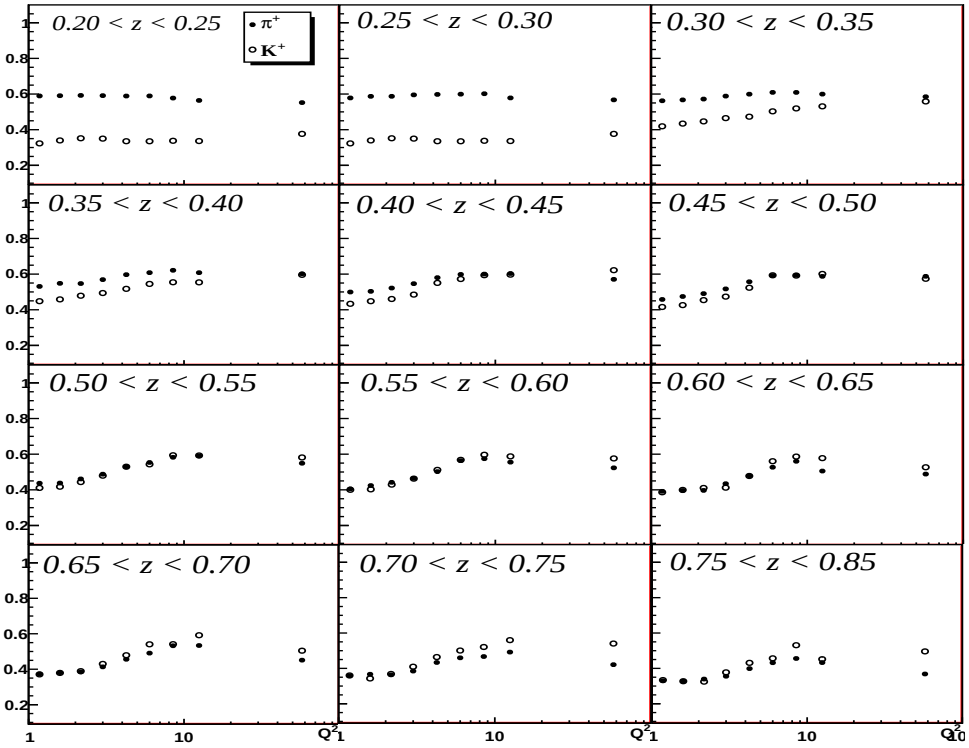

(b) Acceptance in bins of Q^2 and z

Figure 7.16: Acceptance for charge separated pions and kaons.

Chapter 8

Results for π and K Multiplicities

We present here pion and kaon multiplicities, extracted using data collected in 2004 by deeply inelastic scattering of muons off a deuteron target (^{6}LiD). Although the data set used in this work constitutes only 25% of the full 2004 data, it provides already a high precision highligting the great power of COMPASS in terms of statistics. In this chapter are shown the results for charge separated pion and kaon multiplicities as a function of the kinematic variables x, Q^2 and z, corrected for acceptance and smearing effects (section 7.3.2) and for radiative effects (section 7.3.1). The acceptance estimation is the most critical issue in this anaysis and corresponds to the major correction factor. It encodes all details about detector efficiencies and inefficiences and reflects the angular and the geometrical acceptance covered by the COMPASS spectrometer. For its estimation, a large Monte Carlo sample has been produced using a full Monte Carlo chain, describing well data. The final pion and kaon multiplicities are shown, discussed, and compared to theoretical predictions.

8.1 π & K Multiplicities in 12 x bins and 4 z bins

The pion and kaon multiplicities are shown in figures 8.1 and 8.4 respectively as a function of x in 4 z bins ([0.2, 0.3], [0.3, 0.45], [0.45, 0.65], [0.65, 0.85]). They are compared to LO theoretical predictions which have been calculated using the LO definition of hadron multiplicities (Eq. 7.1), the LO DSS parametrization [34] for fragmentation functions (FFs) and the LO MRST 2004 parametrization [38] for unpolarized parton distribution functions (PDFs). The MRST was chosen because of its validity domain which is suitable for the COMPASS kinematics. In each (x, z) bin, the PDFs are evaluated at the mean values of x and Q^2 (see table 8.1) and the FFs are evaluated at the Q^2 mean value and integrated over z between the z bin limits. Both experimental multiplicities and theoretical curves are presented at the mean value of x in each (x, z) bin. The π^+ (figure 8.1(a)) and π^- (figure 8.1(b)) multiplicities show a weak x dependence in the z range [0.2, 0.65], as predicted by LO theoretical calculations. For higher fractional energies z, some discrepancies are observed between experimental multiplicities and LO predictions in the entire x range for both π^+ and π^-. Note that using different paramerization for parton distribution functions, the LO theoretical calculations remain unchanged within less than 2%.

The x dependence of the hadron multiplicities can be used to test the factorization assumption which states that the hadronization of a quark is independent of the initial scattering event from which it originates. If the factorization holds, the fragmentation functions must be independent of the Bjorken scaling variable x. As a consequence, the x dependence of the hadron multiplicities originates from only the x dependence of the parton distributions functions which enter the hadron multiplicities LO definition (cf Eq. 7.1). Figure 8.2 shows the weighted sum of PDFs for favoured to unfavored quark (or antiquark) flavors ($\sum_{q_{favoured}} e_q^2 q(x) / \sum_{q_{unfavoured}} e_q^2 q(x)$)which enter the multiplicity definition (Eq.7.1). Here "favoured" (unfavoured) quark flavors refers to the quark flavors allowing for favoured (unfavoured) fragmentation[1]. The ratio was calculated

[1]For π^+ ($\equiv u\bar{d}$) for example, the quark flavors u and $\bar{d}$ are denoted favoured while the quark flavors $\bar{u}$, d, s and $\bar{s}$ are denoted unfavoured.

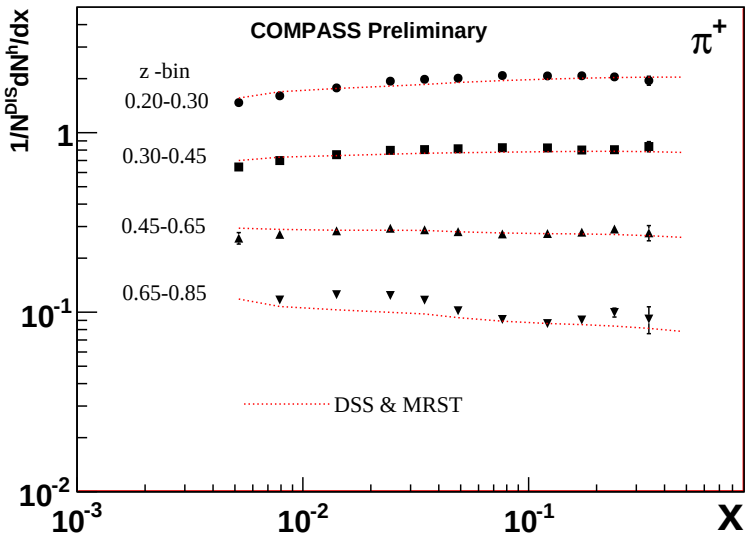

(a) π^+ multiplicities

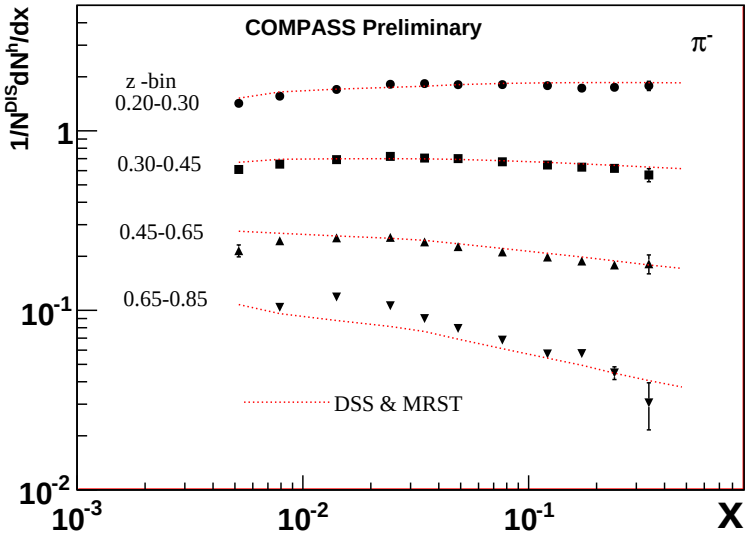

(b) π^- multiplicities

Figure 8.1: π^+ and π^- multiplicities as a function of x in four z bins, compared to LO theoretical calculations performed using the DSS LO parametrization for FFs and the MRST 2004 LO parametrization for unpolarized PDFs. Only statistical errors are shown.

for a deuterium target using the LO MRST 2004 parametrization. In the case of π^+ ($\equiv u\bar{d}$) [π^- ($\equiv \bar{u}d$)] (figure 8.2(a) [8.2(b)]), the ratio rises (decreases) with x due to the dominance of the up valence quarks in the high x region ($x \geq 0.15$). At high z (> 0.65), the x dependence of π^- (figure 8.1(b)) is stronger than that of the parton distribution functions (figure 8.2 left), this observation is predicted by the LO theoretical calculations.

Besides the (x, z) dependent multiplicities, another interesting quantity to study is the ratio of positive to negative pion multiplicities, in which many effects (like acceptance and smearing) cancel out. Figure 8.3 shows the result for this ratio, integrated in the z range [0.2, 0.85], as a function of x. For its calculation, the measured pion multiplicities (figure 8.1) were integrated over z and then divided. The COMPASS measurement is shown in comparison with the E00-108

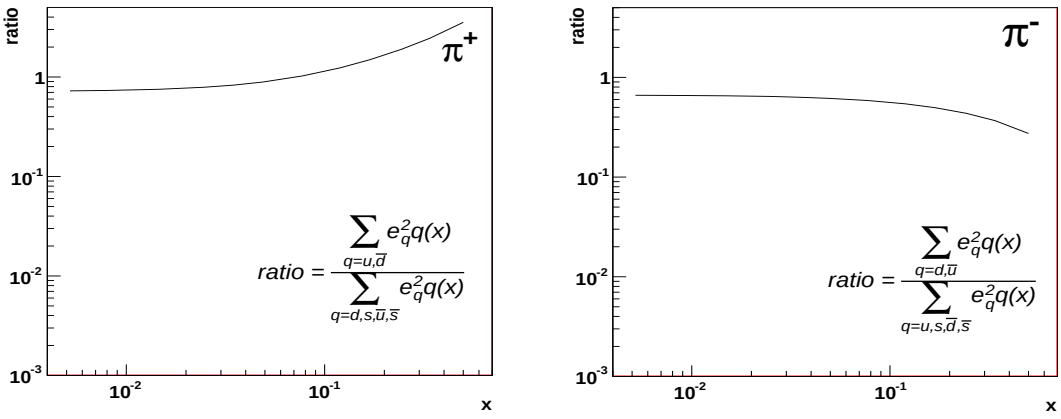

(a) Positive pions (b) Negative pions

Figure 8.2: Ratio of the weighted sum of PDFs for favoured to unfavored quark flavors ($\sum_{q_{favoured}} e_q^2 q(x) / \sum_{q_{unfavored}} e_q^2 q(x)$) for π^+ (left) and π^- (right) using the MRST 2004 LO parametrization.

result (JLab/Hall C) [57] and with the LO calculation. The JLab measurement is performed using a 5.479 GeV/C electron beam scattering off a deuterium target. The selected kinematic domain is restricted to $2 < Q^2 < 4$ [GeV/c]^2, $W > 2$ GeV, $0.2 < x < 0.6$ and $z \in [0.3, 1]$. The COMPASS measurement is performed in a larger kinematic domain ($Q^2 > 1$ [GeV/c ^{2}, $0.004 < x < 0.7$, $0.2 < z < 0.85$) and in two W regions: $5 < W < 7$ GeV/c and $W > 7$ GeV/c. The COMPASS and the JLab measurements are in good agreement in the kinematic region ($5 < W < 7$ GeV and $x > 0.2$); however both results deviate from the LO prediction which was calculated at the corresponding x and Q^2 COMPASS mean values in each bin. COMPASS has the advantage of exploring a wide x range up to small x ($x = 4 \cdot 10^{-2}$) with a high precision, allowing to test the theory in a wide kinematic domain. For $x < 0.025$, the ratio measured by COMPASS is in good agreement with the LO prediction.

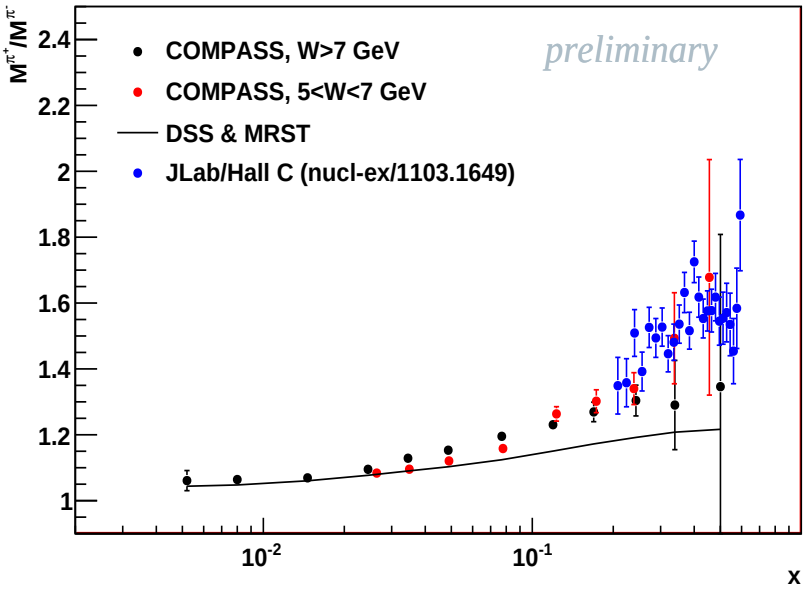

Figure 8.3: Ratio of positive to negative pion multiplicities as a function of x. Values are integrated over z in the range [0.2, 0.85]. Only statistical errors are shown.

Figure 8.4 shows the charge separated kaon multiplicities as a function of x for various z bins, in comparison with LO theoretical calculations performed using DSS parametrization for fragmentation functions and MRST parametrization for unpolarized PDFs.

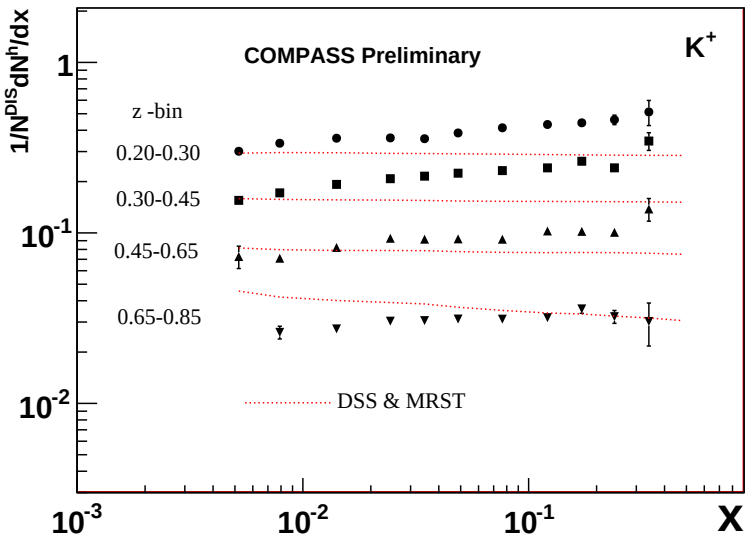

(a) K^+ multiplicities

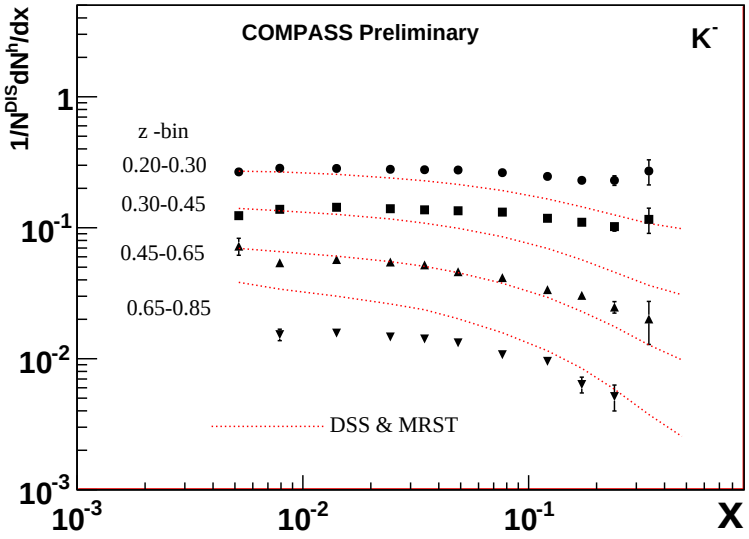

(b) K^- multiplicities

Figure 8.4: K^+ (a) and K^- (b) multiplicities as a function of x in four z bins, compared to LO theoretical calculations performed using the LO DSS for FFs and the LO MRST 2004 for PDFs. Only statistical errors are shown.

For K^+, the multiplicities increase with x in nearly all z bins while for K^-, they decrease. This tendency is more pronounced in the high z region ($z > 0.45$). The K^+ and K^- multiplicities agree with the LO calculations at small x ($x \leq 0.15$) and show significant discrepancies in the high x region. This discrepancy could be due to higher order corrections which are missing in LO calculations and in LO definition of multiplicity (cf Eq. 7.1) or it could be simply due to the poor knowledge of the strange quark distribution ($s(x, Q^2)$) and the strange fragmentation functions into kaons ($D_{\bar{s}}^{K^+}(z)$). In nearly all parametrization for parton distribution functions,

the strange quark distribution is assumed to be related to the sea quark distributions $\bar{u}(x,Q^2)$, $\bar{d}(x,Q^2)$ as follows

$$s(x,Q^2) = \frac{\kappa}{2}(\bar{u}(x,Q^2) + \bar{d}(x,Q^2) \tag{8.1}$$

where κ is a constant obtained by fitting data. Only one measurement of $s(x)$ has been performed by the HERMES collaboration [58] using kaon multiplicities ($M^{K^+ + K^-}$) as a function of x, measured at $Q^2 = 2.5$ [GeV/c]^2 from DIS on a deuterium target. For this purpose, the partial moment of the non-strange fragmentation function needed in the extraction has been extracted from the same data using the CTEQ parametrization for PDFs, and by taking the strange fragmentation function from the DSS parametrization. The resulting $s(x, Q^2 = 2.5)$ was found to be significantly smaller than the CTEQ prediction in the covered x range [0.025 ,0.6] (see [58] for more details). One must note that such discrepancy between the calculations and the experimental kaon multiplicities is not surprising.

For the strange quark fragmentation function (D^K_{str}), no previous measurement exist and our knowledge is limited to the existing FF parametrization where several assumptions are made (see section 3.3.2). The first experimental measurement of this function is presented in this thesis (see chapter 9).

The x dependence of the kaon multiplicties can be explained by the up quark dominance in the high x region. This observation is illustrated in figure 8.5 which shows the ratio of the weighted sum of PDFs for favored to unfavored quark flavors ($\sum_{q_{favored}} e_q^2 q(x) / \sum_{q_{unfavored}} e_q^2 q(x)$), for K^+ ($\equiv \bar{u}s$) (figure 8.5(a)) and K^- ($\equiv u\bar{s}$) (8.5(b)). The multiplicity of K^- is predicted to decrease at high x where the contributions of sea quarks are negligible. However, COMPASS measurements show that the K^- multiplicities do not decrease at high x for $0.2 < z < 0.45$. This difference could be due to higher order corrections missing in LO calculations. It could be also an indication that the strange quark distribution in the nucleon may be different from the existing predictions.

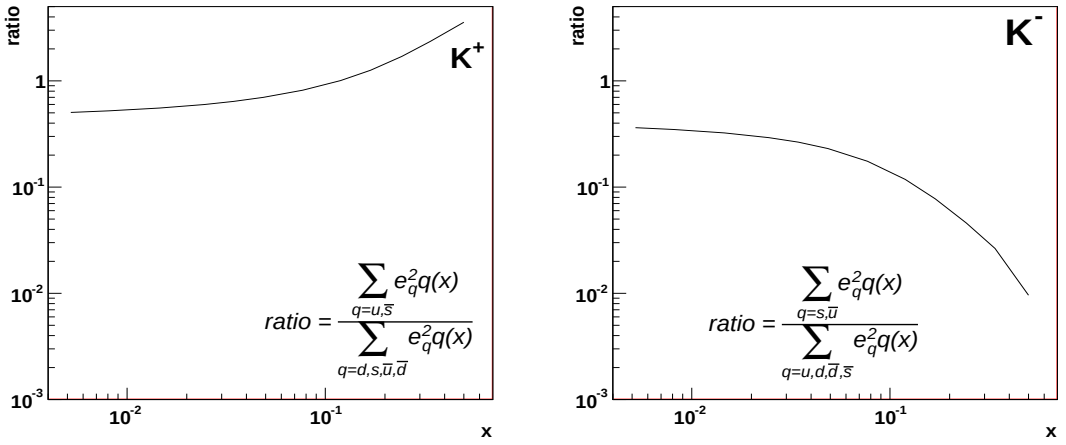

(a) Positive kaons

(b) Negative kaons

Figure 8.5: Ratio of the weighted sum of PDFs for favored to unfavored quark flavors for K^+ (left) and K^- (right) using the LO MRST 2004 parametrization.

Similarly to pions, one can calculate the ratio of positive to negative kaon multiplicities. Figure 8.6 shows this ratio as a function of x in various z bins, calculated using COMPASS kaon multiplicities in comparison with LO theoretical calculations performed using the parametrization MRST and DSS for PDFs and FFs respectively. The LO calculations describe well experimental ratios within errors in nearly the entire kinematic domain. This result is the first experimental measurement of the ratio M^{K^+}/M^{K^-}.

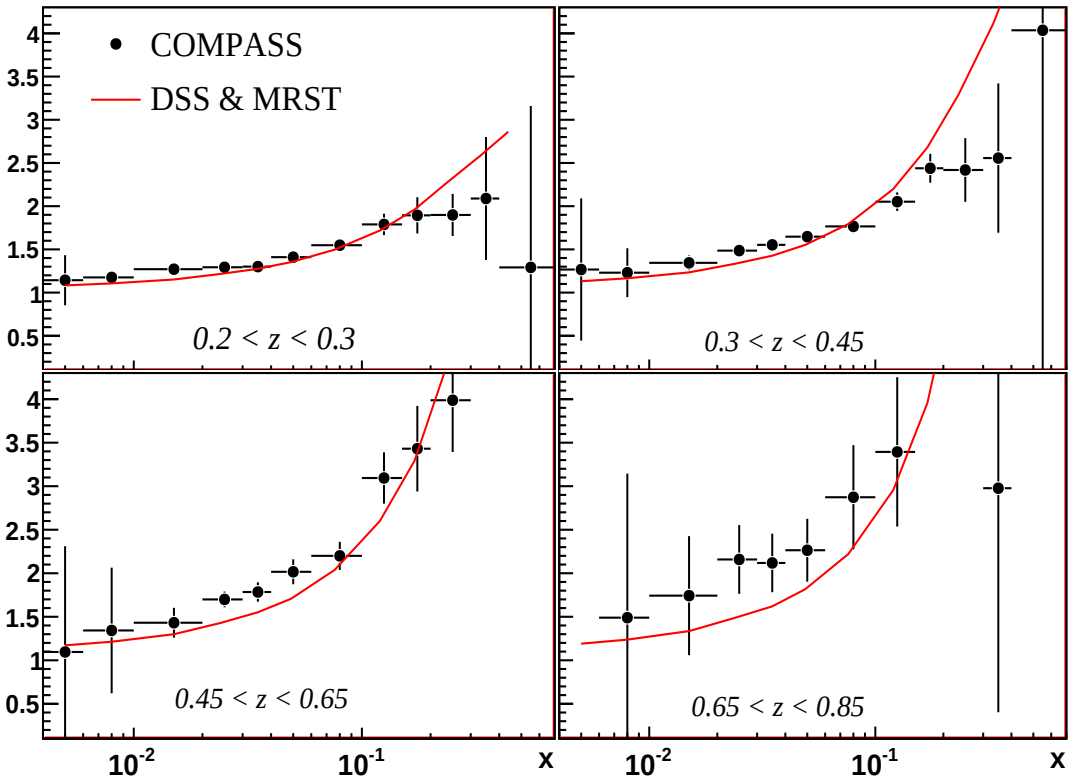

Figure 8.6: Ratio of positive to negative kaon multiplicities as a function of x in various z bins, compared to LO theoretical calculations performed using DSS parametrization for FFs and MRST parametrization for unpolarized PDFs. The errors correspond to the statistical and systematic errors combined in quadrature.

The multiplicities for positive and negative hadrons are shown in figure 8.7 and 8.8, in comparison with LO calculations performed using DSS and MRST parametrizations for FFs and PDFs respectively. LO calculations describe the experimental multiplicities in nearly all (x, z) bins.

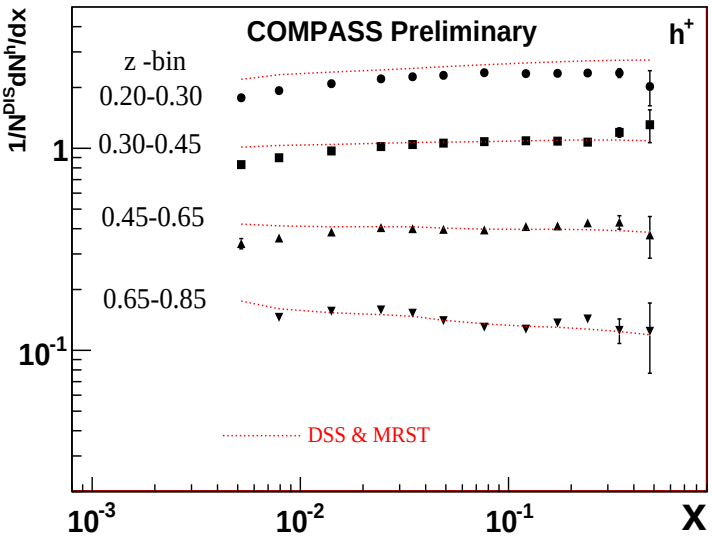

Figure 8.7: Multiplicities for positive hadrons as a function of x for various z bins, compared to LO calculations.

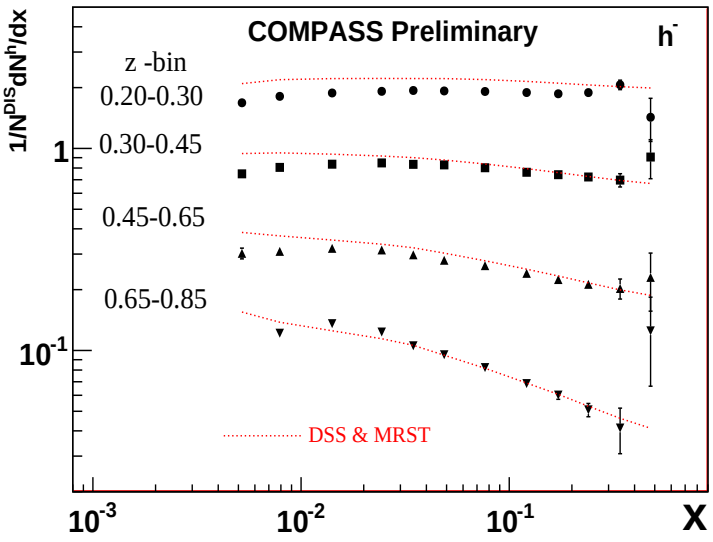

Figure 8.8: Multiplicities for positive hadrons as a function of x for various z bins, compared to LO calculations.

8.2 π & K Multiplicities in 9 Q^2 bins and 12 z bins

The multiplicities are presented, as a function of Q^2 four twelve z bins for π^+ (figure 8.10(a)) and π^- (figure 8.10(b)). The Q^2 dependence is found to be more pronounced at high z, especially for π^-, and follows the trend shown by LO calculations (figure 8.9).

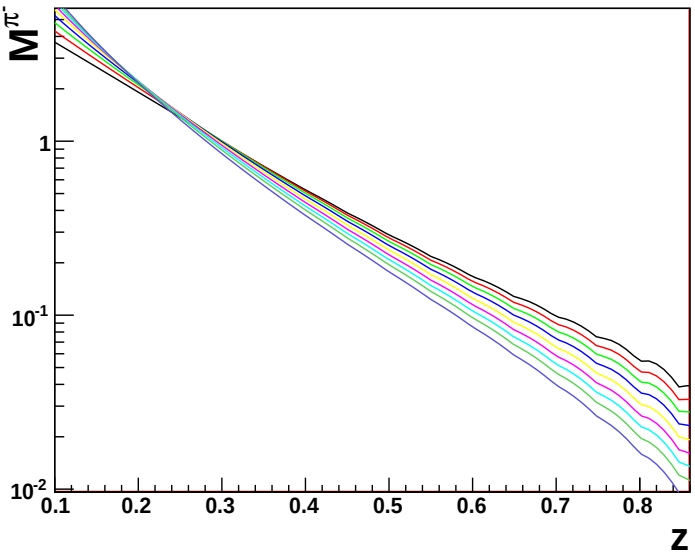

Figure 8.9: LO calculations of π^- multiplicities versus z in nine Q^2 bins, using the LO MRST 2004 parametrization for PDFs and the LO DSS parametrization for FFs. The curves correspond to the Q^2 bins $[1, 1.35, 1.83, 2.5, 3.5, 5, 7, 10, 15, 15, 100]$, starting from the black one.

The kaon multiplicities are presented, as a function of Q^2 for twelve z bins, in figure 8.11. For K^+, the Q^2 dependence is weak in nearly the entire z range while for K^-, it is larger at high z.

This effect is even more visible in figure 8.12 which shows the pion and kaon multiplicities as a function of z for different Q^2 bins (same data).

Experimental multiplicities are compared to LO calculations which have been performed using Eq.7.1 and different choices of parametrization for unpolarized PDFs and FFs. For unpolarized PDFs, MRST and CTEQ parametrizations were chosen and for fragmentation functions, DSS [34] and KRE [33] parametrizations were chosen. For each kinematic bin (Q^2,z), the PDFs were evaluated at x and Q^2 mean values and the fragmentation functions were evaluated at the mean value of Q^2 and then integrated in the corresponding z range.

8.2.1 π & K Multiplicities versus Q^2 for various z bins

The comparison between the calculations and the measured values is shown, as a function of Q^2 for various z bins, in figure 8.13 (8.14) for pions (kaons). In the case of pions, the results agree with the LO calculations using DSS within $5-10\%$ in the range ($z \in [0.25, 0.6]$ & $Q^2 \in [2.5, 100]$) and within $\sim 20\%$ outside this domain. The relatively good agreement in the z range $[0.25, 0.6]$ is well expected since the DSS fit used hadron multiplicities from the Hermes experiment covering this z range while the KRE parametrization fitted only e^+e^- annihilation data.

For kaons, the data differ from the LO calculations performed using KRE parametrization by $50-60\%$. However, data agree with the calculations performed using DSS fragmentation functions within $\sim 20\%$ in the z range [0.45, 0.6]. Outside this range, larger differences ($20-80\%$) are observed. The discrepancy can be due to higher order effects which are not taken into account at LO. In addition, the parametrization of FFs are less constraint by data in the kaon case. Finally one must note that the theoretical calculations are evaluated without uncertainties.

8.2.2 π & K Multiplicities versus z for various Q^2 bins

In figures 8.15 and 8.16, the multiplicities versus z for various Q^2 bins are compared to LO calculations. In the case of pions, results agree with the LO calculation (DSS & KRE) in the entire z range within $5-20\%$. For $z > 0.7$, the multiplicities slightly deviate from the LO calculations, in particular at small Q^2. For kaons, for which the parametrizations are not sufficiently constrainted by previous kaon data, the COMPASS results tend to be well higher than predictions by $20-50\%$.

Figures 8.17 and 8.18 show COMPASS multiplicities compared to LO calculations performed using DSS parametrization for FFs and MRST and CTEQ for unpolarized PDFs. Both LO calculations give the same description of experimental multiplicities.

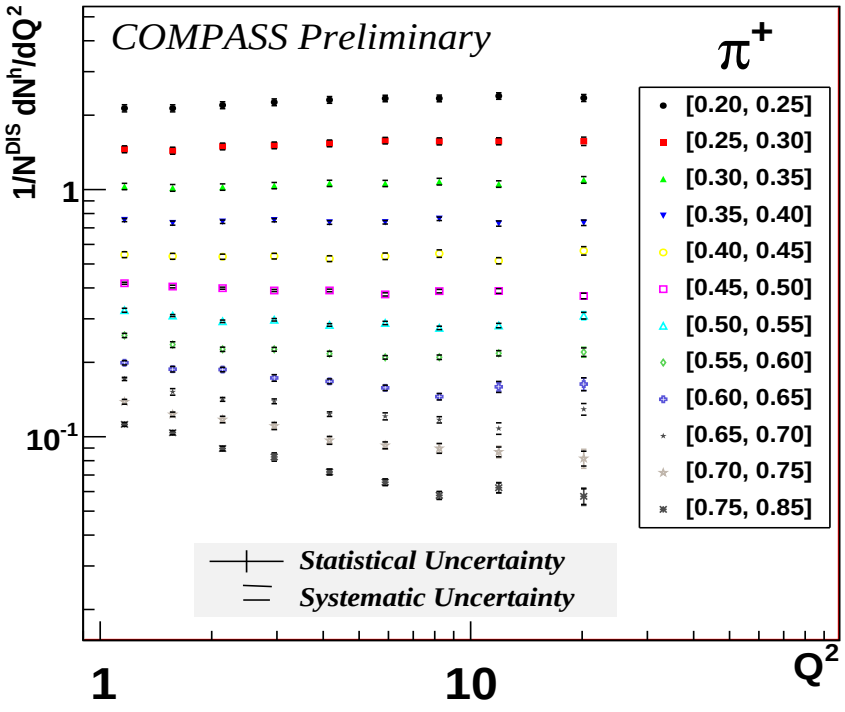

(a) π^+ multiplicities

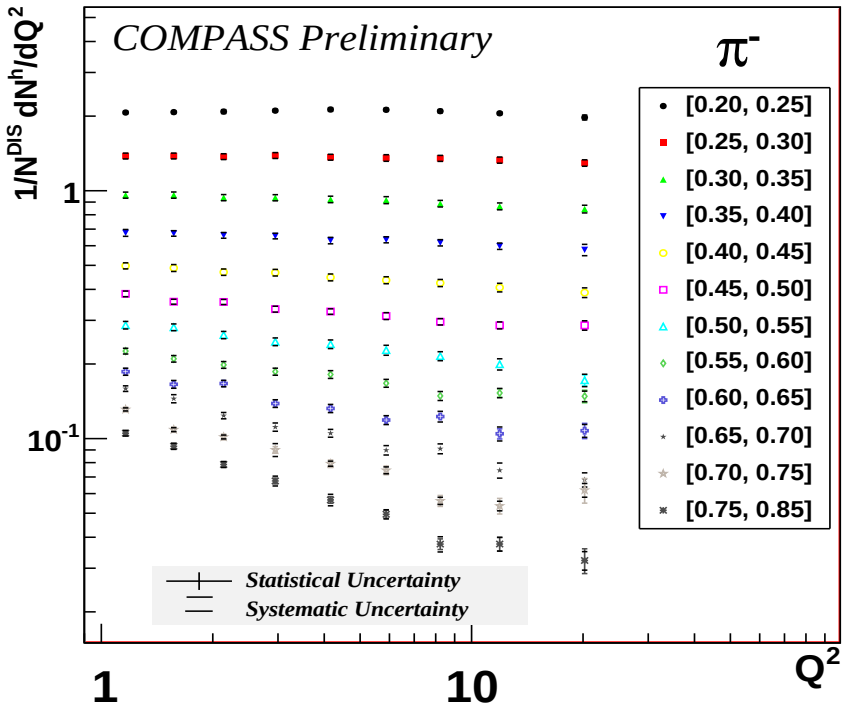

(b) π^- multiplicities

Figure 8.10: Pion multiplicities versus Q^2 in twelve z bins. Both statistical and systematic errors are presented and are given in appendix **??**.

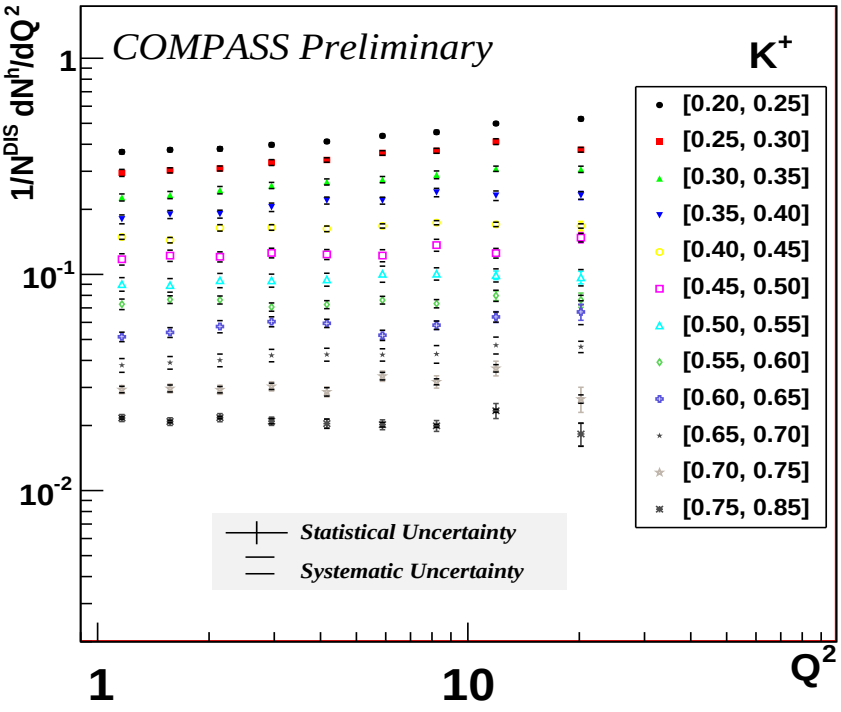

(a) K^+ multiplicities

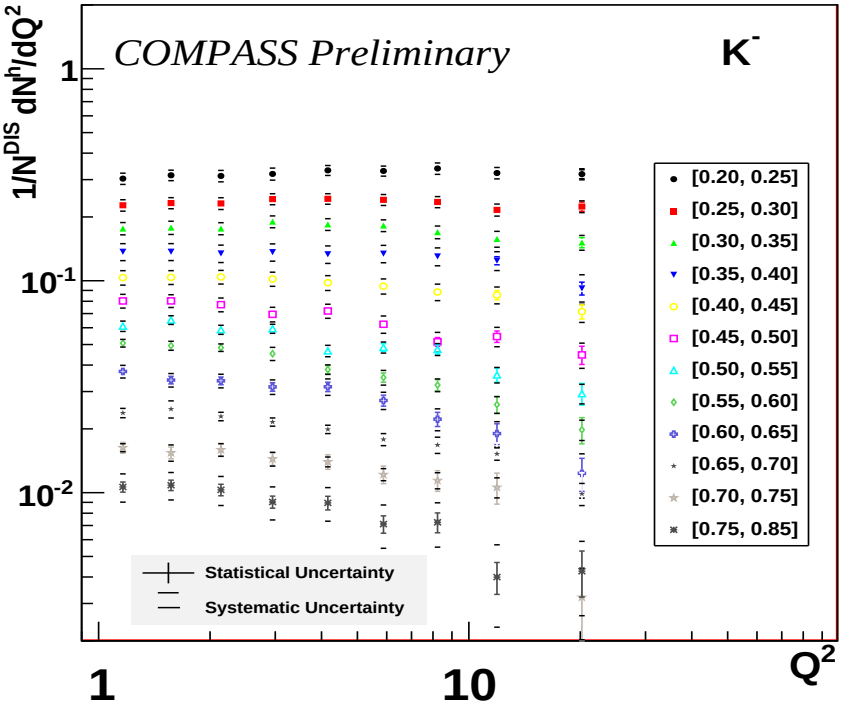

(b) K^- multiplicities

Figure 8.11: Kaon multiplicities versus Q^2 in twelve z bins. Both statistical and systematic errors are presented and are given in appendix **??**.

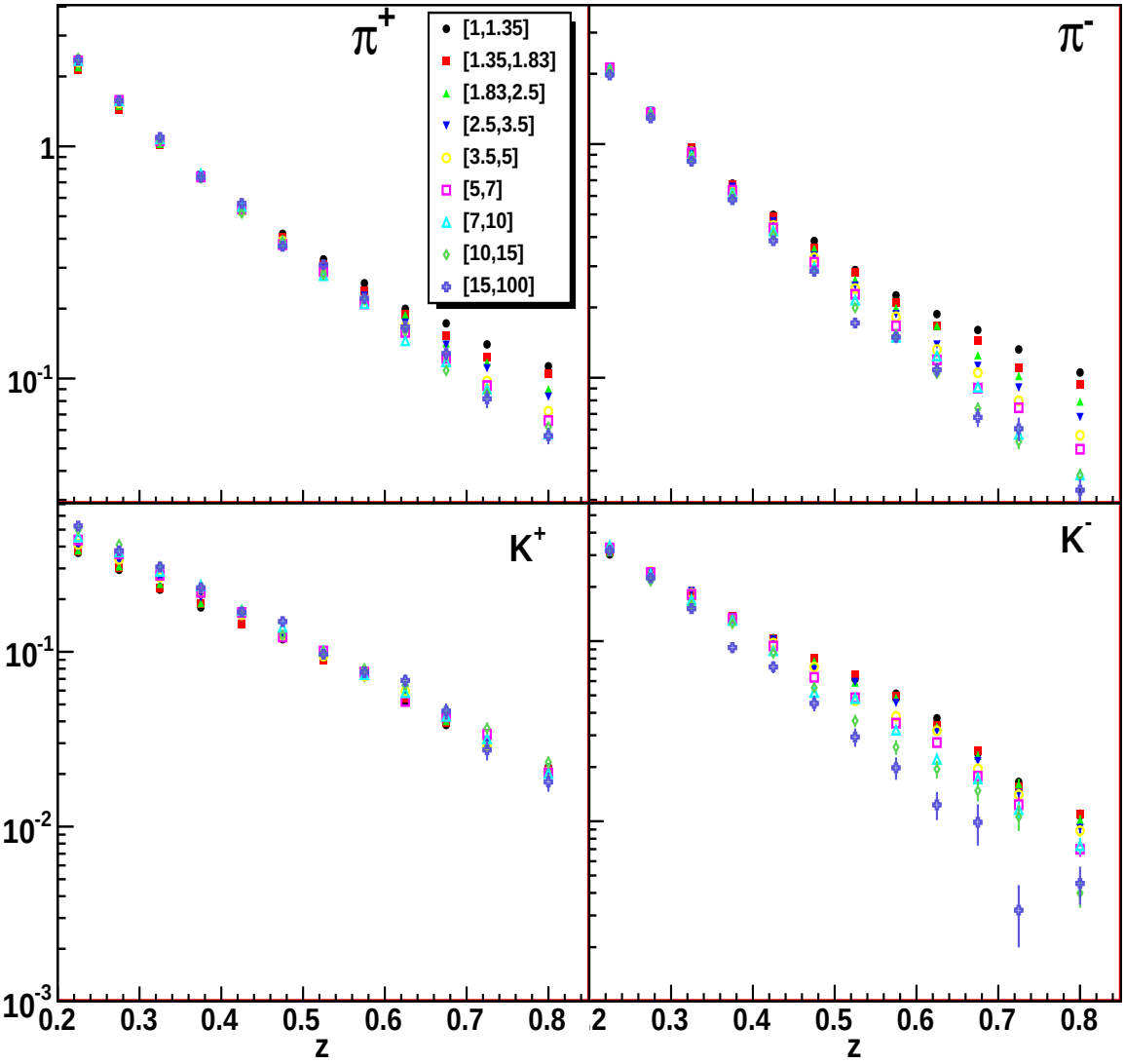

Figure 8.12: Pion and kaon multiplicities as a function of z in nine Q^2 bins: [1, 1.35, 1.83, 2.5, 3.5, 5, 7, 10, 15, 100]. Only statistical errors are shown.

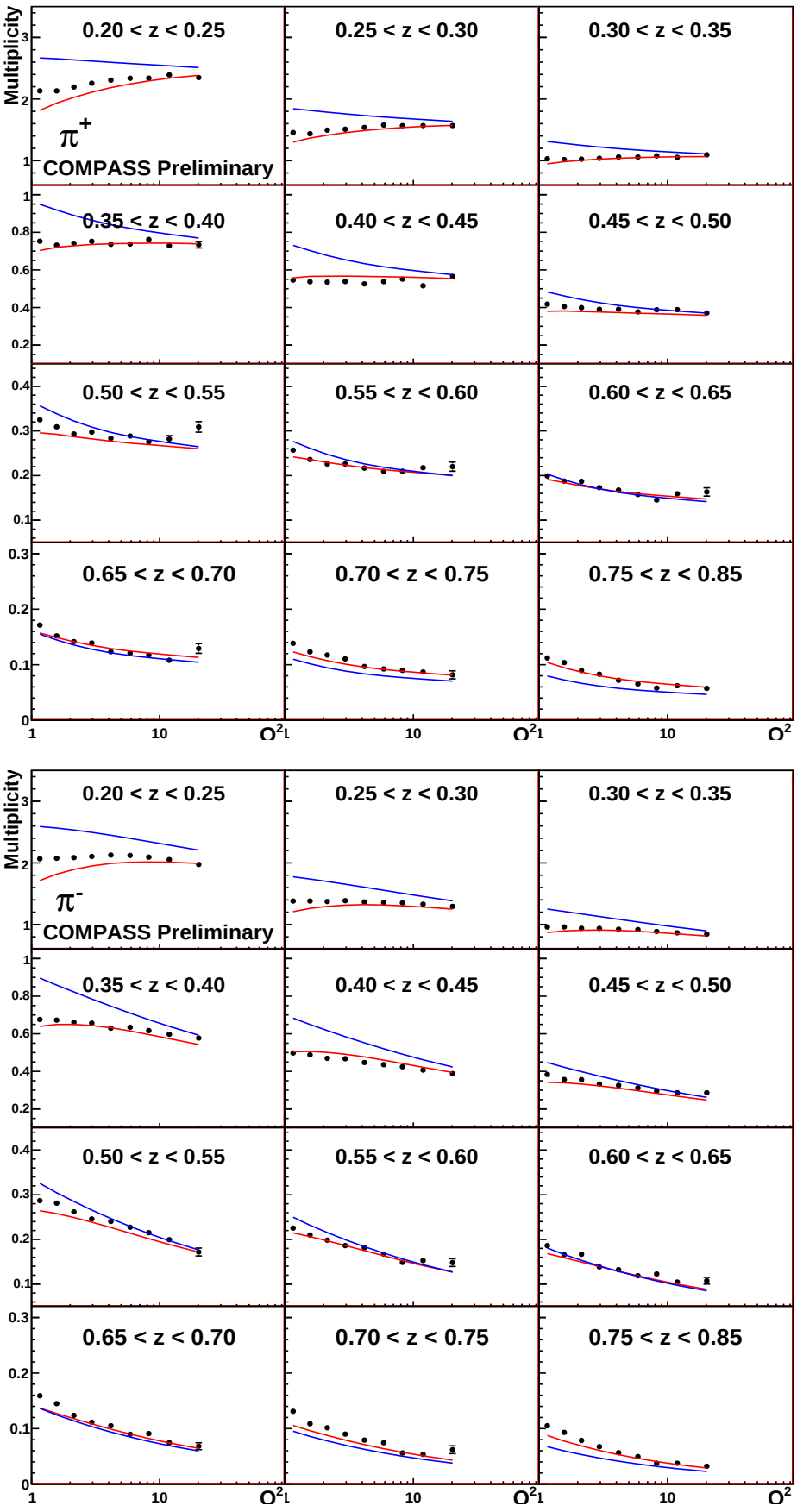

Figure 8.13: Positive (up) and negative (down) pion multiplicities versus Q^2 in twelve z bins compared to LO theoretical calculations performed using MRST parametrization for PDFs and DSS (red curves) and KRE (blue curves) parametrization for quark fragmentation functions.

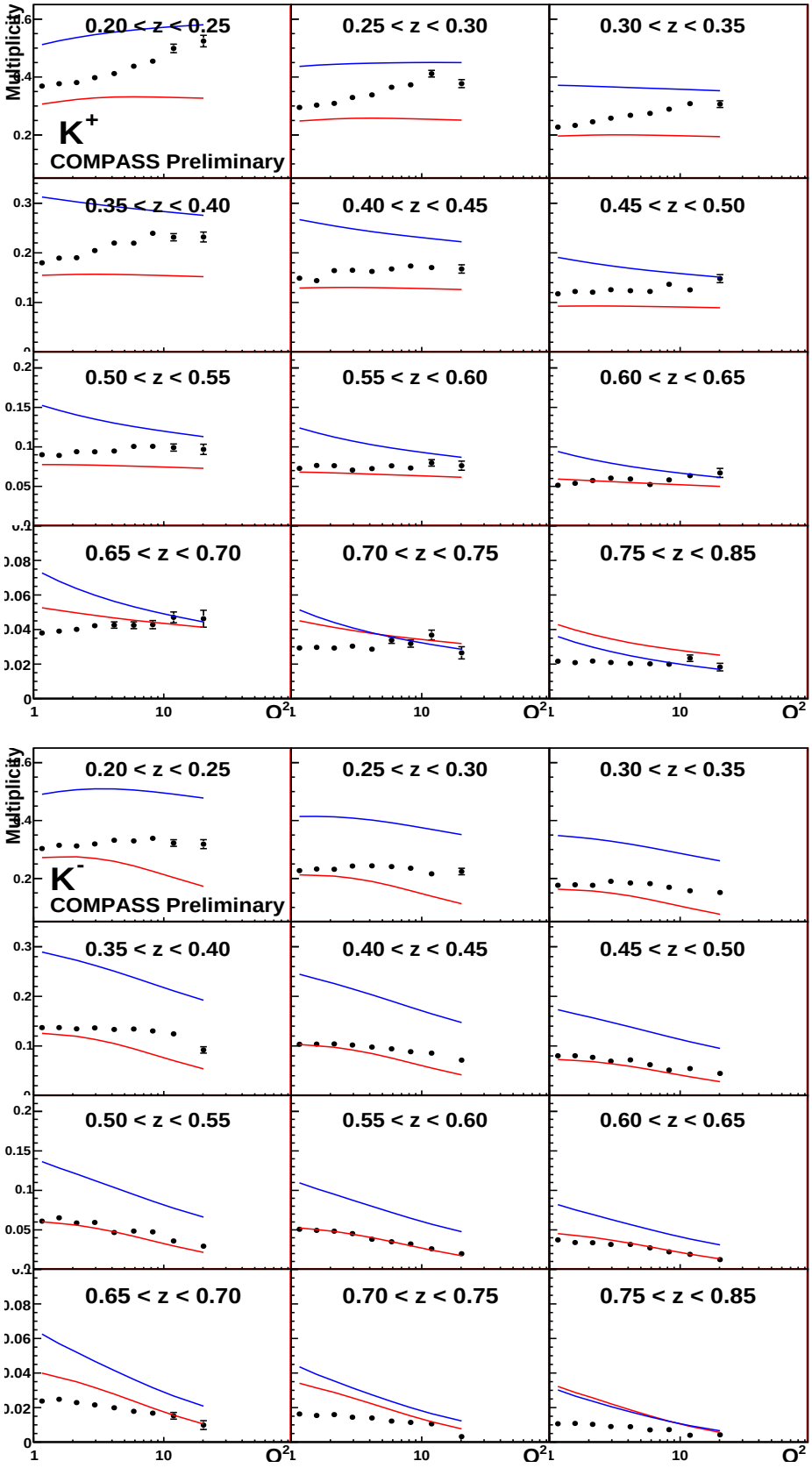

Figure 8.14: Positive (up) and negative (down) Kaon multiplicities versus Q^2 in twelve z bins compared to LO theoretical calculations performed using MRST parametrization for PDFs and DSS (red curves) and KRE (blue curves) parametrization for quark fragmentation functions.

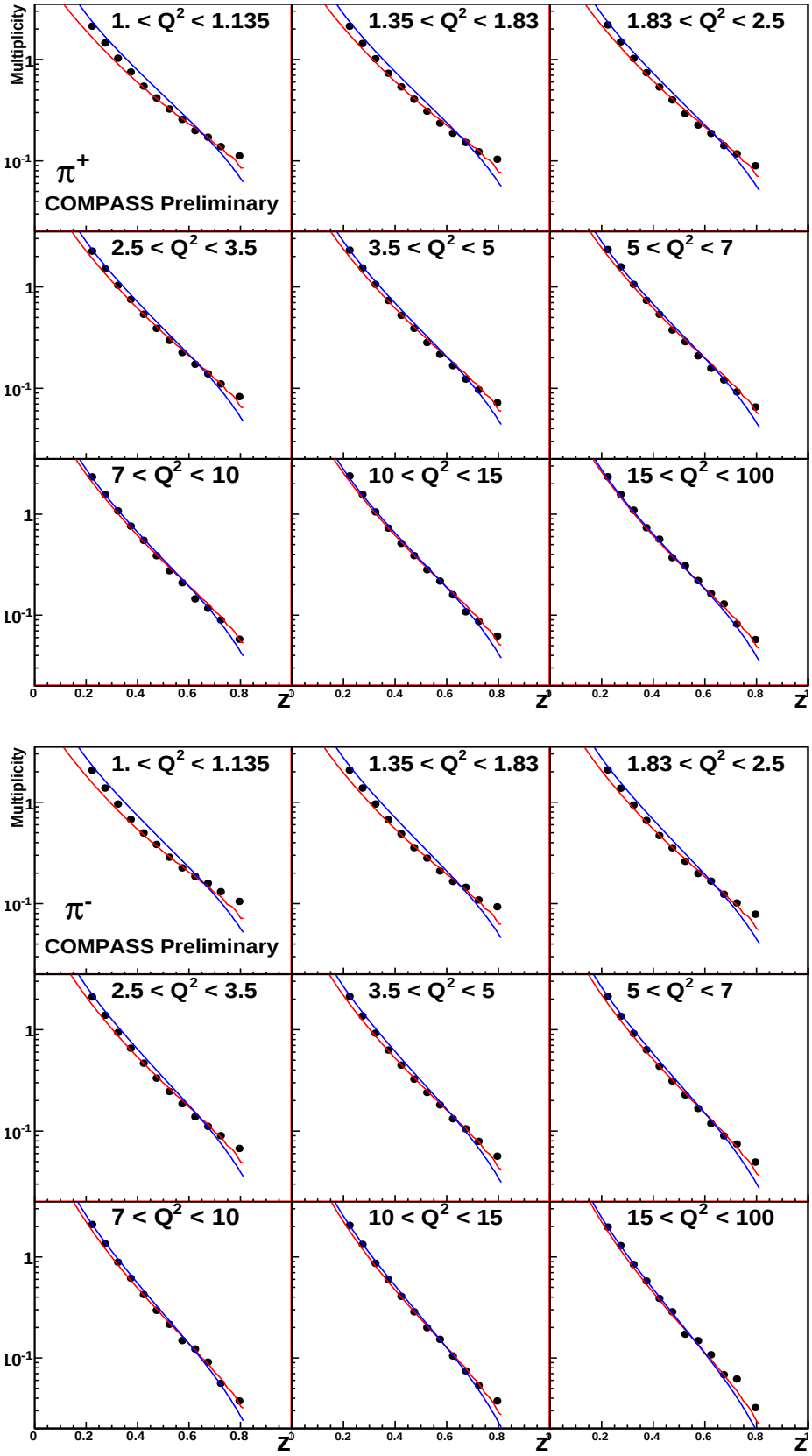

Figure 8.15: Positive (up) and negative (down) pion multiplicities versus z in nine Q^2 bins compared to LO theoretical calculations performed using MRST parametrization for PDFs and DSS (red curves) and KRE (blue curves) parametrization for quark fragmentation functions.

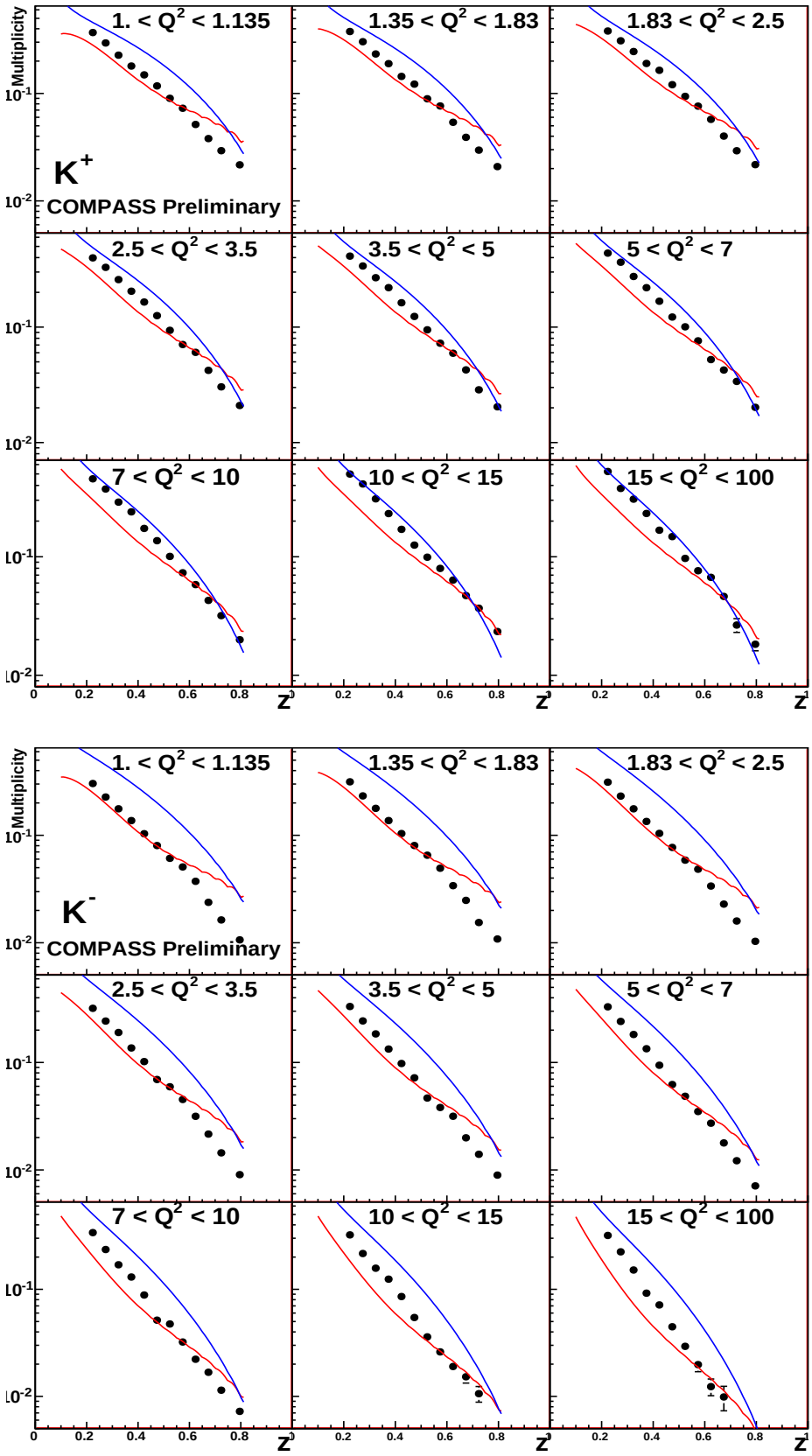

Figure 8.16: Positive (up) and negative (down) Kaon multiplicities versus z in nine Q^2 bins compared to LO theoretical calculations performed using MRST parametrization for PDFs and DSS (red curves) and KRE (blue curves) parametrization for quark fragmentation functions.

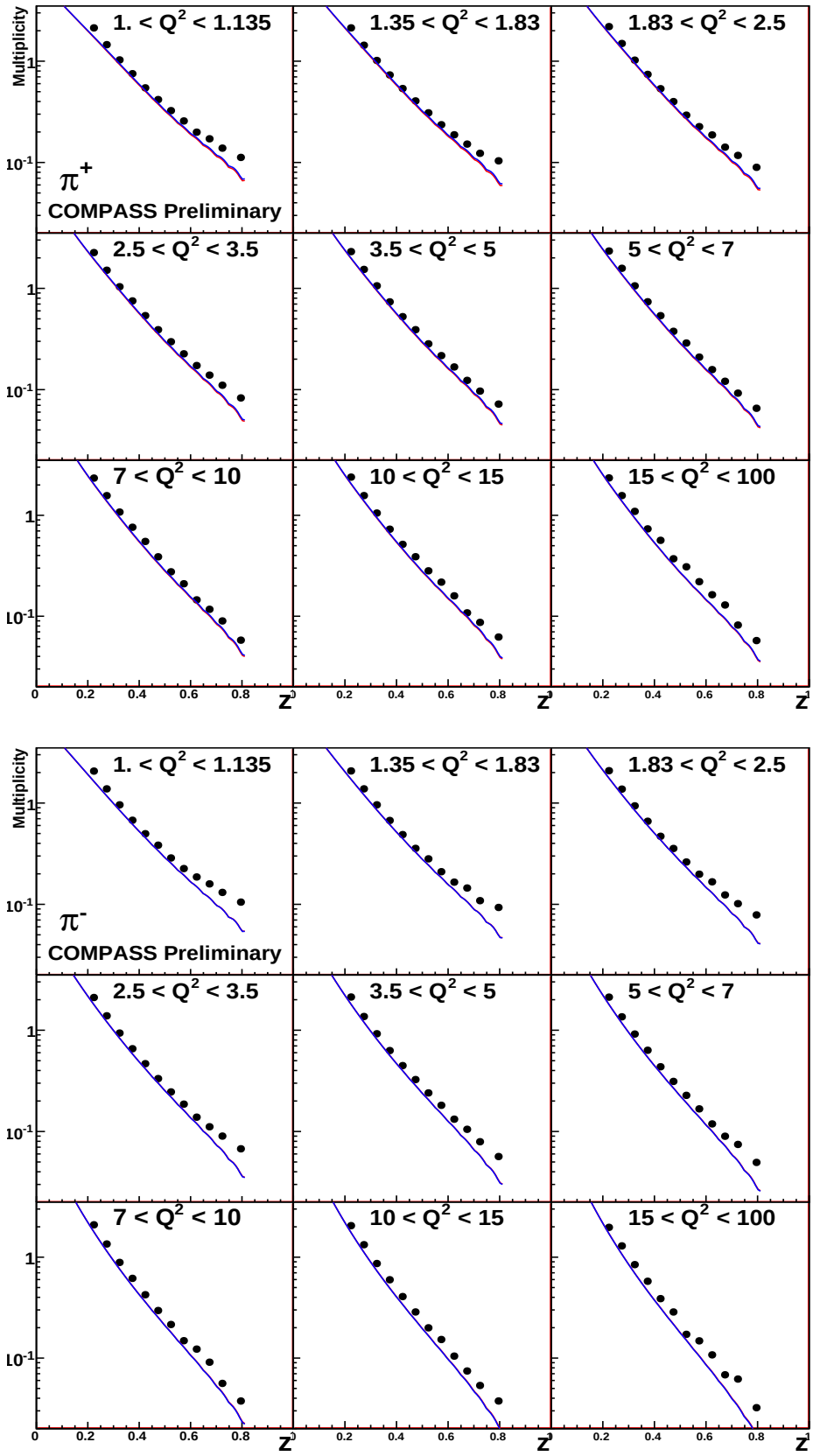

Figure 8.17: Positive (up) and negative (down) pion multiplicities versus z in nine Q^2 bins compared to LO theoretical calculations performed using DSS parametrization for fragmentation functions and MRST (red curves) and CTEQ (blue curves) parametrization for PDFs.

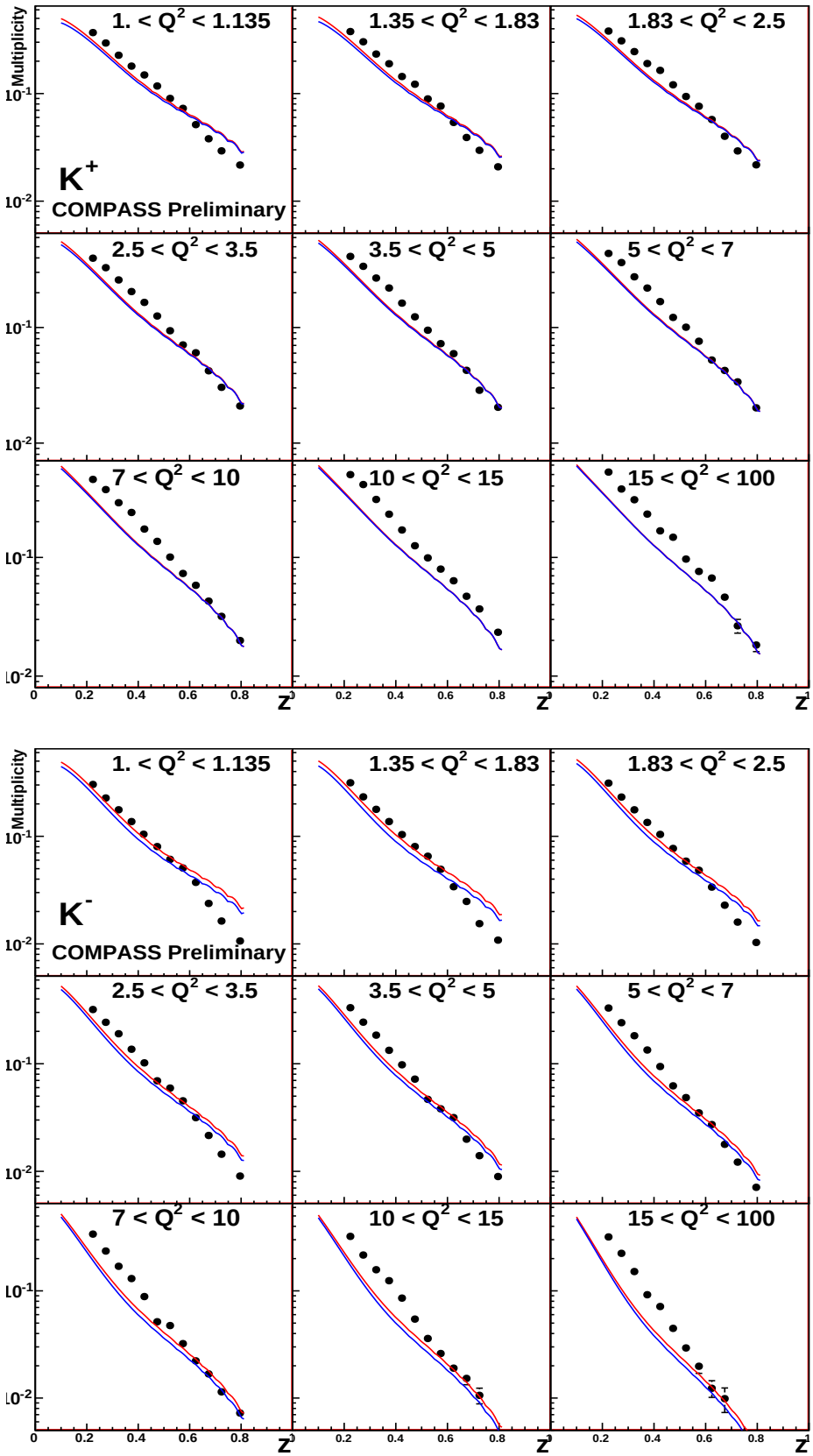

Figure 8.18: Positive (up) and negative (down) Kaon multiplicities versus z in nine Q^2 bins compared to LO theoretical calculations performed using DSS parametrization for fragmentation functions and MRST (red curves) and CTEQ (blue curves) parametrization for PDFs.

8.3 π & K Multiplicities in 12 z bins

The z dependent pion and kaon multiplicities are presented in figures 8.19 and 8.20). They are obtained by integrating the (Q^2,z) multiplicities (section 8.2) over Q^2. These values will be used to extract the quark fragmentation functions into pions and kaons, as discussed in chapter 9.

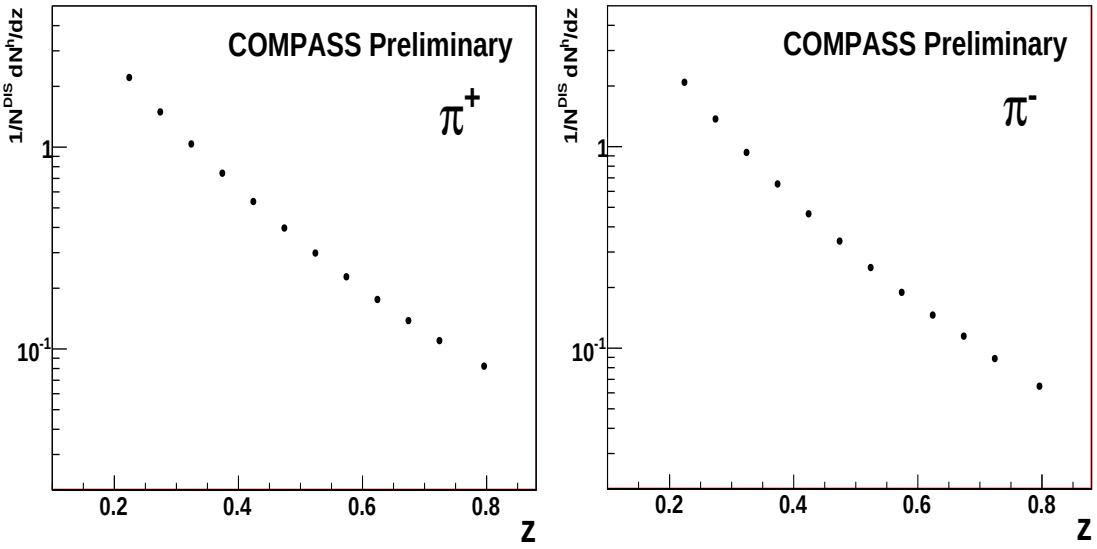

Figure 8.19: Positive (left) and negative (right) multiplicities as a function of z.

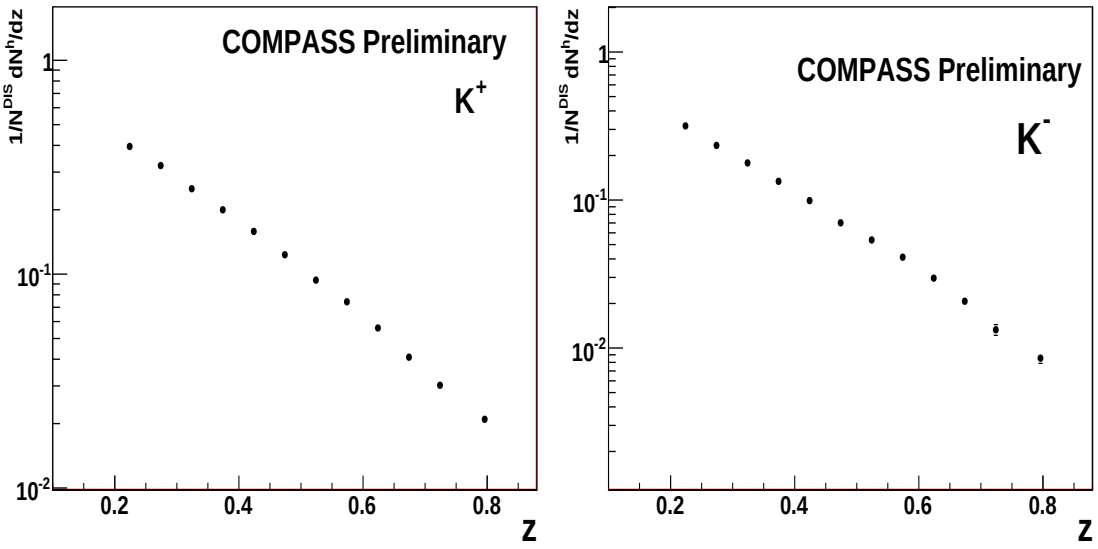

Figure 8.20: Positive (left) and negative (right) kaon multiplicities as a function of z.

8.4 Systematic Studies

The following sources of systematic errors were investigated:

x_{min}	x_{max}	$< x >$	$< Q^2 >$	$< z >$	$< x >$	$< Q^2 >$	$< z >$
		$z \in [0.20, 0.30]$			$z \in [0.30, 0.45]$		
0.004	0.006	0.005	1.17	0.242	0.005	1.15	0.350
0.006	0.010	0.008	1.43	0.243	0.008	1.39	0.359
0.010	0.020	0.015	1.86	0.244	0.015	1.80	0.362
0.020	0.030	0.024	2.53	0.245	0.024	2.42	0.364
0.030	0.040	0.035	3.52	0.245	0.035	3.36	0.364
0.040	0.060	0.049	4.81	0.245	0.049	4.63	0.364
0.060	0.100	0.076	7.06	0.245	0.077	6.88	0.364
0.100	0.150	0.120	10.6	0.245	0.120	10.3	0.365
0.150	0.200	0.170	15.1	0.246	0.170	14.9	0.365
0.200	0.300	0.233	21.3	0.245	0.233	21.1	0.366
0.300	0.400	0.333	31.7	0.243	0.332	31.8	0.364
0.400	0.700	0.438	41.4	0.242	0.439	42.2	0.373
		$z \in [0.45, 0.65]$			$z \in [0.65, 0.85]$		
0.004	0.006	0.006	1.10	0.475	0.000	0.00	0.000
0.006	0.010	0.008	1.23	0.517	0.009	1.10	0.709
0.010	0.020	0.015	1.60	0.528	0.015	1.40	0.732
0.020	0.030	0.024	2.18	0.531	0.024	1.88	0.734
0.030	0.040	0.035	3.10	0.531	0.035	2.66	0.733
0.040	0.060	0.049	4.34	0.531	0.049	3.83	0.731
0.060	0.100	0.077	6.57	0.531	0.077	6.01	0.730
0.100	0.150	0.120	10.0	0.532	0.120	9.31	0.730
0.150	0.200	0.170	14.3	0.533	0.170	13.4	0.732
0.200	0.300	0.235	21.0	0.533	0.231	19.7	0.726
0.300	0.400	0.336	31.4	0.535	0.336	31.1	0.721
0.400	0.700	0.436	44.0	0.545	0.411	38.4	0.692

Table 8.1: Mean values of the variables x, Q^2 and z in 12 x bins and 4 z bins for π^+. Similar values are obtained for π^-, K^+ and K^-.

- Stability of hadron multiplicities versus time: the compatibility of hadron multiplicities obtained from each of the four weeks with the average was studied.
- Acceptance calculation
  - Sensitivity to Lund fragmentation parameters: acceptances, in bins of x, Q^2 and z for each hadron type, are calculated using two different tunings of fragmentation parameters (table 7.4).
  - 2-dimensions versus 3-dimensions acceptances
- RICH for particle identification: Sensitivity to the parameters used for identification

8.4.1 Data Compatibility

To check if the four measurements (corresponding to the four weeks) are statistically compatible, the following pull distribution is built:

$$\frac{M_{i,j} - < M_i >}{\sqrt{\sigma^2_{M_{i,j}} - \sigma^2_{<M_i>}}} \tag{8.2}$$

Here, the index i refers to the kinematic bin ((x,z) or (Q^2,z)) and j refers to the j-th measurement. If the tested measurements are compatible within statistical fluctuations, Eq. 8.2 results in a Gaussian shaped distribution with a mean $x_0 = 0$ and $\sigma = 1$. For the multiplicities measured in bins of x and z, the results are shown in figure 8.21 for both pions and kaons. For each histogram, the number of entries is 192 (12 x bins $\times$ 4 z bins $\times$ 4 weeks). For all distributions, the mean is compatible with zero within the statistical errors. Since σ is larger than 1, a systematic error is estimated in units of the statistical error σ_{stat} by the standard deviation:

$$\sigma_{sys}^{Comp} \leq \sqrt{(\sigma_{pulls} + \delta\sigma_{pulls})^2 - 1)}\sigma_{stat} \tag{8.3}$$

The resulting systematic errors are summarized in table 8.2. The maximum value of the systematic error associated to the data compatibility is of the order of the statistical error.

	π^+	π^-	K^+	K^-
σ_{sys}^{Comp}[(x,z) multiplicities]	$1.1 \cdot \sigma_{stat}$	$0.7 \cdot \sigma_{stat}$	$0.45 \cdot \sigma_{stat}$	$0.6 \cdot \sigma_{stat}$
σ_{sys}^{Comp}[(Q^2,z) multiplicities]	$0.75 \cdot \sigma_{stat}$	$0.5 \cdot \sigma_{stat}$	$0.16 \cdot \sigma_{stat}$	$0.33 \cdot \sigma_{stat}$

Table 8.2: Systematic errors estimated using Eq. 8.3 expressed in units of σ_{stat}.

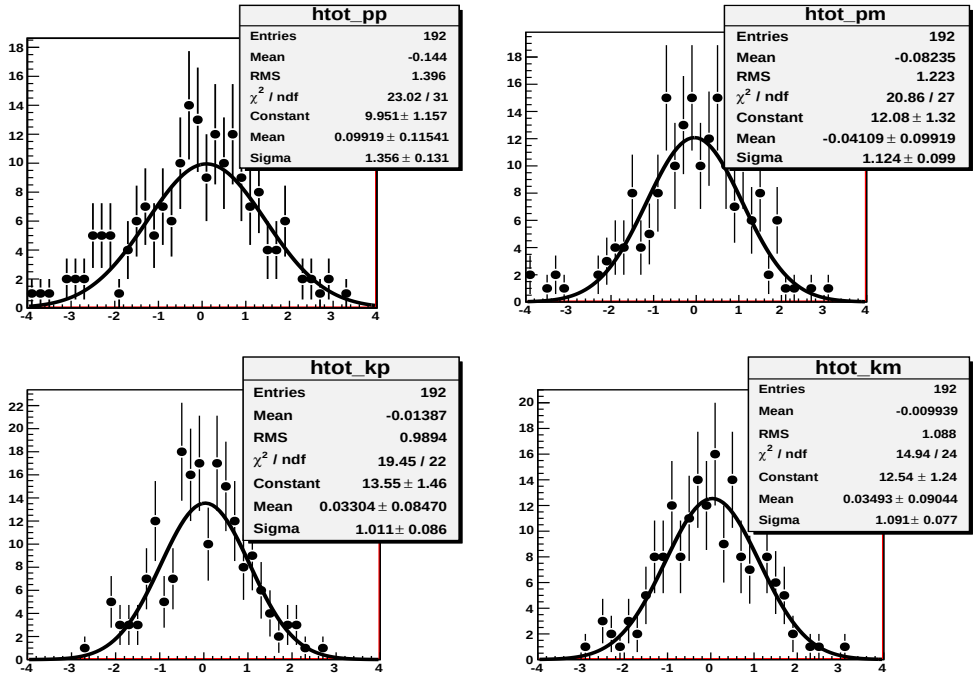

Figure 8.21: Compatibility pull distribution of the multiplicities for positive (top left) and negative (top right) pions as well as for positive (bottom left) and negative (bottom right) kaons.

8.4.2 Acceptance Sensitivity to JETSET Fragmentation Parameters

In the Monte Carlo simulation, used for acceptance calculation, the apparatus does not operate perfectly. As a consequence, the calculated acceptance depends on the physics generator. Using different parameters for the fragmentation process in the generation leads to different acceptances. The uncertainty associated to the choice of the fragmentation parameters is quantified. For this purpose, the acceptance was calculated using the two Monte Carlo sample produced using the "default" and the "high P_T" tunings (discussed in section Tunings). The systematic error is estimated in each kinematic bin i ($i \equiv (x,z)$ bin or (Q^2,z) bin) using the ratio of acceptances ($\epsilon_{highP_T}/\epsilon_{default}$):

$$\sigma_{sys}^{MC}(i) \leq \frac{\epsilon_{highP_T}/\epsilon_{default}(i) - 1}{2} \cdot M_{cor}^{h}(i) \tag{8.4}$$

Figure 8.22 (8.23) shows the ratio $\epsilon_{highP_T}/\epsilon_{default}$ as a function of x (Q^2) in the z range [0.2,0.3]. The systematic errors are given in appendix **??** and **??**.

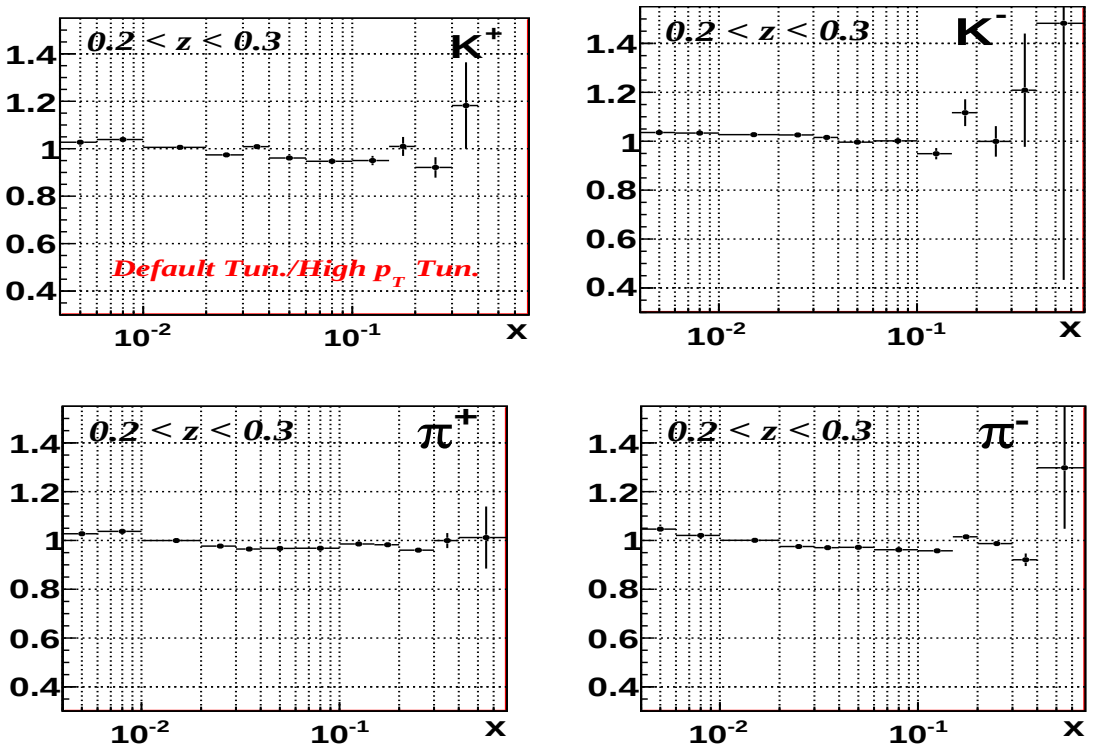

Figure 8.22: Ratio $\epsilon_{highP_T}/\epsilon_{default}$ for pions and kaons as a function of x.

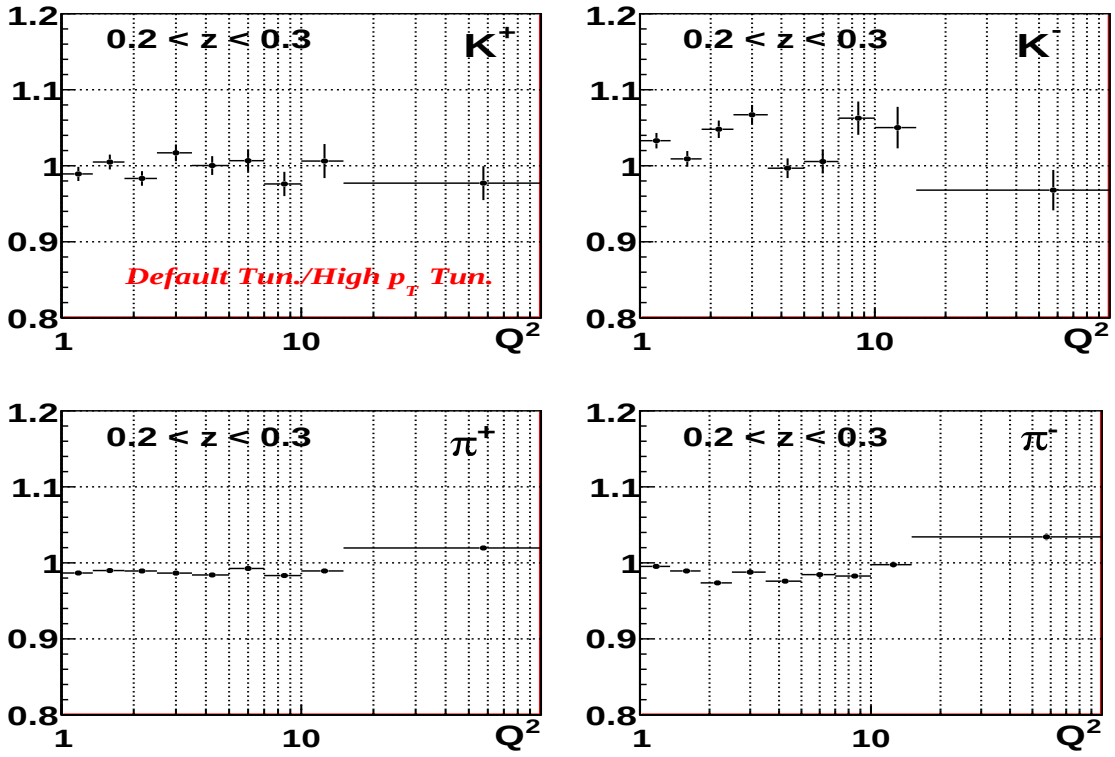

Figure 8.23: Ratio $\epsilon_{highP_T}/\epsilon_{default}$ for pions and kaons as a function of Q^2.

8.4.3 2-3 dimensions Acceptance Calculation

The acceptances (and hadron multiplicities) have been calculated (measured) in two-dimensional binning (x,z) and (Q^2,z) such that the integration is done over the rest of kinematic variables (y, W, P_T, ...). To check that adding a new variable in the acceptance calculation does not affect the final hadron multiplicities, the acceptances and hadron multiplicities have been calculated (measured) in three-dimensional binning (x,z,P_T), (Q^2,z,P_T) and (x,Q^2,z). In each case, the raw multiplicities are measured and then corrected for acceptance as well as for radiative and smearing effects. They are then integrated over the additional variable and compared to the two-dimensional multiplicities. In almost all kinematic bins, the three-dimensional final multiplicities differ by less than 1% from the two-dimensional multiplicities.

Figure 8.24 (8.25) shows the ratio between the two-dimensional (x-z) π^+ (K^+) multiplicities and the three-dimensional (x,z,P_T) multiplicities integrated over P_T. The ratio is compatible with 1. The same result is obtained:

- for positive and negative pions and kaons.
- when comparing $M^h(x,z)$ to $\int_{Q^2} M^h(x,Q^2,z)$, $h \equiv \pi$,K
- when comparing $M^h(Q^2,z)$ to $\int_{P_T} M^h(Q^2,z,P_T)$, $h \equiv \pi$,K
- when comparing $M^h(Q^2,z)$ to $\int_x M^h(x,Q^2,z)$, $h \equiv \pi$,K

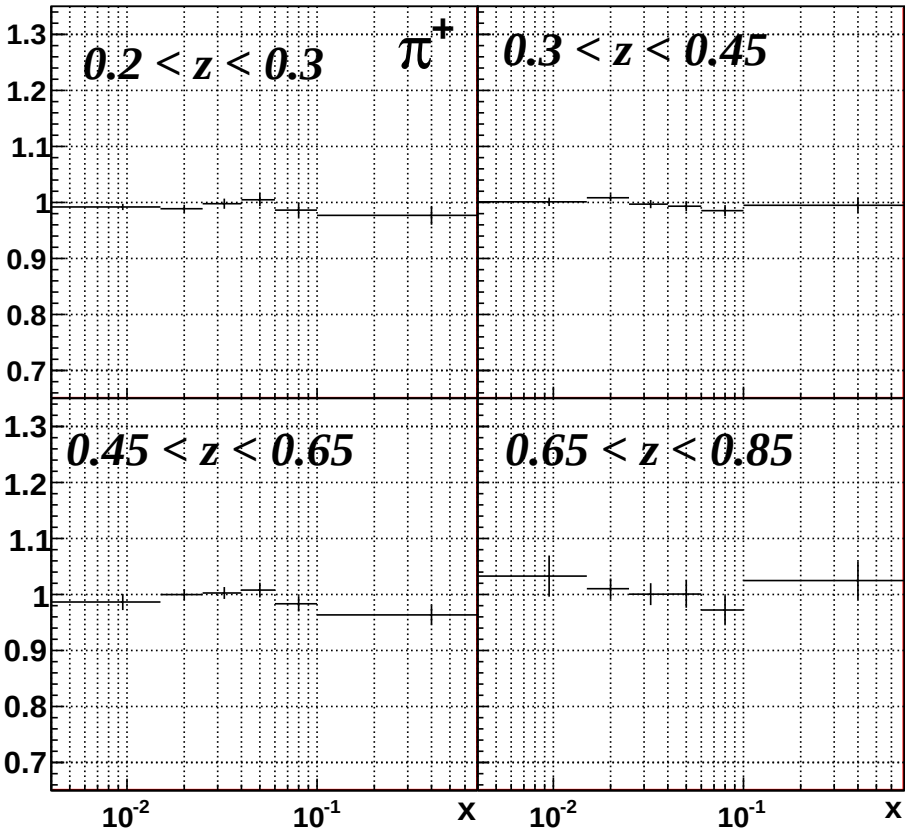

Figure 8.24: Ratio of the two-dimensional (x,z) corrected multiplicities and three-dimensional (x,z,P_T) ones for positive pions.

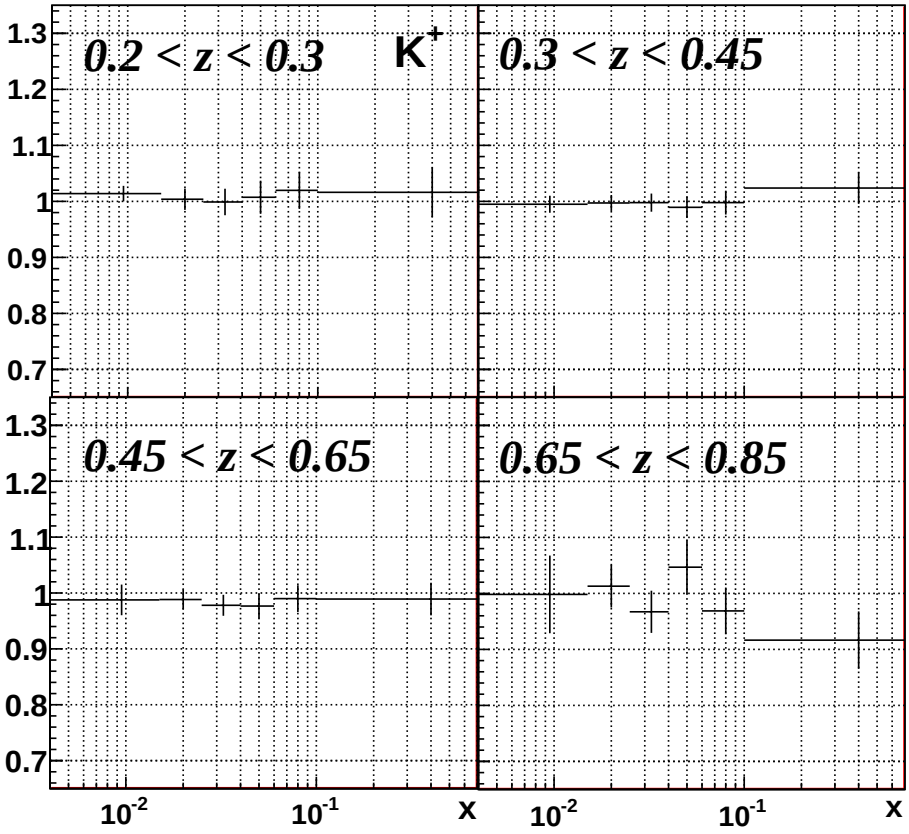

Figure 8.25: Ratio of the two-dimensional (x,z) corrected multiplicities and three-dimensional (x,z,P_T) ones for positive pions.

8.4.4 RICH Systematic Errors

The likelihood cuts which have been used for particle identification, via the RICH, were optimized for the 2004 data [52]. To estimate the systematic errors arising from the identification, one can vary the likelihood cuts around the optimal values while keeping the factor of merit ($S/\sqrt{S+B}$, $S \equiv$ signal, $B \equiv$ background) maximal and constant. Two different sets of likelihood cuts (loose and severe) have been determined (table 8.3). The corresponding RICH efficiencies and misidentification tables are shown in figure 8.26.

	π			K		
	L_π/L_{BG}	L_π/L_K	L_π/L_p	L_K/L_{BG}	L_K/L_π	L_K/L_p
Loose Cuts	0.97	0.98	0.97	1.2	0.98	0.97
Optimal Cuts	1.	1.	1.	1.24	1.02	1.
Severe Cuts	1.1	1.02	1.	1.3	1.04	1.

Table 8.3: Loose, optimal and severe cuts applied on the liklihoods ratios.

The associated systematic error is estimated using the maximum deviation between final multiplicities obtained in the extreme sets (loose & severe) with respect to the nominal set, as follows:

$$\sigma_{sys}^{RICH} = MAX(|M_c^h - M_s^h|; |M_c^h - M_l^h|) \tag{8.5}$$

Here, M_c^h, M_s^h and M_l^h correspond to the final multiplicities obtained using the optimal, severe and loose cuts on the likelihood ratios, respectively. The systematic error are estimated in each kinematic bin ((x,z) or (Q^2,z)) (appendix **??** and **??**). The systematic errors associated to the RICH identification are larger than statistical errors and correspond to the larger contribution

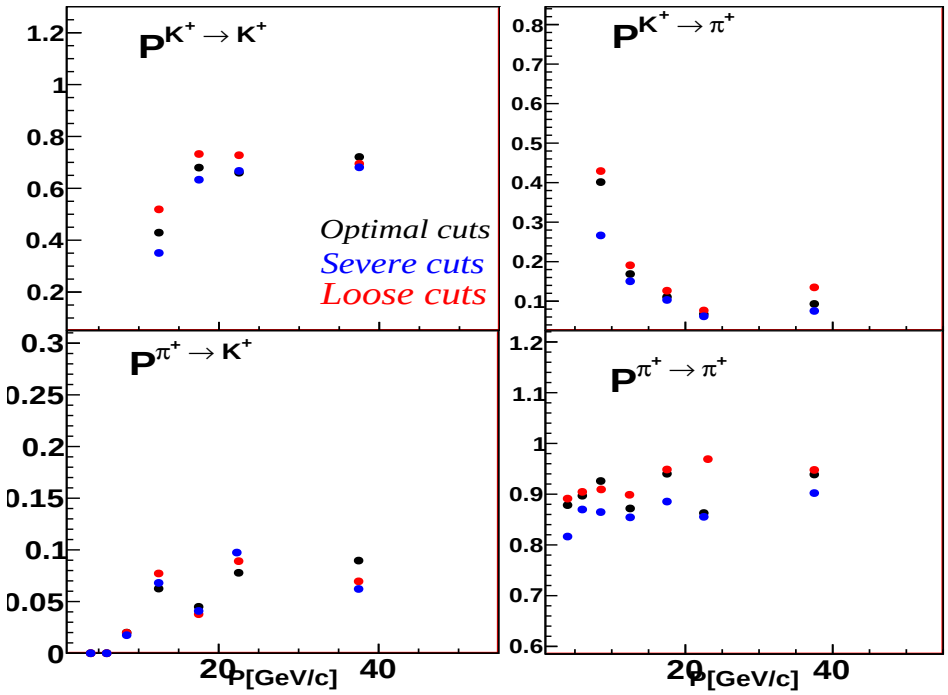

Figure 8.26: Comparison of the RICH efficiency between three sets of cuts (loose, optimal and severe) for positive pion and kaons (flexible corresponds to "loose" cuts). Arrows are directed from left to right

to the systematic errors. Finally, systematic errors evaluated from different sources are added in quadrature.

8.5 Summary and Conclusions

The charge separated pion and kaon multiplicities were measured using data collected by the COMPASS collaboration in 2004 by scattering a 160 GeV/c muons off deuteron target (^{6}LiD). The data cover the kinematic domain: $Q^2 > 1$ [GeV/c]^2, $0.1 < y < 0.9$, $4.10^{-2} < x < 0.7$ and $W > 7$ GeV/c. The z domain was limited to [0.2, 0.85] in order to study the fragmentation process in the current fragmentation region.

The multiplicities, corrected for acceptance as well as for radiative and smearing effects, were measured in bins of the kinematic variables (x, z) and (Q^2,z). They were compared to LO calculations performed using the LO definition of hadron multiplicities in the QCD improved parton model and existing parametrization for FFs and PDFs. For pions, the x dependent and the Q^2 dependent multiplicities are in good agreement with the LO calculations performed using DSS FFs in the range $z < 0.65$ while some discrepancies are observed for higher z. These observations are not surprising since no previous measurements of hadron multiplicities had been performed in this range and consequently the FF parametrization are not well constrained.
The ratio of positive to negative pion multiplicities was measured as a function of x and found to be in good agreement with the recent result from the E00-108 experiment at Jefferson Lab. However, both results differ from the LO predicted ratio.

For kaons, the x dependent multiplicities agree with the LO calculations at small x for $z \in [0.2, 0.65]$ while significant deviations are observed at high x. For $z > 0.65$, the measured multiplicities differ from the calculated ones by more than 60%. The Q^2 dependent multiplicities are better described by the calculations performed using DSS FFs than KRE FFs. This observation is expected since DSS includes kaon multiplicities from the HERMES experiment while KRE

does not.

In summary, the pion and kaon multiplicities are better described by the LO calculations performed using DSS fragmentation functions, an observation well expected. However, the data will provide further constraints to the global fits, especially at small x ($x < 0.2$) and high z ($z > 0.65$).

Chapter 9

Results for Quark Fragmentation Functions

In this chapter, we discuss the LO extraction of quark fragmentation functions into hadrons from pion and kaon multiplicities measured at COMPASS (chapter 8). For this goal, two methods of extraction were tested. To test the validity of the two methods, "pseudo-data", simulating hadron multiplicities, were calculated using the LO definition of multiplicities (Eq. 9.1) in the QCD improved parton model and existing parametrization for parton distribution functions and for quark fragmentation functions. The extracted fragmentation functions were then compared to the initial ones, testing the validity of each method.

The fragmentation functions were extracted from the measured pion and kaon multiplicities using both methods. The resulting fragmentation functions are presented in sections 9.2 and 9.3. A summary is finally given in section 9.4.

9.1 Methods of Extraction

All extraction methods make use of the expression of the hadron multiplicities in the QCD improved parton model (section 2.2.3). For a given hadron h, the multiplicity is given by:

$$M^h(x,Q^2,z) = \frac{1}{\sigma^{incl}(x,Q^2)}\frac{d\sigma^h(x,Q^2,z)}{dxdQ^2} = \frac{\sum_q e_q^2 q(x,Q^2) D_q^h(z,Q^2)}{\sum_q e_q^2 q(x,Q^2)} \tag{9.1}$$

where $q(x,Q^2)$ denotes the parton distribution function (PDF) of a quark of flavor q, $D_q^h(z,Q^2)$ denotes the fragmentation function (FF) of a quark of flavor q into a hadron of type h. In order to extract D_q^h ($D_q^h \equiv D_q^h(z,Q^2)$) from Eq. 9.1, two inputs have to be injected: the hadron multiplicities ($M^h(x,Q^2,z)$) and the PDFs ($q(x,Q^2)$). While the hadron multiplicities are experimentally measured, the PDFs are taken from a certain parametrization which has to be chosen according to COMPASS phase space. For each hadron type ($h \equiv \pi$, K), twelve fragmentation functions, corresponding to six quark flavors and two hadron charges, are defined. For instance, for positive pions (π^+) the six fragmentation functions are: $D_u^{\pi^+}$, $D_{\bar{u}}^{\pi^+}$, $D_d^{\pi^+}$, $D_{\bar{d}}^{\pi^+}$, $D_s^{\pi^+}$, $D_{\bar{s}}^{\pi^+}$ and similarly for π^-. The total number of independent fragmentation functions can be reduced to only six per hadron type by assuming the charge conjugation symmetry ($D_q^{h^+} = D_{\bar{q}}^{h^-}$). Further assumptions can be made in order to reduce the number of unknown FFs, depending on the number of unknowns that can be extracted.
The first method (section 9.1.1) consists in extracting only two unknown fragmentation functions in bins of z and Q^2, using the measured hadron multiplicities in the same bins. The second method (section 9.1.2), however, allows to extract three unknown the fragmentation functions ($\int dz D_q^h(z,Q^2)$) in a given z bin by building more equations corresponding to the multiplicities measured in different x bins.

9.1.1 Method I: π and K FFs in bins of z and Q^2

This method consists in extracting the fragmentation functions (D_q^h) as a function of z in the corresponding Q^2 interval, using the hadron multiplicities measured in z bins. For each hadron

type h, in each (z,Q^2) bin, two equations (one per hadron charge) can be written in terms of six unknown fragmentation functions. They are given, in the case of a deuteron target, by:

$$M^{h^+}(z_0 \pm dz, Q^2) = \frac{4(uD_u^{h^+} + \bar{u}D_{\bar{u}}^{h^+}) + (dD_d^{h^+} + \bar{d}D_{\bar{d}}^{h^+}) + (sD_s^{h^+} + \bar{s}D_{\bar{s}}^{h^+})}{5\mathcal{Q} + 2S}$$

$$M^{h^-}(z_0 \pm dz, Q^2) = \frac{4(uD_{\bar{u}}^{h^+} + \bar{u}D_u^{h^+}) + (dD_{\bar{d}}^{h^+} + \bar{d}D_d^{h^+}) + (sD_{\bar{s}}^{h^+} + \bar{s}D_s^{h^+})}{5\mathcal{Q} + 2S} \tag{9.2}$$

where $q \equiv q(x, Q^2)$ ($q \equiv u$, $\bar{u}$, d, $\bar{d}$, s, $\bar{s}$); $\mathcal{Q}$ denotes the sum of up and down quarks and antiquarks distributions ($\mathcal{Q} \equiv \mathcal{Q}(x, Q^2) = u(x, Q^2) + \bar{u}(x, Q^2) + d(x, Q^2) + \bar{d}(x, Q^2)$) and S denotes the sum of strange quarks and antiquarks distributions ($S \equiv S(x, Q^2) = s(x, Q^2) + \bar{s}(x, Q^2)$). D_q^h ($\equiv D_q^h(Q^2) \equiv \int_{z_0-dz}^{z_0+dz} dz_0 D_q^h(z_0, Q^2)$) correspond to the integrated fragmentation function in a given z bin, at the corresponding Q^2 mean value. In order to extract these independent FFs from only two equations, the number of unknowns must be reduced to only two FFs. For this purpose further assumptions have to be made, depending on the hadron type. The extraction procedure will be detailed in the following for pion (section 9.1.1.1) and kaon (section 9.1.1.2).

9.1.1.1 Pion Fragmentation Functions: $D_{fav}^{\pi}(z, Q^2)$, $D_{unf}^{\pi}(z, Q^6)$

In the case of pions ($\pi^+ \equiv u\bar{d}$, $\pi^- \equiv \bar{u}d$), two favored ($D_u^{\pi^+}$, $D_{\bar{d}}^{\pi^+}$), two unfavored ($D_{\bar{u}}^{\pi^+}$, $D_d^{\pi^+}$) and two strange unfavored ($D_s^{\pi^+}$, $D_{\bar{s}}^{\pi^+}$) fragmentation functions (FFs) describe the pion production in semi-inclusive DIS. Since only two FFs can be extracted, the two favored FFs are assumed to be equal (assumption based on isospin symmetry); and all unfavored FFs (non strange and strange) are assumed to be equal since they are expected to be of the same order of magnitude, as predicted by existing parametrization. The two remaining FFs are:

$$\mathbf{D_{fav}^{\pi}} \equiv D_u^{\pi^+} = D_{\bar{d}}^{\pi^+} = D_{\bar{u}}^{\pi^-} = D_d^{\pi^-}$$

$$\mathbf{D_{unf}^{\pi}} \equiv D_d^{\pi^+} = D_{\bar{u}}^{\pi^+} = D_s^{\pi^+} = D_{\bar{s}}^{\pi^+} = D_{\bar{d}}^{\pi^-} = D_u^{\pi^-} = D_s^{\pi^-} = D_{\bar{s}}^{\pi^-} \tag{9.3}$$

Taking into account these assumptions (Eq. 9.3), the charged pion multiplicities (Eq. 9.2) can be written, in case of a deuterium target, in terms of D_{fav}^{π} and D_{unf}^{π} as follows:

$$M^{\pi^+}(z_0 \pm dz, Q^2) = \frac{(4(u+d) + \bar{u} + \bar{d})\mathbf{D_{fav}^{\pi}} + (u + d + 4(\bar{u} + \bar{d}) + 2(s + \bar{s}))\mathbf{D_{unf}^{\pi}}}{5\mathcal{Q} + 2S} \tag{9.4}$$

$$M^{\pi^-}(z_0 \pm dz, Q^2) = \frac{(u + d + 4(\bar{u} + \bar{d}))\mathbf{D_{fav}^{\pi}} + (4(u+d) + \bar{u} + \bar{d} + 2(s + \bar{s}))\mathbf{D_{unf}^{\pi}}}{5\mathcal{Q} + 2S} \tag{9.5}$$

Here, $D_{fav}^{\pi}(D_{unf}^{\pi}) \equiv \int_{z_0-dz}^{z_0+dz} dz D_{fav}^{\pi}(D_{unf}^{\pi})(z_0, Q^2)$. In each z bin, Eq. 9.4 and Eq. 9.5 form a linear system of two equations with two unknowns: D_{fav}^{π} and D_{unf}^{π}. This system can be written in a matrix form (Eq. 9.6).

$$\vec{M} = B\vec{D} \tag{9.6}$$

For each data point (multiplicity in a z kinematic bin at $< Q^2 >$ and integrated over x in the range [0.004, 0.7]), the parton distribution functions are evaluated at the corresponding mean values of the kinematic variables x and Q^2 using the LO MRST 2004 parametrization [38]. The latter has been taken from the parton distribution functions library LHAPDF [54] (**L**es **H**ouches **A**ccord **PDF**s). The MRST 2004 parametrization has been chosen because of its validity domain ($10^{-5} < x < 1$ and 1.2 [GeV/c]^2 < Q^2 < 10^7 [GeV/c]^2) which is suitable for the COMPASS phase space. In addition, the parametrization is taken at LO because the hadron multiplicities (Eq. 9.1) are derived at LO. Once the B matrix elements are evaluated, they can be injected into the system (Eq. 9.6) and the latter can be solved by inverting the B matrix. The favored fragmentation function is expected to have the largest value.

Note that the pion fragmentation functions (D_{fav}^{π}, D_{unf}^{π}) have been previously extracted by the EMC collaboration [30] in 1989, using the same assumptions. The two fragmentation functions have been extracted for both proton and deuterium targets. The EMC results obtained with deuterium are shown later for comparison.

9.1.1.2 Kaon Fragmentation Functions: $D^K_{str}(z,\, Q^2)$, $D^K_{fav}(z,\, Q^2)$

Similarly to the pion case, six fragmentation functions can be defined for kaons ($K^+ \equiv u\bar{s}$, $K^- \equiv \bar{u}s$): a strange favored ($D^{K^+}_{\bar{s}}$), a favored ($D^{K^+}_{u}$) and four unfavored ($D^{K^+}_{\bar{u}}$, $D^{K^+}_{d}$, $D^{K^+}_{\bar{d}}$, $D^{K^+}_{s}$) fragmentation functions (FFs). Assuming that all unfavored FFs are equal (assumption made in nearly all parametrization without any fundamental symmetry behind), the number of unknowns reduces to three independent FFs (Eq. 9.7).

$$\mathbf{D^K_{fav}} \equiv D^{K^+}_{u} = D^{K^-}_{\bar{u}}$$
$$\mathbf{D^K_{str}} \equiv D^{K^+}_{\bar{s}} = D^{K^-}_{s}$$

$$\mathbf{D^K_{unf}} \equiv D^{K^+}_{d} = D^{K^+}_{\bar{d}} = D^{K^+}_{\bar{u}} = D^{K^+}_{s} = D^{K^-}_{d} = D^{K^-}_{\bar{d}} = D^{K^-}_{u} = D^{K^-}_{\bar{s}} \tag{9.7}$$

Using Eq. 9.2 and Eq. 9.7, the kaon multiplicities are given, in the case of a deuterium target, by :

$$M^{K^+}(z_0 \pm dz, Q^2) = \frac{2\bar{s}\mathbf{D^K_{str}} + 4(u+d)\mathbf{D^K_{fav}} + (u+d+5(\bar{u}+\bar{d})+2s)\mathbf{D^K_{unf}}}{5\mathcal{Q}+2S} \tag{9.8}$$

$$M^{K^-}(z_0 \pm dz, Q^2) = \frac{2s\mathbf{D^K_{str}} + 4(\bar{u}+\bar{d})\mathbf{D^K_{fav}} + (\bar{u}+\bar{d}+5(u+d)+2\bar{s})\mathbf{D^K_{unf}}}{5\mathcal{Q}+2S} \tag{9.9}$$

Here $D^K_{fav} \equiv \int_{z_0-dz}^{z_0+dz} dz D^K_{fav}(z_0, Q^2)$ and similarly for D^K_{str} and D^K_{unf}. Eq. 9.8 and Eq. 9.9 allow to extract only two combinations of fragmentation functions. Since the values of D^K_{fav}, D^K_{unf} and D^K_{str} (Eq. 9.7) are expected to be of different orders of magnitude, no further assumptions are made in this work and one of the three functions is assumed to be known. D^K_{unf} was chosen since it is expected to be the smallest one and thus gives the smallest contribution to the total kaon multiplicities (see figure **??**). In each z bin, D^K_{unf} has been evaluated at the corresponding mean value of Q^2 using a parametrization and then integrated along z between the bin limits. The most appropriate parametrization to be used is DSS since it is the only one that includes pion and kaon multiplicities (preliminary data from Hermes collaboration) in its data set. In addition, the DSS parametrization makes the same assumptions discussed above for kaons. To be consistent with the LO expression of the multiplicities, D^K_{unf} is evaluated at LO and then injected into the following system (obtained from Eqs. 9.8 and 9.9):

$$\begin{pmatrix} M^{K^+} - \frac{(u+d+5(\bar{u}+\bar{d})+2s)}{5\mathcal{Q}+2S} D^K_{unf} \\ M^{K^-} - \frac{(\bar{u}+\bar{d}+5(u+d)+2\bar{s})}{5\mathcal{Q}+2S} D^K_{unf} \end{pmatrix} = \begin{pmatrix} B_{11} & B_{22} \\ B_{21} & B_{22} \end{pmatrix} \cdot \begin{pmatrix} D^K_{str} \\ D^K_{fav} \end{pmatrix} \tag{9.10}$$

The favored (D^K_{fav}) and the unfavored (D^K_{unf}) kaon fragmentation functions have been previously extracted by the EMC experiment [30]. In the EMC analysis, it is assumed that the fragmentation function of strange quark into kaons is related to the favored one (Eq. 9.11). No fundamental argument is given in [30] to justify this assumption.

$$\frac{1}{2}(D^{K^+}_{s} + D^{K^+}_{\bar{s}}) = D^{K^+}_{fav} \tag{9.11}$$

9.1.2 Method II: π and K FFs in 4 z bins using x dependence of M^h

A different method of extraction of fragmentation functions, making use of the x dependence of the hadron multiplicities, is presented. In this work, the pion and kaon multiplicities are determined in 12 x bins and 4 z bins. Thus for each z bin and hadron type, 24 equations (12 x bins $\times$ 2 charges) can be written in terms of six FFs integrated over z in the corresponding z bin (see Eq. 9.2). In these equations, each FF is weighted with a quark distribution of a given flavor ($4uD^{h^+}_{u}$, $4\bar{u}D^{h^+}_{\bar{u}}$, $dD^{h^+}_{d}$, $dD^{h^+}_{\bar{d}}$, $sD^{h^+}_{s}$, $\bar{s}D^{h^+}_{\bar{s}}$ for h^+ for example), evaluated at the mean values of x and Q^2. The extraction of six independent fragmentation functions thus relies on the difference between the six flavors of the PDFs $q(x, Q^2)$. While the up and down quark (u, d) distributions have different shapes and give different weights for the FFs, the sea quark

($\bar{u}$, $\bar{d}$, s, $\bar{s}$) distributions are similar and give similar weights. As a consequence, the number of independent FFs that can be extracted reduces to only three. The method will be detailed in both pion and kaon cases in the following.

9.1.2.1 Pion Fragmentation Functions: D^{π}_{fav}, D^{π}_{unf}, D^{π}_{str}

Three assumptions are made to extract three independent fragmentation functions. Favored FFs are assumed to be equal ($D^{\pi^+}_{u} = D^{\pi^+}_{\bar{d}}$) due to the isospin symmetry, unfavored FFs are assumed to be equal ($D^{\pi^+}_{\bar{u}} = D^{\pi^+}_{d}$) and finally strange unfavored FFs are assumed to be equal ($D^{\pi^+}_{s} = D^{\pi^-}_{\bar{s}}$). The strange unfavored FF is taken as an independent unknown, contrary to the first method where it was assumed to be equal to the unfavored FF. The pion multiplicities can be written in terms of these FFs (D^{π}_{fav}, D^{π}_{unf}, D^{π}_{s}), as given in Eqs 9.12 and 9.13.

$$M^{\pi^+}(x) = \frac{(4(u+d)+\bar{u}+\bar{d})\mathbf{D^{\pi}_{fav}} + (u+d+4(\bar{u}+\bar{d}))\mathbf{D^{\pi}_{unf}} + 2(s+\bar{s})\mathbf{D^{\pi}_{s}}}{5\mathcal{Q}+2S} \tag{9.12}$$

$$M^{\pi^-}(x) = \frac{(u+d+4(\bar{u}+\bar{d}))\mathbf{D^{\pi}_{fav}} + (4(u+d)+\bar{u}+\bar{d})\mathbf{D^{\pi}_{unf}} + 2(s+\bar{s})\mathbf{D^{\pi}_{s}}}{5\mathcal{Q}+2S} \tag{9.13}$$

where $q \equiv q(x,Q^2)$ ($q \equiv u$, $\bar{u}$, d, $\bar{d}$, s, $\bar{s}$), D_{fav} ($\equiv \int_{z_{min}}^{z_{max}} D^{\pi}_{fav}$) is the integrated FF in the z bin $[z_{min}, z_{max}]$. Writing Eqs 9.12 and 9.13 in n x bins, in a given z bin, forms a system of two equations and three unknowns (system given in 9.14). $B^{+}_{1,1}$ ($B^{-}_{1,1}$), $B^{+}_{1,2}$ ($B^{-}_{1,2}$) and $B^{+}_{1,3}$ ($B^{-}_{1,3}$) are respectively the coefficients of D^{π}_{fav}, D^{π}_{unf} and D^{π}_{s} in Eq. 9.12 (9.13).

$$\vec{M} = B \times \vec{D} \Leftrightarrow \begin{pmatrix} M^{\pi^+}_1 \\ M^{\pi^-}_1 \\ M^{\pi^+}_2 \\ M^{\pi^-}_2 \\ . \\ . \\ M^{\pi^+}_{12} \\ M^{\pi^-}_{12} \end{pmatrix} = \begin{pmatrix} B^{+}_{1,1} & B^{+}_{1,2} & B^{+}_{1,3} \\ B^{-}_{1,1} & B^{-}_{1,2} & B^{-}_{1,3} \\ B^{+}_{2,1} & B^{+}_{2,2} & B^{+}_{2,3} \\ B^{-}_{2,1} & B^{-}_{2,2} & B^{-}_{2,3} \\ . & . & . \\ . & . & . \\ B^{+}_{12,1} & B^{+}_{12,2} & B^{+}_{12,3} \\ B^{-}_{12,1} & B^{-}_{12,2} & B^{-}_{12,3} \end{pmatrix} \cdot \begin{pmatrix} D^{\pi}_{fav} \\ D^{\pi}_{unf} \\ D^{\pi}_{s} \end{pmatrix} \tag{9.14}$$

The extraction of three independent fragmentation functions is possible since the x-distributions of up and down quarks are different (see figure 9.1). The extraction of a fourth fragmentation function, for example, is not possible because this would rely on the difference between the sea quark distributions ($\bar{u}$ and $\bar{d}$, s and $\bar{s}$) which is small.

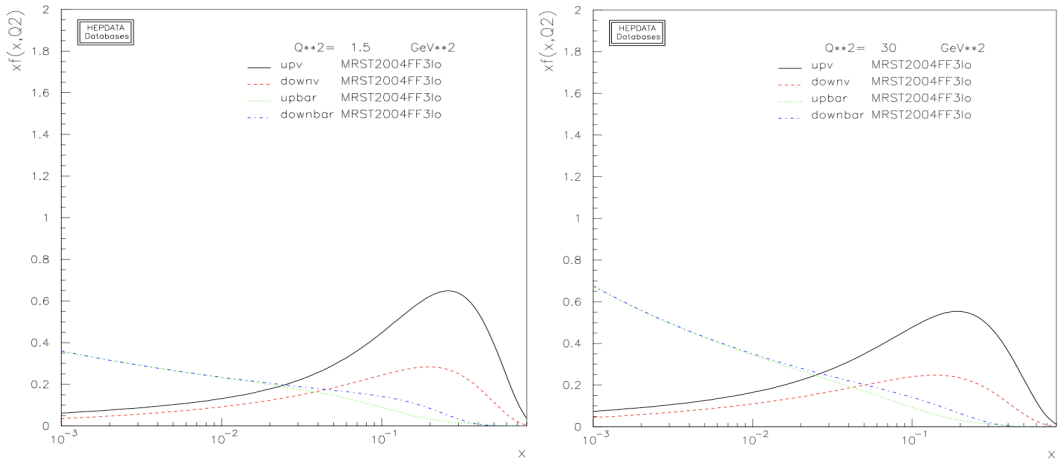

(a) $Q^2 = 1.5$ (GeV/c)^2 (b) $Q^2 = 30$ (GeV/c)^2

Figure 9.1: Up and down quark and antiquarks distributions at $Q^2 = 1.5$ [GeV/c]^2 (a) and at $Q^2 = 30$ [GeV/c]^2(b). Illustrations taken from [70].

9.1.2.2 Kaon Fragmentation Functions: D^K_{str}, D^K_{fav}, D^K_{unf}

The same assumptions (as in section 9.1.1.2) are made here for the kaon fragmentation functions. Consequently, three unknowns (D^K_{str}, D^K_{fav} and D^K_{unf}) can be extracted using two equations.

9.1.3 Testing methods using "pseudo-data"

The methods were tested using "pseudo-data" for both pions and kaons. For this purpose, the hadron multiplicities (Eqs 9.8 - 9.9 and Eqs 9.4 - 9.5) were calculated using the MRST parametrization for PDFs and the DSS parametrization for FFs. In each z bin, the PDFs $q(x, Q^2)$ were evaluated at the mean values of x and Q^2 and the fragmentation functions were integrated within the bin limits. When solving the system, the resulting fragmentation functions were found to be identical to the input ones, confirming the validity of the two methods (I and II) with ideal data (infinitely precised data).

9.2 Results of Method I

Let us remind that methods I (section 9.1.1) leads to the extraction of two independent pion FFs (D^π_{fav} and D^π_{unf}) and two independent kaon FFs (D^K_{str} and D^K_{fav}). The results are shown in two dimensions (12 z bins and 9 Q^2 bins) as well as in one dimension (12 z bins).

9.2.1 Results for Pions: $D^\pi_{fav}(z, Q^2)$ and $D^\pi_{unf}(z, Q^2)$

Results for D^π_{fav} and D^π_{unf} in bins of z and Q^2 bins are presented in section 9.2.1.1. The dependence of the results on the choice of the PDFs parametrization is studied and presented in section 9.2.1.2. Finally the ratio of positive to negative pion fragmentation functions is presented in the last section.
The results are compared to LO and/or NLO predictions (DSS, KRE) as well as to the existing measurements (EMC, JLab).

9.2.1.1 Pion Fragmentation Functions in 12 z bins and 9 Q^2 bins

In figure 9.2 are shown the favored (D^π_{fav}) and the unfavored (D^π_{unf}) pion fragmentation function versus z in nine Q^2 bins. They are compared to the LO fragmentation functions evaluated at the mean value of Q^2 in each kinematic bin in z, as predicted the DSS (red curves) and the KRE (blue curves) parametrization.

Results for D^π_{fav} (figure 9.2(a)) agree with the LO predictions in the entire z range in almost all Q^2 bins. Results for D^π_{unf} (figure 9.2(b)) agree with the predictions in the z range [0.2, 0.6]. For higher z, a significant discrepancy is observed in the Q^2 domain between 1 [GeV/c]^2 and 7 [GeV/c]^2. A similar discrepancy is observed when comparing the pion multiplicities to the LO calculations versus z in the same Q^2 domain (see figure 8.19). Such observed discrepancy for $z > 0.6$ is not surprising since neither DSS nor KRE parametrization fit hadron multiplicities (or semi-inclusive data) in this z domain. While the KRE parametrization uses only e^+e^- data, the DSS parametrization uses, in addition to e^+e^- annihilation and pp collision data, the HERMES hadron multiplicities in the z range restricted to [0.25, 0.6].

In order to compare COMPASS results with the EMC ones [30], the pion fragmentation functions versus z have been extracted from the pion multiplicities integrated over Q^2. Note that the EMC experiment used a 280 [GeV/c] muon beam scattering off a deuterium target. The kinematic domain was restricted to the region: $Q^2 > 4$ [GeV/c]^2, $x > 0.12$, $16 < W^2 < 200$ [GeV/c]^2. While the EMC results are given at the Q^2 mean value of 25 GeV^2, our results are given, in each z bin, at the corresponding mean values of Q^2, which varies between 3.2 [GeV/c]^2 and 3.7 [GeV/c]^2 (see table 9.3). The results are shown in figure 9.3 in comparison with the DSS LO (dashed pink curves) and NLO (full pink curves) predictions and to the KRE LO (dashed blue curves) and NLO (full blue curves) predictions.

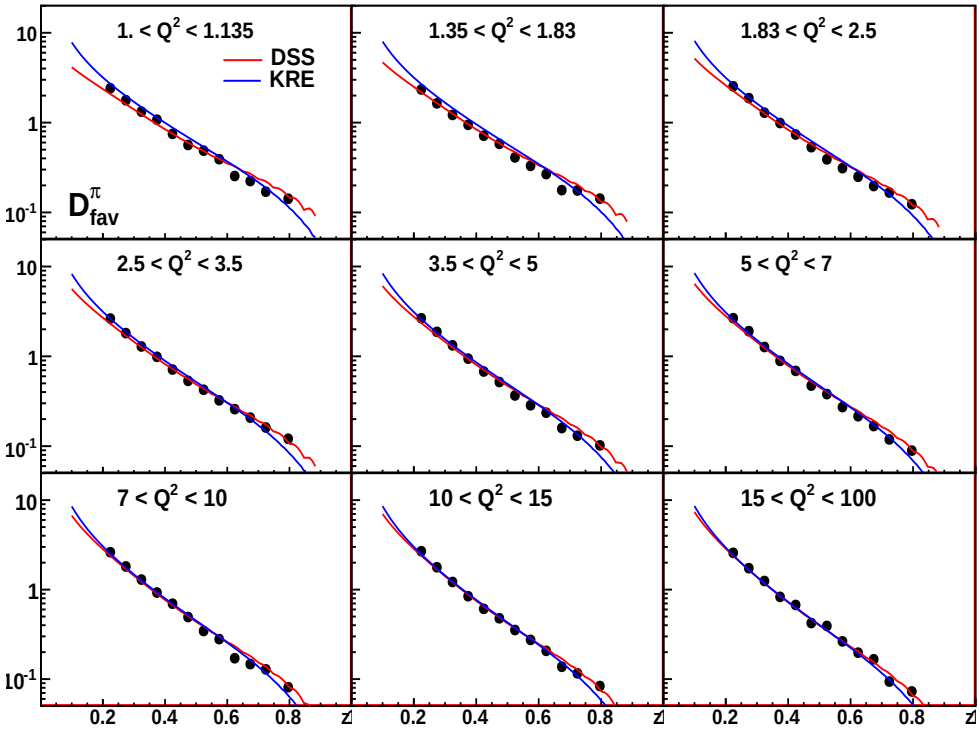

(a) $D^{\pi}_{fav}(z, Q^2)$

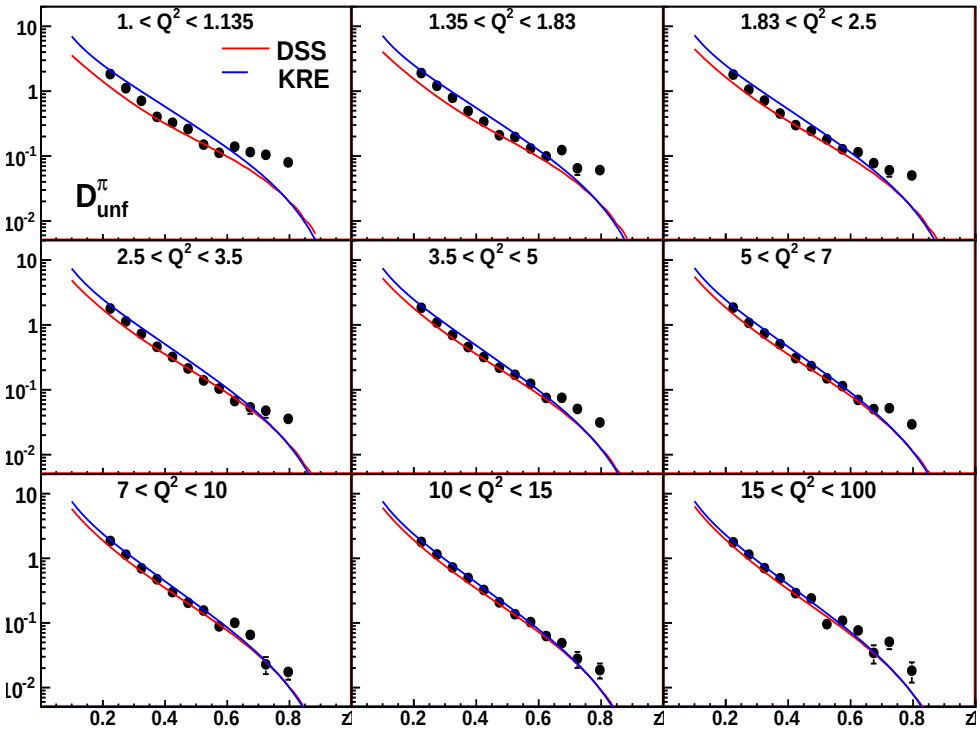

(b) $D^{\pi}_{unf}(z, Q^2)$

Figure 9.2: Favored (a) and unfavored (b) pion fragmentation functions versus z in nine Q^2 bins, compared to LO predictions: DSS (red curves) and KRE (blue curves). The predictions are computed at the Q^2 mean values in each kinematic (z, Q^2) bin. The Q^2 mean values are given in table 9.2, for each Q^2 bin.

The favored (D^{π}_{fav}) and the unfavored (D^{π}_{unf}) fragmentation functions agree with the parametrization (DSS and KRE, LO and NLO) and with the EMC measurement within the errors, for $z < 0.6$. For higher z, the COMPASS results for D^{π}_{fav} are higher than the EMC ones, however they remain in agreement with the parametrization. The unfavored fragmentation function (D^{π}_{unf}) extracted from both COMPASS and EMC deviates from the predictions at $z \sim 0.65$, however both show similar behavior in this z range. The COMPASS D^{π}_{unf} distribution looks smoother than the EMC one.

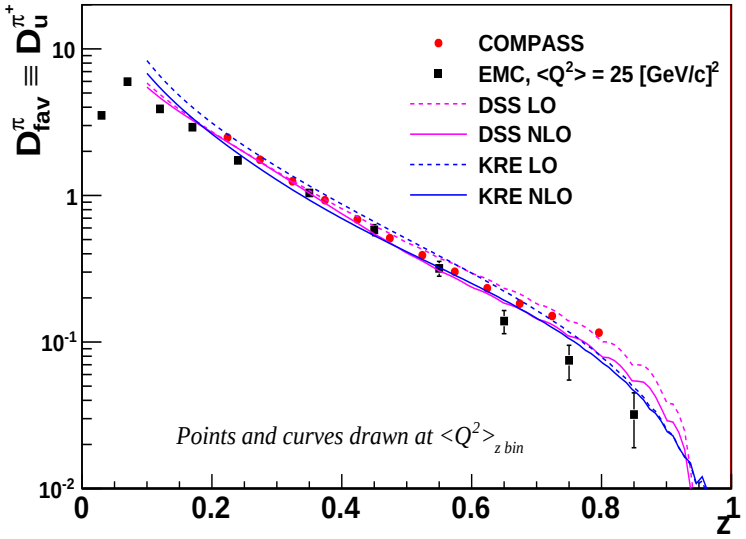

(a) $D^{\pi}_{fav}(z)$

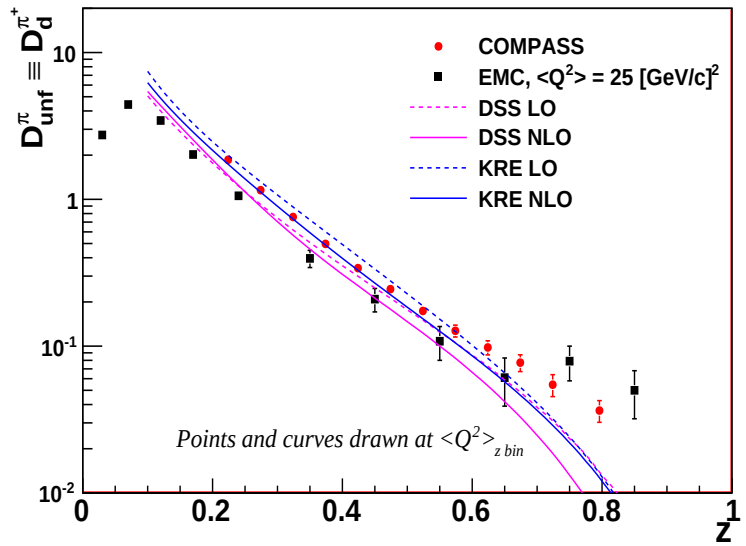

(b) $D^{\pi}_{unf}(z)$

Figure 9.3: Favored (a) and unfavored (b) pion fragmentation functions versus z, compared to the LO (dashed pink curves) and NLO (full pink curves) DSS fragmentation functions, to the LO (dashed blue curves) and the NLO (full blue curves) KRE fragmentation functions.

Finally, the agreement between the COMPASS results and the parametrization as well as previous measurements is expected since pion fragmentation functions are well constrained in the global fits.

9.2.1.2 Sensitivity to parton distribution functions

The extraction of D^{π}_{fav} and D^{π}_{unf} was performed using different parametrizations for parton distribution functions: MRST04 [38], MSTW08 [11] and CTEQ6*l* [56]. These parametrizations make use of different functional forms as well as different data sets in their fir. In addition, they cover different x and Q^2 kinematic domains.

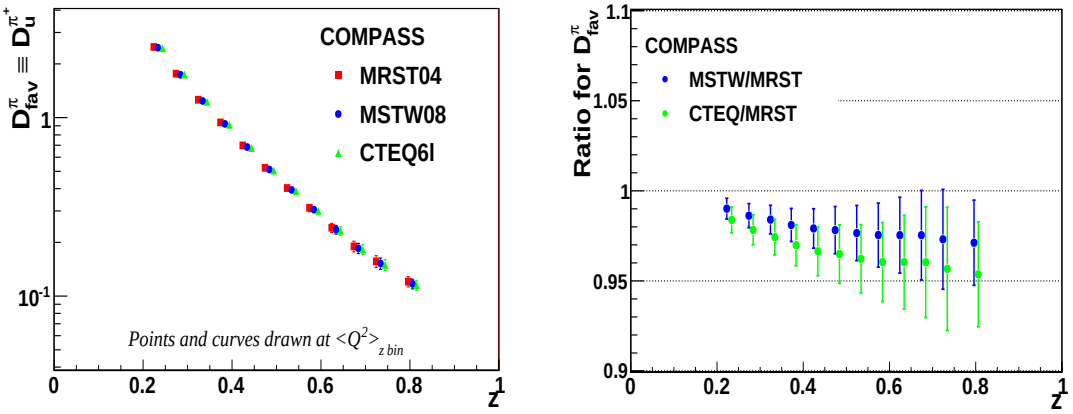

(a) $D^{\pi}_{fav}(z)$ (b) Ratio of $D^{\pi}_{fav}(z)$ for different PDF sets

Figure 9.4: Sensitivity to the PDFs choice: (a) Favored pion fragmentation function (D^{π}_{fav}) versus z obtained using MRST (red markers), MSTW (blue markers) and CTEQ (green markers). Data points (blue and green) are slightly "artificially" shifted to the right. (b) Ratio of D^{π}_{fav} obtained using MSTW or CTEQ parametrization to the one obtained using MRST.

Figure 9.4(a) shows the z distribution of the favored fragmentation function (D^{π}_{fav}) for different parametrization, in comparison with the EMC result. The ratio of D^{π}_{fav} obtained using the MSTW (or CTEQ) parametrization to the one obtained using MRST is shown in figure 9.4(b). Results are found to be compatible within a systematic difference of $\sim 5\%$ in the entire z range. In the case of unfavored fragmentation function (D^{π}_{unf}), the z distributions and the ratios are shown in figures 9.5(a) an 9.5(b) respectively.

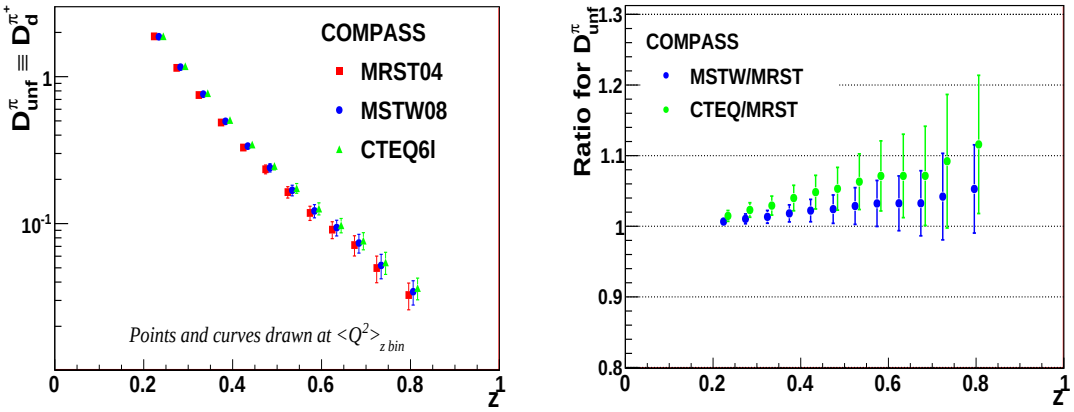

(a) $D^{\pi}_{unf}(z)$ (b) Ratio of $D^{\pi}_{unf}(z)$ for different PDF sets

Figure 9.5: Sensitivity to the PDFs choice: (a) Unfavored pion fragmentation function (D^{π}_{unf}) versus z obtained using MRST (red markers), MSTW (blue markers) and CTEQ (green markers). Data points (blue and green) are slightly "artificially" shifted to the right. (b) Ratio of D^{π}_{unf} obtained using MSTW or CTEQ parametrization to the one obtained using MRST.

The results for D^{π}_{unf} are compatible within less than 10% in the covered z range. For both

D^{π}_{fav} and D^{π}_{unf}, the extracted values are systematically shifted towards lower and higher values respectively. This systematic effect can be taken into account in the systematic errors. In summary the pion fragmentation functions do not show a strong dependence on the choice of PDFs.

9.2.1.3 Ratio of unfavored to favored pion FFs

An interesting quantity to study is the ratio D^{π}_{unf} or D^{π}_{fav} in which many effects cancel out. The COMPASS ratio is shown in figure 9.6 in comparison with EMC (CERN) and E00-108 (Jefferson Lab [57]) results. The E00-108 experiment studied the DIS process using a 5.479 GeV/c electron beam scattering off both proton and deuterium targets. The kinematic domain of data was restricted to: $2 < Q^2 < 4$ GeV^2, $W^2 > 4$ GeV^2, $0.2 < x < 0.6$ and $z > 0.3$.

The COMPASS result agree with the Jlab one in the common z domain ($z > 0.3$). However both COMPASS and JLab results are slightly higher ($\sim 10\%$) than the EMC one. The ratios are compared to the DSS LO (dashed pink curve) and NLO (full pink curve) predictions and to the KRE LO (dashed blue curve) and NLO (full blue curve) predictions. The experimental ratios differ from the predictions in the entire z range. This discrepancy can be interpreted by the missing higher orders corrections, which are not taken into account in the LO extraction. It can also be due an unsuitable functional form assumed in the parametrization. Finally, one must note that both DSS and KRE do not include data (hadron multiplicities) from COMPASS or E00-108 experiments.

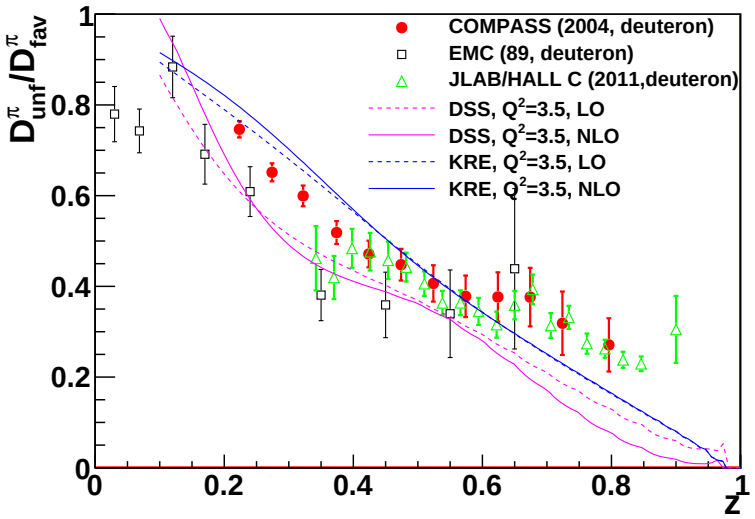

Figure 9.6: Ratio of unfavored to favored pion fragmentation functions as a function of z, drawn at the Q^2 mean value in each z bin, in comparison with the EMC ratio given at $< Q^2 >= 25$ GeV^2, and the recent E00-108 (JLab/Hall C) result. The curves correspond to the DSS LO (dashed pink curve) and NLO (full pink curves) ratios and to the KRE LO (dashed blue curve) and NLO (full blue curve) ratios.

9.2.2 Results for Kaons (D^K_{str} and D^K_{fav}) in 12 z bins

Similarly to pions, kaon fragmentation functions D^K_{fav} and D^K_{str} have been extracted as a function of z. They are presented in the first section and compared to the existing measurements and predictions. The LO predictions are calculated at the mean value of Q^2 in each z bin. For this purpose, in each z bin, the PDFs are evaluated at the mean values of x and Q^2, and the FFs are evaluated at the Q^2 mean value and integrated in the corresponding z bin. In the second section, the dependence on the PDFs choice is studied. In the last section, the dependence on D^K_{unf} is presented.

9.2.2.1 Kaon Fragmentation Functions

The results for the favored D^K_{fav} ($\equiv D^{K^+}_u = D^{K^-}_{\bar{u}}$) and the strange favored D^K_{str} ($\equiv D^{K^+}_{\bar{s}} = D^{K^-}_s$) kaon fragmentation functions are shown in figure 9.7, in comparison with the DSS (pink) and the KRE (blue) LO (dashed curve) and NLO (full curve) predictions.

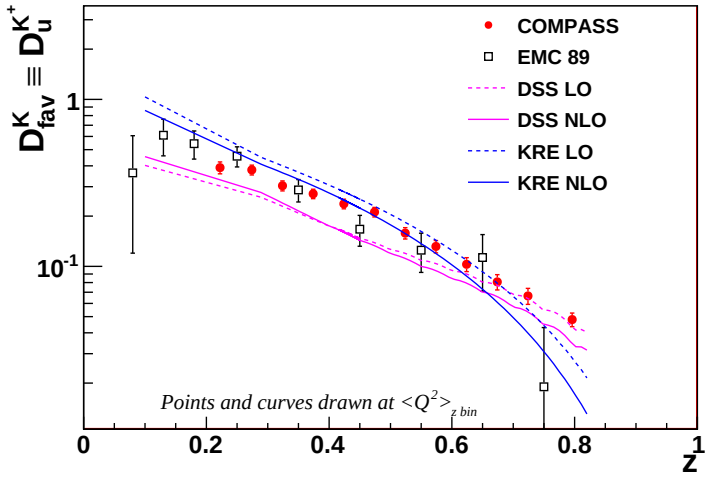

(a) $D^K_{fav}(z)$

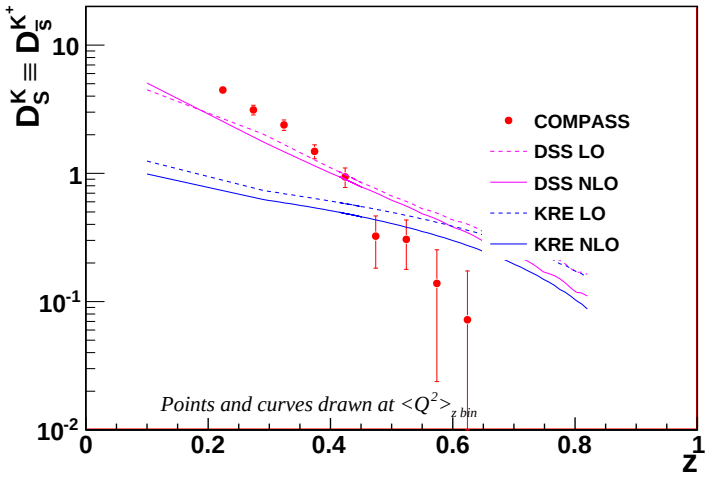

(b) $D^K_{str}(z)$

Figure 9.7: Favored (a) and strange favored (b) kaon fragmentation functions versus z, compared to the DSS LO (dashed pink curve) and NLO (full pink curve) predictions and to the KRE LO (dashed blue curve) and NLO (full blue curve) predictions. The LO calculations are performed at the mean values of Q^2 in each z bin (see table 9.3). D^K_{fav} is also compared to the EMC result extracted at $<Q^2> = 25$ GeV^2.

For D^K_{fav}, the result agrees within the errors with the EMC one. It agrees also with both parametrization DSS and KRE and does not show any tendency to be better described by one parametrization than by the other. No previous measurements of D^K_{str} have been previously performed. A significant discrepancy between the result and the LO and the NLO predictions is observed, especially in the slope of the distribution. COMPASS data favors the fragmentation of strange quarks into kaons with smaller fractional energy z. Finally, one must remember that D^K_{str} was poorly constrained in the FFs parametrization due to the lack of kaon data. As a consequence, such discrepancy is not surprising.

9.2.2.2 Sensitivity to Parton Distribution Functions

Similarly to the pion case, the kaon fragmentation functions have been extracted using three different parametrization for the parton distribution functions. Figure 9.8 shows the D^K_{fav} distributions versus z using MRST04, MSTW08 and CTEQ6l parametrization. The ratios of D^K_{fav} obtained using MSTW/CTEQ parametrization to the one obtained using MRST is also shown in figure 9.8(b). The resulting D^K_{fav} differ by 2 to 20% in the case of MSTW and by ~ 5 to 40% in the case of CTEQ with respect to the MRST parametrization in the low z domain.

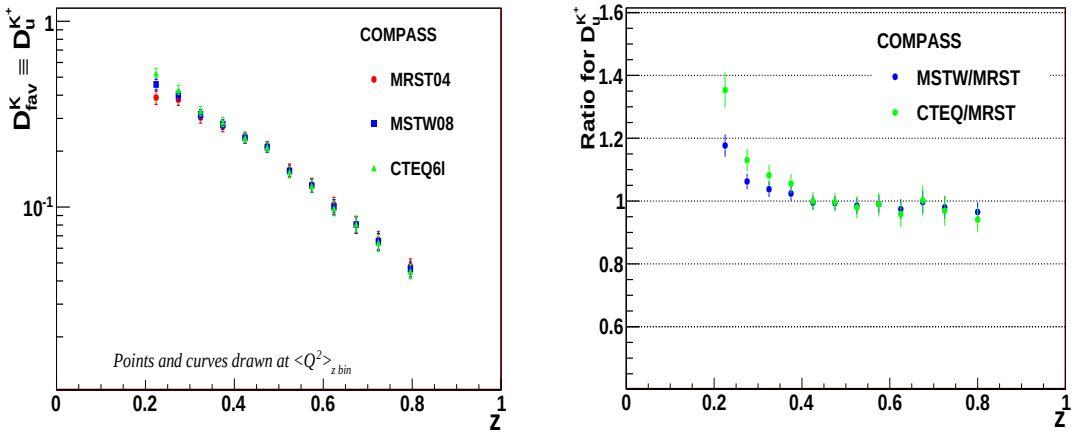

(a) $D^K_{fav}(z)$ (b) Ratio for $D^K_{fav}(z)$

Figure 9.8: Sensitivity to the PDFs choice: (a) Favored kaon fragmentation function (D^K_{fav}) distributions versus z for different PDF parametrizations, compared to EMC result (open marker) and to the LO DSS predictions. (b) Ratio of D^K_{fav} obtained using MSTW or CTEQ parametrization to the one obtained using the MRST parametrization.

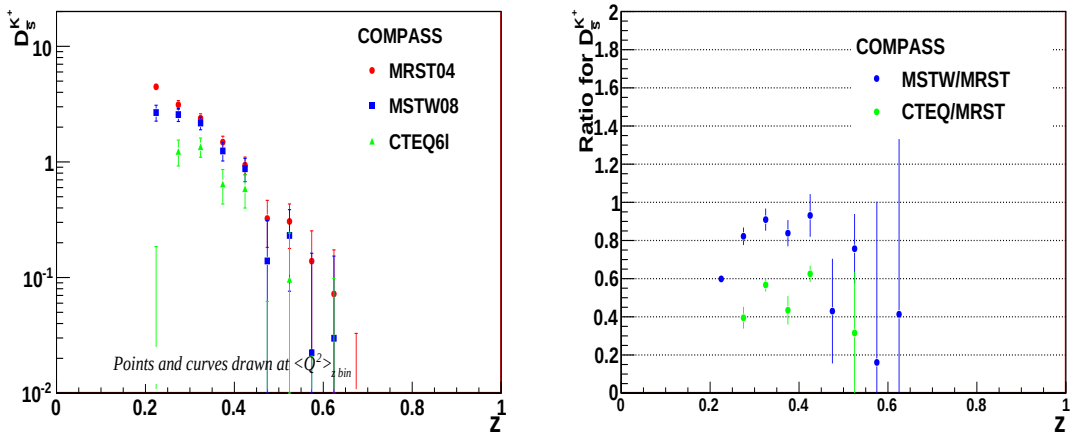

(a) $D^K_{str}(z)$ (b) Ratio for $D^K_{str}(z)$

Figure 9.9: Sensitivity to the PDFs choice: (a) Favored kaon fragmentation function (D^K_{fav}) distributions versus z for different PDF parametrization, compared to EMC result (open marker) and to the LO DSS predictions. (b) Ratio of D^K_{fav} obtained using MSTW or CTEQ parametrization to the one obtained using the MRST parametrization.

Figure 9.9(a) shows results for D^K_{str} and figure 9.9(b) shows the ratios between results obtained with different PDFs. The D^K_{str} obtained using MSTW(CTEQ) parametrization are systematically $\sim$ 20% ($\sim$ 40%) higher than using MRST in the nearly all z bins. The difference likely

originates from the difference in the strange quark distribution between MRST, MSTW and CTEQ, as can be seen in figure 9.10. The dependence of the results on the PDF choice can be taken into account in the systematic errors.

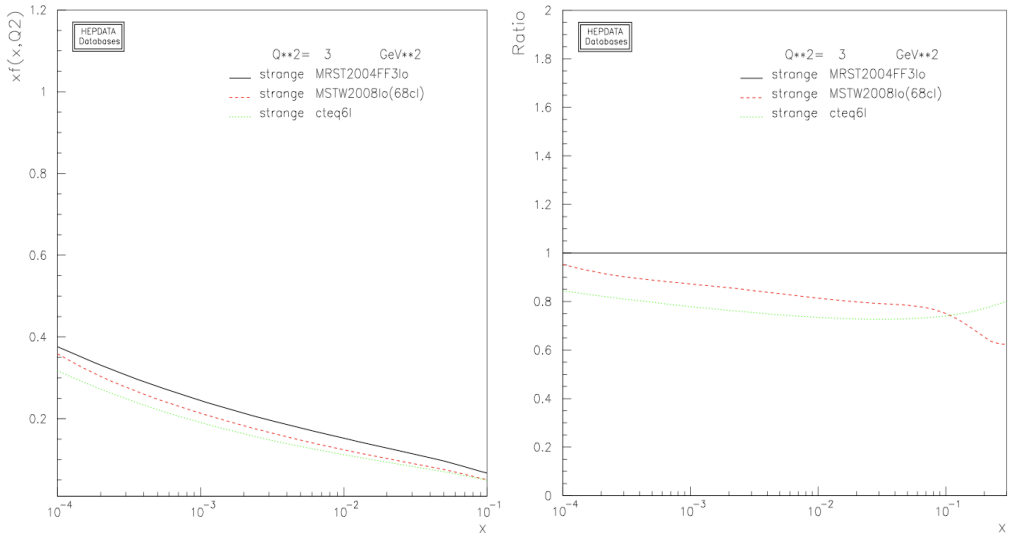

(a) (b)

Figure 9.10: (a) Strange quark distributions at $Q^2 = 3$ [GeV/c]^2 as a function of x, given by MRST2004, MSTW2008 and CTEQ6l parametrization. (b) Ratios of MSTW and CTEQ strange distributions to the MRST one. Illustrations taken from [70].

9.2.2.3 Sensitivity to D^K_{unf} choice

The sensitivity of the D^K_{fav} and D^K_{str} results to the choice of D^K_{unf} can be studied and quantified by changing the latter by a given factor. For this purpose, D_{unf} has been varied between two extreme sets of values: the DSS and the KRE parametrization (table 9.1). For each z bin, D^K_{fav} and D^K_{str} have been extracted for 4 different values of D^K_{unf}:

$$D^{K,i}_{unf} \in [D^{K,DSS}_{unf}, D^{K,KRE}_{unf}]$$

$$D^{K,i}_{unf} = D^{K,DSS}_{unf} + i \times \frac{(D^{K,KRE}_{unf} - D^{K,DSS}_{unf})}{3}, \quad i = 0,1,2,3 \tag{9.15}$$

In the following, $D^{K,DSS}_{unf}$ ($D^{K,KRE}_{unf}$) will be denoted by D^1_{unf} (D^4_{unf}). Figure 9.11(a) shows the resulting D^K_{fav} obtained for different D^K_{unf} and figure 9.11(b) shows the ratios of D^K_{fav} obtained using D^i_{unf} ($i \equiv 2,3,4$) to the one obtained using D^1_{unf}. A strong dependence of D^K_{fav} on the choice of D^K_{unf} is observed in the entire z range, in particular, at small z ($z < 0.4$) where the results differ by a factor of 2.

For D^K_{str}, the resulting distributions are shown in figure 9.12(a). For all values of D^K_{unf}, except the one given by the DSS parametrization, unphysical results are obtained for D^K_{str} which is found to be negative in nearly all z bins. This observation confirms that the Kretzer (KRE) parametrization, which fits FFs from only e^+e^- annihilation data, does not describe the fragmentation process in the COMPASS kinematic domain. In summary, both favored and stranged favored kaon fragmentation functions depend strongly on the choice of D^K_{unf}.

Other extractions have been performed using different assumptions. At first, D^K_{fav} was assumed to be known from external parametrization and both D^K_{str} and D^K_{unf} were extracted. A second

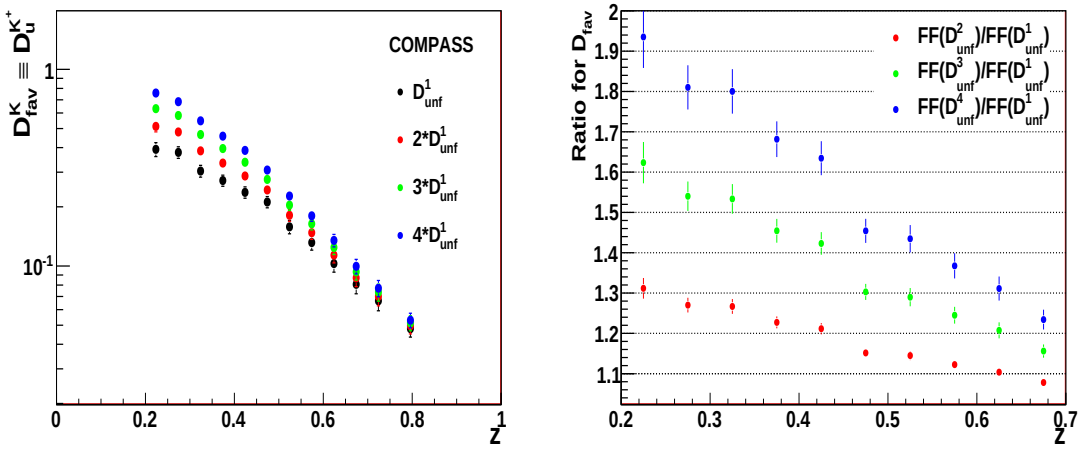

(a) $D^K_{fav}(z)$ (b) Ratio of $D^K_{fav}(z)$ for different D^K_{unf}

Figure 9.11: (a): Favored kaon fragmentation function (D^K_{fav}) distributions versus z for different values of D^K_{unf}, compared to EMC result (open marker) and to the LO DSS predictions. (b): Ratio of D^K_{fav} obtained using D^i_{unf} to the one obtained using D^1_{unf}.

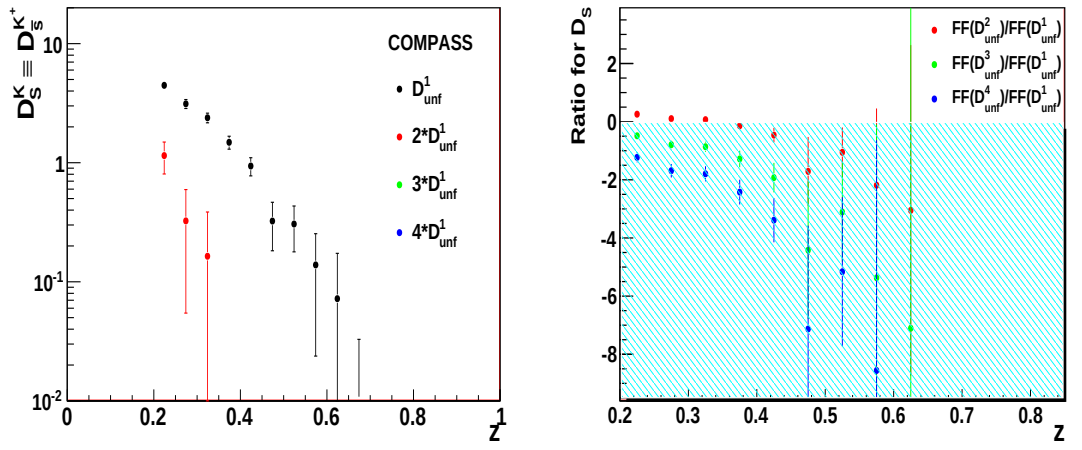

(a) $D^K_{str}(z)$ (b) Ratio of $D^K_{str}(z)$ for different D^K_{unf}

Figure 9.12: (a): Favored kaon fragmentation function (D^K_{str}) distributions versus z for different values of D^K_{unf}, compared to the LO DSS predictions. (b): Ratio of D^K_{str} obtained using D^i_{unf} to the one obtained using D^1_{unf}.

assumption which relates D^K_{unf} to the two other has been tested. This assumption has been used by the EMC analysis. In both cases, the obtained results were found to be different from the presented ones. More details and results can be found in [75].

9.3 Results of Method II

The particularity of this method is to treat simultaneously several x bins in order to get more equations and thus to extract a larger number of FFs (three instead of two). The method II makes use of the hadron multiplicities measured in 12 x bins and 4 z bins. In each z bin, it allows in principle to extract three independent fragmentation functions integrated over z in the corresponding z range. This extraction takes advantage of the different shapes of the

z bin	D^1_{unf}	D^2_{unf}	D^3_{unf}	D^4_{unf}
$[0.20, 0.25]$	0.091660	0.212773	0.333887	0.455000
$[0.25, 0.30]$	0.045960	0.148113	0.250267	0.352420
$[0.30, 0.35]$	0.029420	0.110513	0.191607	0.272700
$[0.35, 0.40]$	0.022640	0.084447	0.146253	0.208060
$[0.40, 0.45]$	0.012880	0.062973	0.113067	0.163160
$[0.45, 0.50]$	0.011160	0.043193	0.075227	0.107260
$[0.50, 0.55]$	0.007020	0.029940	0.052860	0.075780
$[0.55, 0.60]$	0.006500	0.022620	0.038740	0.054860
$[0.60, 0.65]$	0.003420	0.014093	0.024767	0.035440
$[0.65, 0.70]$	0.004500	0.010800	0.017100	0.023400
$[0.70, 0.75]$	0.002580	0.006107	0.009633	0.013160
$[0.75, 0.85]$	0.001170	0.002837	0.004503	0.006170

Table 9.1: Values of D^K_{unf} taken for the study of the sensitivity of D^K_{str} and D^K_{fav} to the choice of D^K_{unf}.

Bin n°	Q^2 bin	$< Q^2 >$	$< x >$
1	$[1, 1.35]$	1.165	0.011
2	$[1.35, 1.83]$	1.57	0.015
3	$[1.83, 2.5]$	2.14	0.02
4	$[2.5, 3.5]$	2.95	0.03
5	$[3.5, 5.0]$	4.16	0.042
6	$[5.0, 7.0]$	5.88	0.061
7	$[7.0, 10.]$	8.27	0.086
8	$[10., 15.]$	11.9	0.121
9	$[15, 100]$	20.2	0.189

Table 9.2: Mean values of Q^2 and x in the 9 Q^2 bins. This applies to all the following figures.

Bin n°	z bin	$< z >$	$< x >$	$< Q^2 >$
1	$[0.20, 0.25]$	0.224	0.0356	3.584
2	$[0.25, 0.30]$	0.274	0.0366	3.608
3	$[0.30, 0.35]$	0.324	0.0375	3.634
4	$[0.35, 0.40]$	0.374	0.0383	3.652
5	$[0.40, 0.45]$	0.424	0.0396	3.701
6	$[0.45, 0.50]$	0.474	0.0407	3.698
7	$[0.50, 0.55]$	0.524	0.0419	3.716
8	$[0.55, 0.60]$	0.574	0.0429	3.702
9	$[0.60, 0.65]$	0.624	0.0429	3.598
10	$[0.65, 0.70]$	0.674	0.0433	3.517
11	$[0.70, 0.75]$	0.724	0.0425	3.355
12	$[0.75, 0.85]$	0.796	0.0421	3.198

Table 9.3: Mean values of z, Q^2 and x in the twelve z bins.

quark distributions versus x (section 9.1.2).The method has been tested, using infinitely precise pseudo-data, and found to be valid. Using experimentally measured multiplicities, however, some limitations appear due to the limited precision of the data. The results obtained for both pions and kaons are discussed.

9.3.1 Pion Fragmentation Functions D^{π}_{fav}, D^{π}_{unf} and D^{π}_{s}

In principle, three pion fragmentation functions (favored, unfavored and strange) can be extracted using this method. Their contributions to the total π^+ (Eq. (9.16a)) and π^- (Eq. (9.16b)) multiplicities were calculated using the MRST parametrization for PDFs and the DSS one for FFs. They are shown in figure 9.13 (figure 9.14) for π^+ (π^-) together with the ratio of each contribution to the total multiplicity. The contribution of the strange pion FF is found to be small ($< 6\%$) compared to the two other contributions. This observation indicates that pion multiplicities are not sensitive to D^{π}_{s} (unsignificant sensitivity). Using COMPASS multiplicities, no meaningful result was obtained for D^{π}_{s} (values given in table 9.4).

$$M^{\pi} = \alpha + \beta + \gamma$$

$$\text{For } \pi^+ : \alpha = \frac{4(\mathrm{u}+\mathrm{d})+\bar{\mathrm{u}}+\bar{\mathrm{d}}}{5\mathcal{Q}+2\mathrm{S}}\mathrm{D}^{\pi}_{\mathrm{fav}}, \quad \beta = \frac{\mathrm{u}+\mathrm{d}+4(\bar{\mathrm{u}}+\bar{\mathrm{d}})}{5\mathcal{Q}+2\mathrm{S}}\mathrm{D}^{\pi}_{\mathrm{unf}}, \quad \gamma = \frac{2(\mathrm{s}+\bar{\mathrm{s}})}{5\mathcal{Q}+2\mathrm{S}}\mathrm{D}^{\pi}_{\mathrm{s}} \tag{9.16a}$$

$$\text{For } \pi^- : \alpha = \frac{\mathrm{u}+\mathrm{d}+4(\bar{\mathrm{u}}+\bar{\mathrm{d}})}{5\mathcal{Q}+2\mathrm{S}}\mathrm{D}^{\pi}_{\mathrm{fav}}, \quad \beta = \frac{4(\mathrm{u}+\mathrm{d})+\bar{\mathrm{u}}+\bar{\mathrm{d}}}{5\mathcal{Q}+2\mathrm{S}}\mathrm{D}^{\pi}_{\mathrm{unf}}, \quad \gamma = \frac{2(\mathrm{s}+\bar{\mathrm{s}})}{5\mathcal{Q}+2\mathrm{S}}\mathrm{D}^{\pi}_{\mathrm{s}} \tag{9.16b}$$

Here, $q \equiv q(x,Q^2)$ ($q \equiv u, d, s, \bar{u}, \bar{d}, \bar{s}$) and $D^h_q \equiv \int_{0.2}^{0.85} D^h_q(z,Q^2)$.

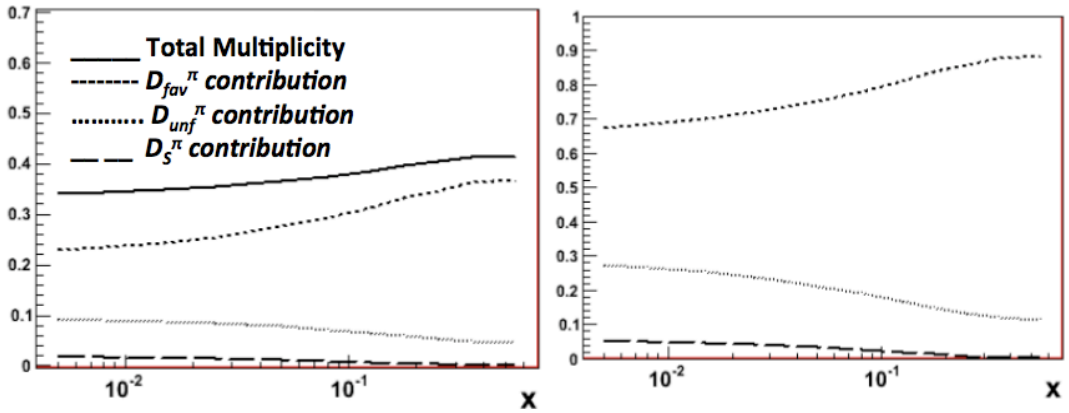

Figure 9.13: left: Contribution of the three fragmentation function to the total π^+ multiplicity (Eq. 9.16a) versus x calculated using MRST (for PDFs) and DSS (for FFs) parametrization. right: Ratio between each contribution and the total multiplicity.

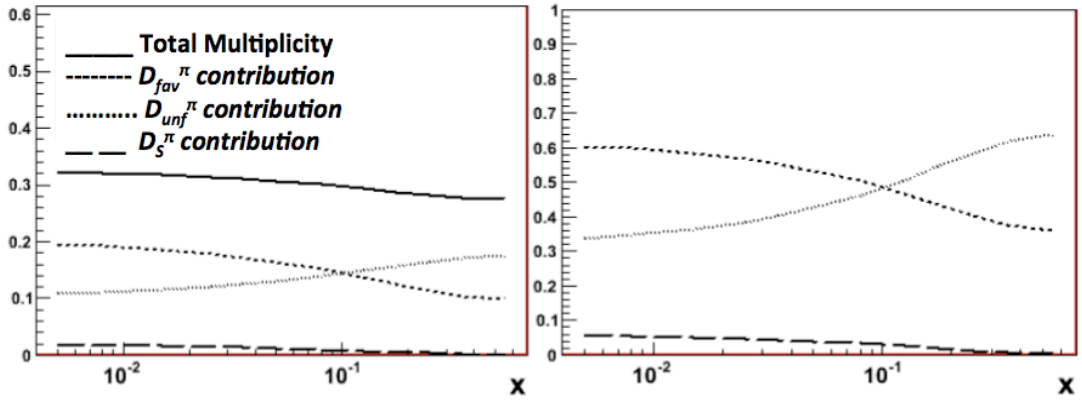

Figure 9.14: same as in figure 9.16 for π^-.

The contributions of D^{π}_{fav} and D^{π}_{unf} are different in the entire x range in both π^+ and π^- cases. This is due to the difference between up and down quark distributions and indicates that D^{π}_{fav} and D^{π}_{unf} can be extracted as two independent unknowns. Results are shown in figure 9.15 and found to be compatible with the results obtained from method I (section 9.2.1).

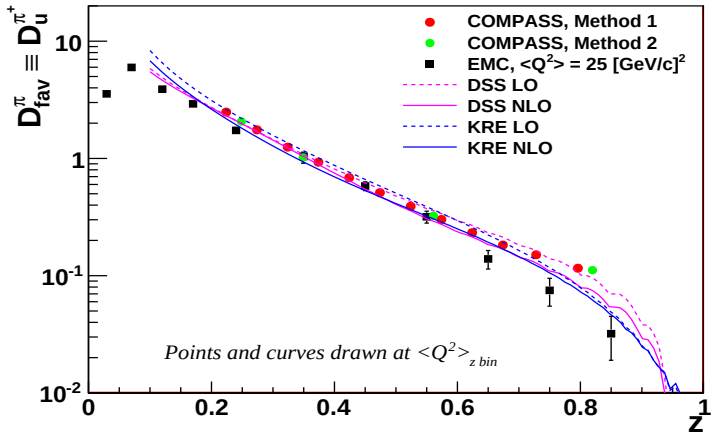

(a)

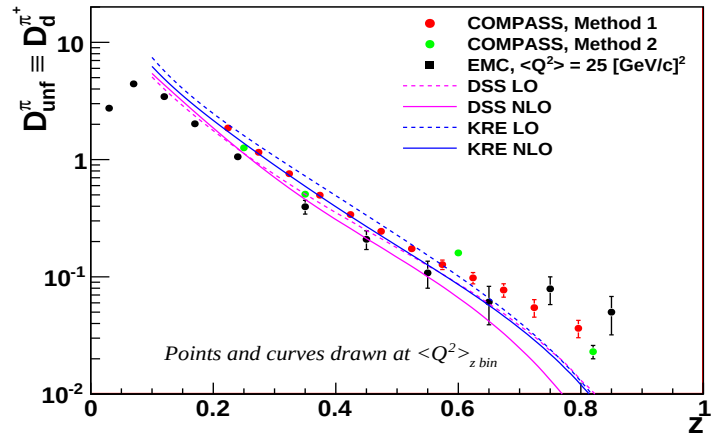

(b)

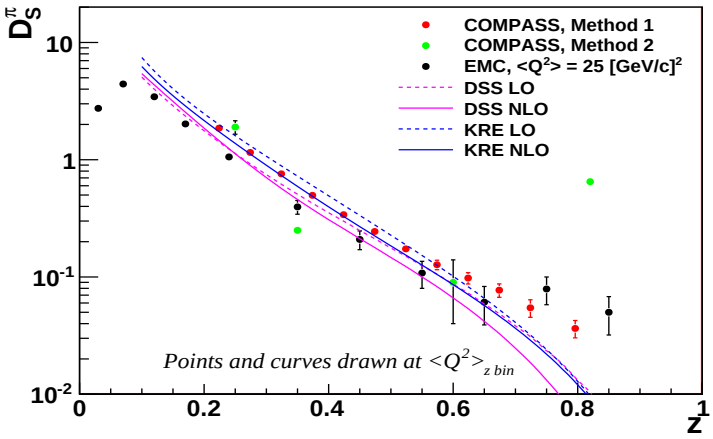

(c)

Figure 9.15: Favored (a), unfavored (b) and strange (c) pion fragmentation functions as a function of z, extracted from method 1 (red markers) and method 2 (green markers). For the strange FF, red points correspond to D^{π}_{unf} since method 1 allows to determine only two FFs, thus $D^{\pi}_{S} = D^{\pi}_{unf}$.

z bin	D^{π}_{fav}	D^{π}_{unf}	D^{π}_{s}
$[0.20, 0.30]$	2.05 ± 0.03	1.26 ± 0.027	1.9 ± 0.25
$[0.30, 0.45]$	1.01 ± 0.11	0.507 ± 0.011	0.25 ± 0.107
$[0.45, 0.65]$	0.40 ± 0.005	0.16 ± 0.005	0.09 ± 0.05
$[0.65, 0.85]$	0.11 ± 0.003	0.023 ± 0.003	0.65 ± 0.03

Table 9.4: Favored ($D^{\pi^+}_{u}$), unfavored ($D^{\pi^+}_{\bar{u}}$) and strange ($D^{\pi^+}_{s}$) pion fragmentation functions extracted using method II.

9.3.2 Kaon Fragmentation Functions

In the case of kaons, the three unknown fragmentation functions are: D^{K}_{str}, D^{K}_{fav} and D^{K}_{unf}. The contribution of each one to the total K^+ (Eq. (9.17a)) and K^- (Eq. 9.17b) multiplicities is shown in left part of figures 9.16 and 9.17 respectively. The ratio between each contribution and the total multiplicity is also shown for K^+ (9.16 right) and K^- (9.17 right).

$$\text{For } \mathrm{K}^+ : \frac{2\bar{\mathrm{s}}}{5\mathcal{Q}+2\mathrm{S}}\mathrm{D}^{\mathrm{K}}_{\mathrm{str}}, \quad \frac{4(\mathrm{u}+\mathrm{d})}{5\mathcal{Q}+2\mathrm{S}}\mathrm{D}^{\mathrm{K}}_{\mathrm{fav}}, \quad \frac{\mathrm{u}+\mathrm{d}+5(\bar{\mathrm{u}}+\bar{\mathrm{d}})+2\mathrm{s}}{5\mathcal{Q}+2\mathrm{S}}\mathrm{D}^{\mathrm{K}}_{\mathrm{unf}} \tag{9.17a}$$

$$\text{For } \mathrm{K}^- : \frac{2\mathrm{s}}{5\mathcal{Q}+2\mathrm{S}}\mathrm{D}^{\mathrm{K}}_{\mathrm{str}}, \quad \frac{4(\bar{\mathrm{u}}+\bar{\mathrm{d}})}{5\mathcal{Q}+2\mathrm{S}}\mathrm{D}^{\mathrm{K}}_{\mathrm{fav}}, \quad \frac{5(\mathrm{u}+\mathrm{d})+\bar{\mathrm{u}}+\bar{\mathrm{d}}+2\bar{\mathrm{s}}}{5\mathcal{Q}+2\mathrm{S}}\mathrm{D}^{\mathrm{K}}_{\mathrm{unf}} \tag{9.17b}$$

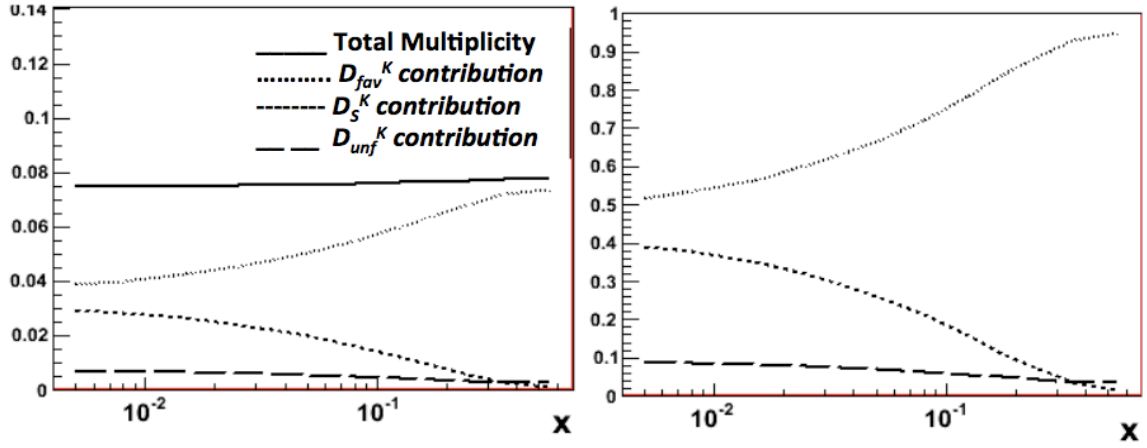

Figure 9.16: (a): Contribution of the three fragmentation function terms to the total K^+ multiplicity as a function of x. The multiplicity is calculated using Eqs. 9.15(c) and 9.15(c). The MRST and the DSS parametrizations are used for the parton distribution functions and the quark fragmentation functions respectively. (b): Ratio between each contribution and the total multiplicity.

Similarly to the case of pions, two limitations appear which prevent from extracting the three FFs. First, the contributions of both D^{K}_{str} and D^{K}_{fav} to the K^- multiplicity (see Eq. 9.17b) have the same shape and the same order of magnitude in the entire x range. This observation indicates that the extraction of the two independent fragmentation functions D^{K}_{fav} and D^{K}_{str} cannot be performed using data with limited precision. Second, the contribution of D^{K}_{unf} to the K^+ multiplicity is small (10%) in the entire x range conpared to the other contributions, implying that the K^+ multiplicity is not sensitive to D_{unf}. As a consequence, the extraction of D^{K}_{str}, D^{K}_{fav} and D^{K}_{unf} could not be performed.

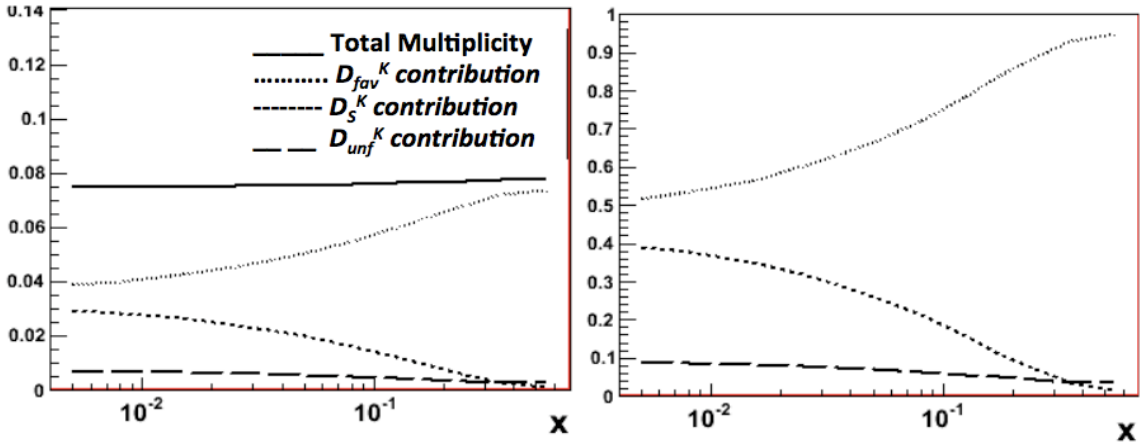

Figure 9.17: same as in figure 9.16 for K^-.

9.4 Summary and Conclusions

Pion and kaon fragmentation functions have been extracted using the pion and kaon multiplicities measured at COMPASS and the LO definition of hadron multiplicity in the QCD improved parton model. In the case of pions, using the isospin symmetry, only two fragmentation functions have been extracted assuming that the fragmentation function of strange quarks into pions is equal to the unfavored fragmentation function. They have been extracted in one dimension (12 z bins) and in two dimensions (12 z bins and 9 Q^2 bins). They were compared to previous results performed by the EMC experiment in 1989, as well as to LO and NLO predictions given by the two parametrization DSS and KRE. These two parametrization have been chosen because they reflects two extreme cases. While the KRE parametrization includes only e^+e^- data and fits only two fragmentation functions for pions and kaons, the DSS parametrization includes e^+e^- annihilation data; pp collisions data as well as semi-inclusive deep inelastic scattering data (hadron multiplicities) and fits a larger number of fragmentation functions. The pion fragmentation functions are found to be in agreement with the existing results and predictions. The results obtained using different parametrization for the parton distribution functions are compatible within less than 5% for D^π_{fav} and 10% for D^π_{unf}.

The ratio of unfavored to favored pion fragmentation functions has been derived and compared to the results from the EMC experiment at CERN (1989) and from the E00-108 experiment at JLab. The obtained ratio shows a better agreement with the JLAB result than with the EMC one. However, all experimental ratios disagree with the LO and the NLO predictions given by DSS and KRE.

In the case of kaons, the number of unknown fragmentation functions was reduced to three: strange favored (D^K_{str}), favored (D^K_{fav}) and unfavored (D^K_{unf}) fragmentation functions. Since the number of equations permit to extract only two fragmentation functions, the third one was assumed to be known and it has been taken from the DSS [34] parametrization. The resulting D^K_{fav} was found to be in agreement the EMC result as well as with the LO and NLO predicted distributions. The D^K_{fav} result depends on the parton distribution functions within less than 10% and depends on the D^K_{unf} value within less than 6%. For D^K_{str}, the result disagrees with the predictions in the entire z range. The D^K_{str} distribution has a slope which is different from the predicted one. Using different parametrizations for the parton distribution functions and different values of D^K_{unf}, D^K_{str} varies by more than 20%, the slope however remains unchanged.

In conclusion, the extracted pion fragmentation functions are in agreement with the existing measurements and predictions, as expected since pion fragmentation functions are known with a limited precision. For the kaons, however, the fragmentation function of strange quarks disagree with existing predictions. This result was also expected since this function is poorly known.

Chapter 10

Conclusions

In the framework of the study of the nucleon structure and the nucleon spin structure, the hadron production is investigated in the regime of deep inelastic scattering of leptons off nucleons. The pion and kaon multiplicities are measured using COMPASS data collected in 2004 by scattering a 160 GeV/c muon beam on deuterium (^{6}LiD) target. The analysis covers the kinematic domain: $Q^2 > 1$ [GeV/c]^2, $W > 7$ GeV/c, $0.1 < y < 0.9$, $4 \cdot 10^{-3} < x < 0.7$ and $0.2 < z < 0.85$. The measurement is performed in bins of the kinematic variables x, Q^2 and z, the latter being the most relevant variable to study the quark fragmentation process. To correct the hadron multiplicities for the acceptance of the spectrometer, a full Monte Carlo simulation has been produced using the LEPTO physics generator with a specific tuning of the fragmentation parameters in the Lund model, which were optimized for COMPASS data. In addition to the acceptance, the hadron multiplicities are corrected for radiative and smearing effects. The resulting multiplicities are compared to Leading Order (LO) theoretical calculations performed using two choices of quark fragmentation functions. The DSS parametrization for quark fragmentation functions, which is the most advanced fit to date, gives the best description of the pion multiplicities especially in the z range [0.2, 0.65], where previous measurements exist. For kaons, the data lie generally in between the two predictions.

The quark fragmentation functions are extracted from the measured pion and kaon multiplicities. The extraction is based on the LO definition of hadron multiplicities, valid under the factorization assumption in the QCD improved parton model. It requires the knowledge of the parton distribution functions. To reduce the number of unknown quark fragmentation functions, charge conjugation symmetry and isospin invariance relations are applied. Additional relations between the expected smallest fragmentation functions are assumed.
The two pion favored ($D_u^{\pi^+} = D_{\bar{u}}^{\pi^-}$) and unfavored ($D_d^{\pi^+} = D_{\bar{d}}^{\pi^-}$) fragmentation functions are extracted as a function of z and (Q^2,z). The results are in agreement within $\sim 20\%$ with previous EMC measurements and features better precision. They agree also with existing parametrizations of fragmentation functions (DSS and KRE), in the z range [0.2, 0.6]. Similarly to pions, only two kaon fragmentation functions, the strange ($D_{\bar{s}}^{K^+} = D_s^{K^-}$) and the favored ($D_u^{K^+} = D_{\bar{u}}^{K^-}$) ones, are extracted as a function of z. Results for $D_u^{K^+}$ are in agreement with EMC measurement and with predictions in the entire z range. In contrary, $D_{\bar{s}}^{K^+}$, never measured before, differs from all existing predictions. Finally, the fragmentation function of strange quarks into kaons favors a value of Δs close to zero.

Bibliography

[1] M. Ge-ll-Mann, A shematic model of baryons and mesons, Phys. Lett. 8, 214-215 (1964)

[2] F. Halzen and A.D Martin, Qaurks and Leptons, an introductory course in Modern Particle Physics, New York: Wiley, 1984

[3] E. Leader, The longitudinal spin structure of the nucleon, 12th HANUC lectures, Torino, March 2009

[4] K. Nakamura et al. (Particle Data Group), J. Phys. G 37, 075021 (2010)

[5] ZEUS Collaboration, ZEUS Results on the Measurement and Phenomenology of F_2 at Low x and Low Q^2, DESY-98-121

[6] J. D. Bjorken, Phys. Rev. D1 (1970) 1376

[7] J. Ellis and R. L. Jaffe, Phys. Rev. D10 (1974) 1669

[8] M. Anselmino, A. Effremov and E. Leader, The theory and phenomenology of polarized deep inelastic scattering, hep-ph/9501369v2

[9] SMC, Phys. Lett. B420 (1998) 180.

[10] COMPASS Collaboration, Flavour Separation of Helicity Distributions from Deep Inelastic Muon-Deuteron Scattering, Phys. Lett. B 680 (2009)

[11] A.D. Martin, W.J. Stirling, R.S. Thorne, G. Watt, Eur. Phys. J. C63:189-285, 2009

[12] K. Nakamura et al. (Particle Data Group), J. Phys. G 37, 075021 (2010)

[13] D. de Florian, R. Sassot, M. Stratmann, W. Vogelsang, Phys. Rev. Lett, 101 (2008) 072001; Phys. rev. D80 (2009) 034030.

[14] E. Leader, A.V. Sidorov and D.B. Stamenov, arxiv:1010.0574

[15] J. Bluemlein and H. Boettcher - Nucl. Phys. B636 (2002) 225.

[16] E.Leader, A.V.Sidorov and D.B.Stamenov, Phys. Rev. D73 (2006) 034023

[17] Asymmetry Analysis Collaboration - M. Hirai and S. Kumano; arXiv:0808.0413v2.

[18] E. Leader, A. V. Sidorov a,d D. Stamenov, arXiv:1103.5979v1.

[19] COMPASS Collaboration, Quark Helicity Distributions from Longitudinal Spin Asymmetries in Muon-Proton and Muon-Deuteron Scattering, Phys. Lett. B 693 (2010)

[20] HERMES Collaboration, Phys. Rev. D 71 (2005) 012003.

[21] COMPASS Collaboration, Phys. Lett. B. 680 (2009) 217.

[22] X. Artru and G. Mennesier, Nucl. Phys. B70, 93 – 115 (1974).

[23] COMPASS collaboration, Release Note, Polarized parton distributions measured in SIDIS reactions, October 4 2008.

[24] B. Andersson, G. Gustafson, G. Ingelman and T. Sjostrand, Parton Fragmentation and String Dynamics, Phys. Rept. 97, 31-145 (1983).

[25] T. Sjöstrand, The Lund String, IPPP, Durham, UK, 2009

[26] R.D. Field and R.P. Feynman, A parametrization of the properties of quark jets, Nucl. Phys. B136, 1-76(1978)

[27] SLD Collaboration, K. Abe et al., Phys. Rev. D 59, 052001 (1999).

[28] ALEPH Collaboration, D. Buskulic et al., Phys. Lett. B 357, 487 (1995).

[29] TP Collaboration, H. Aihara et al., Phys. Rev. Lett. 61, 1263 (1988).

[30] J. J. Aubert et al. (EMC), A Determination of Fragmentation Functions of u Quarks into Charged Pions, Phys. Lett. B160, 417-420 (1985).

[31] M. Arneodo et al. (EMC), Measurements of the u valence quark distribution function in the proton and u quark fragmentation functions,Nucl. Phys. B321, 541-560 (1989).

[32] B. A. Kniehl, G. Kramer and B. Pötter, Nucl. Phys. B582 (2000) 514

[33] S. Kretzer, Phys. Rev. D, volume 62, 054001

[34] D. de Florian, R. Sassot and M. Stratmann, Phys. Rev. D75 (2007) 114010; Phys. Rev. D76 (2007) 074033

[35] M. Hirai, S. Kumano, T. H. Nagai and K. Sudoh, Phys. Rev. D75 (2007) 094009

[36] S. Albino, B. A. Kniehl and G. Kramer, Nucl. Phys. B803 (2008) 42

[37] D. de Florian, R. Sassot, M. Stratmann, W. Vogelsang, Phys. Rev. Lett, 101 (2008) 072001; Phys. rev. D80 (2009) 034030.

[38] A.D. Martin, W.J. Stirling, R.S. Thorne, Phys. Lett. B363 (2006) 259.

[39] COMPASS Collaboration, V. Yu. Alexakhin et al., Phys. Lett. B647 (2007) 8. [55] http://lapth.in2p3.fr/ffgenerator/

[40] http://coral.web.cern.ch/coral/

[41] J. Kodaira, S. Matsuda, K. Sasaki ad T. Uematsu, Nucl. Phys. B159 (1979) 99; J. Kodaira, S. Matsuda, K. Sasaki ad T. Uematsu, Phys. Rev. D20 (1979) 627.

[42] R. Mertig and W. L. van Neerven, Z. Phys. C70 (1996) 637. W. Vogelsang, Phys. Rev. D54 (1996) 2023.

[43] G.Ingelman, A. Edin and J. Rathsman , April 1996, http://www.isv.uu.se/thep/lepto/

[44] http://home.thep.lu.se/ torbjorn/Pythia.html

[45] G. Corcella et al., HERWIG6: An event generator for hadron emission reactions with interfering gluons (including supersymmetric processes), JHEP 01, 010:1-96(2001).

[46] C.Hoeppner, Release Note, august 2010

[47] B. Badelek, D. Bardin, K. Kurek and K. Scholz, Z. Phys. C 66 (1995) 591

[48] Torbjörn Sjöstrand, hep-ph/9508391

[49] High P_T group, High P_T Relese Note, September 2011

[50] N. Makke, Analysis Meeting, February 2011

[51] COMPASS software, http://wwwcompass.cern.ch/compass/software/offline/input/stab/index.html

[52] R. Gazda, Asymmetries of identified particles, Analysis Meeting, November 2007

[53] COMPASS Collaboration, The Compass Experiment at CERN, NIMA 577 (2007) 455Ð518

[54] http://projects.hepforge.org/lhapdf/

[55] http://www2.pv.infn.it/ radici/FFdatabase/

[56] J. Pumplin, D.R. Stump, J. Huston, H.L. Lai, P. Nadolsky and W.K. Tung, New Generation of Parton Distributions with Incertainties from Global QCD Analysis, hep-ph/0201195v3

[57] R. Asaturyan et al., Semi-Inclusive Charged-Pion Electroproduction off Protons and Deuterons: Cross Sections, Ratios and Access to the Quark-Parton Model at Low Energies, nucl-ex/1103.1649v2

[58] A. Airapetian et al., Phys. Lett. B 666 (2008) 446, Measurement of Parton Distributions of Strange Quarks in the Nucleon from Charged-Kaon Production in Deep Inelastic Scattering on the Deuteron,

[59] COMPASS Collaboration, COMPASS-II Proposal, CERN-SPSC-2010-014

[60] Y. Giomataris, P. Rebourgeard, J. P. Robert and G. Charpak. Micromegas: A high granularity position-sentisitive gaseous detector for high particle-flux environments. Nucl. Instrum. Meth., A469:133-146, 2001

[61] Gilles Barouch and Gaell Puill. Garfield Manual.
http://consult.cern.ch/writeup/garfield/examples/mm/Welcome.html

[62] F. Sauli, Principles of operation of multiwire proportional and drift chambers, CERN 77-09

[63] W.R. Leo. Techniques for nuclear and particle physics experiments. Springer-Verlag.

[64] A. Sharma, Properties of some gas mixtures used in tracking detectors. SLAC-JOURNAL-ICFA-16-3, II B

[65] D. Thers et al., Micromegas as a large microstrip detector for the COMPASS experiment, Nucl. Instrum. Meth. A 469 (2001) 133

[66] COMPASS collaboration, Addendum 2 to the COMPASS Proposal, CERN-SPSC-2009-025, June 21 2009

[67] M.J. French et al., Design and results from the APV25, a deep sub-micron CMOS front-end chip for the CMS tracker, Nucl. Instrum. Meth. A 466 (2001) 359

[68] private communication with Y. Bedfer

[69] D. Neyret et al, New pixelized micromegas detector for the COMPASS exepriment, arxiv eprint:0909.5402

[70] http://hepdata.cedar.ac.uk/pdf/pdf3.html

[71] S. Kolbitz. Determination of the Gluon Polarization from Open Charm Production at COMPASS. PhD thesis, University of Mainz, 2008.

[72] http://wwwcompass.cern.ch/runLogbook/dirphp/

[73] A. Hillenbrand, Measurement and Simulation of the Fragmentation Process at HERMES, PhD. thesis, Fridrich-Alexander-Universitaet Erlangen (Germany), September 2005.

[74] R. Asaturyan et al., Semi-Inclusive Charged-Pion Electroproduction off Protons and Deuterons: Cross Sections, Ratios and Access to the Quark-Parton Model at Low Energies, arxiv:1103.1649.

[75] N. Makke, Update on quark fragmentation functions from pion and kaon multiplicities, COMPASS analysis meeting, Nov 2011.

List of Figures

List of Tables